



MONASH University

Control and Aerodynamic Analysis of Quadcopters in Confined Spaces

Chi Hei Vong

Master of Advanced Mechanical Engineering

Bachelor of Mechatronics Engineering (Honours)

A thesis submitted for the degree of Doctor of Philosophy at
Department of Mechanical and Aerospace Engineering
Monash University
Australia
in February 2021

Copyright Notice

1. © Chi Hei Vong (2021). Under the Copyright Act 1968, this thesis must be used only under the normal conditions of scholarly fair dealing. In particular, no results or conclusions should be extracted from it, nor should it be copied or closely paraphrased in whole or in part without the written consent of the author. Proper written acknowledgment should be made for any assistance obtained from this thesis.
2. I, Chi Hei Vong, certify that I have made all reasonable efforts to secure copyright permissions for third-party content included in this thesis and have not knowingly added copyright content to my work without the owner's permission.

Abstract

There are many potential applications to utilise aerial robots in hazardous tunnel-like environments. For example, aiding human operators with inspections of small railway culverts or mineral mappings of mining tunnels. Nevertheless, such confined environments pose many challenges for quadcopters to navigate through. Suspended dust particles, poor lighting conditions and feature-less/excessive features in the surroundings make localisation difficult. Furthermore, the fluid interactions between the rotors' downwash and the surfaces of the surroundings create aerodynamic disturbances, which threaten the quadcopter's stability and increase its risk of collision in the restricted confined space, not to mention the longitudinal wind gusts.

This thesis uses computational fluid dynamics (CFD) and physical experimental methods to investigate the fluid interactions/aerodynamic disturbances for a quadcopter hovering at various locations inside a square cross section tunnel. In this thesis, these aerodynamic disturbances are called the *Tunnel Effects* for quadcopters. The width/height of the tunnel used in this study is approximately 10 times the radius of the quadcopter's propeller and two times the width of the quadcopter's width. The Reynolds-averaged Navier-Stokes (RANS) method and a Spalart-Allmaras turbulence model are used to resolve the flow field and account for the turbulent effects of the fluid domains. Both the simulations and experimental results show that at the horizontal centre of the tunnel, the total thrust increases positioning the quadcopter from the centre of the tunnel to the ceiling, while the thrust decreases positioning the quadcopter from the centre of the tunnel to the ground. Near the wall (or once the quadcopter deviates from the horizontal centre of the tunnel), there is an induced rolling moment acting on the quadcopter due to the imbalance in lift generation between the rotors. This causes the quadcopter to accelerate toward the wall that it is closest to. At the ceiling-wall corner, there is a significant increase in thrust compared to other locations. Near the wall, as the quadcopter transitions from the centre of the tunnel to the ground, thrust decreases. However, when the quadcopter is closest to the ground, ground effect becomes more apparent and slightly increases the thrust of the quadcopter (but still lower compared to the thrust at the centre of the tunnel). Overall, the quadcopter experiences higher thrust near the wall compared to when it is at the horizontal centre of the tunnel. This is predominately driven by the significant increase in thrust in the rotor pair closer to the centre of the tunnel.

In order to mitigate the *Tunnel Effects* for quadcopters, an integral backstepping (IBS) controller was designed and implemented to enable quadcopters to robustly fly in tunnel-like confined environments, in presence of the disturbances. The location information is provided by a cross-sectional localisation scheme using Hough Scan Matching with a simple kinematic Kalman filter for providing reliable vertical and lateral position information. Combined, a semi-autonomous system is proposed with self-stabilisation in the vertical and lateral axes while a pilot provides commands in heading and the longitudinal direction of the tunnel. This allows operators without any piloting skills to command the system to perform tasks inside tunnel environments. The proposed system has been tested in both simulated tunnel environments and a real railway tunnel with generated trajectories, and the IBS controller has shown superior tracking performance in comparison with a PID controller (a baseline controller).

Declaration

This thesis is an original work of my research and contains no material which has been accepted for the award of any other degree or diploma at any university or equivalent institution and that, to the best of my knowledge and belief, this thesis contains no material previously published or written by another person, except where due reference is made in the text of the thesis.

Acknowledgment

Hoam and Kris, I am so grateful and fortunate to have you guys as my supervisors. Hoam, I still remember on first day of my PhD journey, you told me I was no longer a garage hobbyist. Looking back on it now, I am amazed by how much my perspectives have changed and how much I have grown. I have learnt so much from you both, either in life and research knowledge. I am very thankful for all the time and effort you have invested in me, especially being so patient with my writing! I still hope one day that I can catch up with the level of critical thinking and the problem solving skills that you two have.

To all my friends who were there for me during my darkest hours, thanks for all your moral support and pulling me out of the dark. Friends from IITB and the postgrad office, thank you for all your help and support. Mum and dad, thank you so much for everything you have done for me, and letting me choose this path.

Finally, I greatly appreciate the support from Ravi and the Institute of Railway Technology, and the financial support from the Rail Manufacturing Cooperative Research Centre (funded jointly by participating rail organisations and the Australian Federal Government's Business Cooperative Research Centres Program) through Project R3.7.6 – Control and navigation of micro UAV in small railway culverts and tunnels. I also thank HQprop for providing the 3D model of the propeller used in this research.

Nomenclature

Greek Alphabet Symbols

α	Angle of attack
α_e	Local effective angle of attack
α_i	Induced angle of attack
Λ	Propeller radius to motor spacing ratio
λ	Specific gas constant
ρ	Fluid density
Ω	Rotation speed of the propeller
ω_y	Vorticity about the y -axis
Γ	Circulation
δ_y	Gap between the tunnel wall and the tip of the propeller
Θ	Absolute temperature

Latin Alphabet Symbols

A_{rotor}	Area made up by the spinning propeller disk
c	Blade chord length
C_T	Thrust coefficient
d_{bottom}	Vertical distance between bottom of the fluid volume and the propeller
d_{top}	Vertical distance between top of the fluid volume and the propeller
\mathcal{F}_q	Body frame
\mathcal{F}_W	World frame
h_q	Height of the quadcopter

h_t	Height of the tunnel
K_m	Mesh refinement factor
K_{gr}	Inflation layer growth rate
L'	Lift per unit span on the airfoil
ν	Kinematic viscosity of air
N	Number of mesh elements
n_ℓ	Total number of inflation layers
p	Pressure
R	Radius of propeller
R_q	Distance between the centre of the quadcopter and a propeller
Re	Reynolds number
s	A line enclosing the tip vortex core
T_{ICE}	Thrust in ceiling effect
T_{IGE}	Thrust in ground effect
T_{OCE}	Thrust out of ceiling effect
T_{OGE}	Thrust out of ground effect
\mathbf{V}	Flow velocity vector
\mathbf{V}'	Fluctuating flow velocity vector
$\bar{\mathbf{V}}$	Mean flow velocity vector
V_i	Volume of mesh element i
v	Free stream flow velocity
v_{tip}	Velocity at the propeller's tip
w_q	Width of the quadcopter
w_t	Width of the tunnel
x_m	Average mesh element dimension
\bar{y}	Normalised coordinate in the y -axis
\bar{z}	Normalised coordinate in the z -axis

Contents

1	Introduction	11
1.1	Motivation	11
1.2	Research Challenges	12
1.3	Objectives and Scope	14
1.4	Research Contributions	14
1.5	Thesis Structure Organisation	15
2	Literature Review	16
2.1	Rotorcraft-Boundary Fluid Interaction in Proximity Flights	16
2.2	Quadcopters Control and Navigation in Confined Spaces	19
3	System Design, Modelling and Test Environment	21
3.1	System Requirements	21
3.2	Quadcopter Platform Design	22
3.2.1	Development of the Early Designs	22
3.2.2	Current Prototype	23
3.3	Quadcopter Dynamics	24
3.4	Testing Tunnel Environments	26
4	Disturbance Analysis Methods	28
4.1	Computational Fluid Dynamics Method	28
4.1.1	Simplified Quadcopter Model for Numerical Simulations	28
4.1.2	Coordinate System and Dimensional Analysis	29
4.1.3	Simulation Setup	32
4.1.4	Fluid Domains and Geometries	32
4.1.5	Governing Equations	34
4.1.6	Boundary conditions	35
4.1.7	Mesh	35
4.1.8	Analysis Methods	39
4.2	Physical Experimental Method	45
4.2.1	Calibration	46
4.2.2	Static Thrust Experiments in Open Space	47

4.2.3	Static Thrust Experiments in Tunnel Environments	48
4.2.4	Experimental Error	48
4.2.5	Discrepancy from Literature	54
5	Quadcopters Fluid Interactions in Tunnel Environments	58
5.1	Fluid Interactions at the Tunnel Origin	58
5.1.1	Vorticity and Flow Field in CFD Simulations	58
5.1.2	Blade Pressure Field in CFD Simulations	62
5.1.3	Impact on Thrust	66
5.2	Fluid Interactions near Ground and Ceiling	71
5.2.1	Difference in Thrust along H_0	71
5.2.2	Near Ground Fluid Interactions	71
5.2.3	Near Ceiling Fluid Interactions	80
5.2.4	Comparison with Quadcopter Open Space IGE and ICE	84
5.3	Fluid Interactions near Wall	87
5.3.1	Differences between H_4V_0 and O_T	87
5.3.2	Difference in Thrust along H_4	99
5.3.3	Difference in Rolling Moment along H_4	99
5.3.4	Near Ceiling and Wall Corner Fluid Interaction	101
5.3.5	Near Ground and Wall Corner Fluid Interaction	110
5.3.6	Impact on Attitude	121
5.3.7	Comparison with Quadcopter Open Space IGE and ICE	121
5.4	Quadcopters in Tunnel Effects	121
5.5	The Effect of Tunnel Size	126
6	Control of Quadcopters under Tunnel Effects	132
6.1	Localisation Strategy	132
6.1.1	Hough Transform	132
6.1.2	Hough Scan Matching	134
6.1.3	Kalman Filtering	136
6.1.4	Localisation Validation	138
6.2	Controller Design	141
6.2.1	Benchmark Controller	141
6.2.2	Integral Backstepping Controller Design	141
6.3	Flight Performance	143
6.3.1	IBS versus PID Hover Performance	143
6.3.2	IBS versus PID Trajectory Tracking Performance	144
6.3.3	Flight Performance in Real-World Tunnel	149
7	Conclusions and Future Work	154
7.1	Conclusions	154
7.2	Recommendations for Future Work	155

7.2.1	Tunnel Effect Analysis	155
7.2.2	Quadcopter System	156

Chapter 1

Introduction

1.1 Motivation

Over the last decade, along with increasing popularity in the research community, quadcopters have been deployed as Unmanned Aerial Vehicles (UAV) for a wide range of operations. Remote sensing for fire detection (He et al., 2020), agricultural field surveying (Christiansen et al., 2017), search and rescue (Hashim and Tamizi, 2018), power line inspections (Hamelin et al., 2019) and bridge inspections (Ikeda et al., 2017), are a few examples from the abundant research of applying UAVs in open, outdoor environments to reduce cost and risk for the humans involved in executing the operations.

For confined indoor environments, the risk for humans to performance tasks or operation has drastically increased. Environments such as railway culverts or sewer tunnels (Figure 1.1) often requires frequent inspection to ensure soundness of the structure. Depending on size of the tunnel, these confined environments could be difficult for an average adult to crawl in. In addition, toxic gases, liquid chemical and venomous insects or animals which occupy these habitats pose potential hazards to the inspectors. As a result, inspections in confined spaces are costly and time-consuming due to the extra safety precautions needed and the associated risks involved. Although mining tunnels are relatively larger tunnels, surveying the tunnels or mining stopes are still potentially dangerous due to unstable structure or rock falls. Furthermore, logistically it is often very time-consuming for engineers or geologists to travel deep in the mine to perform simple surveying tasks. In some cases, humans are prohibited to perform the surveying tasks at certain locations (which have high value in performing surveys at) because of the unsupported surroundings. For explorations or search and rescue missions in natural cave environments, the surrounding is even more unpredictable and such missions are certainly hazardous tasks for humans.

Originating from these high risk operations for human, the Defense Advanced Research Projects Agency (DARPA) in US has recently issued the Subterranean Challenge¹. The challenge encourages researchers to come forward with innovative robotic solutions which aid combat operations or disaster response in settings like tunnel systems, urban underground and natural cave networks. This challenge has spiked an increase in interest for subterranean/indoor aerial robotics and also

¹DARPA SubT Challenge: <https://www.subtchallenge.com/>



Figure 1.1: Commercial sewer inspection².

highlighted the great potential for using aerial robots to aid humans by conducting various tasks in such high risk, confined environments.

1.2 Research Challenges

Our research group was fortunate to be invited to a real mining site to witness these problems first-hand during the early stages of this research project. Figure 1.2 shows the entrance of a flooded mining tunnel, which all personnel are forbidden to enter due to safety concerns. Manual flights by a skilled pilot were conducted to inspect the cause of the flood. The water was highly acidic and it was constantly dripping from the ceiling at various locations in the tunnel. Inside the tunnel, loose wire meshes and cables were hanging off the ceiling, and rocks falling occasionally. All these obstacles not only make autonomous navigation challenging, but also poses physical threats to the aerial robots' safety. It was found that a section of the tunnel had collapsed, causing a blockage which resulted in the flood. It was extremely hard for the pilot to fly in such an optically dim environment while avoiding all obstacles. The occasional wind gust going in or out the tunnel also made controlling the quadcopter complex. These challenges for a human pilot also reflect the difficulty of developing a robust UAV system which can overcome the same problems.

Controlling aerial robots in enclosed and confined spaces poses many challenges which do not exist in open environments. These stem from the aerodynamic disturbances created by the interaction between the robot's propellers and the surfaces of its surroundings, and the reduction in space to regulate its attitude and position perturbed by such disturbances. In a real-world application, an aerial robot would be required to fly close to the walls or ceiling of the confined environment to

²Image source: <http://rasmith.com.au/scope-of-services/sewer/>



Figure 1.2: Entrance of a flooded mining tunnel.

conduct detailed inspections or perform certain tasks with manipulators. Hence, the aerodynamic disturbances have a huge impact on the robot's stability, reducing its capacity to complete the required tasks (Robinson et al., 2014, 2016; Sanchez-Cuevas et al., 2017), especially for light-weight systems. Furthermore, the presence of suspended dust particles, poor lighting conditions and visually similar repetitious features are the typical characteristics of tunnel-like confined spaces, which makes localisation difficult.

1.3 Objectives and Scope

To further the development of utilising quadcopter UAVs in small confined environments, such as small railway culverts, the first major objective of the research outlined in this thesis is to investigate and analyse the *Tunnel Effects* for quadcopters, which is the aerodynamic disturbances associated with quadcopter flights in confined spaces, e.g. a small tunnel. In order to characterise these disturbances, Computational Fluid Dynamics (CFD) simulations were used to visualise the flow field and understand the physics behind such phenomena. Physical experiments were also conducted to validate the result of the CFD simulations as well as providing additional information on the disturbances behaviours.

The second major objective of this thesis is to develop a robust control system capable of stabilising the quadcopter under *Tunnel Effects*. A low-level cross-sectional localisation scheme was designed for tunnel navigation, with the focus of providing reliable position information for stabilisation purposes. Using this position information, a controller was designed to mitigate the impact of the disturbances. Combined, these create a semi-autonomous system which allows a non-skilled human operator to fly the UAV in tunnel environments. Finally, the system will be tested through a comprehensive set of experiments and compared against a benchmark controller to evaluate the system's performance.

1.4 Research Contributions

Although a few studies have looked at quadcopters in ground effect (IGE), in ceiling effect (ICE), or near wall effect, the combination of these effects inside a tunnel is still yet to be investigated. One of the main contributions of this study is the investigation of the *tunnel effects* for quadcopters inside square tunnels. This is achieved through the use of CFD simulations and a series of experiments. This thesis will show that the tunnel effects for the quadcopter are complex in nature and the disturbances' behaviours change according to the quadcopter's relative position inside the tunnel. Using a baseline control system, the flight experiments also indicate that the tunnel effects caused the quadcopter's flight performance to deteriorate.

Since navigating quadcopters inside relatively smaller tunnels would require more precise position control due to the limited space to react to disturbances, a robust localisation scheme using Hough Scan Matching (HSM) was developed. This allows robust localisation in the tunnel's vertical and lateral axis, providing a semi-autonomous system with self-stabilisation in the tunnel's vertical cross section. With this localisation strategy, an IBS controller was designed and implemented to stabilise

quadcopters under tunnel effects, a low-level control system can achieve precise position tracking for stability purpose.

1.5 Thesis Structure Organisation

This thesis starts by reviewing the relevant prior work from literature in Chapter 2. This includes: rotorcraft fluid interaction in proximity flights and the control and navigation of quadcopters in confined space. Chapter 3 outlines the system requirements and the design of the quadcopter platform, as well as stating the quadcopter dynamics and the testing environments used in this work. A detailed methodology for the disturbance analysis is described in Chapter 4. This includes the computational fluid dynamic (CFD) and physical experimental method used to investigate fluid interaction between the tunnel boundaries and the rotors. A comprehensive analysis of the results obtained from the CFD and physical experiments are discussed in Chapter 5. This includes: comparing the fluid interaction behaviours at various locations in the tunnel and how they differ from the aerodynamic characteristics in open space, and a brief discussion how the size of the tunnel influences the characteristics of the disturbances. Chapter 6 outlines the localisation strategy, controller design and the system's flight performance against in presence of these disturbances. Finally, concluding remarks and recommendations for future work are made in Chapter 7.

Chapter 2

Literature Review

This chapter provides an overview of the existing literature on the fluid interactions between a rotorcraft and the surrounding boundaries for helicopters and quadcopters in proximity flights where quadcopters need to fly close to obstacles or boundaries, as well as the control and navigation of quadcopters in proximity flights and in confined environments.

2.1 Rotorcraft-Boundary Fluid Interaction in Proximity Flights

Proximity flight is one of the key challenges for rotorcraft as it can have adverse effects on flight stability (Robinson et al., 2016). A helicopter In Ground Effect (IGE) is one of the more well-known phenomenon that has received considerable attention in helicopter aerodynamic research (Cheeseman and Bennett, 1955; Curtiss et al., 1984; Light, 1993). When a helicopter is close to the ground, such as during take-off, landing or hovering, the vertical downwash generated by the propeller transitions into radial outwash parallel to the ground, which constrains the development of the rotor wake. The slipstream velocity and the induced velocity will then be altered, which causes a change in rotor thrust and power (Sanchez-Cuevas et al., 2017). A potential flow model using the method of images (PFI) was proposed by Cheeseman and Bennett (1955), a simple analytical model to describe the effect of full scale single rotor helicopters IGE. This has been experimentally validated for full scale helicopters IGE by many researchers as seen in Figure 2.1.

Following advancement in microelectronics, micro scale helicopters have started to gain popularity in the research community over the last decade. Researchers have used techniques such as Particle Image Velocimetry (PIV) (Lee et al., 2010) and CFD (Lakshminarayan et al., 2013) to study the interactions between the ground plane and the tip vortices of micro scale helicopters. CFD has allowed researchers to have a visual insight of the flow field and explore a variety of variables in the parameter space, which is more challenging to achieve using analytical methods such as PFI. Kutz et al. (2012) used an unsteady Reynolds averaged Navier-Stokes (URANS) solver to numerically simulate a helicopter IGE. The study found that the flow is unsteady and recirculating in the inner region (where the wake interactions between the adjacent rotors) of the rotor. As the rotor-ground distance decreases, the blade vortex remains close to the rotor disk and interferes with the consecutive blade passing via pressure waves. This causes increased pressure on the bottom

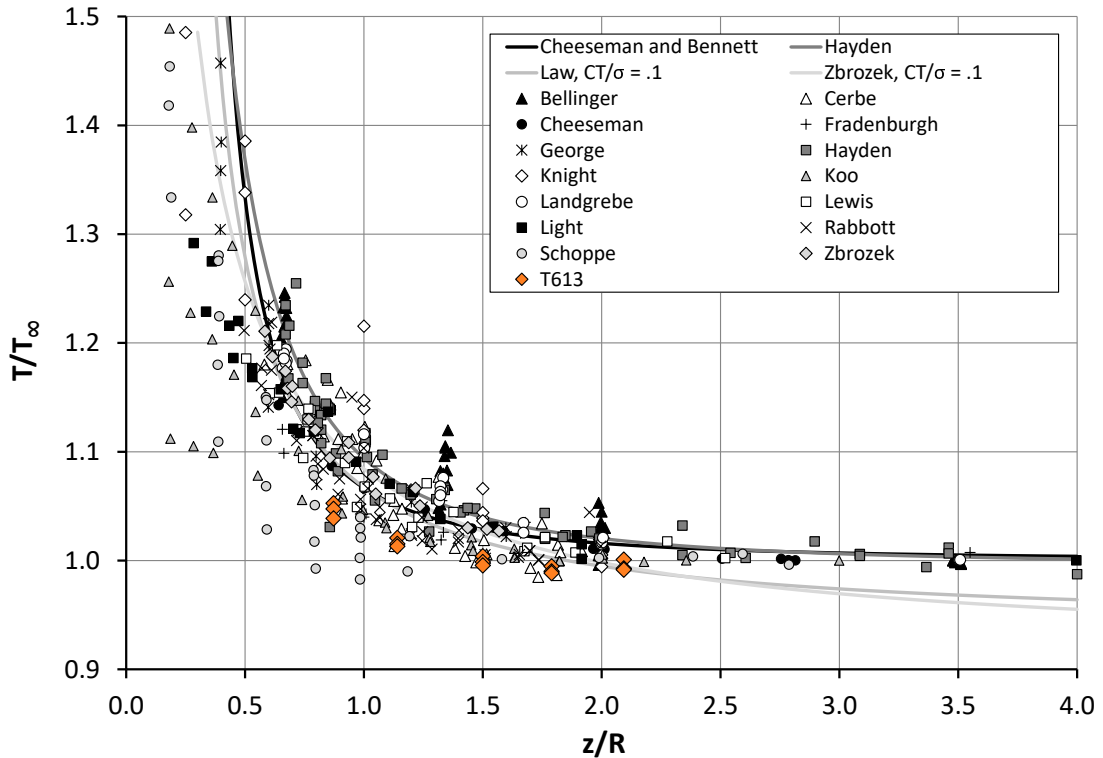


Figure 2.1: Experimental validation of helicopter in ground effect models from literature (Tanner et al., 2015).

blade surface while decreasing the pressure on the top blade surface, resulting in an increase in lift as the rotor-ground gap decreases.

In more recent work, Robinson et al. (2016) has investigated the ceiling effect of a micro helicopter using CFD simulations. The study has shown that by decreasing the rotor-ceiling gap, the local effective angle of attack along the rotor blade span increases. Therefore, increasing the sectional lift across the blade and results in improvement in the rotor efficiency. Nevertheless, the rotor was found to experience less improvement in efficiency in comparison to a rotor IGE.

However, for a small scale quadcopter, the fluid interactions between the rotors changes the aerodynamics. Yoon et al. (2016) examined the interactions and influence of changing the distance between rotors on a quadcopter in open space. The study has shown there is a decrease in thrust generation as the distance between rotors is reduced. This contributes up to 4% thrust reduction compared to a single isolated rotor. A similar study has also experimentally determined the optimal gap distance between the rotors for a quadcopter, with various combinations of propeller size and rotation speed (Kaya et al., 2017). Nevertheless, the study only presents an empirical evaluation of the relationship between the rotor gap distance and thrust, without providing an explanation about the physical mechanism which causes the phenomenon.

For quadcopter IGE, Sanchez-Cuevas et al. (2017) has found that the PFI ground effect model proposed by Cheeseman and Bennett (1955) does not show good correlation with the experimental data for a quadcopter, as illustrated in Figure 2.2. Based on this, the study proposed a new ground effect model for quadcopters which was validated using CFD and physical experiments. The study

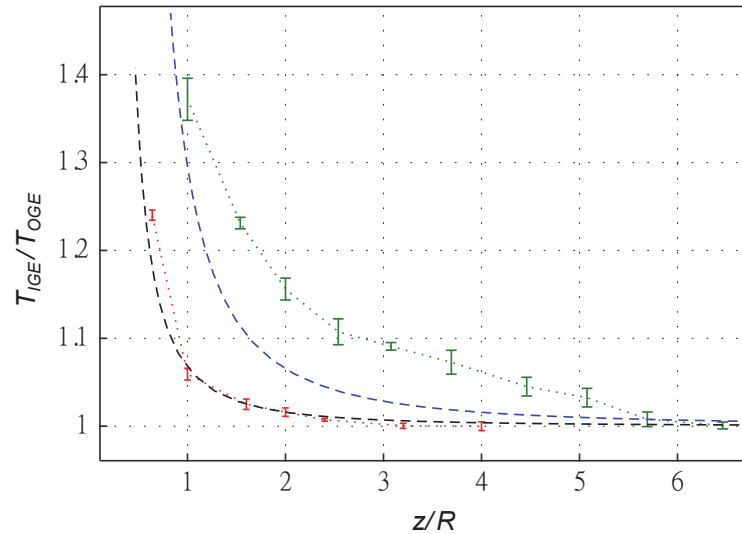


Figure 2.2: Experimental and theoretical (PFI) ground effect comparison for a quadcopter (Sanchez-Cuevas et al., 2017). The PFI approximations for a single rotor and quadcopter are shown in the black and blue dashed lines respectively. The red and green dotted line with error bars are the experiment results for a single rotor and quadcopter respectively.

also describes a phenomenon called the multirotor partial ground effect which cause asymmetrical thrusts between the rotors when not all rotors are hovering close to a ground plane. Gao et al. (2019) undertook a similar study using Stereo Particle Image Velocimetry (SPIV) to investigate the flow field and lift efficiency for quadcopters IGE, and has also found that the lift efficiency for quadcopters IGE is higher than predicted by Cheeseman and Bennett (1955)’s model. Nevertheless, Conyers et al. (2018b)’s work on quadcopters IGE has shown an underestimation of the lift profile for a quadcopter IGE compared to the two prior studies ((Sanchez-Cuevas et al., 2017; Gao et al., 2019)). The study has explored the impact of rotor rotation speed, rotor spacing and the size of rotor for quadcopters IGE using experimental methods. The results were empirically evaluated and clearly showed that these three parameters have different influences on the characteristics of the lift profile for a quadcopter IGE. These discrepancies between studies may be due to the differences in the experimental setup and the parameters which are yet to be explored (e.g. rotor separation distance).

Recently, He and Leang (2020) has conducted a more comprehensive study to explore the effect of rotor blade geometry (including pitch angle, solidity and radius), rotor spacing and rotation speed on ground effect for dualrotor, trirotor and quadrotor configurations. The study provides a novel three dimensional presentation of quadcopter IGE illustrating the relationship between IGE thrust ratio, rotor-ground distance and rotor spacing. This three dimensional relationship shows correlations with the prior studies and the discrepancy between the studies is further discussed. Similar to quadcopter IGE, quadcopters in ceiling effect (ICE) is another phenomenon that has drawn researchers’ attentions (Powers et al., 2013; Hsiao and Chirarattananon, 2018; Conyers et al., 2018a; Gao et al., 2019). These studies have all shown improvement in lift as the rotor-ceiling gap decreases, which resembles the behaviour of a single rotor ICE.

Flying close to walls or obstacles is another typical scenario for proximity flights. However,

it is still a relatively new research topic despite the increasing interests in using UAV in indoor environments. For rotor interactions with vertical walls, Robinson et al. (2014) has investigated micro helicopter (single rotor) flights in proximity to a wall. The study found that there are disturbance moments acting on the rotor blade due to the wake asymmetry phenomena when a micro helicopter is flying near a wall. This is caused by the asymmetry in vortex wake circulation and the periodic fluctuation of lift as a function of the rotor azimuth angle. Ultimately, this induced moment which varies as a function of the rotor-wall gap and rotor attitude causes an adverse impact on the micro helicopter's attitude stabilisation. More recently, Conyers (2019) has investigated ground, ceiling and near wall effects individually for quadcopters. The study indicates that quadcopter near wall effects create unbalanced thrust between the motors causing the quadcopter to accelerate towards the wall when flying near it. Paz et al. (2020) has undertaken a similar study using numerical method, and the results also show that there is an induced moment acting on the quadcopter when flying close to obstacles.

Although there is increasing number of studies focusing on quadcopter IGE and ICE, not many have investigated the effects of other parameters such as rotor separation distance on quadcopters IGE or ICE. The study of the near wall effects for quadcopters is also rare. No study to date has investigated the aerodynamics of quadcopters inside fully enclosed environments, a tunnel for example, where the impact of the planar surfaces (i.e. wall, ground and ceiling) on flying quadcopters are significant.

2.2 Quadcopters Control and Navigation in Confined Spaces

Quadcopters UAV control and navigation have been popular research topics over the last decade. Researchers have attempted to use quadcopters in a wide range of outdoor operations (Segun et al., 2018; Patel et al., 2013; Waite et al., 2019; Li et al., 2018) and many have studied wind disturbances on quadcopters (Xiang et al., 2016; Bannwarth et al., 2016; Allison et al., 2019, 2020) to improve flight stability in order to better carry those operations. However, indoor flight presents a different set of challenges compared to outdoor. For example, the absence of GPS for guidance and clustered environments increases the chance of collisions with obstacles or the enclosure both increase the flight risk.

In recent years, as the advancement of microelectromechanical system (MEMS) brought down the size of avionics, the interest of using quadcopters inside more enclosed environments, such as building-like indoor environments, started to increase. Mac et al. (2018) were able to autonomously navigate inside a small room using visual markers with an improved potential field method and track the target trajectory using a multi-objective particle swarm optimization based PID controller. Shen et al. (2013) have also successfully used a simplified occupancy grid-based incremental SLAM to autonomously navigate and map a building across multiple floors. More recently, researchers even attempted autonomous quadcopter racing using visual inertial odometry (VIO) and convolutional neural network (Delmerico et al., 2019; Kaufmann et al., 2019).

For a different kind of indoor navigation approach, Falanga et al. (2018) developed a shape morphing quadcopter which changes its morphology in order to adapt to its surrounding environment.

This allows the quadcopter to fly through small gaps or near a surface. A continuous-time infinite-horizon linear-quadratic regulator (LQR) control law was used to stabilise the system according to its current morphology. This morphing quadcopter has been tested in a laboratory environment with promising results. Although there exists many studies about localisation and mapping in indoor building environments (Yang et al., 2017; Forster et al., 2016; Achteplik et al., 2009; Lu and Song, 2015; Schmid et al., 2013), not many have implemented systems for tunnel-like environments and they pose different challenges to navigate in than indoor buildings.

Since the announcement of the DARPA Subterranean Challenge, the amount of interest in underground aerial robotics has increased. For flights inside tunnel-like environments, Mansouri et al. (2019) utilised the darkness centroid of a mining tunnel using the Otsu's threshold and generates the desired velocities for a nonlinear model predictive controller to autonomously navigate inside an underground mine. However, the system appears to oscillate a lot in the lateral axis of the tunnel which may not be desirable in a smaller tunnel or for close-up inspection of walls or ceilings. Özaslan et al. (2015) have implemented a Rao-Blackwellized particle filter based localisation scheme with a PD position controller to navigate in a penstock of a dam. Nevertheless, they did not manage to achieve reliable localisation along the longitudinal axis of the penstock even with the 2D LIDAR (Light Detection and Ranging) sensing the horizontal plane. Later, Özaslan et al. (2017) have improved their system using 3D LIDAR fusing visual odometry and IMU data with an unscented Kalman filter, and reported a promising result navigating inside a penstock autonomously. Jones et al. (2020) has also utilise rotating LIDAR and inertia measurement unit (IMU) with 3D simultaneous localisation and mapping (SLAM) (Zlot and Bosse, 2014) to achieve autonomous waypoints navigation in underground mines. The system has been tested in a several case studies to survey mining tunnels and analysis the structure of stopes.

Papachristos et al. (2019) explored the use of two different navigation systems with a model predictive controller for position control in underground mine application. The first proposed system relies on visual-inertial sensing, fusing data from a stereo camera, thermal camera and IMU together for localisation and mapping. Over time, the visible light stereo camera system suffers from drift in localisation, as well as the degraded performance due to the suspended dust particles and poor lighting condition. Yet, thermal camera remains unaffected to these factors and able to provide longer views down the tunnel as it relies on the radiation of the environment instead of the onboard illumination. For the second proposed system, a LIDAR-inertial sensing system was used. Although this system was able to provide more consistent performance over the visual-inertial system, it requires a significant increase in the payload which ultimately decreases the flight duration.

However, the implementation of a localisation system for confined tunnel-like environments, together with the controller considering the disturbances from aerodynamic interactions between the rotors' downwash and surrounding structures, and its impact on controlling a rotorcraft are very rare. Nevertheless, such systems are likely to be needed when flying through narrow gaps/channels, close to obstacles or wall boundaries inside tunnels to perform tasks such as inspections.

Chapter 3

System Design, Modelling and Test Environment

This chapter outlines the design requirements, specifications and hardware design of the proposed quadcopter platform, which is specifically targeted for tunnel environment navigation. A brief history of the previous designs is also included to show how the system was evolved to the current prototype. Additionally, the coordinate system is defined here and the quadcopter dynamics is also derived. In this work, since only the cross-sectional stability of the quadcopter in the tunnel is concerned, the dynamics is simplified to a cross-sectional dynamics to be used with the proposed controller later described in Chapter 5.

3.1 System Requirements

In this work, inspections in small tunnel environments, i.e. a railway culvert, is the target operation scenario for the system. In Australia, standard small box culverts³ ranges from 300mm to 1200mm in height, while large box culverts⁴ ranges from 600mm to 3600mm in height. This system should aim to be flyable around the larger spectrum of the small culvert and the lower spectrum of the large culvert.

Since the system is aimed to be an assistive tool for human inspectors, the quadcopter platform should be easy to control even for an unskilled pilot. Therefore, the system should be autonomous or semi-autonomous for ease of use. Tunnel environments are often harsh environments with poor lighting conditions and have dull or abundant features, the localisation sensing system should be capable to delivering reliable position information under these conditions. Furthermore, the system should have certain level of protection from water/moisture and dust, as these are also the typical conditions in these environments. In order to allow inspectors to have sufficient time to perform detailed inspections of the infrastructures, the system's battery life should last for at least 10 minutes. To achieve this, the system should be as light weight as possible, and be compact in size for navigating in smaller environments.

³Standard small box culverts dimensions - <https://www.bcp.com.au/v2/small-box-culverts.html?id=1213143>

⁴Standard large box culverts dimensions - <https://www.bcp.com.au/v2/large-box-culverts.html?id=1213151>

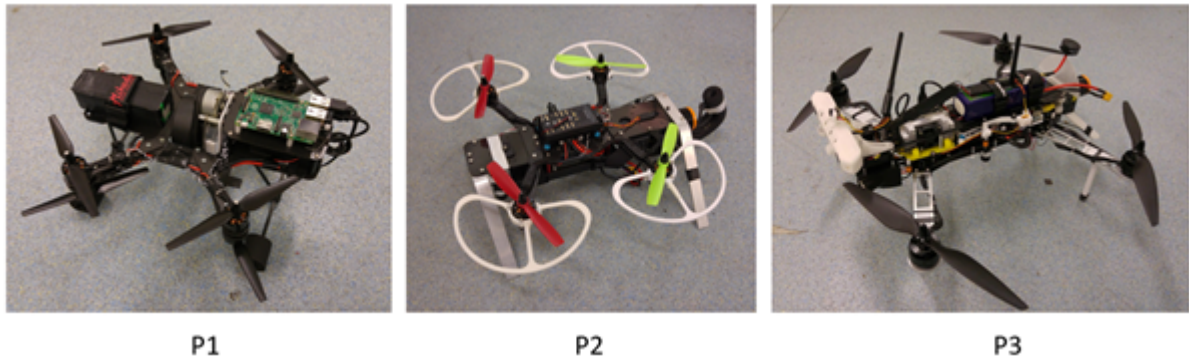


Figure 3.1: Evolution of the early prototypes from P1 to P3, with P1 being the oldest.

3.2 Quadcopter Platform Design

3.2.1 Development of the Early Designs

This first prototype, P1 was a proof of concept design for this research work, which was intended to navigate through a small custom built wooden tunnel with a 1.2m x 1.2m cross section. It was a 450mm size (450mm motor-to-motor diagonally) X8 coaxial octocopter using 6 inch propellers. There was a cut-out at the centre of the frame to fit a 360° LIDAR, the RPLIDAR A1⁵ for sensing the tunnel cross section. A simple PID controller was implemented in this system and the prototype was able to hover inside the 1.2m tunnel with observable oscillation in both the vertical and lateral axes. The main issue with this design was that the large rotating LIDAR introduced a fair amount of vibration to the system which ultimately degraded the stability and performance of the system. This prompted for better hardware choices in the system design.

The P2 prototype had an upgraded LIDAR, using the Hokuyo UST-10LX LIDAR (a more detailed description of this LIDAR is presented in Section 3.2.2). P2 had the same motor spacing as P1 but in a quadcopter configuration instead of a X8. Using the same control system and flying in the same 1.2m tunnel, improved performance was observed after tuning the controller. Nevertheless, this prototype weighed just under 2kg and only had an approximately 1.5 thrust to weight ratio. This made the system slightly under powered in presence of external disturbances.

During the design of P3, a decision was made to switch to a slightly larger frame design and testing tunnel. Using a larger tunnel can make testing and controlling the system easier. The aim was to develop a well-performed system first then focus on making the system flyable even in smaller tunnels. On the other hand, increasing the frame size allows more payload (battery and other equipment, i.e. camera for inspection tasks) to be added while maintaining a good thrust to weight ratio. P3 was a 550mm size frame using 12 inch propellers. The thrust to weight ratio was about 2 after adding lighting, camera and video transmitter module.

⁵SLAMTEC RPLIDAR A1 - <https://www.slamtec.com/en/Lidar/A1>

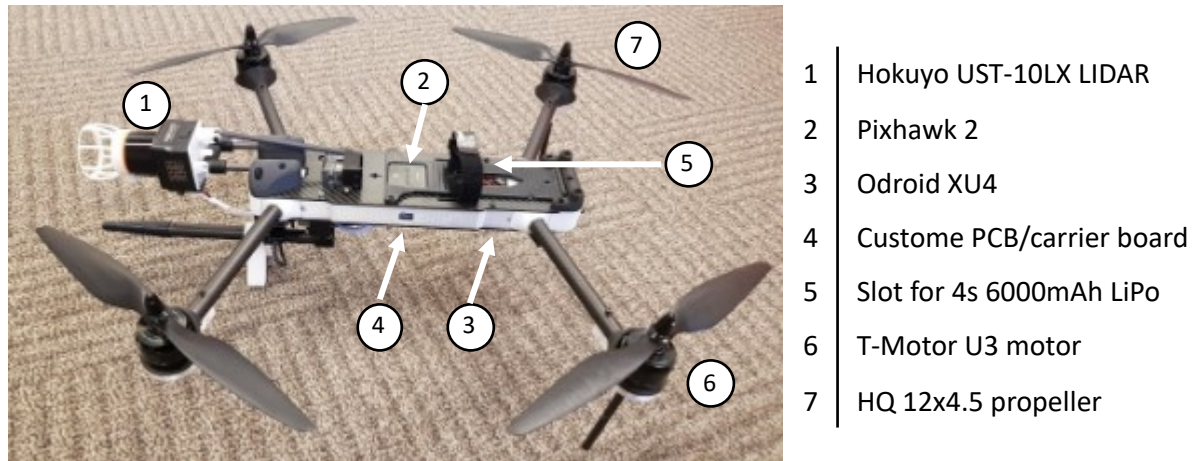


Figure 3.2: The proposed quadcopter platform with list of major hardware components.

3.2.2 Current Prototype

The following unmanned aerial system (UAS) is the current prototype for this work. It is a custom quadcopter designed specifically for flights inside tunnel environments. The quadcopter platform as well as a list of hardware used in the system are summarised in Figure 3.2 and the system diagram is illustrated in Figure 3.3. Similar to P3, the quadcopter is a 550mm size frame (motor-to-motor diagonally), with overall dimensions of 715mm(W) \times 300mm(H) (without the propellers). The body of the quadcopter is a sandwich structure with carbon fibre plates at the top and bottom layers and 3D printed vertical plates on the side to minimise weight while maintaining structure strength. Most of the avionics are hidden within the sandwiched body to minimise exposure to dust and risk of water drops from the environments.

The system weighs 2.3kg and has approximately 15-minute flight time on a 4S 6000mAh LiPo battery. Using a 12 inch propeller, the T-MOTOR U3 motor⁶ can generate approximately 0.58kg thrust at 50% throttle and 1.6kg thrust at 100%. This means the system has a 2.8 thrust to weight ratio, which provides plenty of power to react to external disturbances quickly and can allow around 0.9kg of payload to be added onboard.

For the avionics, the onboard computer is an Odroid XU4⁷ and the flight controller is the Pixhawk 2⁸. As seen in Figure 3.3, the onboard computer receives data from the LIDAR, then computes the position of system using the localisation algorithm (discussed in Section 6.1). The flight controller receives this information from the onboard computer via UART, and then using the embedded control system described in Section 6.2, it sends commands to the LittleBee 30A electronic speed controller⁹ (ESC) to control the motors. A custom PCB was designed as a carrier board for the Pixhawk 2, which also integrates the avionics and the onboard computer to achieve a compact form factor to be hidden inside the sandwich structure of the quadcopter frame. Note that

⁶T-MOTOR U3 - <https://store-en.tmotor.com/goods.php?id=317>

⁷Hardkernel Odroid XU4 - <https://www.hardkernel.com/shop/odroid-xu4-special-price/>

⁸Pixhawk 2 autopilot - <http://www.proficnc.com/content/13-pixhawk2>

⁹FVT LittleBee 30A ESC - <https://fvt-littlebee.com/>

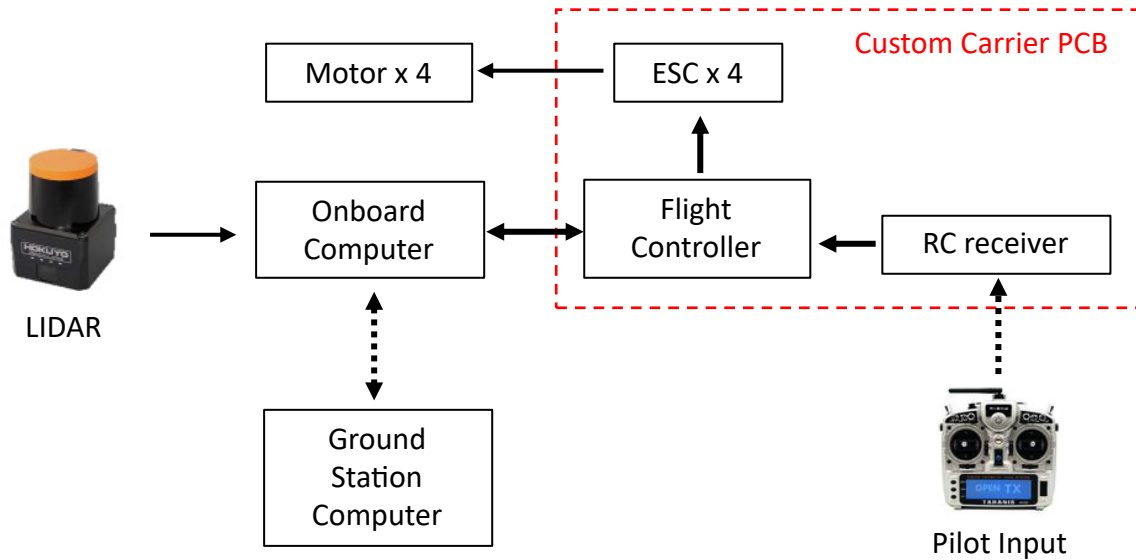


Figure 3.3: System Diagram

the Pixhawk 2 runs a custom version of the open-source Arducopter¹⁰ autopilot firmware which embeds the proposed controller and position estimator described in Chapter 5.

The main sensor for position estimation is the Hokuyo UST-10LX LIDAR¹¹ with 270° Field-Of-View, angular resolution of 0.5° and $\pm 40\text{mm}$ accuracy at 40Hz sampling frequency. It weighs only 130g, and is one of the more compact and light weight LIDAR available, making it ideal for UAV systems. The LIDAR is mounted at the front of the quadcopter such that it takes scan images of the vertical cross section of the tunnel. Hence, optimising the localisation accuracy and capability in the vertical and lateral axes of the surrounding environments. Since LIDAR sensors become unreliable when sensing reflective surfaces, i.e. water puddles commonly seen in tunnel-like environments, the blind spot of the LIDAR is placed to face downward so that its FOV mainly focuses on gathering the features of the ceiling to minimise unusable data points. This LIDAR placement is chosen over the typical top mounted - horizontal sensing placement to maximise sensing capability and position accuracy in the lateral and vertical axis of the tunnel, which ultimately allows more precision 2D position control in tunnel environments.

3.3 Quadcopter Dynamics

The coordinate system and reference frames are defined in Figure 3.4. Assuming a tunnel with constant cross-sectional shape, the world frame, \mathcal{F}_W is located at the centre of the bottom edge of the cross-sectional shape. The assumption is further explained in Chapter 5

A quadrotor can be modelled as an underactuated six degree-of-freedom (DOF) multi-input multi-output (MIMO) system with only four control inputs

$$\mathbf{u} = \begin{bmatrix} u_1 & u_2 & u_3 & u_4 \end{bmatrix}^T, \quad (3.1)$$

¹⁰Ardupilot source code - <https://ardupilot.org/copter/>

¹¹Hokuyo UST-10LX - <https://www.hokuyo-aut.jp/search/single.php?serial=167>

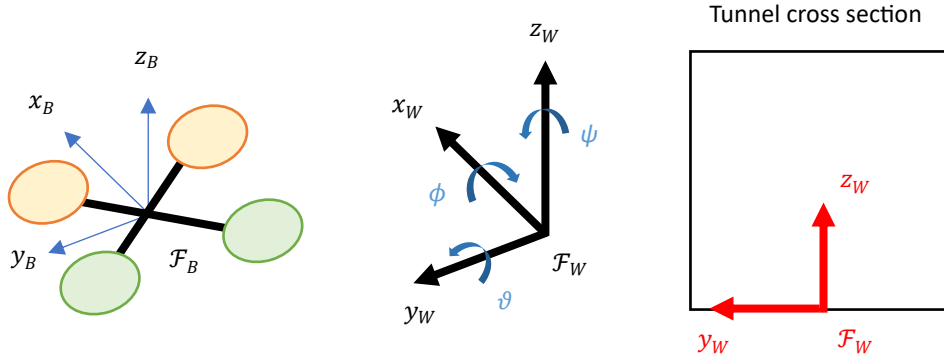


Figure 3.4: Quadcopter body frame and the location of the world frame in the tunnel.

where u_1 is the net thrust generated by the four propellers, and u_2 , u_3 and u_4 are the net body moments in the x-, y- and z-axis respectively.

The quadrotor dynamics can be derived using the Newton-Euler equations (Luukkonen, 2011) and the equations of motion of the system are

$$m\ddot{\mathbf{r}} = \mathbf{g} + \mathbf{R}\mathbf{T} \quad (3.2)$$

$$\mathbf{I}\dot{\boldsymbol{\omega}} = \boldsymbol{\tau} - \boldsymbol{\omega} \times (\mathbf{I}\boldsymbol{\omega}), \quad (3.3)$$

where $\mathbf{T} = [0 \ 0 \ u_1]^\top$, $\boldsymbol{\tau} = [u_2 \ u_3 \ u_4]^\top$, m is the mass of the system, \mathbf{r} is the position vector in the world frame, $\boldsymbol{\omega}$ is the vector of angular velocities in the body frame, \mathbf{I} is the diagonal inertial matrix of the quadrotor, g is the gravitational force, $\mathbf{g} = [0 \ 0 \ -g]^\top$,

$$\mathbf{R} = \begin{bmatrix} C_\theta C_\psi & S_\phi S_\theta C_\psi - C_\theta S_\psi & C_\phi S_\theta C_\psi + S_\phi S_\psi \\ C_\theta S_\psi & S_\phi S_\theta S_\psi - C_\theta C_\psi & C_\phi S_\theta S_\psi - S_\phi C_\psi \\ -S_\theta & S_\phi C_\theta & C_\phi C_\theta \end{bmatrix}, \quad (3.4)$$

which is the rotation matrix from body frame to world frame. Note that S_x denotes $\sin x$ and C_x denotes $\cos x$.

Assuming that ψ , the vehicle's heading, is regulated by a low-level controller and ψ is small, the translational dynamics of the quadrotor can be simplified to

$$\begin{bmatrix} \ddot{x} \\ \ddot{y} \\ \ddot{z} \end{bmatrix} = \begin{bmatrix} u_1 \cos \phi \sin \theta \\ -u_1 \sin \phi \\ u_1 \cos \phi \cos \theta - g \end{bmatrix}. \quad (3.5)$$

As discussed in Section 1.3, this work only focuses on the cross sectional localisation in the tunnel. Hence only the y-z plane is considered in system dynamics, we can define the system to be

$$\begin{aligned} \dot{\mathbf{x}}_1 &= \mathbf{x}_2 \\ \dot{\mathbf{x}}_2 &= \mathbf{f} + \mathbf{b}u_1, \end{aligned} \quad (3.6)$$

with

$$\mathbf{x}_1 = \begin{bmatrix} y \\ z \end{bmatrix}, \quad \mathbf{x}_2 = \begin{bmatrix} \dot{y} \\ \dot{z} \end{bmatrix},$$

where $\mathbf{f} = \begin{bmatrix} 0 \\ -g \end{bmatrix}$, and $\mathbf{b} = \begin{bmatrix} -\sin \phi \\ \cos \phi \cos \theta \end{bmatrix}$.

3.4 Testing Tunnel Environments

Since real-world tunnels are not easily accessible for prototype testing, two different in-house tunnel-like environments were used in this project (Figure 3.4):

- [1] **2.4m tunnel:** a standard 20ft shipping container with internal cross sectional dimensions of 2.35m(W) \times 2.39m(H) and 6.06m in length
- [2] **1.5m tunnel:** a custom built wooden tunnel placed inside the shipping container, with internal cross sectional dimensions of 1.5m(W) \times 1.5m(H) and 2,5m in length

The 1.5m tunnel was constructed with a wooden frame and using 5mm thick corflute sheets as panels. During all the experiments relating to the 1.5m tunnel, it was placed at the centre of the 2.4 tunnel. The widths of the 2.4m tunnel and the 1.5m tunnel are approximately three times and two times the width of the quadcopter respectively, restricting the amount of space for the system to react to disturbances. These two tunnels satisfied the target tunnel size described in Section 3.1 and the detailed usage will be described in Chapter 4 and 5.



Figure 3.5: Testing tunnels used in this project.

Chapter 4

Disturbance Analysis Methods

In this chapter, the characteristics of the aerodynamic disturbances created from flying a quadcopter in tunnel environments are investigated. Both computational fluid dynamics (CFD) and physical experiments are used in this study. The CFD simulations allows various flow properties to be explored within the computational domain as well as providing flow visualisation for understanding the physics behind the aerodynamic phenomena. The physical experiments are arguably more efficient to obtain certain parameters (i.e. thrust generated from the propellers) at multiple locations within the tunnel. The methodology of the CFD simulations is first outlined in this chapter, followed by the experimental method. The work described in Chapter 4 and 5 is under preparation to be submitted for publication at the time of writing (Vong et al., 2021a).

4.1 Computational Fluid Dynamics Method

4.1.1 Simplified Quadcopter Model for Numerical Simulations

A quadcopter is a complex mechanical model and including all the geometries of a quadcopter in a CFD simulation is computationally expensive. For simplicity, the quadcopter frame has been neglected. This approach follows prior studies (Céspedes and Lopez, 2019; Misiorowski et al., 2019) who have successful results simulating quadcopters fluid dynamics using the four rotors only as a model in the simulations. The limitation for this four-rotor-only model is that the effect of the fuselage has been neglected. Studies (Yoon et al., 2017; Ventura Diaz and Yoon, 2018) have shown up to 7% different on the total thrust generated by the rotors due to the fuselage, and this difference is reflected in the experiment results and the discussion in Chapter 5. However, including the fuselage in the model introduces a whole new set of parameters to study, focused upon the shape, size and location of the fuselage, which is beyond the scope of this project. Furthermore, the four-rotor-only model is sufficient to highlight the relative aerodynamic differences between a quadcopter hovering in open space and tunnel environments.

For a quadcopter, Yoon et al. (2016) found that the separation distance between the propellers can affect the efficiency of lift generation up to 4% due to the wakes' interactions. Nevertheless, for the scope of this research, the radius of the quadcopter (distance between the centre of the

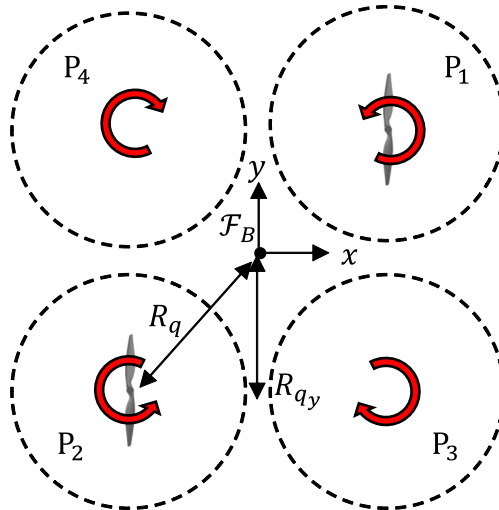


Figure 4.1: Quadcopter configuration and location of its body frame, \mathcal{F}_B . The placement of the four propellers is symmetrical about its origin. The dotted circles represent the rotor disks as described in Figure 4.4. The propellers/rotor disks are labelled from P_1 to P_4 .

quadcopter and a propeller), R_q , is chosen to be fixed. The radius of the propeller is defined as R , and the size of the quadcopter chosen for the disturbance analysis (used in Chapter 4 and 5) is $R_q = 2R$. The arrangement of the propellers on the quadcopter model is indicated in Figure 4.1. The dotted circles in Figure 4.1 represent the fluid domains enclosing the rotor, which are described in Figure 4.4.

4.1.2 Coordinate System and Dimensional Analysis

For convenience of the analysis in this chapter, the world frame, \mathcal{F}_W is placed at the centre of the simulation tunnel, as shown in Figure 4.2.

When studying aerodynamic parameters of rotorcraft, all length variables are normalised by the rotor radius. For example, the non-dimensionalised distance, z/R describes the height of a helicopter from the ground in ground effect. However, for a quadcopter inside an enclosed square tunnel, z/R or y/R do not provide sufficient information about the quadcopter's relative position to all boundaries. In addition, unlike single-rotor helicopters, the width and height of a quadcopter also determine its size other than the size of its rotors. Hence, a new dimensionless coordinate is introduced in order to provide a more comprehensive knowledge of the quadcopter's position as well as its scale relative to the tunnel. The dimensionless coordinate is defined using

$$\bar{y} = \frac{2y}{w_t - w_q}, \quad (4.1)$$

$$\bar{z} = \frac{2z}{h_t - h_q}, \quad (4.2)$$

where w_t and w_q are width of the tunnel and the quadcopter (the maximum distance between the left and right propeller tip) respectively, and h_t and h_q are the height of the tunnel and the quadcopter respectively. The placement of the quadcopter is limited to, $y \in \left[\frac{-(w_t - w_q)}{2}, \frac{(w_t - w_q)}{2} \right]$ and

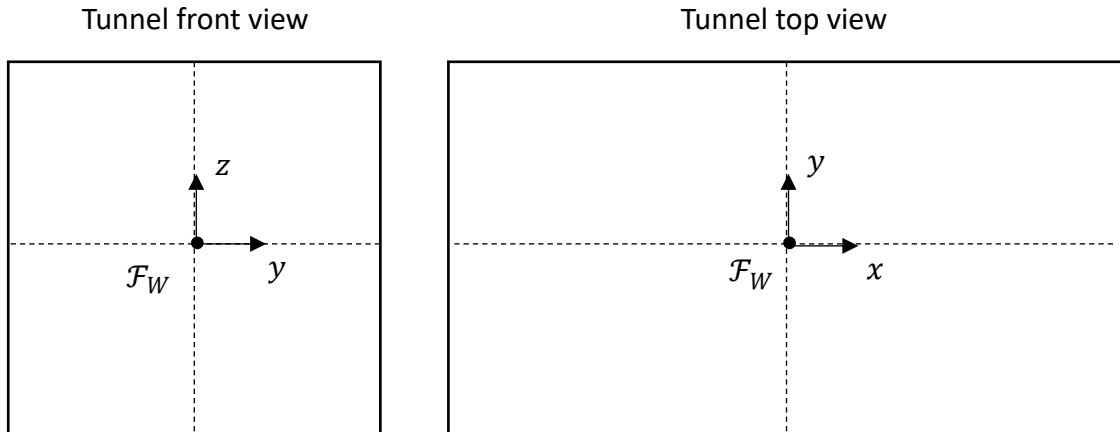


Figure 4.2: Location of the world coordinate frame, \mathcal{F}_W inside the simulation tunnel.

$z \in [-\frac{(h_t-h_q)}{2}, \frac{(h_t-h_q)}{2}]$ to prevent the quadcopter contacting the tunnel's boundaries. This means $\bar{y} \in [-1, 1]$ and $\bar{z} \in [-1, 1]$. The value of -1 or 1 in \bar{y} or \bar{z} indicates the quadcopter is in contact with the tunnel's wall, ceiling or ground. The dimensions of the simulation tunnel (the 1.5m tunnel described in Section 3.4) used in this chapter are $w_t \approx 2w_q$ and $h_t \approx 5h_q$ and $w_t = h_t \approx 9.8R$, which is a relatively small tunnel for a quadcopter to navigate in.

The propellers used in this research is the 12x6 propeller from HQprop¹². The quadcopter consists of two clock-wise (CW) rotation and two counter clock-wise (CCW) rotation propellers. Each propeller has a radius, R , of 152.4 mm (6 inches) and a 6-inch pitch. For a propeller, the Reynolds number, Re , is typically defined using

$$Re = \frac{v_{tip}c}{\nu}, \quad (4.3)$$

where v_{tip} is the velocity at the propeller's tip, c is the blade chord length and ν is the kinematic viscosity of air. Note that since the chord length of the chosen propeller is non uniform, the value of c chosen in thesis is 25mm, which is taken as the chord length at $0.5R$ of the propeller. The Reynolds number is approximately 132,000 at the propeller tip when the rotation speed is at 5000RPM. The quadcopter size is $R_q = 310\text{mm}$ which is slightly larger than the quadcopter system described in Section 3.2.2.

For the convenience of referring to the different locations in the tunnel, a label has been assigned to each of the 42 key locations employed in the CFD simulations and the physical experiments. Figure 4.1 illustrates how the labels are assigned to the tunnel and Table 4.1 is a summary of the labelled locations and their corresponding position in (\bar{y}, \bar{z}) . For example, location $(\bar{y}, \bar{z}) = (0.2, 0.95)$ is H_1V_3 and $(\bar{y}, \bar{z}) = (0.4, 0)$ is H_2V_0 . The origin of the tunnel has a special label and it is referred to as O_T . When referring to a column of locations, e.g. $\bar{y} = 0.6$, the label H_3 is used without combining with V. Similarly, for referring to a row of locations, e.g. $\bar{z} = 0$, V_0 is used.

¹²HQProp 12x6 propeller - <https://www.getfpv.com/hqprop-12x6-cw-propeller-thin-electric-2-blade-2-pack.html>

Table 4.1: Location label definition in the normalised coordinate systems, (\bar{y}, \bar{z}) and $(\frac{y}{R}, \frac{z}{R})$

Label	V_{-3}	V_{-2}	V_{-1}	V_0	V_1	V_2	V_3
\bar{z}	-0.95	-0.64	-0.32	0	0.32	0.64	0.95
z/R	-3.75	-2.5	-1.25	0	1.25	2.5	3.75

Label	H_0	H_1	H_2	H_3	H_4	H_5
\bar{y}	0	0.2	0.4	0.6	0.8	0.99
y/R	0	0.5	1	1.5	2	2.5

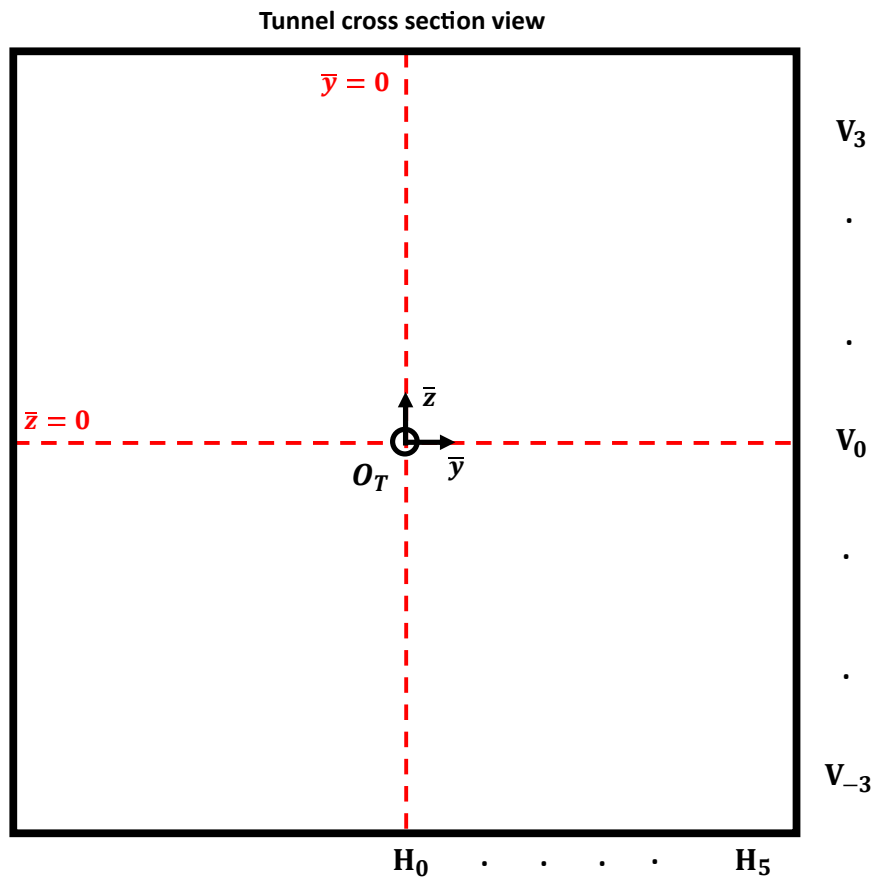


Figure 4.3: Location label in the tunnel cross section view. The red dashed lines are the symmetry lines. The right hand side of the tunnel is divided into 6 columns (from H_0 to H_5) and 7 rows (from V_{-3} to V_3). The origin of the tunnel is labelled as O_T .

4.1.3 Simulation Setup

The simulations have been run on ANSYS Fluent v18.1 using a pressure-velocity solver with the SIMPLEC scheme (ANSYS Inc., 2016). The transient formulation is set to be Bounded Second Order implicit (ANSYS Inc., 2016) for higher accuracy. As for the flow convergence criteria, the residuals of continuity, the velocities and the turbulent dissipation are required to be below 1×10^{-4} to ensure qualitative convergence.

The rotation speed of the propellers is chosen to be 5000RPM, hence, the tangential velocity at the tip of propeller is $v_{tip} = 79.8\text{m/s}$. This means the maximum flow velocity is at Mach 0.23 which allows the simulations to be modelled with incompressible flow. The timestep size was chosen according the Courant-Friedrichs-Lewy (CFL) condition (De Moura and Kubrusly, 2013) to ensure the stability of the numerical solution. The timestep size was set to be $\Delta t = 3 \times 10^{-5}\text{s}$, which has a Courant number less than 1 and satisfies the CFL condition. Each timestep is equivalent to 0.0025 (0.9°) of a rotation of the propeller.

In order to minimise computation time, all simulations were first initialised with the hybrid initialisation (ANSYS Inc., 2016) and using the $K_m = 4$ mesh (as described in Section 4.1.7) to run the “initialisation simulations” for 2800 timesteps with a timestep size of $3 \times 10^{-4}\text{s}$, which is equivalent to 70 revolutions of the propellers. Then, the simulations were run using the fine mesh ($K_m = 12$) and initialised with the interpolated solutions of the “initialisation simulations” using the chosen timestep size of $\Delta t = 3 \times 10^{-5}\text{s}$. The simulations were run until the computed mean thrust of the propeller has less than 0.2% variation per revolution. In most cases, this takes approximately 3000 timesteps. Therefore, all simulations were set to run until 4000 timesteps to ensure the generated thrust has converged to steady state. All the simulations were run on the Monash University MonARCH High-performance computing (HPC) facility. Each simulation took approximately 22 days using 28 CPU cores, 2 GPUs and 128GB of memory.

For Section 5.1 to 5.3 in Chapter 5, the simulations include 14 locations in the 1.5m tunnel. They are H_0V_2 to H_0V_{-2} and H_4V_2 to H_4V_{-2} . For Section 5.5, all the simulations were run at tunnel location O_T (centre of the tunnel) but with various size of the square tunnel. Further details for the tunnel’s geometry is described in Section 4.1.4.

4.1.4 Fluid Domains and Geometries

Propeller Disk:

The propeller is modelled as a rigid body and it is enclosed by a cylindrical fluid domain, which is illustrated by Figure 4.4. Since the chord length, c of the propeller varies along the blade, $c = 25\text{mm}$ is used. The method to determine the dimensions for the fluid domain is detailed in Section 4.1.7.3. The combination of four propeller disks following the configuration of Figure 4.1 forms the simulation quadcopter model.

Open Space (Out-of-Tunnel):

For the open space simulation, the fluid domain of the space is considered to be a cylinder with radius, height from the origin and height below the origin being $32R_q$, $16R_q$ and $32R_q$ respectively. This follows the work of Robinson et al. (2016), but R_q is used instead of R . This is to minimise the

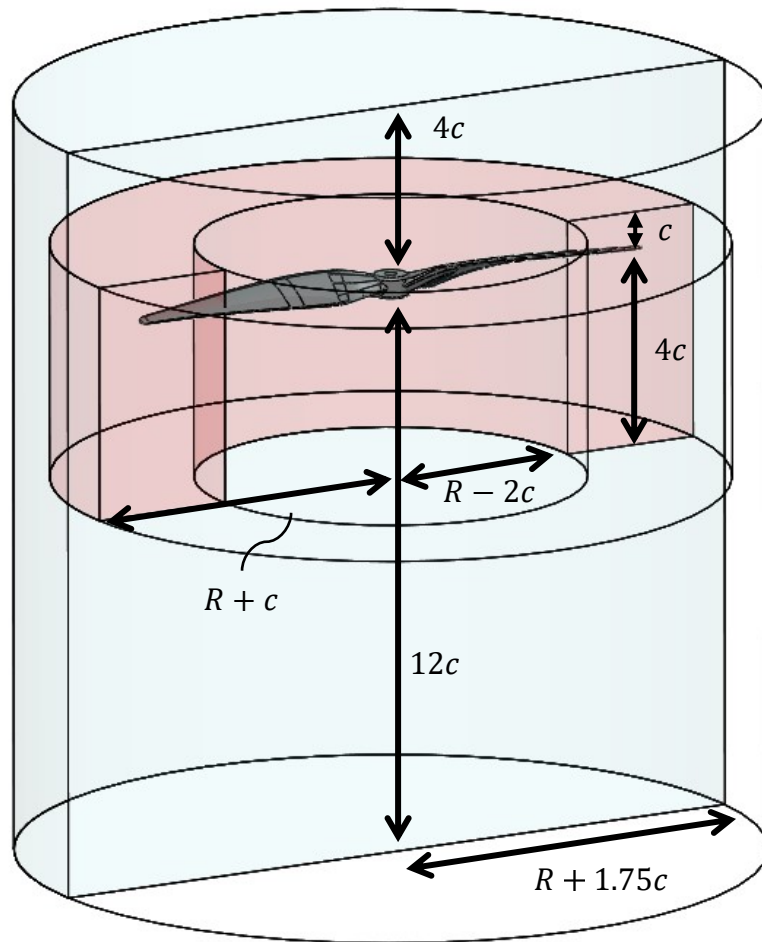


Figure 4.4: Cut away view of the fluid domain surrounding a propeller, which is also the mesh refinement region 1 (blue). The ring-shaped region indicates the refinement region 2 (red) of the propeller.

effects of the fluid interactions at the far field boundaries, considering the four rotors configuration instead of a single rotor.

In-Tunnel:

The fluid domain for the simulated tunnel is modelled as a rectangular box with both ends set to the boundary condition described in Section 4.1.6. For Section 5.1 to Section 5.3, the width and height of the tunnel are $w_t = 10R$ and $w_h = 10R$ respectively, and its length is $60R$. The quadcopter model is placed at $x = 0$ and different locations z - y plane of the tunnel to examine the effect of its relative position to the surface boundaries. For the tunnel size study in Section 5.5, the variation of tunnel sizes are $w_t = \{6R, 7.5R, 10R, 15R\}$.

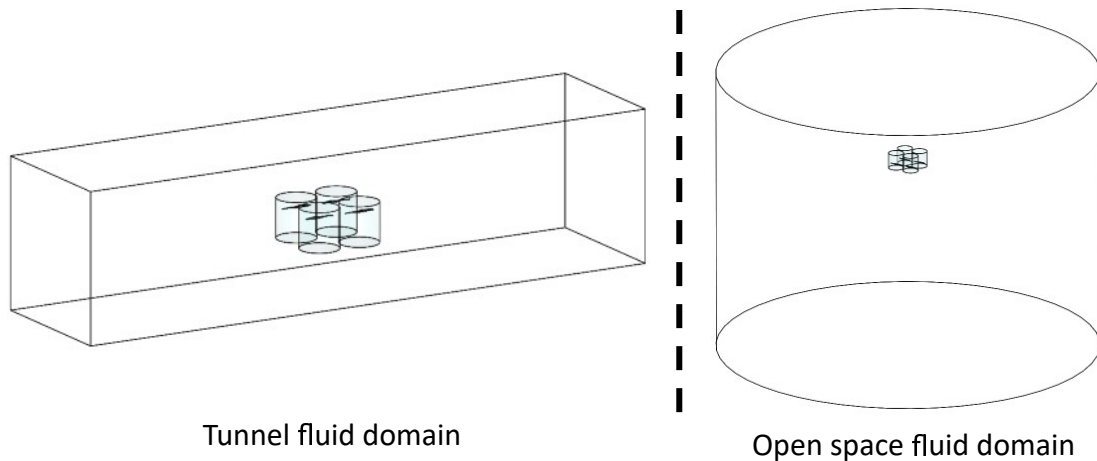


Figure 4.5: The fluid domains of the quadcopter model in open space and in simulation tunnel. Note that this figure only shows an example placement of the quadcopter in the tunnel, the location of the quadcopter changes with the different simulations.

4.1.5 Governing Equations

4.1.5.1 Navier-Stokes Equations and Turbulence Modelling

The fluid dynamics of the system are governed by the Navier-Stokes equations. For incompressible flow the Navier-Stokes equations may be written in the following form,

$$\frac{\delta \mathbf{V}}{\delta t} + \mathbf{V} \cdot \nabla \mathbf{V} = -\frac{1}{\rho} \nabla p + \nu \nabla^2 \mathbf{V}, \quad (4.4)$$

where \mathbf{V} , ρ , p and ν are the flow velocity vector, fluid density, pressure and kinematic viscosity respectively. Note that the body forces are implicit.

In order to derive the numerical solution of the Navier-Stokes equations in the computational domain for a discretised mesh of fluid elements with limited computational resources, Equation (4.4) was modelled as the Reynolds-Average Navier-Stokes (RANS) equations. The limitation for the RANS model is the reduced accuracy in reproducing the entire flow field since the flow properties have been time averaged. However, compared to more accurate models such the direct numerical simulation (DNS) (Moin and Mahesh, 1998) and large-eddy simulation (LES) (Mason, 1994), the RANS model requires significantly less computation resources while providing sufficient information of the flow properties (Guruswamy, 2013).

The flow velocities are decomposed into the mean and fluctuating components

$$\mathbf{V} = \overline{\mathbf{V}} + \mathbf{V}', \quad (4.5)$$

where $\overline{\mathbf{V}}$ and \mathbf{V}' are the mean and fluctuating flow velocities respectively. The mean flow velocity component, $\overline{\mathbf{V}}$ is obtained at each timestep using

$$\overline{\mathbf{V}} = \frac{1}{\Delta t} \int_t^{t+\Delta t} \mathbf{V} dt. \quad (4.6)$$

After substituting Equation (4.5) into Equation (4.4), (4.4) becomes (Galdi, 2011)

$$\frac{\delta \rho \bar{\mathbf{V}}}{\delta t} + \nabla \cdot (\rho \bar{\mathbf{V}} \otimes \bar{\mathbf{V}}) = -\nabla p + \nabla \cdot (\tau - \rho \bar{\mathbf{V}}' \otimes \bar{\mathbf{V}}'), \quad (4.7)$$

where $\rho \bar{\mathbf{V}}' \otimes \bar{\mathbf{V}}'$ is the Reynolds stress term which considers the effects of the turbulent motions of on the mean stresses (Alfonsi, 2009). In order to close Equation (4.7) a turbulence model is needed. The Spalart-Allmaras (SA) (Spalart and Allmaras, 1992) one-equation turbulence model was chosen for a good compromise between computational cost and accuracy. As a one equation turbulence model, it is less computationally expensive than two equation based models such as shear stress transport (SST) $k - \omega$ model (Menter, 1994). Additionally, it is also commonly used in literature relating to flow around micro rotors (Kang and Kwon, 2002; Robinson et al., 2016; Lakshminarayan et al., 2013).

4.1.5.2 Sliding Mesh Method

Following the work from Steijl and Barakos (2008), the sliding mesh method was chosen to simulate the rotating the four propeller disks (as described in Section 4.1.4) within the tunnel fluid domain. It is a common technique adopted by researchers in studies related to rotating propellers or rotors (Misirowski et al., 2018; Liu and Luo, 2017; Yang et al., 2018). The sliding mesh allows motion between two non-conformal interfaces provided the interfaces remain in contact with each other. At each timestep, the flow information is transferred and interpolated across the boundaries of the interfaces.

4.1.6 Boundary conditions

For all the in-tunnel cases, the wall boundaries (the propellers' surfaces and the tunnel walls) are treated as no-slip walls, meaning that the fluid will have zero velocity at the boundary. The ends of the tunnels, and the ends of the fluid cylinder of the open space case are treated as pressure outlets (ANSYS Inc., 2016), which the pressures are set to be 0Pa and backflow is allowed. This acts as "opening" boundaries (ANSYS Inc., 2010) where the gauge pressure is set to 0Pa and the flow is free to travel in and out of the boundary.

4.1.7 Mesh

The meshing techniques of this research were adopted from the work of Robinson et al. (2016). Unstructured tetrahedral meshes were generated by ANSYS 17.1 (ANSYS Inc., 2016) with various refinement regions added to each mesh to ensure the rotor wakes are resolved accurately. For meshing sizing, a global scaling factor, K_m was used in order to simplify the mesh scaling progress. A comprehensive mesh convergence study has been conducted to determine an acceptable value of K_m , which is detailed in Section 4.1.7.2. The value $K_m = 12$ was used in this study.

To improve the accuracy of the boundary layers around the propellers and the tunnel walls, prism layers, or inflation layers have been added to the surface boundaries. The total number of

inflation layers was calculated using (Robinson et al., 2016)

$$n_\ell = \frac{\log(1 - 4K_m(1 - K_{gr}))}{\log K_{gr}}, \quad (4.8)$$

where the growth rate K_{gr} was set to be 1.033 (which was found to be sufficient in Robinson et al. (2016)'s study to resolve boundary layers), and n_ℓ is the number of inflation layers which is rounded up to the nearest integer value.

4.1.7.1 Refinement regions

Two refinement regions have been added to each of the propeller disk domains as illustrated in Figure 4.4. Refinement region 1 has the same dimension as the propeller disk geometry and refinement region 2 is a smaller cylindrical ring region around the propeller tips within the propeller disk domain. It is used to capture the tip vortices of the propellers more accurately. Refinement has also been added to the interfaces between the tunnel fluid domain and the propeller disk domains to ensure the flow information can be transferred more accurately using the sliding mesh technique.

Since the rotor wake is expected to interact with the tunnel walls, refinement and inflation layers have been added adjacent to the tunnel boundaries. For the tunnel boundaries, $K_{gr} = 12$ and 15 inflation layers were found to be sufficient for this study. A zoomed-in view of the propeller mesh is shown in Figure 4.6, and a overview of the refinement for the tunnel walls, propeller disks and the sliding interfaces is shown in Figure 4.7. A summary of the mesh regions and their maximum element dimension is shown in Table 4.2.

Table 4.2: Summary of the parameterised mesh element size of the different fluid domains in terms of R and K_m

Mesh region	Maximum element dimension
Global	$\frac{16R}{K_m}$
Tunnel surface	$\frac{R}{5}$
Propeller surface	$\frac{3R}{50K_m}$
Propeller disk	$\frac{4R}{5K_m}$
Refinement ring	$\frac{2R}{5K_m}$
Disk interface	$\frac{3R}{5K_m}$

4.1.7.2 Mesh convergence study

A mesh convergence study has been conducted to ensure the mesh refinement is sufficient to minimise the spatial discretisation error and resolve the flow features to an acceptable level of accuracy. The

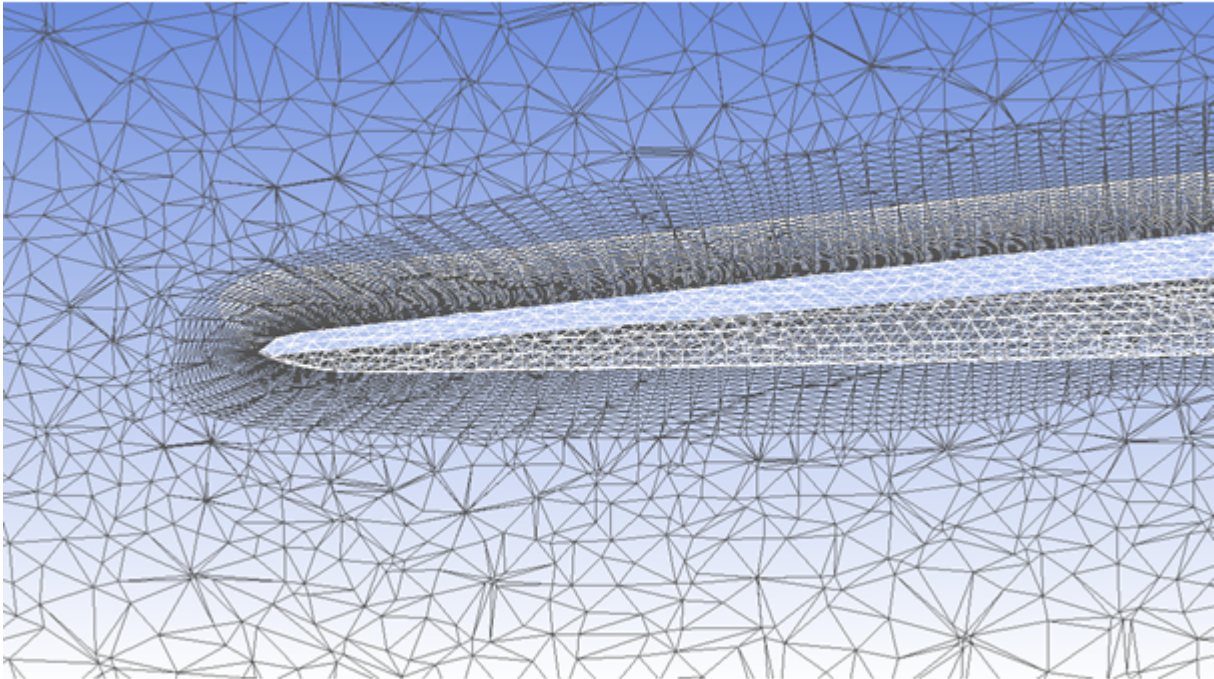


Figure 4.6: A zoomed-in view of the mesh near the tip of the propeller.

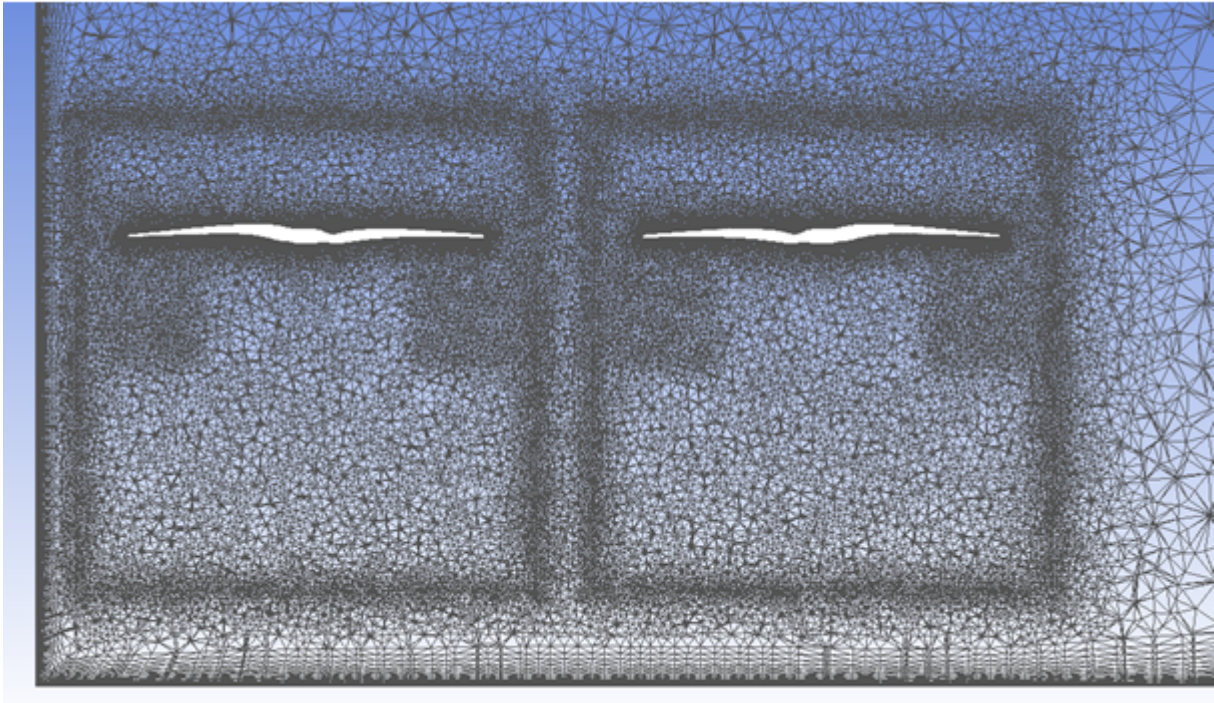


Figure 4.7: A cross-sectional view of the mesh showing the refinement regions around the propellers and the sliding mesh interfaces.

Table 4.3: Summary of mesh convergence study result

K_m	x_m/R	N	T % error
4	0.653	555,567	6.93
6	0.497	1,260,229	9.30
9	0.369	3,078,789	9.15
12	0.295	6,000,329	3.37
15	0.248	10,110,775	1.24

study involved running the single rotor hovering case (described in Section 4.1.4) with the different refinement factors, $K_m \in \{4, 6, 9, 12, 15\}$. The average element dimension, x_m , of each mesh was estimated using

$$x_m = \left(\frac{1}{N} \sum_{i=1}^N V_i \right)^{\frac{1}{3}}, \quad (4.9)$$

where N and V_i are the number of elements and the volume of element i respectively.

The Richardson extrapolation (Roache and Knupp, 1993) is used to estimate the solution at zero grid spacing

$$f_{x=0} = f_{n+1} + \frac{(f_n - f_{n+1})r^p}{r^p - 1}, \quad (4.10)$$

where f_n is the solution of mesh n and $x_n < x_{n+1}$, and the refinement ratio between the meshes, $r = x_{n+1}/x_n$. A smaller value of n indicates a more refined mesh. The order of convergence (Roache, 1998), p is calculated using

$$p = \ln\left(\frac{f_{n+1} - f_n}{f_n - f_{n-1}}\right) / \ln(r). \quad (4.11)$$

Since the rotor thrust, T , is a key variable of interest, it is used as a monitored variable in the mesh convergence study.

4.1.7.3 Domain size study

Beside the mesh convergence study, a domain size study was completed to ensure the dimensions of the fluid cylinder containing the propeller had minimal influence on the flow characteristics around the propeller.

The size of the propeller's fluid domain has been determined experimentally through a series of simulations by varying the size of the domain and monitor its impact on the thrust generated by the propeller. A set dimensions is selected when the generated thrust is less than 5% difference from the smaller and larger set of dimensions. The vertical distance from the top, d_{top} , and from the bottom, d_{bottom} , of the cylinder was first determined. Then using selected set of d_{top} and d_{bottom} , another

Table 4.4: Summary of domain size study - rotor disk radius variation

disk radius	$R + 1c$	$R + 1.75c$	$R + 2.5c$	$R + 3.25c$	$R + 4c$
difference [%]	-0.41	0.21	1.02	0.21	-

Table 4.5: Summary of domain size study - rotor disk height variation

d_{top}	$4c$	$4c$	$8c$
d_{bottom}	$6c$	$12c$	$24c$
difference [%]	9.5	-	0.6

set of experiment was conducted to determine the radius of the cylindrical domain. A summary of the experiment can be shown in Table.4.4 and Table.4.5.

4.1.8 Analysis Methods

The CFD simulations not only provides visualisation of the flow fields, but also allows access to variables of the flow domains in the parameter space. Using the numerical solutions from the simulations, the following provides detailed descriptions of the methods and background theory used in Chapter 5 when analysing the characteristics of the tunnel effects.

4.1.8.1 Effective Angle of Attack

The local effective angle of attack, α_e may be used to describe the lift produced by the propeller. Figure 4.8 illustrates the relationship between lift, L and α_e . Since the freestream velocity, v_∞ is assumed to be fixed with the rotation speed, the induced angle of attack, α_i increases with the induced velocity magnitude, v_i . Thus, the induced drag component, D_i increases which results in a decrease in lift. This relationship can be defined using

$$\alpha_e = \alpha - \alpha_i, \quad (4.12)$$

where α and $\alpha_i = \arctan \frac{v_i}{\Omega r}$ are the angle of attack of the propeller and the induced angle of attack respectively. Note that the propeller used in this thesis is a twisted airfoil. Due to the lack of specification from the manufacturer, the exact α of the propeller is not known in this study. However, since α remains constant for the propeller, using the relative change in the induced angle of attack, α_i is sufficient to infer the change in the local effective angle of attack, α_e for the purpose of analysis reported in this thesis.

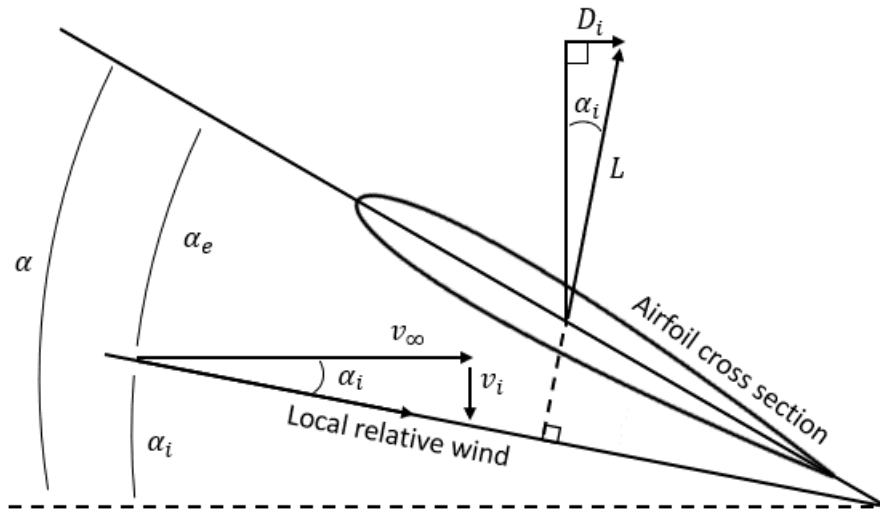


Figure 4.8: Illustration for the relationship between the induced angle of attack, induced velocity and lift on a cross section of an airfoil.

4.1.8.2 Induced Velocity

As seen in Equation (4.12), the induced velocity information is needed to compute the local effective angle of attack. Using the results from the CFD simulations, the induced velocity going through the propellers is estimated using the annular axial velocity interpolation method by Guntur and Sørensen (2014). In this study, eight surface annuli are created at heights of $h_a = \pm\frac{1}{8}R, \pm\frac{2}{8}R, \pm\frac{3}{8}R \pm\frac{4}{8}R$. The inner and outer radius of each annulus are $r_a - 0.5\Delta r_a$ and $r_a + 0.5\Delta r_a$ respectively, where r_a is the annulus radius and $\Delta r_a = 0.05R$ is the annulus width. The annuli setup is illustrated in Figure 4.9. From the CFD simulation results, the average axial velocity (i.e. z velocity) of each surface annulus is calculated. Using the eight surface annuli, the induced velocity, v_i at the rotor disk (at height $h_{a,0}$) is computed using the Lagrangian polynomial interpolation,

$$f(h_{a,0}) = \sum_{i=1}^8 \left[f(h_{a,i}) \left(\prod_{j=1, j \neq i}^8 \frac{h_{a,0} - h_{a,j}}{h_{a,i} - h_{a,j}} \right) \right], \quad (4.13)$$

where $h_{a,i}$ is the height of the annulus, $f(h_{a,i})$ is the average axial velocity of the surface annulus and the solution of the Lagrangian polynomial interpolation, $f(h_{a,0})$ is the estimated induced velocity at radial position r_a . This estimated induced velocity is then computed from $r_a = 0.2R$ to $r_a = 0.95R$ with $0.05R$ increments.

For all the H_0 ($\bar{y} = 0$) simulation cases, the induced velocity is only computed for Propeller 1, since all four propellers are considered to have negligible difference in their flow characteristics at those locations. For all the H_4 ($\bar{y} = 0.8$) cases, the flow characteristics is observed to be only symmetrical about the $y - z$ plane (with negligible difference), hence, the induced velocity is computed for Propeller 1 and 3 (front propeller pair) for the analysis. To provide further insight about the distribution of v_i across the propeller, the annuli are split into four equally spaced 90° segments as

illustrated in Figure 4.10. Segment a is considered to be in the inner rotor region while Segment b is considered to be in the outer rotor region (Detailed definition of inner and outer rotor region is provided in Chapter 5).

The induced velocity can be influenced by the vorticity near the rotor. Using a point vortex as an analogue to a high vorticity region near the rotor, Figure 4.11 shows three different scenarios of a propeller in an inviscid flow field with a point vortex at different locations relative to the propeller. In Figure 4.11a, the point vortex is positioned higher than rotor, this induces more vertical velocity in the rotor's upstream flow, hence, increasing the induced velocity magnitude going through the rotor. Whereas, in Figure 4.11b, a point vortex at a similar vertical position as the rotor induces more horizontal component of velocity into the rotor's upstream flow. This induces a reduction in induced velocity magnitude. A strong vortex below the rotor can have similar effect of reducing the induced velocity magnitude as shown in Figure 4.11c. This scenario is seen in Section 5.2.2.1 and 5.3.5.1, that a recirculation region which is contained below the rotor can have this effect. Given this, in an inviscid flow field, thin airfoil theory allows the opportunity to describe the effect of induced velocity on lift. However, this effect is diminished if the rotor blade is passing through a region with a high magnitude of vorticity. For incompressible flow, the Navier-Stokes equations may be simplified and expressed as

$$\rho \frac{D\mathbf{V}}{Dt} - \mu \nabla^2 \mathbf{V} = -\nabla p. \quad (4.14)$$

Note that body forces (i.e. gravity) are not considered here. In this case, the diffusion term in the Navier-Stokes equations becomes more significant and reduces the impact of the additional vortices

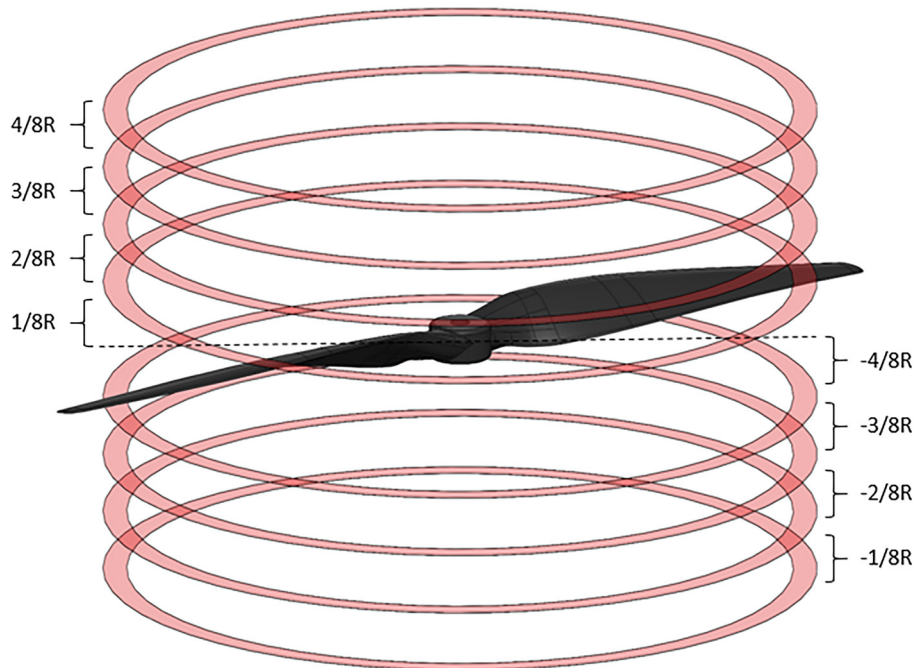


Figure 4.9: The eight the annuli in the stream wise positions at which the axial velocities are extracted to compute the induced velocity going through the propeller.

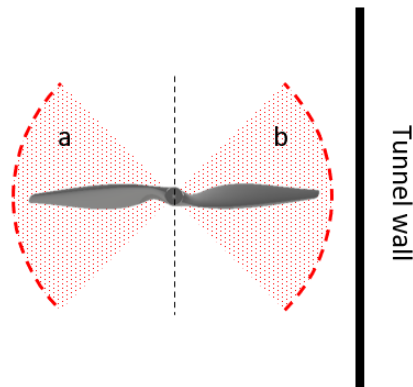


Figure 4.10: Segmentation of the annuli described in Figure 4.9.

on the blade surface pressure. This increased significance of the diffusion term due to the blade passing through the high vorticity region ultimately has a strong influence on pressure. Thus, this may lead to a reduction in lift when compared to a baseline case. This situation observed and discussed in Section 5.3.5.1 and 5.5.

4.1.8.3 Circulation

Circulation within the tip vortex is another parameter which relates to how lift is generated on the rotor. The Kutta-Joukowski theorem states that the lift per unit span on a two-dimensional body is directly proportional to the circulation around the body (Anderson Jr, 2010), and this relationship is given by

$$L' = \rho_{\infty} v_{\infty} \Gamma, \quad (4.15)$$

where L' , ρ_{∞} and Γ are the lift per unit span on the airfoil, fluid density and circulation respectively. In the simulations, the circulation within the tip vortex is extracted along a closed circular path enclosing the vortex core with radius c , at where the peak vorticity of the tip vortex occurs. The circulation is then computed by integrating the flow velocity vector, \mathbf{V} along that closed path using

$$\Gamma = \oint \mathbf{V} ds, \quad (4.16)$$

where s is the line enclosing the tip vortex core.

4.1.8.4 Baseline Flow Field for a Single Rotor

In this section, the flow field of a single rotor in open space is established as a baseline for comparison in Chapter 5. The cross-section flow field shown in Figure 4.12 indicates that the flow field of the rotor is symmetrical about its rotational axis. It is later discussed Section 5.1 that this symmetry no longer holds for the quadcopter configuration.

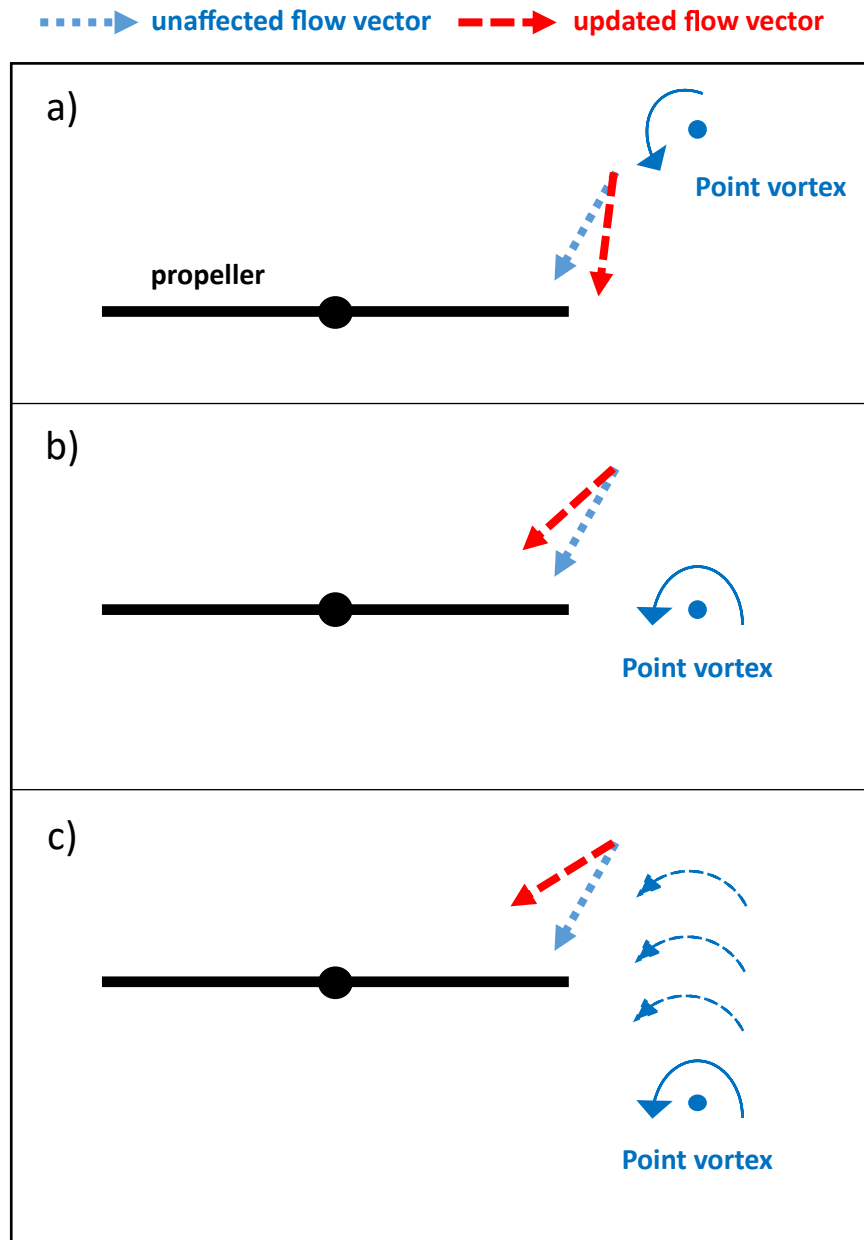


Figure 4.11: Illustration of the influence of a point vortex on the rotor's upstream flow vector in three different scenarios. The red dashed arrow is the flow vector without the influence of a point vortex. The blue dotted arrow is the flow vector under the influence of a point vortex.

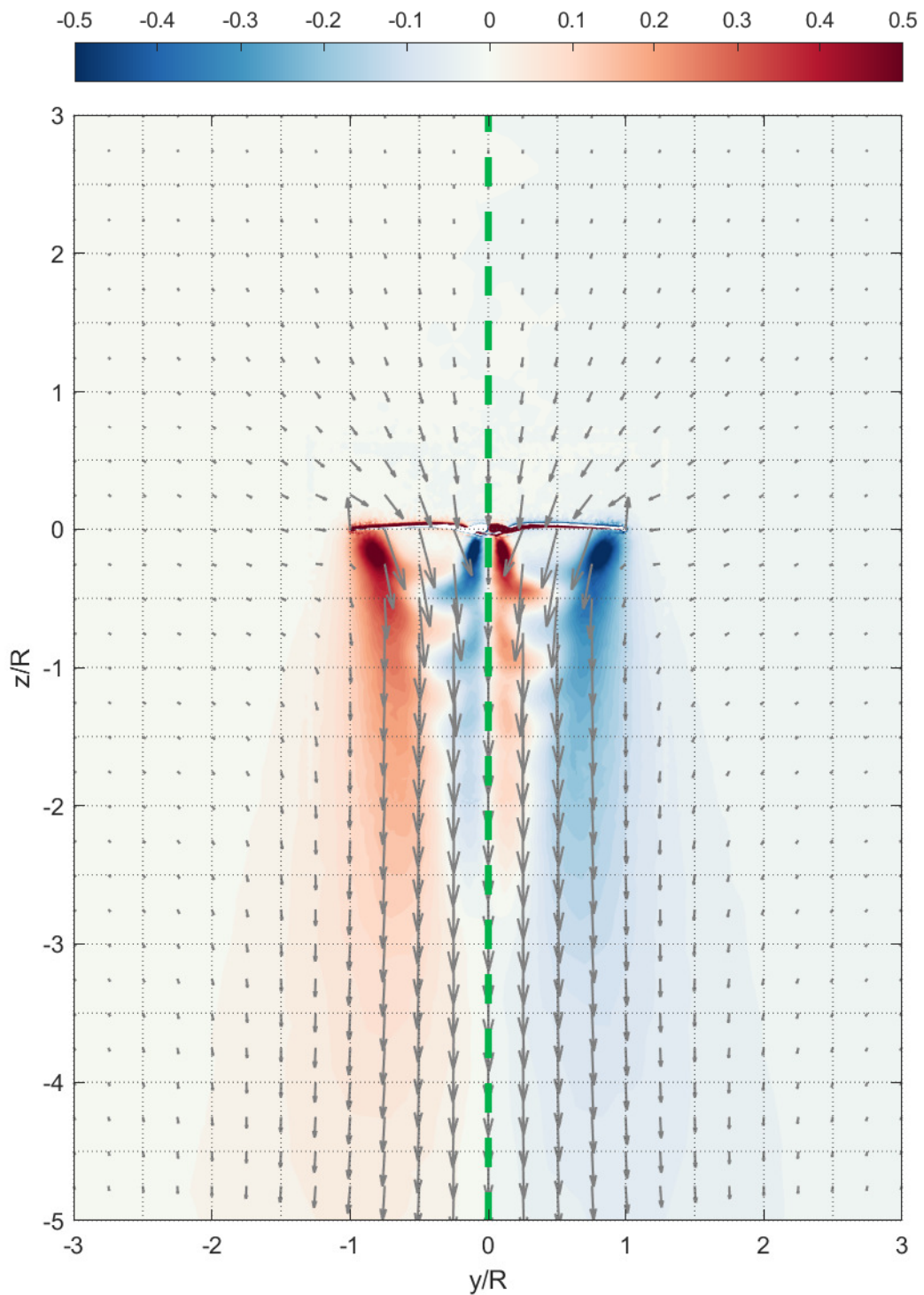


Figure 4.12: Cross-sectional flow field and vorticity contour of the single rotor baseline case. The green dash line is the flow symmetry line. The contour plots show the x - z component of vorticity normalised by the rotation speed, ω_y/Ω .

4.2 Physical Experimental Method

The quadcopter model was also analysed through physical experiments, measuring the thrust generated by the propellers at various locations inside a tunnel (the 1.5m tunnel shown in Figure 3.4). The location of the quadcopter system relative to the tunnel is one of the the main variables of interest in the parameter space for this study, as it is arguably more efficient to explore this via experiments given the computation expense of completing numerically.

A quadcopter frame was designed to match the parameters of the quadcopter model described in Section 4.1.1, with the same motor spacing. The construction of the frame consists of four 20x20mm T-slot Aluminium extrusion beams¹³ as arms and using 3D printed parts as mountings. In the early stage of the physical experiment, it was found that the driving frequency (rotor rotation speed) is close to the natural frequency of the whole setup which caused strong resonance in the system, distorting the desired signal measurement. Later, counterweights were added between the motor along with vibration dampening pads to reduce the vibration in the system. A picture of the quadcopter frame for the experiment is illustrated in Figure 4.13. For the open space experiment, the quadcopter frame was mounted on a vertical 45x45x2400mm T-slot Aluminium extrusion beam¹⁴ which was supported by four legs, similar to the structure of a tripod. For the in-tunnel experiment, the quadcopter frame and the vertical beam was mounted in the centre of the 1.5m tunnel. VETEK single point 1kg load cells¹⁵ were fitted at the end of each arm, which were also connected to the 30A LittleBee ESC and T-motor U3 motors. In order to make the experiment and the CFD simulations more comparable, the propellers used were the same 12x6 propeller model used by the CFD.

The analogue signals from the loadcells were amplified by a custom-designed data acquisition PCB which consists of 4 differential amplifiers using TL072 op-amps¹⁶ from Texas Instruments and a STM32F405 microcontroller¹⁷ (MCU). These signals were then sampled at 1.33kHz (chosen as it was more than ten times of the 83.3Hz (5000RPM) driving frequency from the motors). The overall system was initially powered by lithium-ion polymer (LiPo) batteries. However, later it was found that the voltage variation in the batteries as they were discharged caused a significant impact on the measurements. Hence, a laboratory power supply was then used as the power source to supply 15V to the whole system.

The static thrust experiment were run with the quadcopter frame mounted at different locations at both the open space or inside the 1.5m tunnel. At each location (variation/a set of experiment), the experiment was run 10 times and each run had a 1 minute duration. Before beginning each set of experiments at each location, the motors' rotation speed were checked and calibrated to 5000 ± 15 RPM using an optical tachometer to ensure the motors were running at consistent speed across all locations.

The experiments were conducted across multiple days due to long setup time and duration

¹³20x20mm T-slot aluminium profile: <https://aluminiumprofile.com.au/product/profile-20x20/>

¹⁴45x45mm T-slot aluminium profile: <https://aluminiumprofile.com.au/product/profile-45x45/>

¹⁵VETEK single point 1kg load cell - <https://www.vetek.com/load-cell-1-kg-single-point-aluminium-oiml-article>

¹⁶TI TL072 op-amps - <https://www.ti.com/product/TL072>

¹⁷ST MCU - <https://www.st.com/en/microcontrollers-microprocessors/stm32f405-415.html>

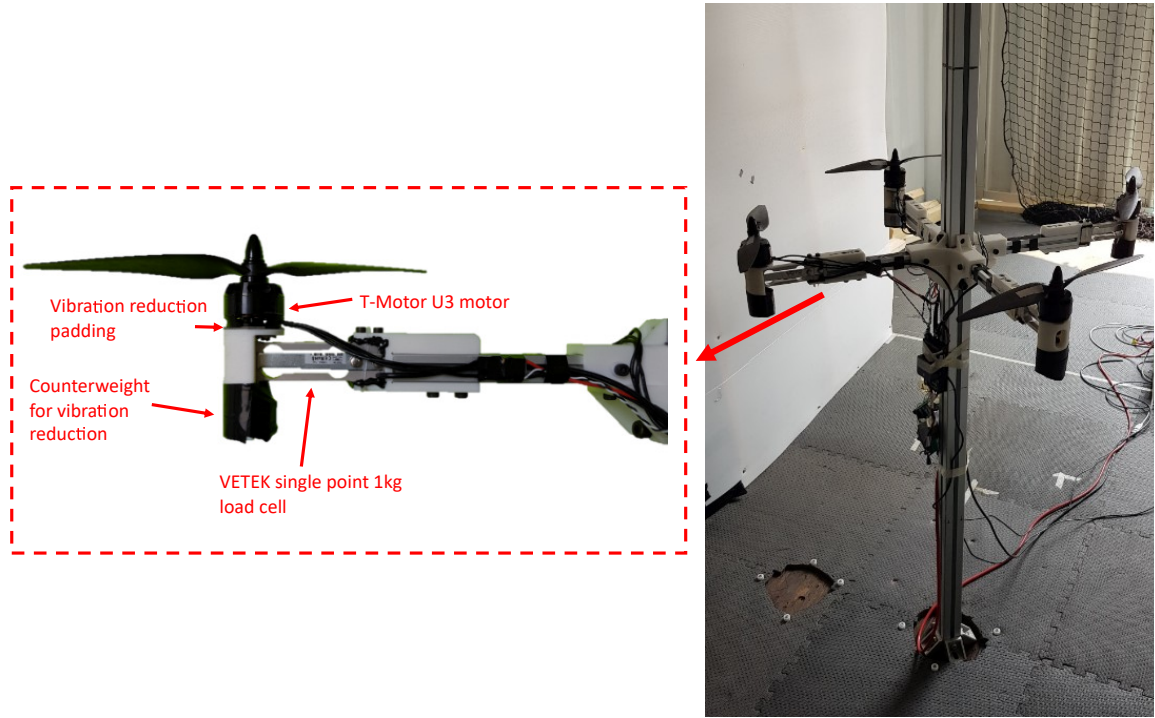


Figure 4.13: Construction of the quadcopter frame for the static thrust experiments. The vertical beam in the picture was fixed to the ground and the ceiling of the 1.5m tunnel.

between sets. Temperature data was also recorded at the end of each run for the purpose of data analysis to compensate for the change in air density. The air density, ρ is calculated using

$$\rho = \frac{p}{\lambda\Theta}, \quad (4.17)$$

where p is the absolute pressure, λ is the specific gas constant and Θ is the absolute temperature. Dry air is considered in this study since the effect of humidity on air density is an order of magnitude lower than temperature. Hence, $\lambda = 287.058 J/(kg \cdot K)$ and $p = 101325 Pa$ were used for the analysis. All the raw measurements recorded from the experiments were converted into the thrust coefficient, C_T using

$$C_T = \frac{\sum_{i=1}^4 T_i}{0.5\rho\Omega^2 R^2 A_{rotor}}, \quad (4.18)$$

where T_i is the raw thrust measurement of each motor, Ω is the rotation speed of the propeller and A_{rotor} is the area made up by the spinning propeller disk.

4.2.1 Calibration

4.2.1.1 Measurement Calibration

Loadcells Calibration: Each loadcell was calibrated using a digital force gauge. Measurements were taken by pushing the loadcell with the digital force gauge manually. Ten random force samples were taken within the desired operating range of the loadcell, which is between 0.5kg to 1kg. A

regression line was then fitted to this sample pool to determine the relationship between force and voltage measured by the loadcell. This procedure was repeated until the correlation coefficient of the regression line is greater than 0.98 to minimise the human error factor during the process.

Variations in Propeller: During the calibration process, it was found that the manufacturing tolerance of the propeller can produce up to 8% thrust difference between the propellers. Particularly, this difference was seen more obviously between the CW and CCW propellers. A sorting process was carried out to select the propeller pairs which produce similar thrust in the same condition. After the selection, the thrust difference within the CW/CCW propellers was approximately 1%. The difference between the CW and CWW propellers was approximately 3%. These differences appeared to be constant after repeated testing. Therefore, they were treated as constant offsets and adjustments were made in reporting the experiment measurements.

4.2.1.2 Rotation Speed Calibration

In the beginning of each experiment run, the rotation speed of the propellers were calibrated using a handheld tachometer. In order to allow the motors' rotational speed to stabilise, the motors were run for one minute (from stationary) before beginning to take the measurement. At certain locations, for example near the ceiling or ground, the variation in rotation speed was observably larger. After tuning the rotation speed of the motors, in the worst case the motors were running at 5000RPM with ± 15 RPM variation. The rotation speed was checked again 30 seconds after the calibration to ensure the target speed was stable.

4.2.2 Static Thrust Experiments in Open Space

The performance of the quadcopter model in a large open environment set the baseline for comparing its performance in tunnel environments. To establish the baseline, three experiments were designed:

1. OS: static thrust measurement in a large open space
2. GND: static thrust measurement near a ground plane at variable distance from the boundary of $z/R \in \{0.75, 1, 1.25, 1.5, 1.75, 2, 3, 4, 5, 6\}$
3. CEIL: static thrust measurement near a ceiling plane at variable distance from the boundary of $z/R \in \{0.75, 1, 1.25, 1.5, 1.75, 2, 3, 4, 5\}$

These experiments/cases will be referred to as OS, OS_g and OS_c in the following sections for convenience from now on. All three experiments were conducted inside a large room, with an approximate radius of 3m to the closest obstacle and 3m ceiling height from the ground. The overall setup structure for the OS case is illustrated in Figure 4.14.

For OS, the thrust coefficient of the total thrust, $C_{TOS} = 0.1056$ and the standard deviation of the measurement is $\sigma_{OS} = 3.5 \times 10^{-4}$.

For the OS_g experiment, the ground plane is made of four 900mm x 900mm x 5mm corflute panels supported by triangular beam members at the bottom. This ensured that each propeller was

at least $5.9R$ distance away from the closest edge of the ground plane, which was considered to be sufficiently far for in this study. The ground plane was fixed to the vertical beam and supported by 16 regular tripods from the bottom to counter the propellers' downwash. Figure 4.15 shows a photo of the OS_g setup. The OS_c experiment used the same panel and the corners of panel were supported by 4 tripods at 2200mm height from the floor. This ensured the floor had minimal impact on the thrust measurement. A photo of the OS_c setup is illustrated in Figure 4.16. The result of OS_g and OS_c are shown in Figure 4.19 and 4.18 respectively. The results from several similar studies are include in these two figures for comparisons.

4.2.3 Static Thrust Experiments in Tunnel Environments

To simulate the effect of a tunnel, the 1.5m tunnel described in Section 3.4 was used. The quadcopter was placed in the middle of the tunnel in the longitudinal axis during the experiment. In order to fixed the position of the quadcopter frame relative to the tunnel, a 45x45x2400mm T-slot Aluminium extrusion beam was mounted through the centre of the quadcopter frame. The Aluminium beam was then mounted to the ground and the ceiling of the wooden tunnel. Figure 4.13 shows an example of the quadcopter frame mounted at one location of the 1.5m tunnel. During the experiment, both end of the shipping container were closed to remove the possible effect of external wind gust.

The experiments were conducted at 42 locations inside the tunnel described in Table 4.1 and Figure 4.1. Refer to Figure 4.17 for the thrust measurement.

4.2.4 Experimental Error

In this experiment study, the sum of the measurement error and RPM error is considered to be the experimental error, which is depicted in the figures of the experiment results. The measurement error is computed as the standard deviation of the 10 runs of each set. The RPM error originates from the variation in the propellers' rotation speed. Using a tachometer to manually measure the rotation speed during the experiments, it was observed that on average, the speed fluctuation is approximately ± 15 RPM. At 5000RPM, this fluctuation contributes to approximately $\pm 0.6\%$ change in the C_T using Equation (4.18). Note that the error described here is simplified and expressed as a simple sum for the sake of representing the approximate error in the analysis. In reality, these error terms are likely to be codependent to each other.

There was another form of error in the experiments that was observed but was not included in the error measurement. This error could be due to the variation in the propellers aeroelasticity, which is more commonly known as propeller "flapping". During the experiment, it was observed that the thrust generated by each individual propeller had different an offset from the mean thrust of all four propellers. This offset varied nonlinearly at different location inside the tunnel. A possible reason this phenomenon is that due to the small variation in aeroelasticity between each propeller, they all behaved differently when subjected to different loading conditions at different location inside the tunnel. Since it is very difficulty measurement this phenomenon and it was not the main focus of this study, this error was not reflected in the error bar. This discussion is added so that the reader is aware of this issue when reading Chapter 5. The thrust coefficient calculated in this work

considers the total thrust of the whole system, so the variation in the individual propeller may not have a significant impact. However, when considering the moment acting on the quadcopter, the disparity in the thrust offset does have a direct impact.



Figure 4.14: Setup of the OS case. The closest walls/objects shown in the picture is further than 3m.



Figure 4.15: Setup of the OS_g case. 16 tripod were evenly distributed at the bottom of the corflute panel to support the structure.



Figure 4.16: Setup of the OS_c case.

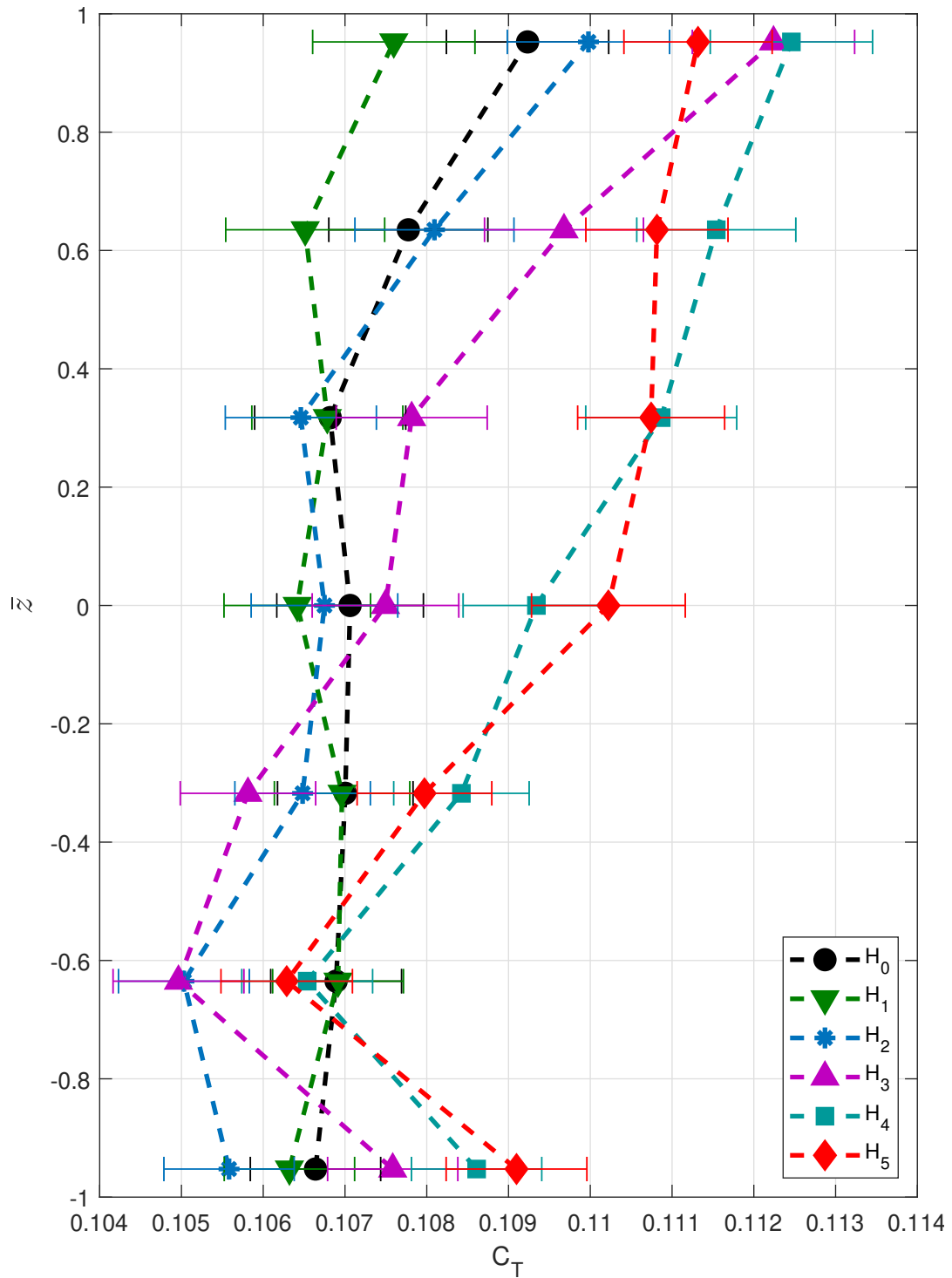


Figure 4.17: Thrust coefficient of the total thrust at various locations inside the tunnel. The curves represent the horizontal position from H_0 (near centre) to H_5 (near wall). The short vertical lines extended from each marker are the error bars of the data points.

4.2.5 Discrepancy from Literature

The OS_c result is comparable with the other two studies (Conyers et al., 2018a; Gao et al., 2019) (Figure 4.18). However, there is a clear difference in the OS_g case across the four studies (Conyers et al., 2018b; Gao et al., 2019; Sanchez-Cuevas et al., 2017) as depicted in Figure 4.19. Nevertheless, the red circle curve from Conyers (2019) shows some resemblance with the OS_g result and can be considered to be in the same category, while the studies from Sanchez-Cuevas et al. (2017) and Gao et al. (2019) can be considered to be in the other. To analysis this further, Conyers (2019) has conducted a quadcopter ground effect experiment with different propeller radius to motor spacing (diagonal) ratios. Let's define this ratio as,

$$\Lambda = \frac{\text{motor spacing}}{\text{propeller radius}}. \quad (4.19)$$

Figure 4.20 combines this ratio study from Conyers (2019) with the OS_g result. The figure indicates that as the value of Λ varies, the characteristics of the curves also change. It is also worth noting that the Λ value for OS_g is not within the range of Conyers (2019)'s study and the pitch of the propeller is not considered in this ratio. In order to determine whether this ratio has an impact on the characteristics of the curves in Figure 4.20, we can try to normalise the axes using Λ .

Figure 4.21 is an example of considering the effect Λ for quadcopter IGE. The figure shows that the local minima (indicated by the black arrow) has been collapsed closer together by multiplying $\Lambda^{0.095}$ to the IGE thrust ratio. This implies the rotor spacing, Λ is an aerodynamic similarity parameter and has some influence on the thrust generation, which agrees with Yoon et al. (2016)'s finding on rotor separation distance. A hypothesis for this phenomenon is that the Λ value changes the location of the vortices formed by the downwash-floor fluid interaction, which in term causing a local minimum in thrust efficiency at certain height from the ground. However, from $z/R = 2$ to $z/R = 7$ in Figure 4.21, the curves do no collapse together or into a similar pattern. This infers that there are some other similarity parameters that have not been explored. For example, the pitch of the propellers (Conyers (2019)'s study uses propellers with different pitch) or varying the motor spacing in Equation (4.2.5) instead of varying the propeller radius. Figure 4.22 shows the experimental results from He and Leang (2020) for quadcopter IGE. The 3D surface plot in Figure 4.22a shows that there is local minimum approximately between $d/R \in (0, 2.5]$. This highlights the correlation of the Λ value having an influence of the characteristics of the IGE thrust ratio curve. As this is not in the scope of this study, more future work is needed in order to gain better understanding of this phenomenon.

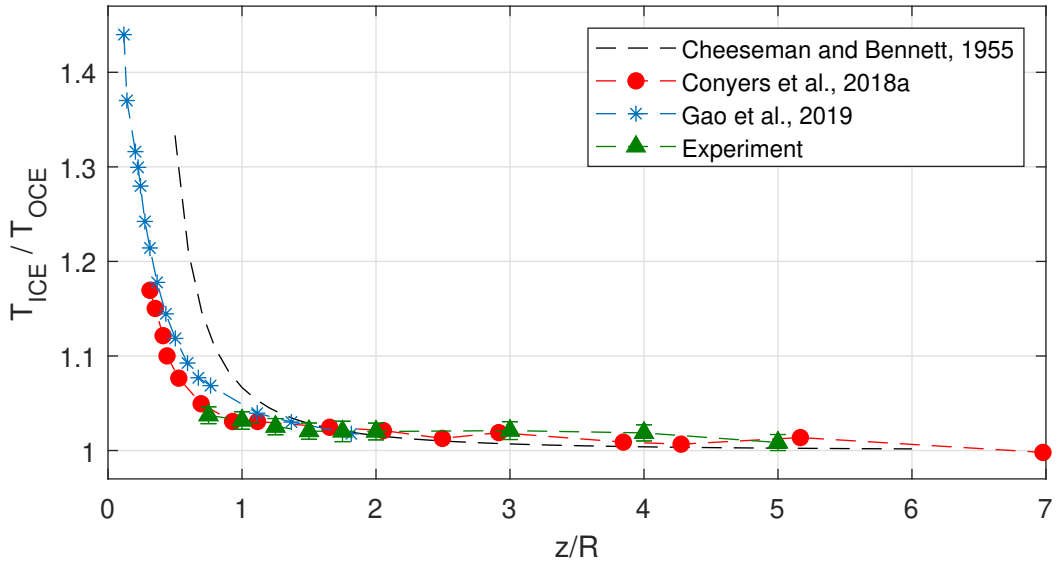


Figure 4.18: The experimental result of OS_c vs other similar ceiling effect studies. T_{ICE} is the thrust ICE while T_{OCE} is the thrust out of ceiling effect, i.e. thrust in open space. The horizontal bars of the OS_c dataset markers (green triangle) is the error bar of the dataset. Note that the curve from Conyers et al. (2018a) is the 690mm spacing, 7000RPM dataset.

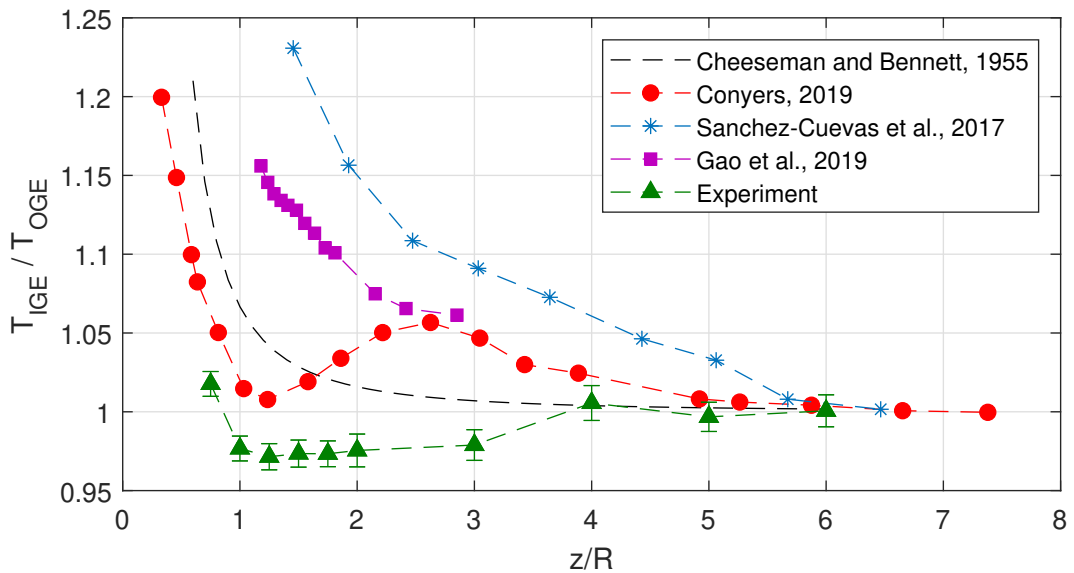
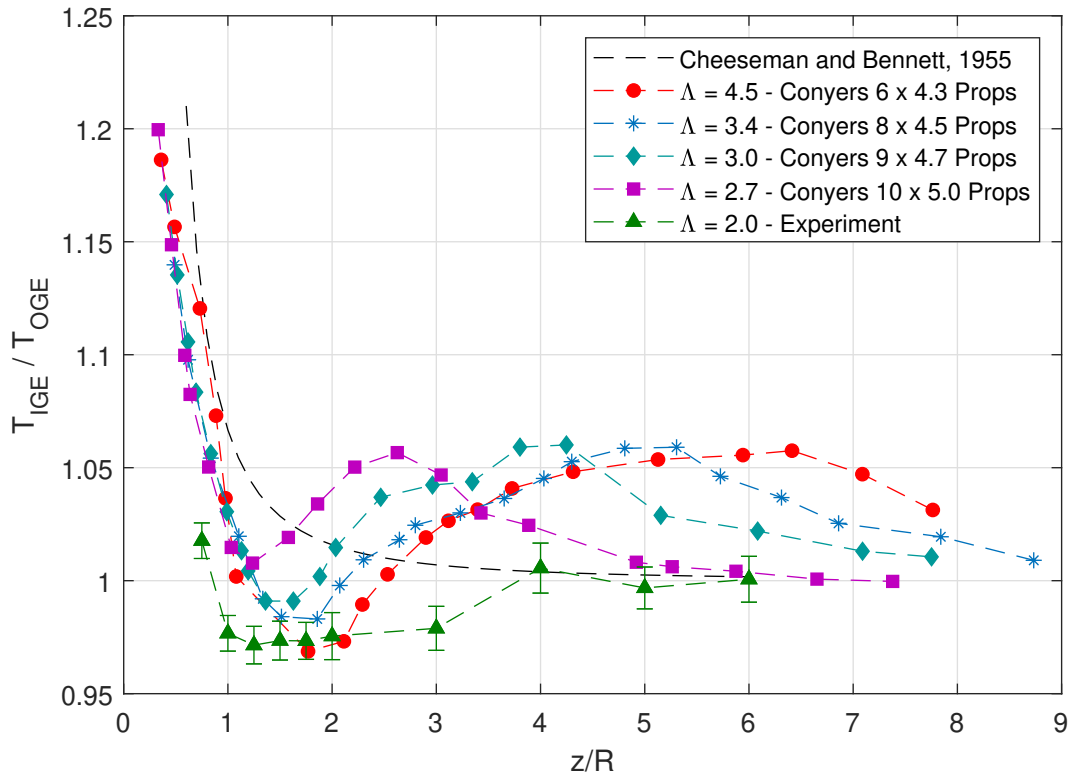
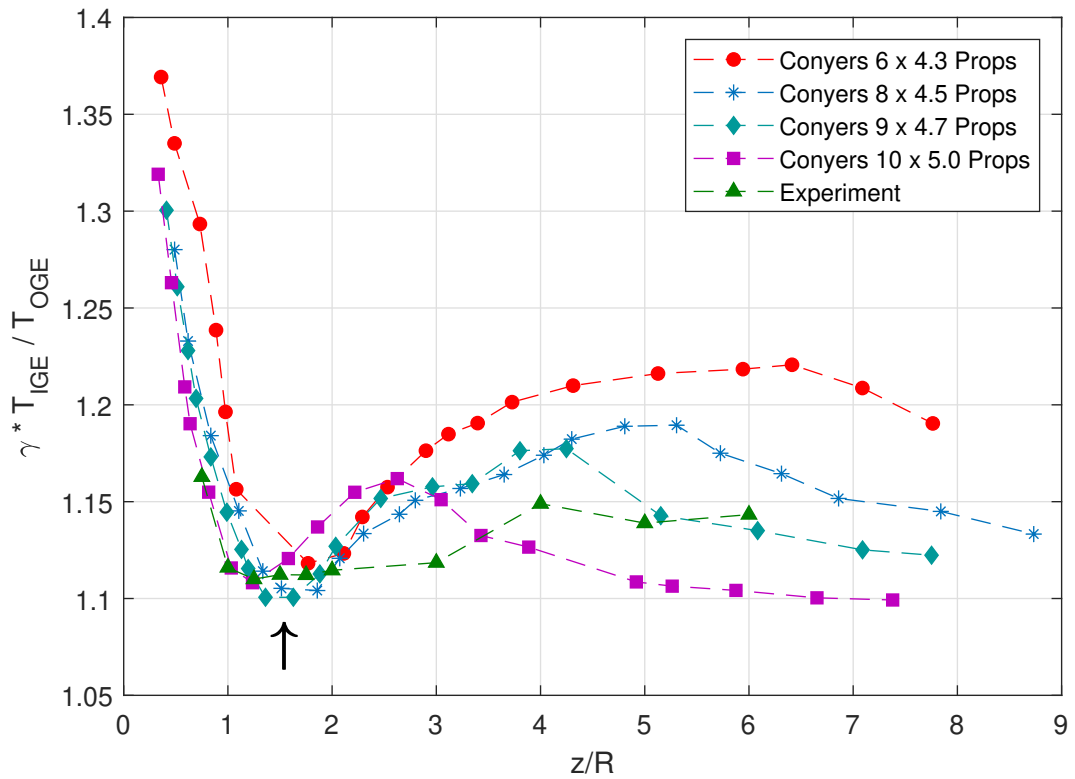


Figure 4.19: The experimental result of OS_g vs other similar ground effect studies. T_{IGE} is the thrust IGE while T_{OGE} is the thrust out of ground effect, i.e. thrust in open space. The horizontal bars of the OS_g dataset markers (green triangle) is the error bar of the dataset. Note that the curve from Conyers (2019) is the 690mm spacing, 10x5.0 Props dataset. Note that the black dashed line is the analytical ground effect mode proposed by Cheeseman and Bennett (1955).


 Figure 4.20: Quadcopter IGE comparison with different Λ values.

 Figure 4.21: Quadcopter IGE comparison: an example effect of including $\gamma = \Lambda^{0.095}$ in T_{IGE}/T_{OGE} . The black arrow indicates the approximate position of the local minima of the curves.

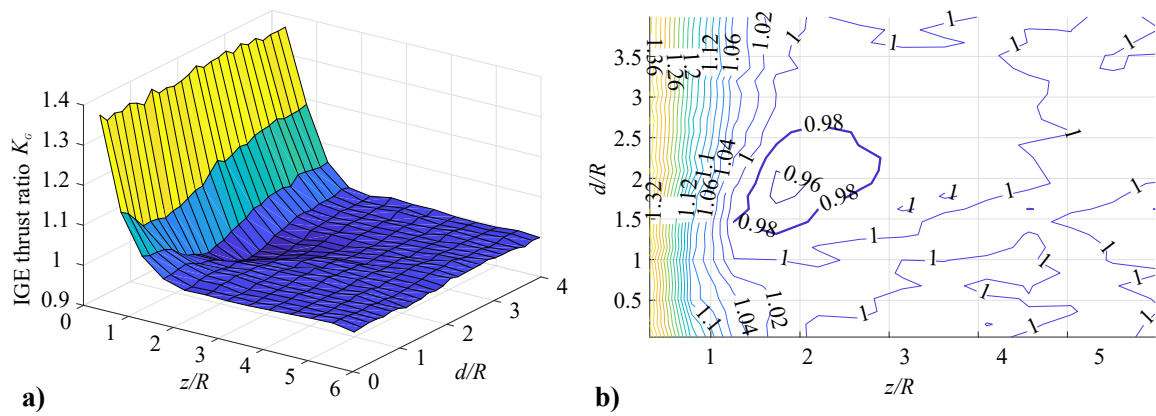


Figure 4.22: Experimental result of quadcopter IGE, incorporating the rotor separating distance, d as the third dimension in the surface and contour plots (Figure 20 from He and Leang (2020)).

Chapter 5

Quadcopters Fluid Interactions in Tunnel Environments

Following the methodologies outlined in the previous chapter, this chapter presents the results and discussions of the CFD simulations and the physical experiments. A quadcopter hovering in open space (OS) and at origin of the tunnel (O_T) are first established as two different baseline cases in Section 5.1. This then leads to separate discussions on the tunnel effects near the tunnel centre in Section 5.2 and near wall in Section 5.3, followed by an overview of the influence of tunnel effects on quadcopter flights inside tunnel environments in Section 5.4. The physical experiment results of the quadcopter in tunnel, IGE and ICE are also included in the analysis for comparison. Finally, the influence of the tunnel-to-quadcopter size ratio is discussed in Section 5.5.

In the following analysis, the CFD related figures only illustrate one or two of the propellers instead of all four propellers to simplify visualisation and discussion. This is because CFD simulations in this research are considered to be ideal environments and flow symmetry was observed in OS and all H_0 cases in simulations. The flow field around the front and back propellers (along the tunnel) are also symmetrical about the y - z plane. A break in symmetry occurs when the quadcopter is positioned horizontal away from the centre of the tunnel, close to the wall (details in Section 5.3).

Here, the inner rotor region is defined as the centre region of the quadcopter where the flow of all four rotors interact. The outer rotor region is the region of the rotor facing outward with minimal flow interaction with the adjacent rotors. These regions are illustrated in Figure 5.1. Note that these regions are only a general description for the sake of discussion, so they do not have sharply defined physical regional boundaries.

5.1 Fluid Interactions at the Tunnel Origin

5.1.1 Vorticity and Flow Field in CFD Simulations

Typically, the rotor wake for a single rotor contracts radially as the flow convects away from the rotor disk and the rotor wake is symmetrical about the rotation axis (shown in Section 4.1.8.4). For a quadcopter in open space (OS case), the wakes of the rotors are entrained together due to the low

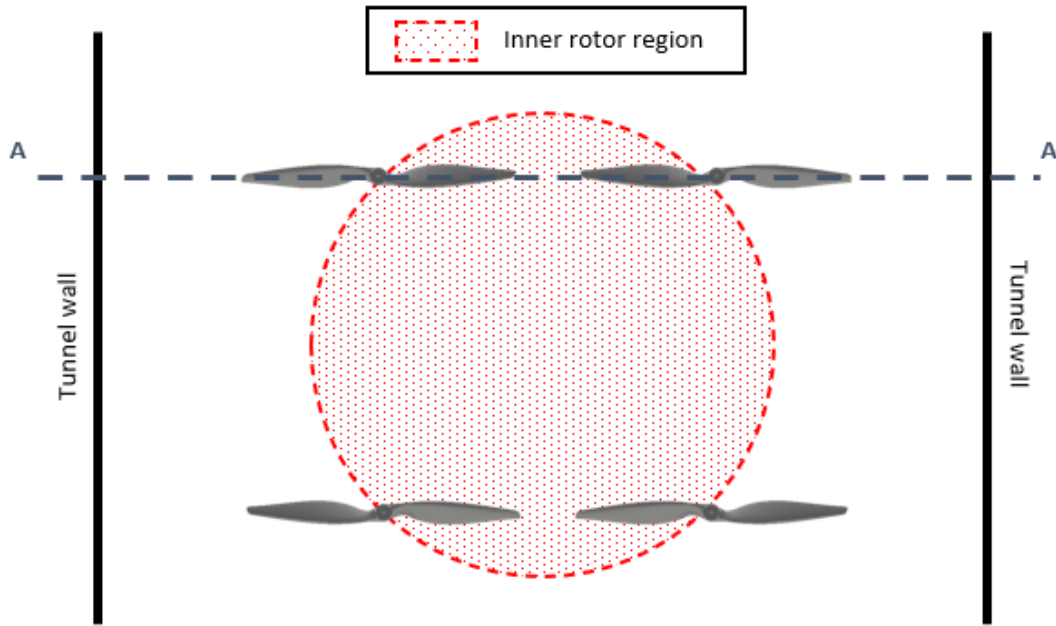


Figure 5.1: Illustration of the outer and inner rotor regions. Outer rotor region is outer boundary (white space) of the quadcopter where this flow interaction is minimal. The dark grey dotted line shows the Cross Section AA which is used in the following analysis. Note that the diagram is not to scale and the tunnel walls are not present in the the OS case.

pressure region at the centre of the quadcopter wake created by the rotor downwash. This results in each rotor wake being angled toward the centre of the quadcopter. The wakes are symmetrical about the y - z plane as seen in Figure 5.2. Symmetry was also observed about the x - z plane in the CFD simulations. The vertical dominant flow close to the symmetry line shown in the figure also reduces the amount of flow rotation in the tip vortex in the inner rotor region compared to the tip vortex in the outer rotor region. Therefore, a slight reduction in the circulation of the tip vortex of the inner rotor region can also be seen in Figure 5.4.

When the quadcopter is positioned at the centre of the tunnel (O_T case), Figure 5.3 shows that the slipstream boundary of the wake has been straightened out vertically due to the presence of the side wall and ground plane. The ground plane induces a stagnation point below the rotor which causes a horizontal component of flow. As the fluid inside the wake boundary approaches the ground, the flow close to the boundary separates into two streams at the stagnation point directly below the rotor, diverting the vertical wake momentum radially outward. This is well described from inviscid flow theory, indicating that this effect is dominated by inviscid forces. In the inner rotor region, the diverted wake that travels horizontally approaches the symmetry plane formed from the adjacent rotor, creating a saddle point along the symmetry line. The flow is then forced to travel upward to conserve momentum.

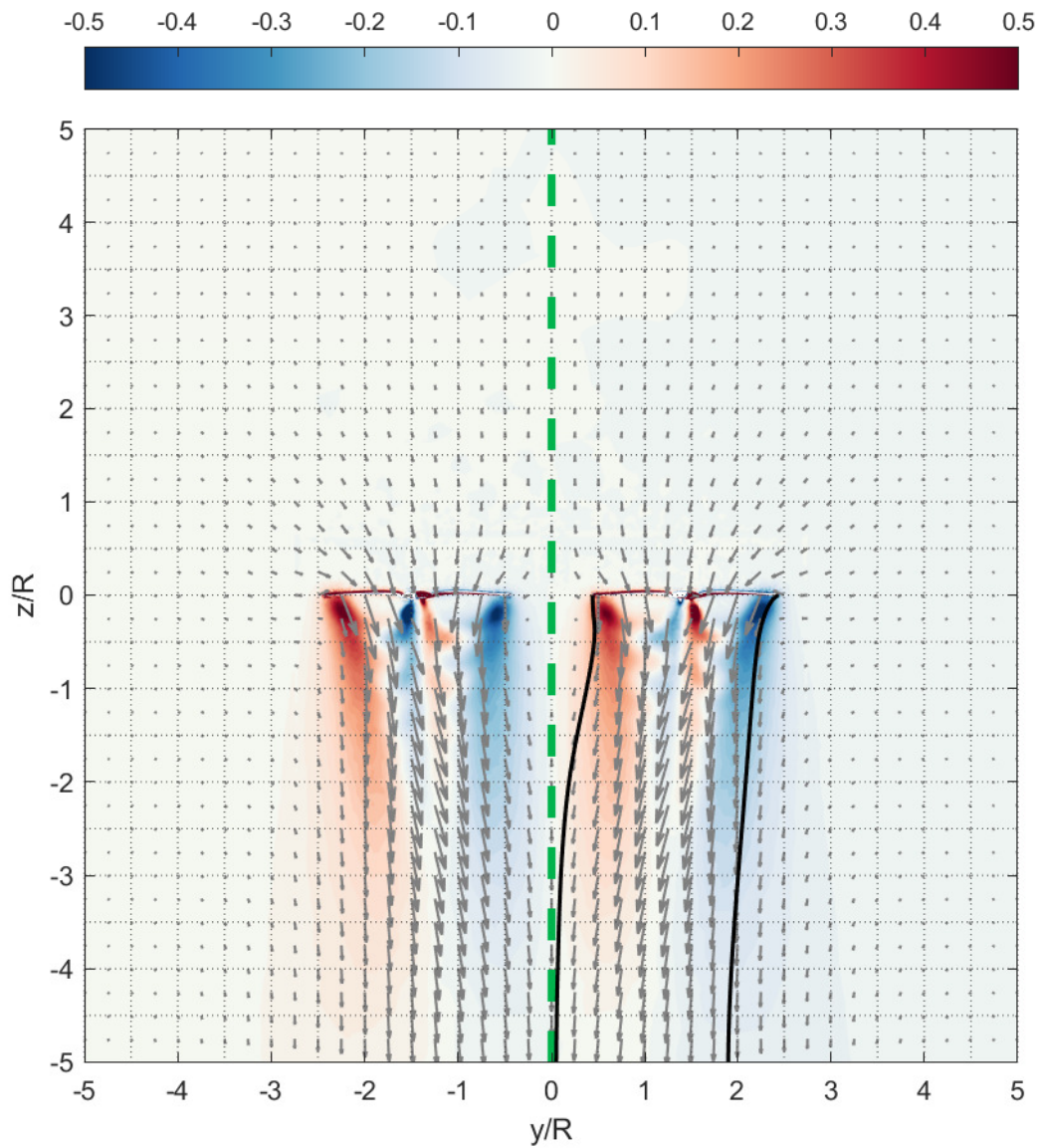


Figure 5.2: Flow field in Cross Section AA, showing the front two propellers in the OS baseline case. The green dash line is the symmetry line between the left and right propellers. The contour plots show the $x-z$ component of vorticity normalised by the rotation speed, ω_y/Ω . The solid black lines represent the streamlines starting from the propeller's tip.

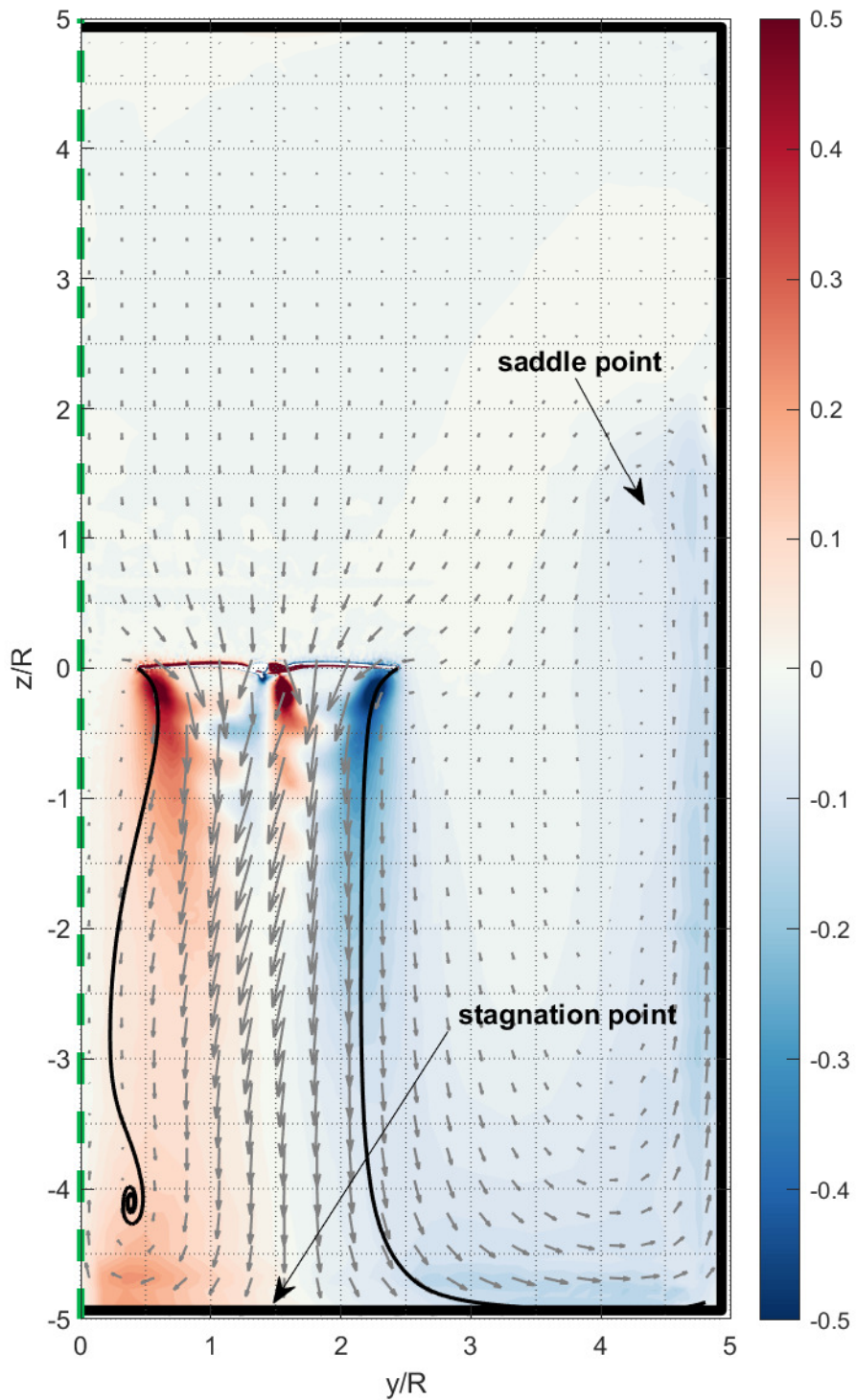


Figure 5.3: As per Figure 5.2 but for quadcopter located at O_T . The arrows indicates the approximate position of the saddle point and the stagnation point.

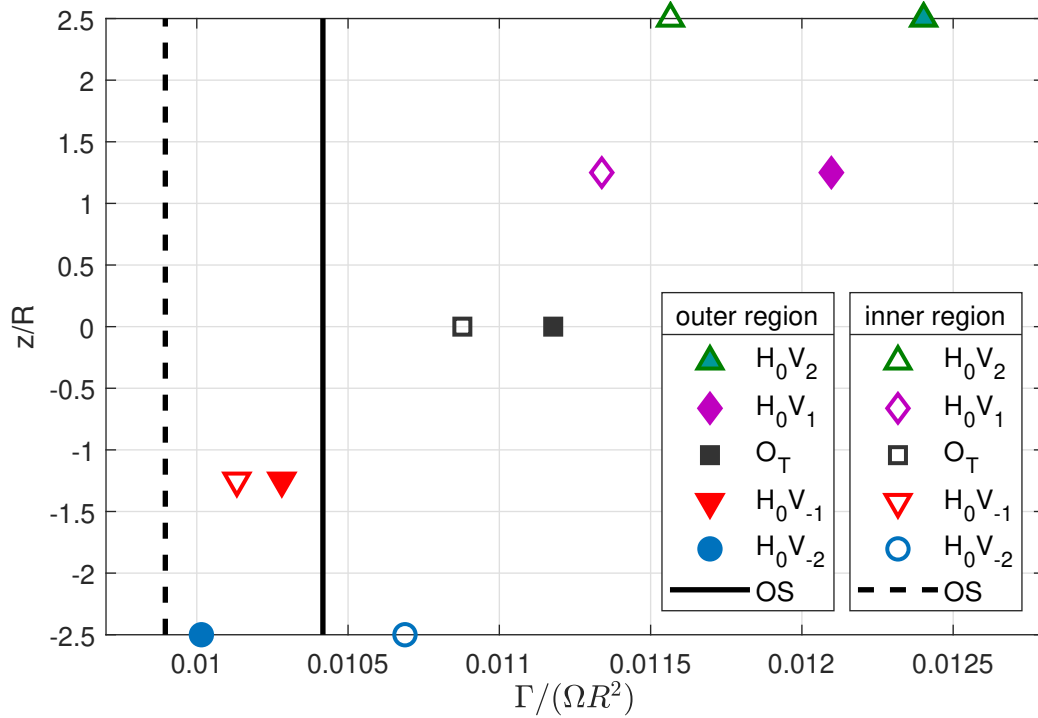


Figure 5.4: The averaged normalised circulation of the rotor tip vortex at different tunnel locations vs OS. A comparison between the outer rotor region tip vortex (solid marker/line) and the inner rotor region tip vortex (hollow marker/dash line) is also shown.

The side wall induces a vertical component of velocity in vicinity of the wall. In the outer rotor region, vorticity formed within the boundary layer from the ground surface is lifted and travels along the vertical wall. The flow continues to travel along the wall passing above the position of the rotor before transitioning into becoming the upstream flow of the rotor. As this recirculated flow approaches the ceiling, an adverse pressure gradient along the wall reduces the vertical component of velocity, creating another saddle point in between the wall and rotor (close to the rotor's upstream flow intake) as seen in Figure 5.3. This becomes a “pumping effect” as the flow circulates from the saddle point of the return cycle to advecting into the upstream flow of the rotor. Due to the wall of the tunnel, the flow momentum has become vertically dominant which consequentially pulls the wake towards the wall instead of tilting toward the centre of the quadcopter.

5.1.2 Blade Pressure Field in CFD Simulations

The pressure field on the propeller blades is another important parameter to consider. The pressure differential between the top and bottom surfaces of the blades changes the lift and drag forces acting on the propeller and is the dominant component of the lifting force. In the following analysis, the pressure fields of OS and O_T are compared. The pressure of the top and bottom surfaces of the propeller were taken at different angular positions of the propeller as illustrated in Figure 5.5. Note that a phase shift in C_T between the two cases was observed (as discussed in Section 5.1.3). However, the blade pressure are not compared at the C_T maxima or minima in this analysis, instead being compared at common angular positions illustrated in the figure. The common angular positions

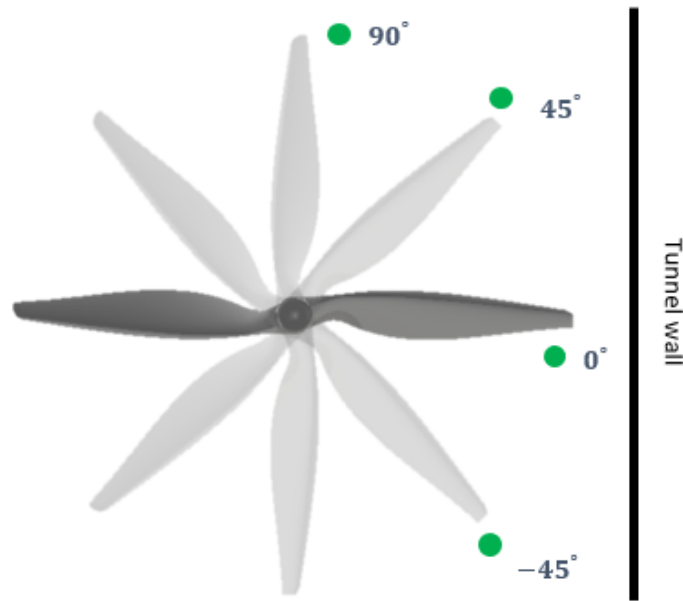


Figure 5.5: The angular positions of the propeller at which the blade pressure field plots were taken. The green dot is an indicator to determine which side the propeller blade is on.

relative to the wall were chosen for the comparison because it was assumed this has a dominant effect on the flow field. In addition, comparing the rotors from different simulation at the same angular position relative to the wall can help with highlighting the contributing factors which alter the blade pressure.

By observing the pressure fields of OS and O_T there is indiscernible difference; correspondingly the changes in the local effective angle of attack is small as seen in Figure 5.11. To further examine the subtle change in pressure, Figure 5.6 shows the differences in the pressure fields for both the top and bottom surfaces of the rotor blade by subtracting the blade pressure fields of O_T by OS. Using the blade pressure difference, Δp from Figure 5.6, the mean cross sectional Δp is computed across the spanwise direction of the blade for both the top and bottom surfaces, and the result is shown in Figure 5.7. The figures show that the pressure difference profiles show are finite difference for the top and bottom blade surface. The combined effect of which is to decrease the pressure on the upper surface in the outer region, while simultaneously increasing the pressure on the lower surface. In the inner region, the reverse is largely true (that is, for $\gamma = 0^\circ, 45^\circ, 90^\circ$). The recirculation region created by the walls also have a different influence on the inner and outer rotor region (as indicated by the left and right rotor blades in the figure). To aid discussion, the total difference was calculated (defined as the surface pressure difference measured on the bottom surface minus the surface pressure difference measured on the top surface). These findings are shown as green triangles in Figure 5.7. A positive value indicated by a green triangle means that O_T has higher lift than OS while negative value indicates lower lift. Note that the majority of lift is produced toward the tip of rotor blade. Judging from the pressure profiles in Figure 5.7, on average at O_T the rotor produces slightly more thrust than OS on the inner and outer region rotor blades, resulting in a slight increase in thrust.

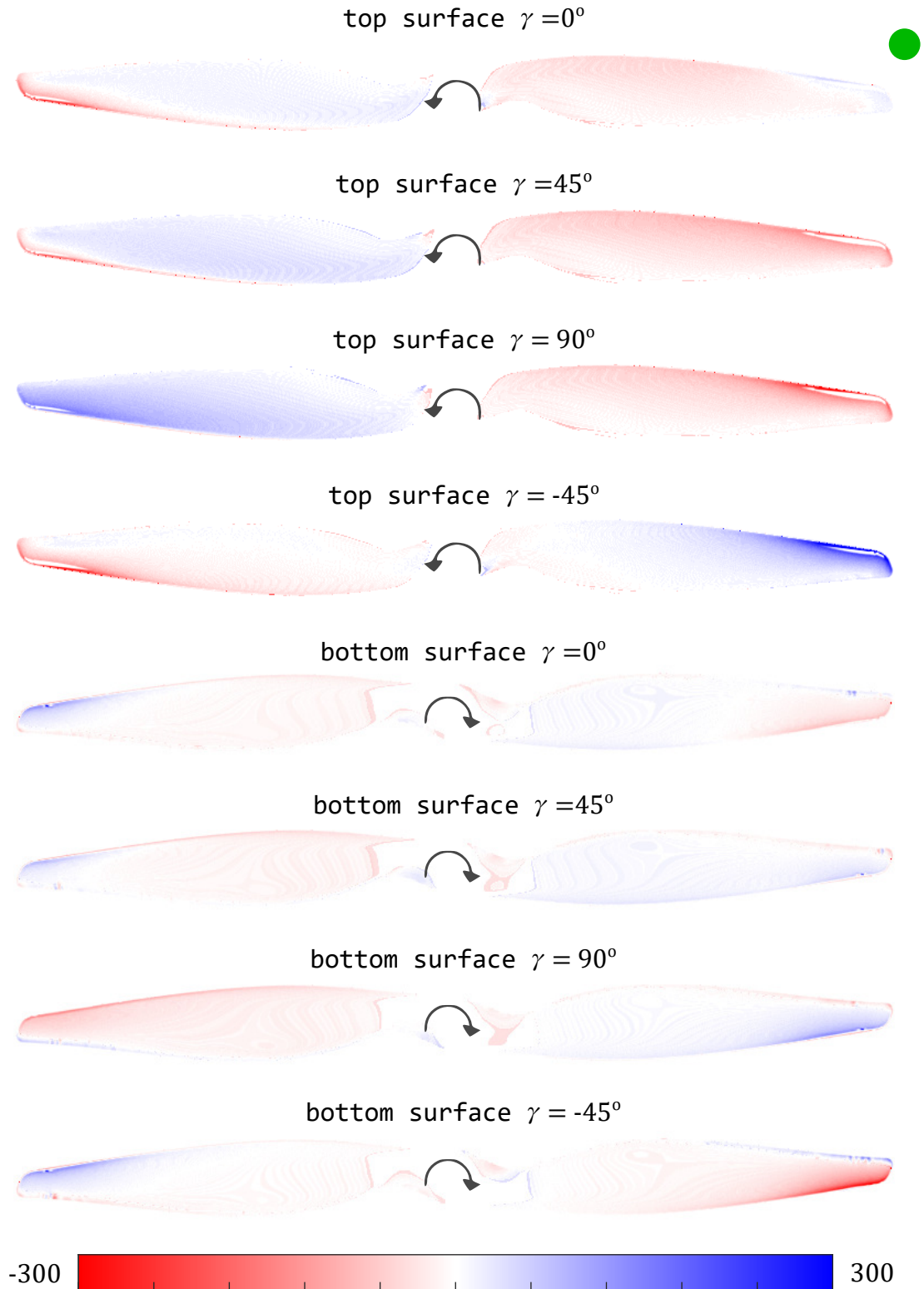


Figure 5.6: Blade surface pressure difference between O_T and O_S at different angular positions of the propeller. The location of the green dot corresponds to the blade position shown in Figure 5.5. The blue contour means O_T has a higher pressure value. Pressure unit in pascal. The pressure range on the individual rotor is approximately $[-3000, 1500]$.

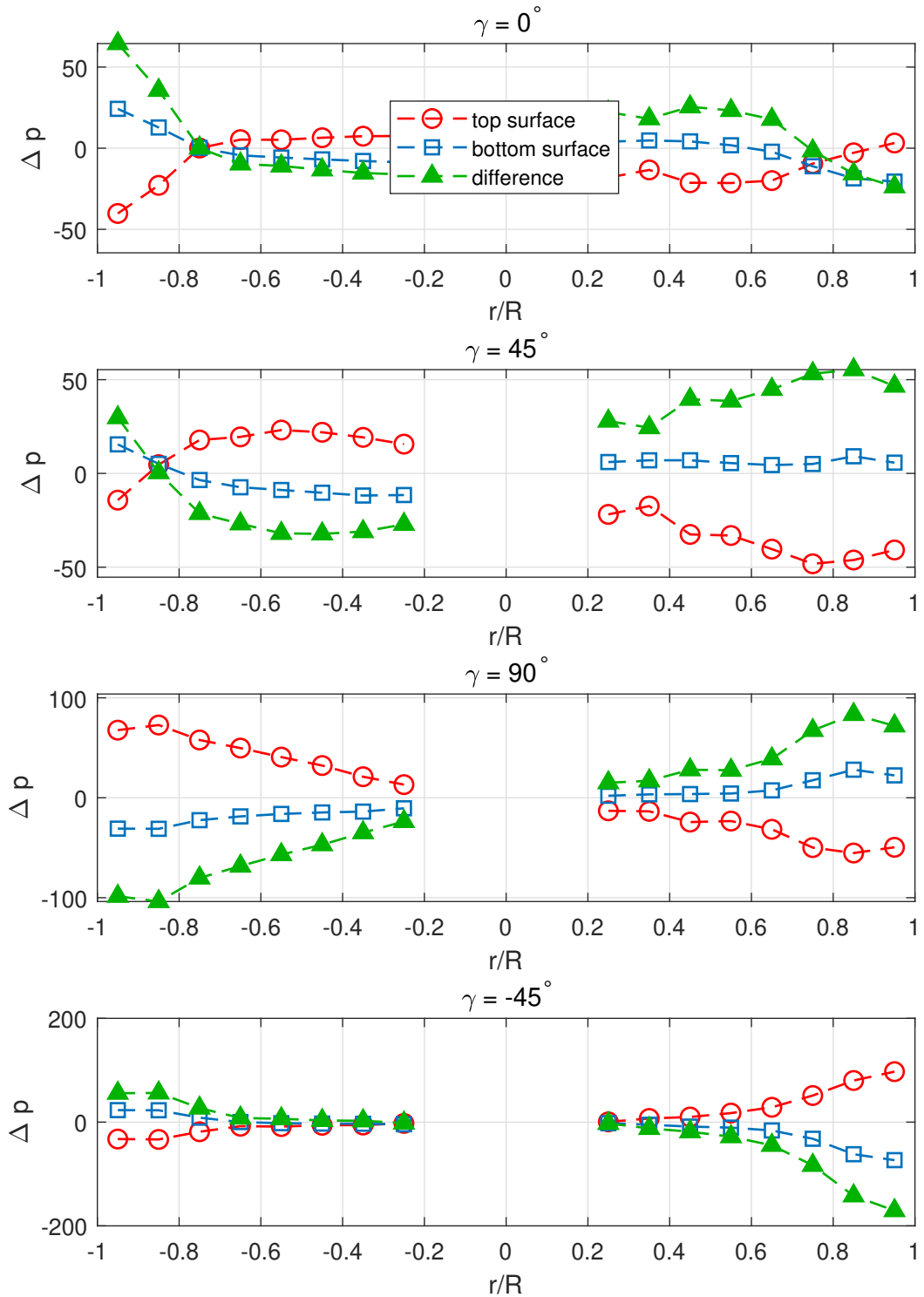


Figure 5.7: Cross sectional blade surface pressure difference between O_T and O_S at different angular positions of the propeller (Figure 5.5). The x -axis of the plots is the radial position along the blade. The pressure difference profile has the same rotor orientation as Figure 5.7. The green triangle curve is the difference between the bottom and top surface. A positive value in the green triangle suggests higher C_T in O_T . Pressure unit in pascal.

5.1.3 Impact on Thrust

The total thrust coefficients for OS and O_T computed from both the CFD and physical experiments are summarised in Table 5.1. O_T only has a minimal increase in C_T compared to OS in the simulation, while this increment is slightly more apparent in the physical experiment, showing 1.42% difference. Returning to the CFD results, Figure 5.8 and 5.9 show the numeric induced velocity comparison between the inner and outer rotor region when the C_T value of the rotor is close to its maximum, average and minimum. O_T shows a higher fluctuation as well as a phase shift in C_T compared to OS. The mass flow rate going through the rotors is influenced by both inviscid and viscous forces close to the rotor. When comparing OS and O_T , it is speculated that fluctuations in C_T may be directly related to variations in the vertical component of the inlet rotor mass flow rate, particularly near the blade tip of the rotor nearest to the wall. In the tunnel, vorticity in the wake is transferred vertically upwards and entrained into the inlet flow stream. Focusing on the O_T case, as the blade traverses this region of vorticity, there is a significant impact on C_T . This entrainment of mass containing wake vorticity is not observed in the OS case. The entrained negative (counterclockwise) vorticity, above and to the right of the rotor, adds an additional horizontal component of flow near the blade's tip. As shown in Section 4.1.8.2, this alters v_i , increasing the lift generated. This effect dominates the variation in lift observed in the OS case as the blades traverse from the outer rotor region to the inner rotor region. Ultimately, this results in a phase lag and increase in magnitude of oscillation in C_T for the O_T case. This phase difference and low frequency oscillation is noted for all tunnel cases and is noted to vary with the position of the quadcopter in the tunnel as shown in the discussion of Section 5.2 and 5.3.

In Figure 5.8, there is a clear difference in v_i near the tip of the propeller (where the majority of thrust is generated) between the inner and outer rotor region for the OS case. Whereas, for O_T , the return cycle (recirculated flow) near the wall reduces the induced velocity near the tip of the propeller in the outer rotor region as shown in Figure 5.9. Comparing the time-averaged induced velocity passing through the whole rotor, Figure 5.10 shows that OS has a slightly higher v_i than O_T , despite the upstream flow of O_T having a slightly more vertical dominant velocity component compared to OS. OS and O_T have a similar induced velocity profile along the rotor blade until the rotor tip region, where O_T experiences slight decrease in v_i as shown in Figure 5.10. Since the time-averaged induced velocity of the rotor in O_T is lower, the induced angle of attack also decreases accordingly (Figure 5.11), which is equivalent to an increase in the effective angle of attack of the rotors using Equation (4.12). This corresponds to O_T having a higher C_T value compared to OS as indicated in Table 5.1. **Compared to OS, at O_T the return cycle alters the upstream flow of the rotor by slightly decreasing the induced velocity which increases the effective angle of attack. Thus, increasing the lift production at O_T .**

The CFD and physical experiment result comparison in Table 5.1 shows that the CFD simulations overestimate C_T in both OS and O_T , by 8% and 6.5% respectively. As discussed in Section 4.1.1, this difference is expected because of the absence of the fuselage in the simulation model. Since the scope of this research is to determine the relative differences of the C_T values in OS and different locations in the tunnel, direct comparison of the absolute C_T values are deemed less

Table 5.1: Thrust coefficient, C_T comparison between OS and O_T in CFD and experiment.

	OS	O _T	difference [%]
CFD	0.1140	0.1141	0.09
Experiment	0.1056	0.1071	1.42
difference [%]	8	6.5	

relevant but reported in full.

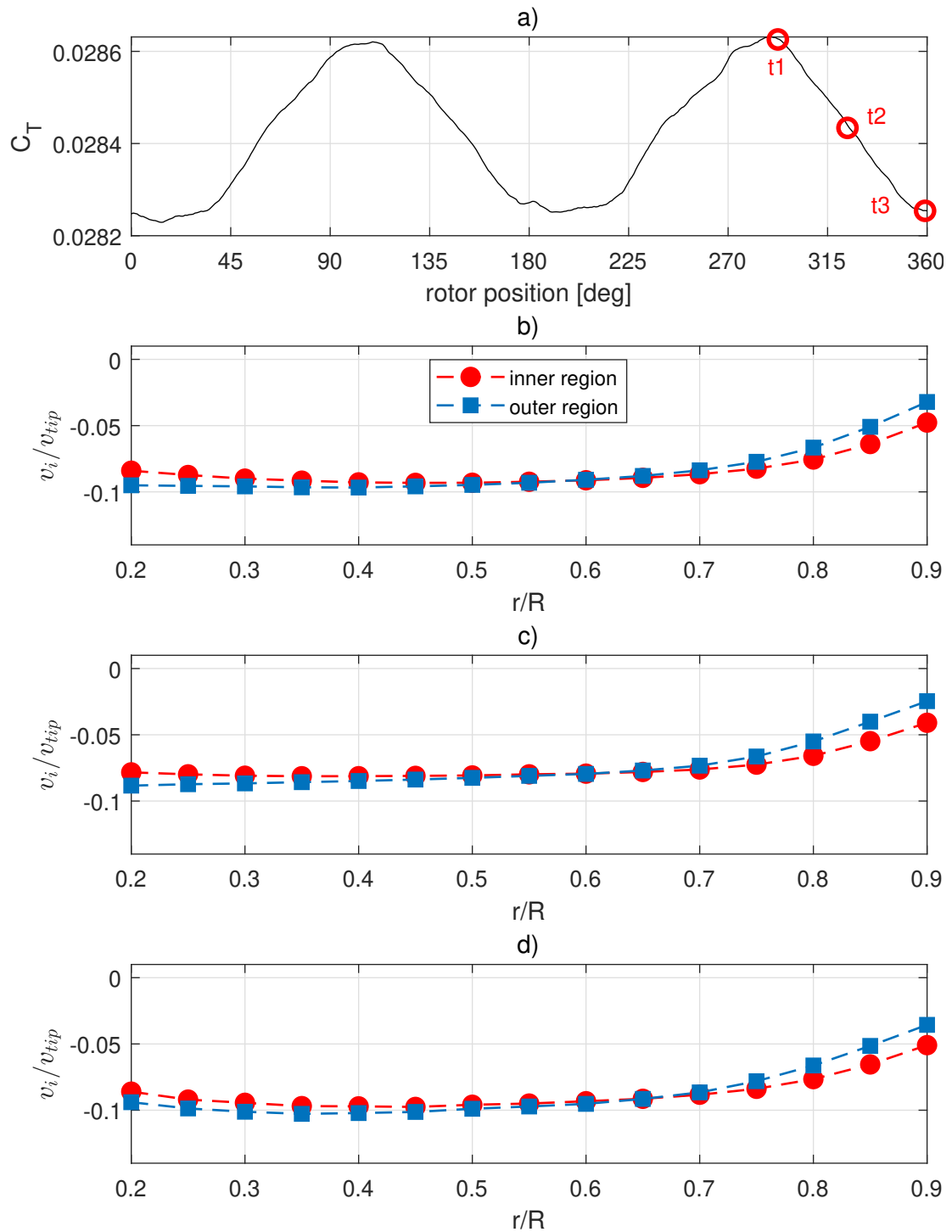
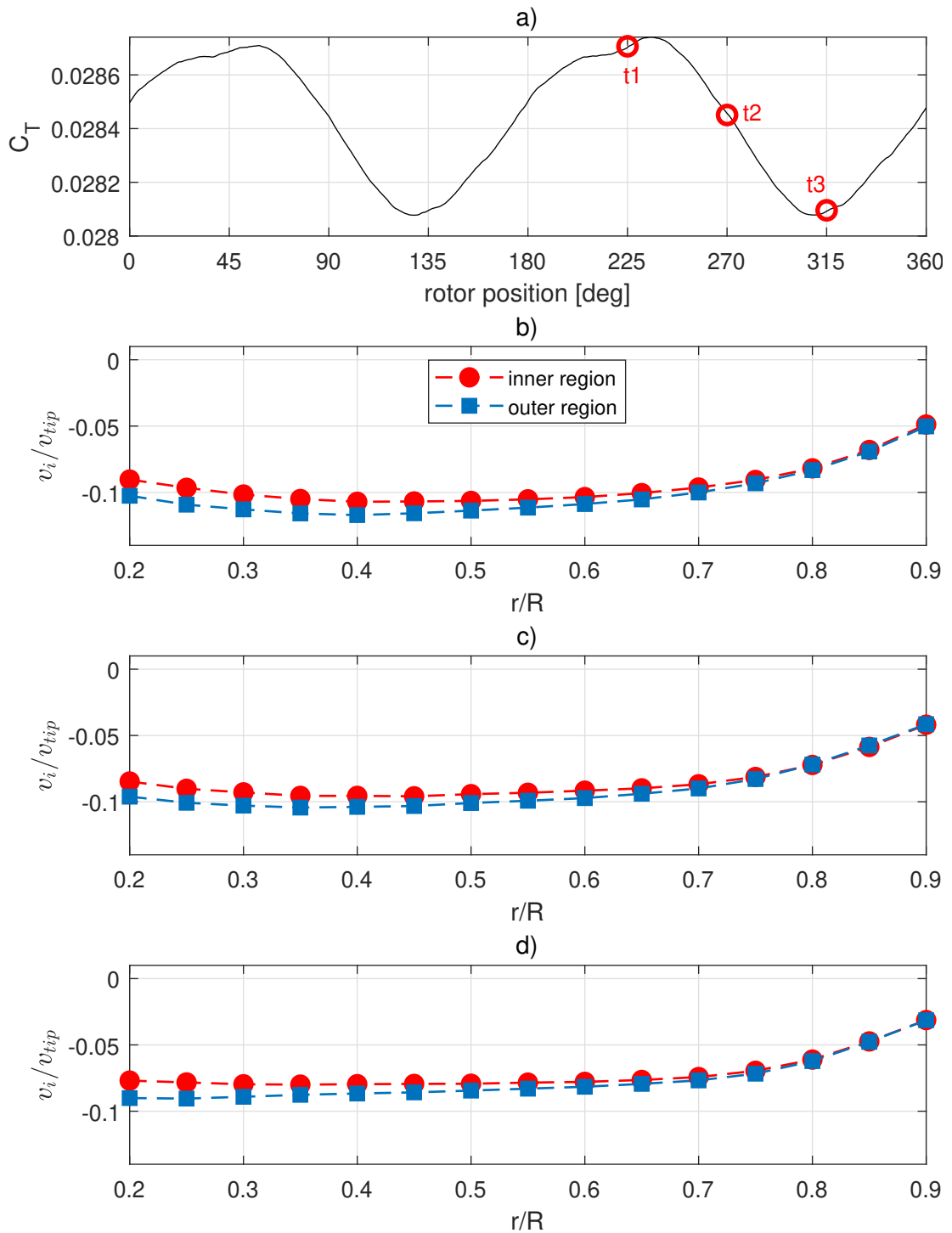


Figure 5.8: Induced velocity comparison between the inner and outer rotor region at different angular rotor positions for the OS case. a) Computed C_T from CFD vs a rotor revolution. The red circles indicates the chosen angular rotor positions for the induced velocity comparison. b), c) and d) correspond to position t1, t2 and t3 respectively. The induced velocity is normalised by the speed at the rotor tip and the x -axis is the radial position along the rotor blade. Note that b), c) and d) share the same legend.

Figure 5.9: As per Figure 5.8 but for the O_T case.

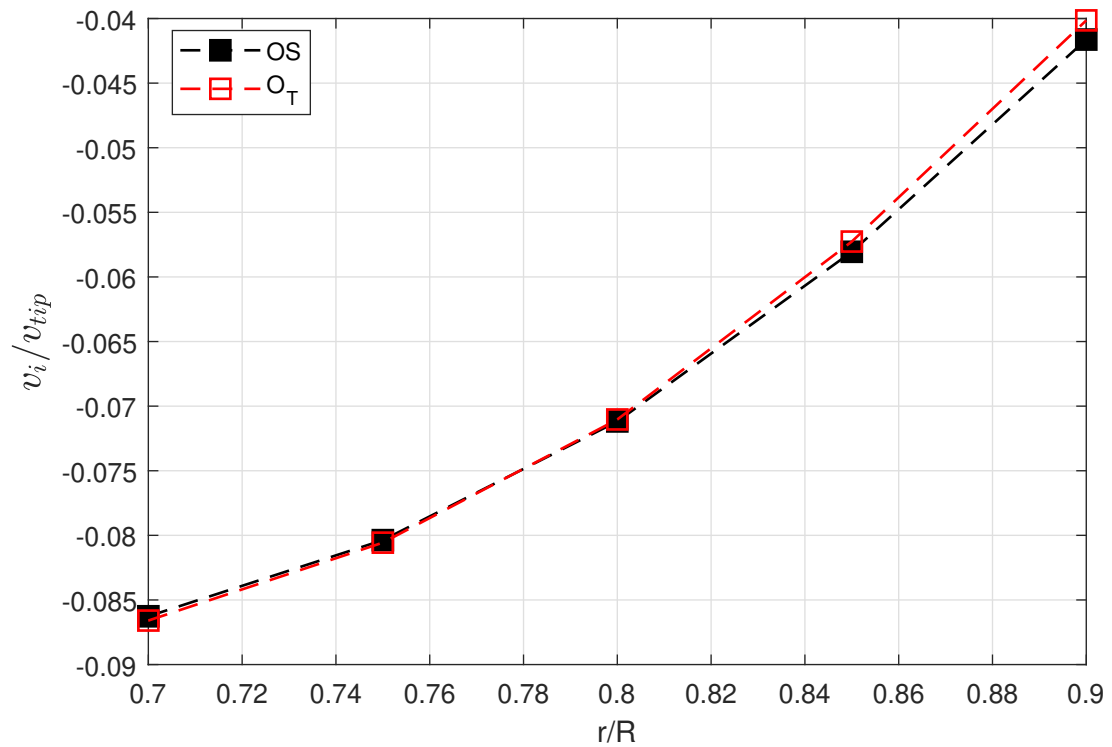


Figure 5.10: Comparison between OS and O_T of the time-averaged induced velocity going through the rotor. The induced velocities are normalised by the rotor tip velocity and the x -axis is the radial position along the rotor blade.

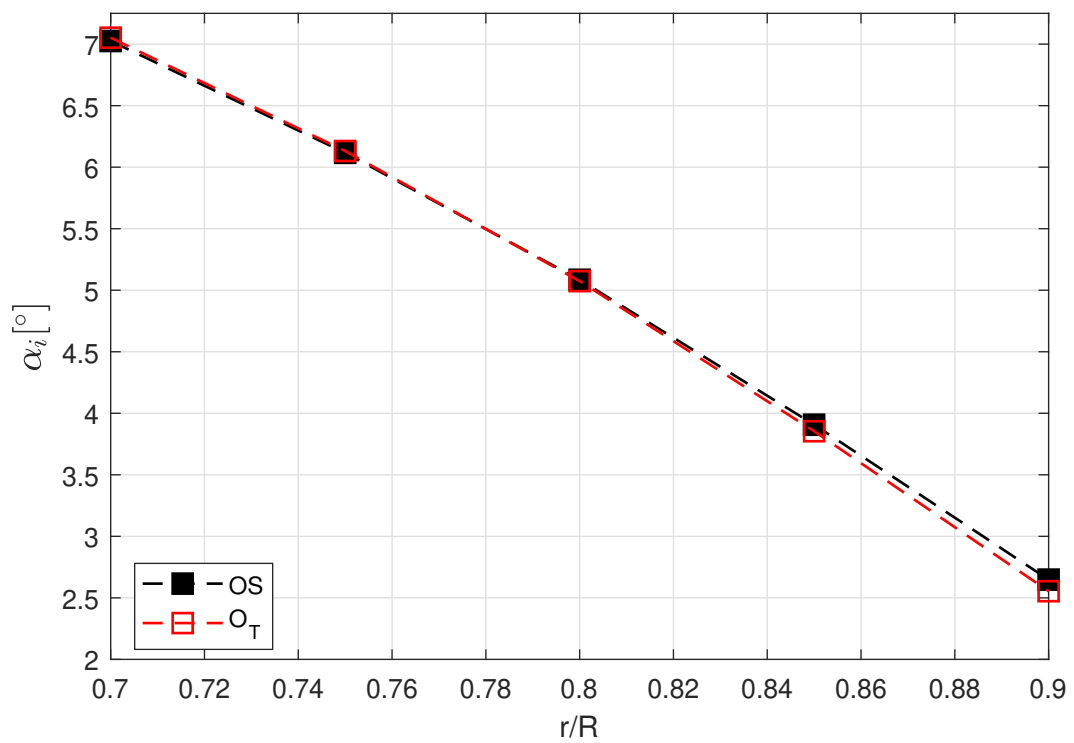


Figure 5.11: Comparison between OS and O_T of the time-averaged induced angle of attack of the rotor. The x -axis is the radial position along the rotor blade.

5.2 Fluid Interactions near Ground and Ceiling

5.2.1 Difference in Thrust along H_0

As the position of the quadcopter is moved from the ceiling to the ground at H_0 , there is a corresponding decrease in C_T , as shown in Figure 5.12. On average the CFD simulations overestimate C_T at H_0 by approximately 7.3% compared to the physical experiments, which is in a similar range as the difference discussed in Section 5.1.3. Additionally, as shown in the figure, there is a difference in the C_T gradient between the CFD simulations and the physical experiments. This is likely due to the presence of the fuselage having a dominant effect on the rotor wake diminishing the effect of the surrounding tunnel boundaries as a result. The location of the stagnation point (as indicated in Figure 5.3) in the physical experiment is also different because of the wake blockage from the fuselage. At H_0V_{-2} , the increase in C_T in the simulations compared to the ongoing gradual decreasing slope shown in the results of physical experiment could also be the result of not modelling a fuselage in the CFD simulations.

5.2.2 Near Ground Fluid Interactions

5.2.2.1 Vorticity and Flow Field in CFD Simulations

Similar to O_T , for the near ground case H_0V_{-2} (Figure 5.13), the rotor wake expands outward radially near the ground plane. The outer rotor region of the redirected rotor wake travels upward along the wall and recirculates back to transit into the rotors' upstream flow. However, since the rotor-ground distance decreases compared to O_T , the wake has less distance to propagate and

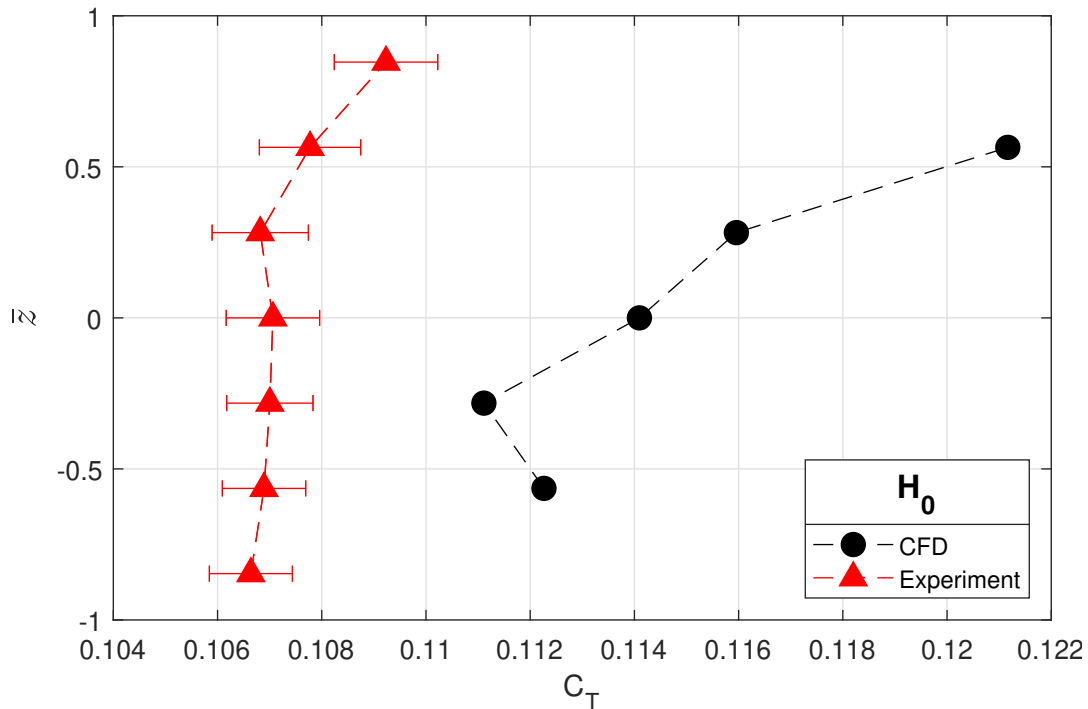


Figure 5.12: Thrust coefficient comparison between the CFD and physical experiments at H_0 .

develop before reaching the stagnation point on the ground. In other words, the wake boundary expands radially outward more rapidly. As shown in Figure 5.13, the outer wake boundary of H_0V_{-2} expands further outward compared to O_S and O_T . Since the quadcopter is positioned further away from the saddle point of the return cycle near the wall compared to O_T , there is more distance to allow the vertical momentum to build up which increases the induced velocity. Although not directly measured, the increase in induced velocity also increases the kinetic energy within the outer rotor wake. For energy to be conserved, the kinetic energy of the tip vortex must decrease which drives a reduction in the circulation of the tip vortex in the outer rotor region (Robinson, 2016), as shown in Figure 5.4.

The recirculation region in the inner wake at H_0V_{-2} is significantly different to the outer wake. This variation is particularly evident when compared to the other positions as seen in Figure 5.13. This is due to the juxtaposition of the ground plane and the symmetry plane confining the flow of the inner wake, causing a strong recirculated flow travelling up to the inner rotor blade. This confined recirculation region delays the dissipation of vorticity when compared to other quadcopter locations. As described in Section 4.1.8.2, this is a reduction in the induced velocity in the inner rotor region due to this confined recirculation region below the rotor. Thus, this also correlates to the significant increase of the circulation of the tip vortex in the inner rotor region compared to the outer rotor region, as depicted in Figure 5.4.

5.2.2.2 Blade Pressure Field

As seen in Figure 5.15, at H_0V_{-2} the rotor experiences large pressure variations when compared to O_T . In particular, the inner rotor region near the rotor tip for $\gamma = 0^\circ, 45^\circ, 90^\circ$ and along the entirety of the leading edge for the outer rotor blade. Numerical noise is also noted primarily at the trailing edge - this is a result of post processing and is not physical.

When compared to O_T , the quadcopter's proximity to the ground plane increases the pressure fluctuation on the rotor blade surfaces which also correlates to the higher fluctuation in C_T as shown in Figure 5.19. Figure 5.16 indicates that the majority of the blade pressure difference between H_0V_{-2} and O_T occurs near the tip of the rotor blades, particularly for the inner rotor region. Although the figure suggests that the rotor produces less lift in the outer rotor region at H_0V_{-2} (for $\gamma = 0^\circ, 45^\circ$ and 90°), the inner rotor region produces much more lift compared to O_T . This is particularly noticeable at the tip region. Overall, this results in a slight increase in thrust at H_0V_{-2} .

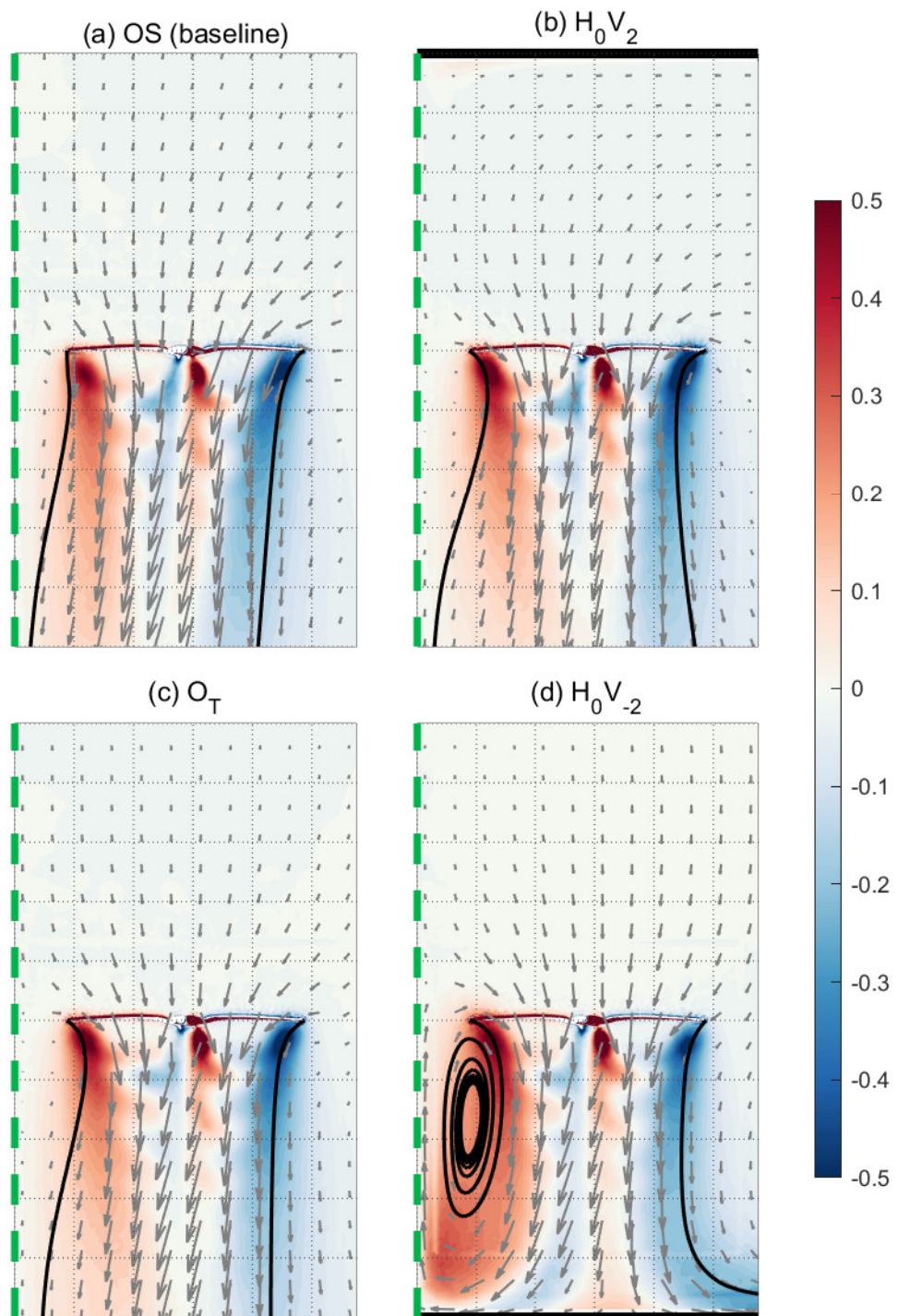


Figure 5.13: Flow field in Cross Section AA of the right propeller at different tunnel locations. The green dash line is the symmetry line between the left and right propellers. The contour plots show the $x-z$ component of vorticity normalised by the rotation speed, ω_y/Ω . The solid black lines represent the streamlines starting from the propeller's tip. The solid black line in (b) and (d) represents the ceiling and ground plane respectively. The grid line spacing is $0.5R$.

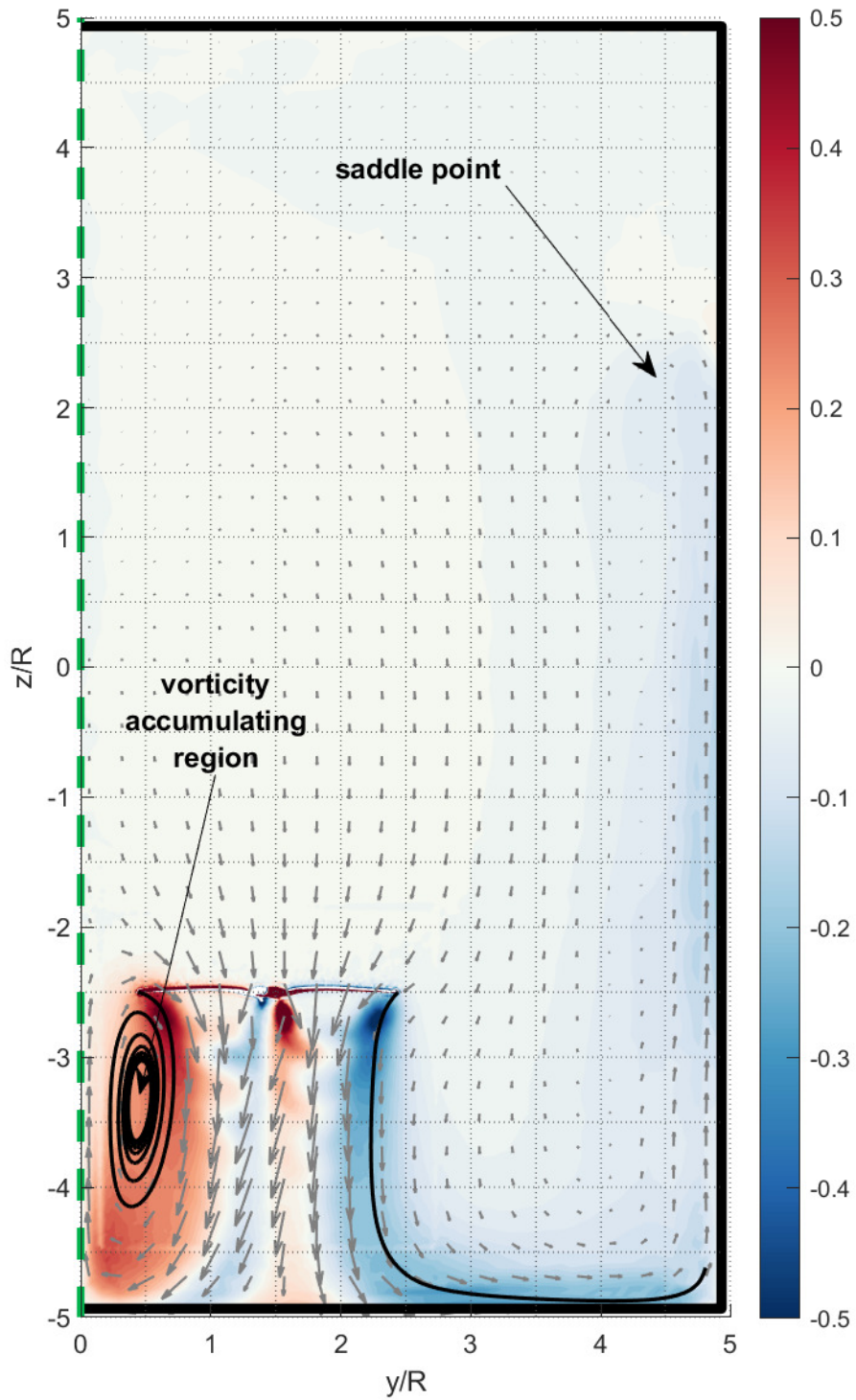


Figure 5.14: As per Figure 5.2 but for quadcopter located at H_0V_{-2} .

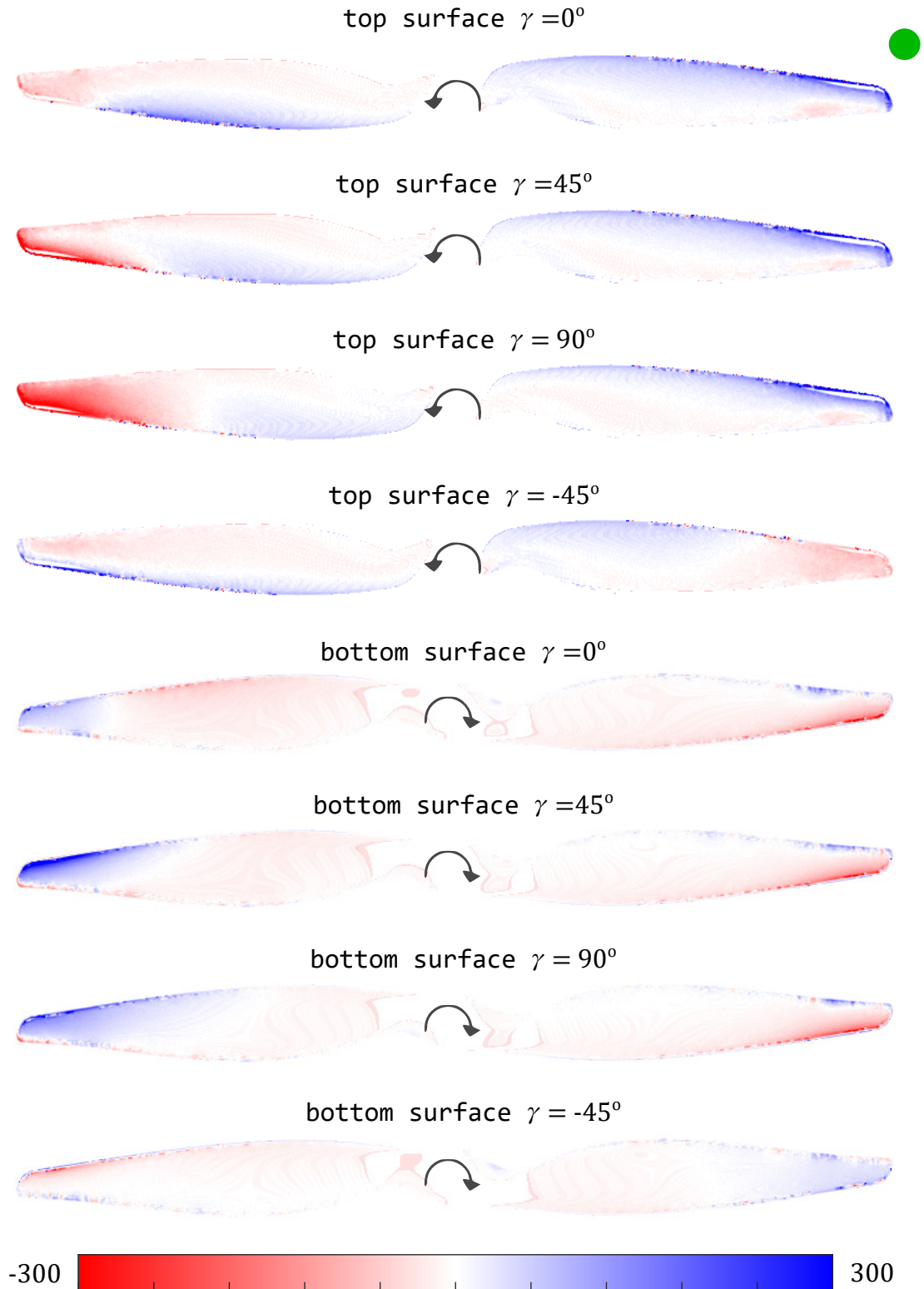


Figure 5.15: As per Figure 5.6 but for the pressure difference between H_0V_{-2} and O_T . Blue contour indicates H_0V_{-2} has higher pressure. The pressure range on the individual rotor is approximately $[-3000, 1500]$

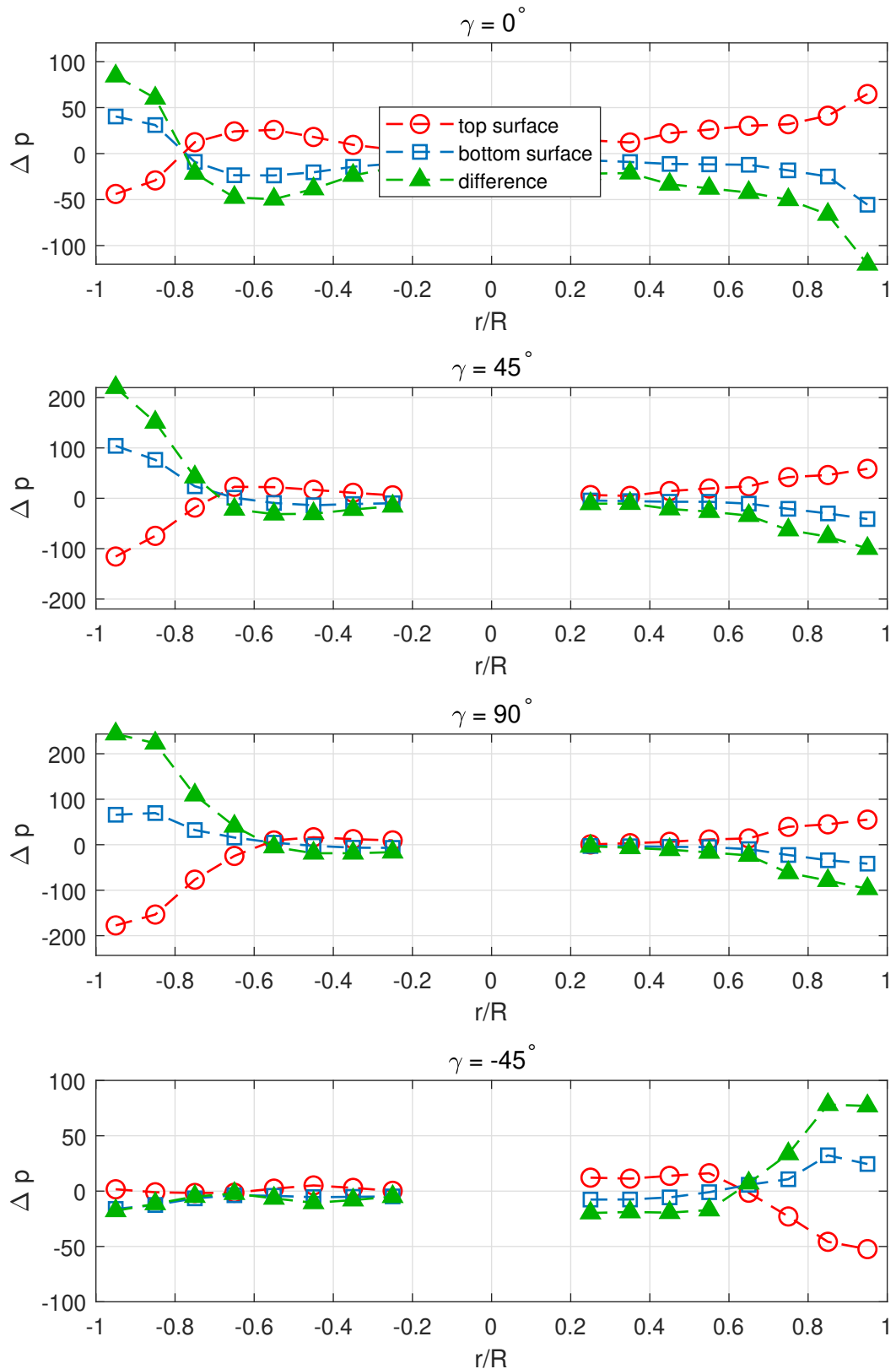


Figure 5.16: As per Figure 5.7 but for the difference between H_0V_{-2} and O_T . A positive value in the green triangle suggests higher C_T in H_0V_{-2} .

5.2.2.3 Impact on Thrust

Compared to O_T , Figure 5.17 indicates a slight increase in the time-averaged induced velocity at H_0V_{-2} . As shown in Figure 5.19, the inner rotor region experiences less induced velocity compared to the outer region. This is driven by the increased circulation at H_0V_{-2} in the inner rotor region (Figure 5.4) as discussed in Section 5.2.2.1. **Although the increased circulation in the inner rotor region drives an increase in lift, this is countered by the reduction in the radial component of velocity due to the return cycle, resulting in a lift reduction in the outer rotor region. Thus, the rotor at H_0V_{-2} still generates less thrust than O_T overall.**

Note that Figure 5.12 indicates there is a slight increase in C_T from H_0V_{-1} to H_0V_{-2} , which only occurred in the CFD simulations but not the physical experiments. The presence of the quadcopter fuselage in the physical experiment is an obstruction inhibiting the flow recirculation, restricting the formation of the tip vortex in the inner rotor region. This reduces the effect of the accumulated vorticity in the inner rotor region, hence, increasing the induced velocity in the physical experiments. Therefore, the C_T remains in a gradual decreasing trend from O_T to H_0V_{-2} in the physical experiments which does not fully agree with the CFD result, as seen in Figure 5.12.

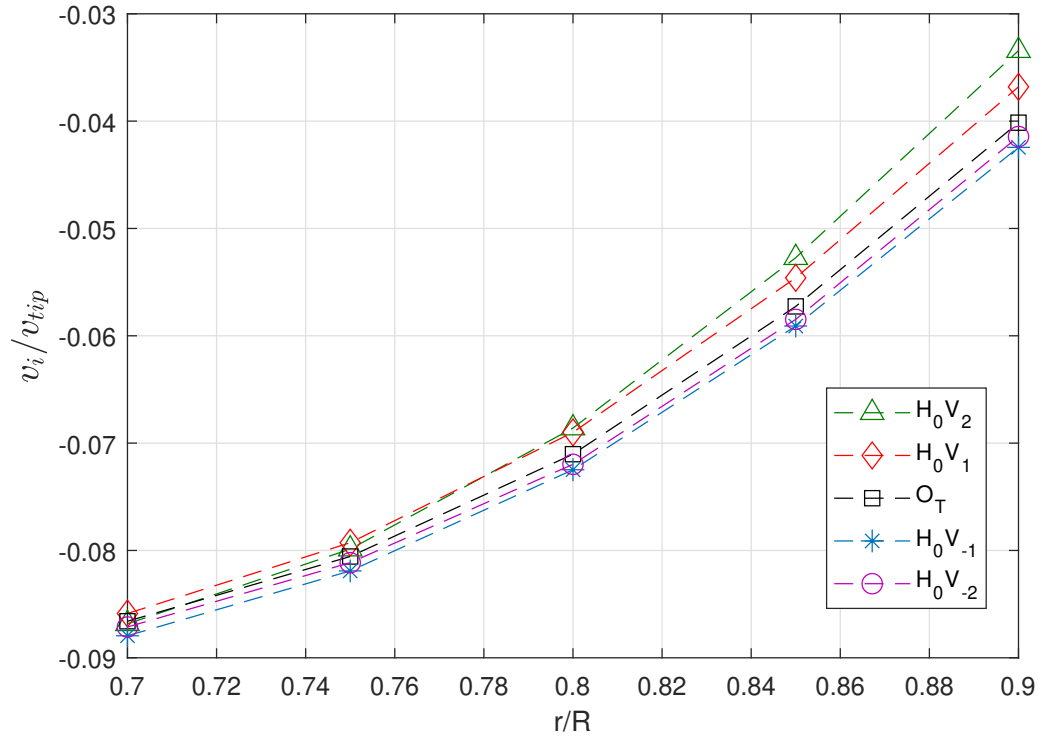


Figure 5.17: Time-averaged induced velocity comparison of the H_0 cases along the radial position of the rotor blade. The induced velocities are normalised by the rotor tip velocity.

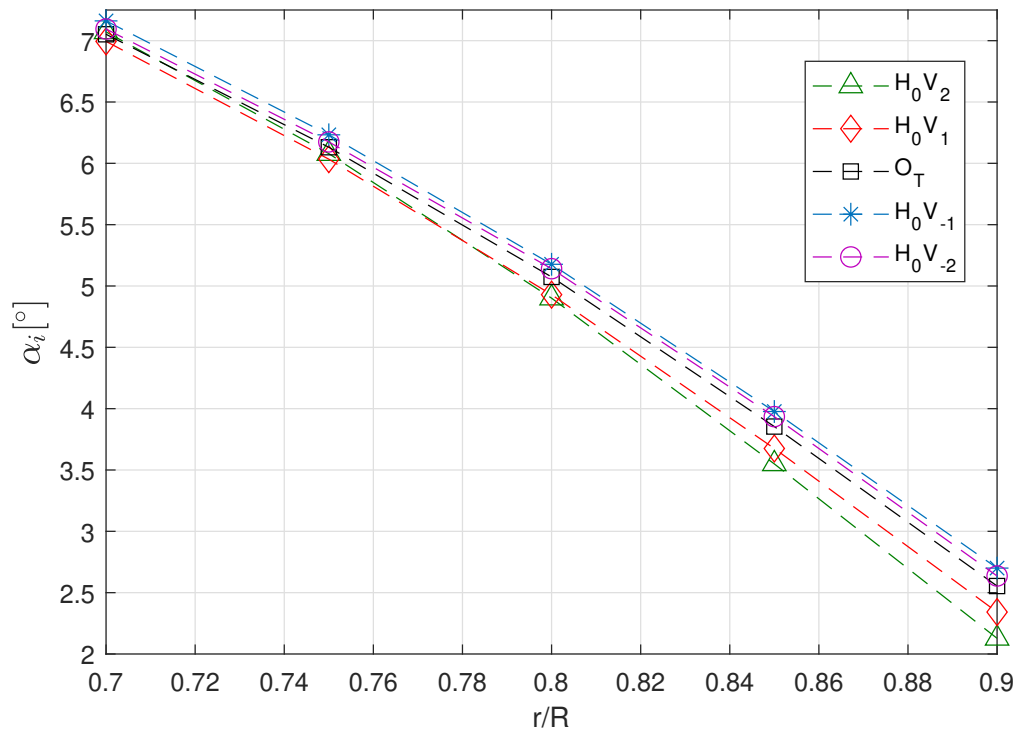
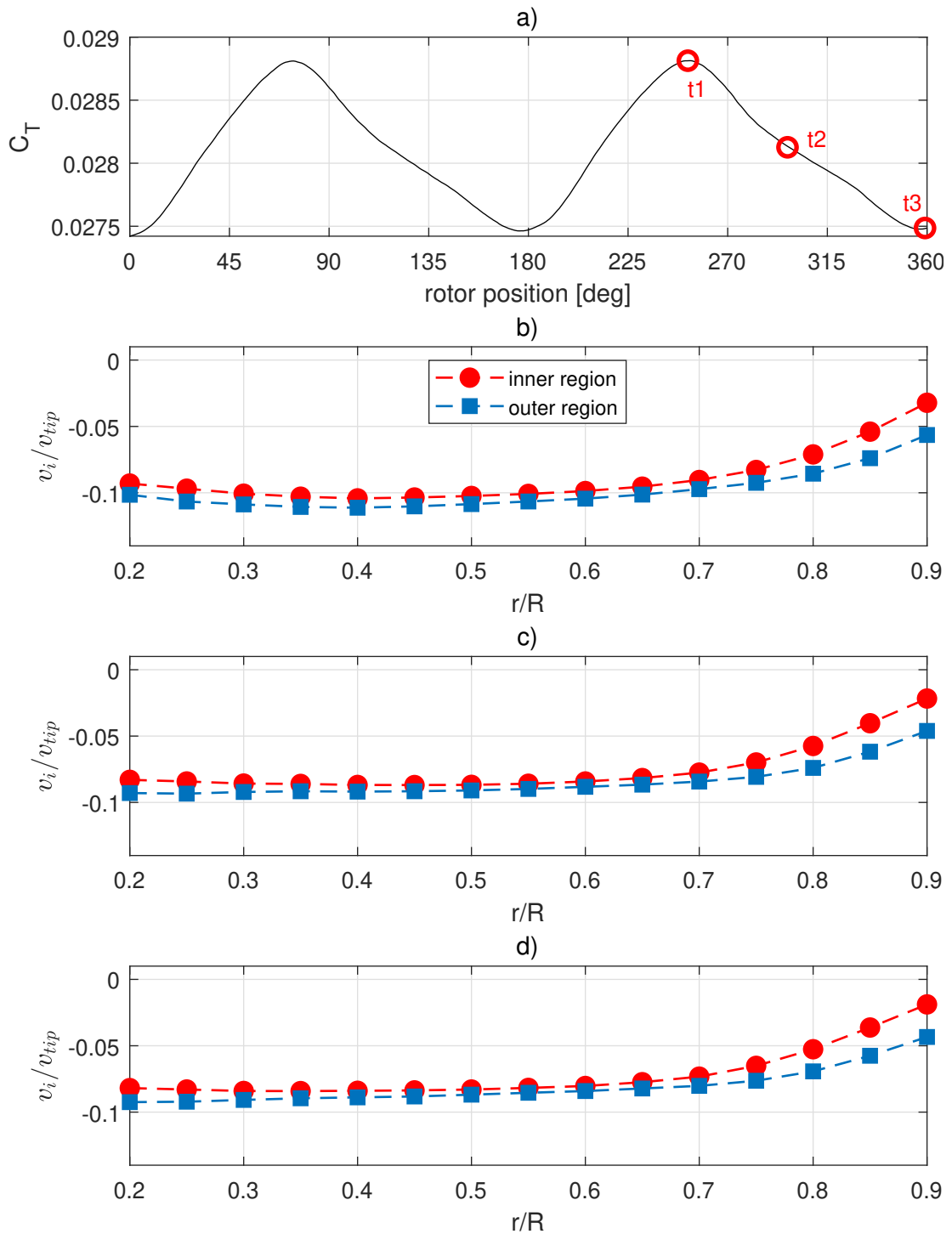


Figure 5.18: Time-averaged induced angle of attack comparison of the H_0 cases along the radial position of the rotor blade. Note that an increase in the induced angle of attack is equivalent to a reduction in the effective angle of attack.

Figure 5.19: As per Figure 5.8 but for the H_0V_{-2} case.

5.2.3 Near Ceiling Fluid Interactions

5.2.3.1 Vorticity and Flow Field in CFD Simulations

The upstream flow characteristics in H_0V_2 differs greatly from O_S , O_T and H_0V_{-2} as depicted in Figure 5.20 and 5.13. Note that in the outer rotor region, as the quadcopter is repositioned close to the ceiling, the adjacency to the ceiling induces a reduction in the vertical component of the flow momentum. Therefore, there is a higher portion of the upstream flow travelling parallel to the ceiling plane in order to conserve momentum compared to O_T . This inlet flow also induces a radial contraction of the rotor wake. At H_0V_2 , Figure 5.4 shows the rotors also experience the highest circulation within the tip vortices, which is coincident with the peak C_T shown in Figure 5.12. This phenomenon resembles the aerodynamic characteristic of a single rotor near the ceiling (Robinson et al., 2016). However, note that shortly after the radial contraction of the rotor wake boundary near the rotor, unlike O_S , the wake boundary does not continue to contract. Since the rotor-ground distance has increased, the viscous effect of the tip vortices has less influence on the wake further downstream and the wake of the rotors merge into a single jet. The stagnation point that is directly below the rotor in the other cases no longer exists at H_0V_2 as the wakes of all rotors have already merged into a single stream. As the jet approaches the ground plane, it causes the wake boundary to expand radially away from the stagnation point at the symmetry line. This is well described by inviscid flow theory of an impinging jet.

5.2.3.2 Blade Pressure Field

Compared to H_0V_{-2} , H_0V_2 has more consistent pressure difference with O_T as seen in Figure 5.21. The majority of the pressure difference occurs at the tip of the rotor for both the top and bottom blade surfaces. The Δp profiles of H_0V_2 show more resemblance between the inner and outer rotor region than the other H_0 cases as illustrated in Figure 5.22. The reduction in the vertical component of velocity in the flow upstream of the rotor, due to the ceiling significantly reducing the top blade surface pressure, as illustrated in the figure. This behaviour is consistent with a single rotor ICE in open space (Robinson et al., 2016). Overall, the pressure differential (green triangle curves) in Figure 5.22 indicate an increase in thrust at H_0V_2 across all angular position compared to O_T .

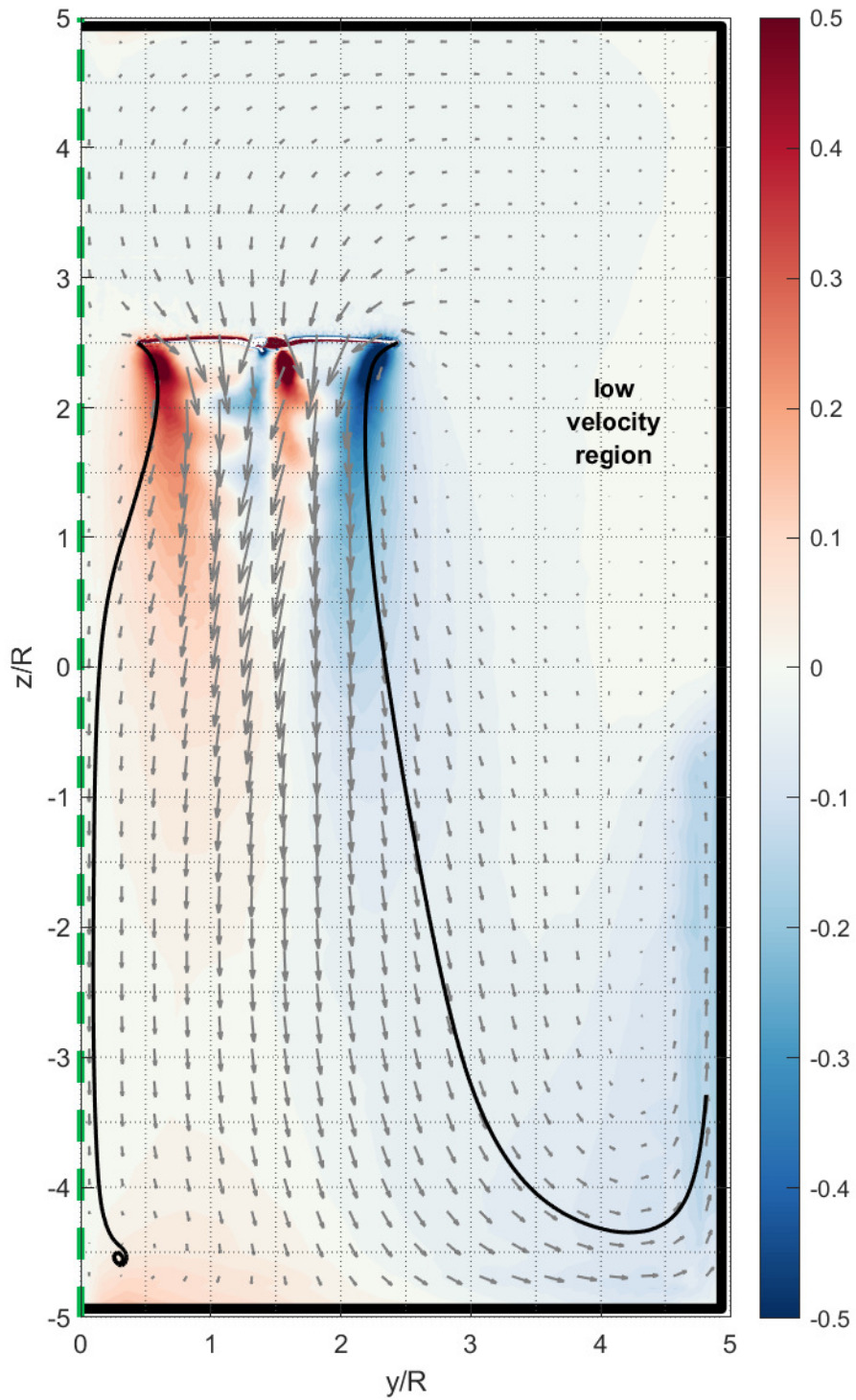


Figure 5.20: As per Figure 5.2 but for quadcopter located at H_0V_2 .

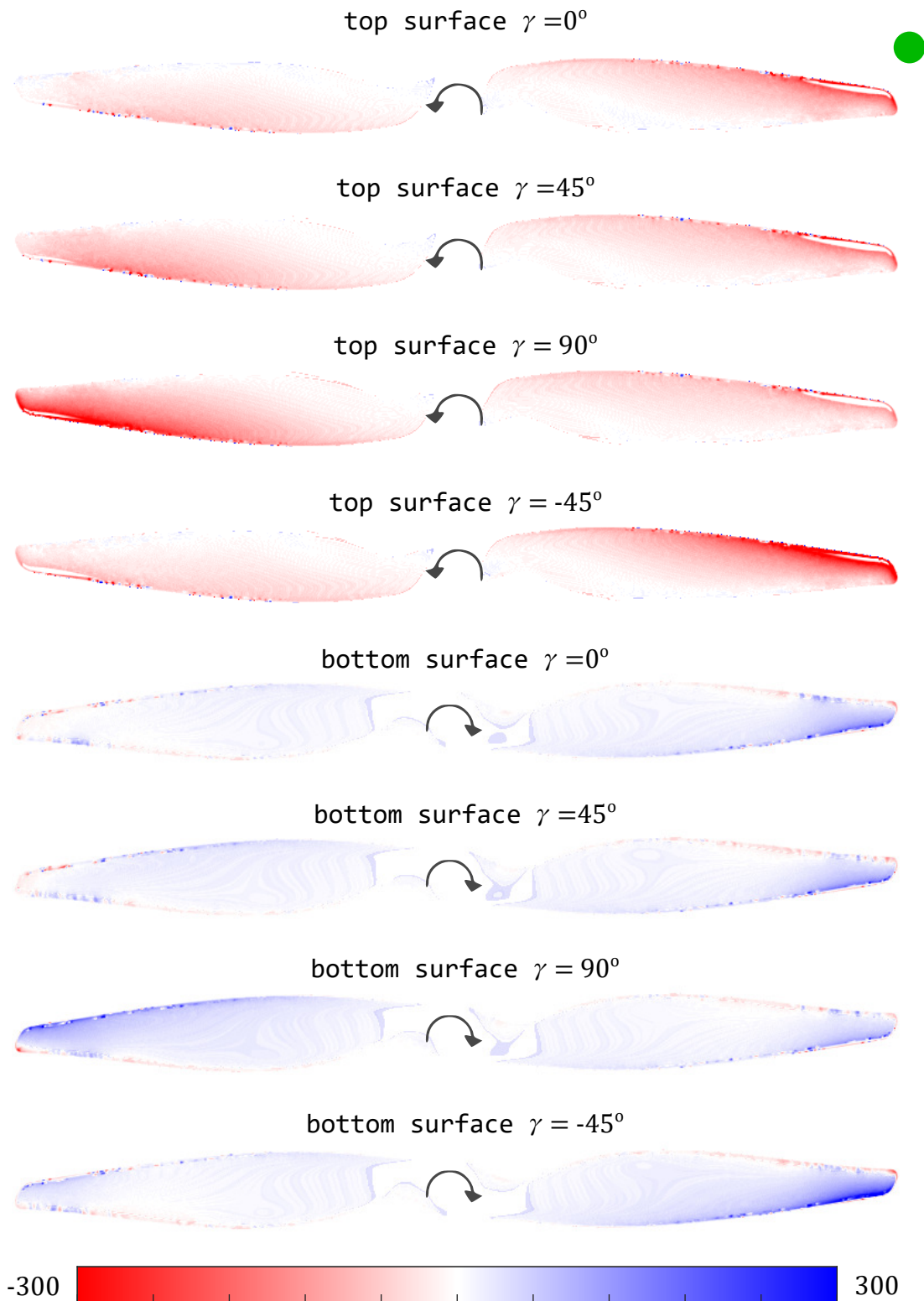


Figure 5.21: As per Figure 5.6 but for the pressure difference between H_0V_2 and O_T . Blue contour indicates H_0V_2 has higher pressure.

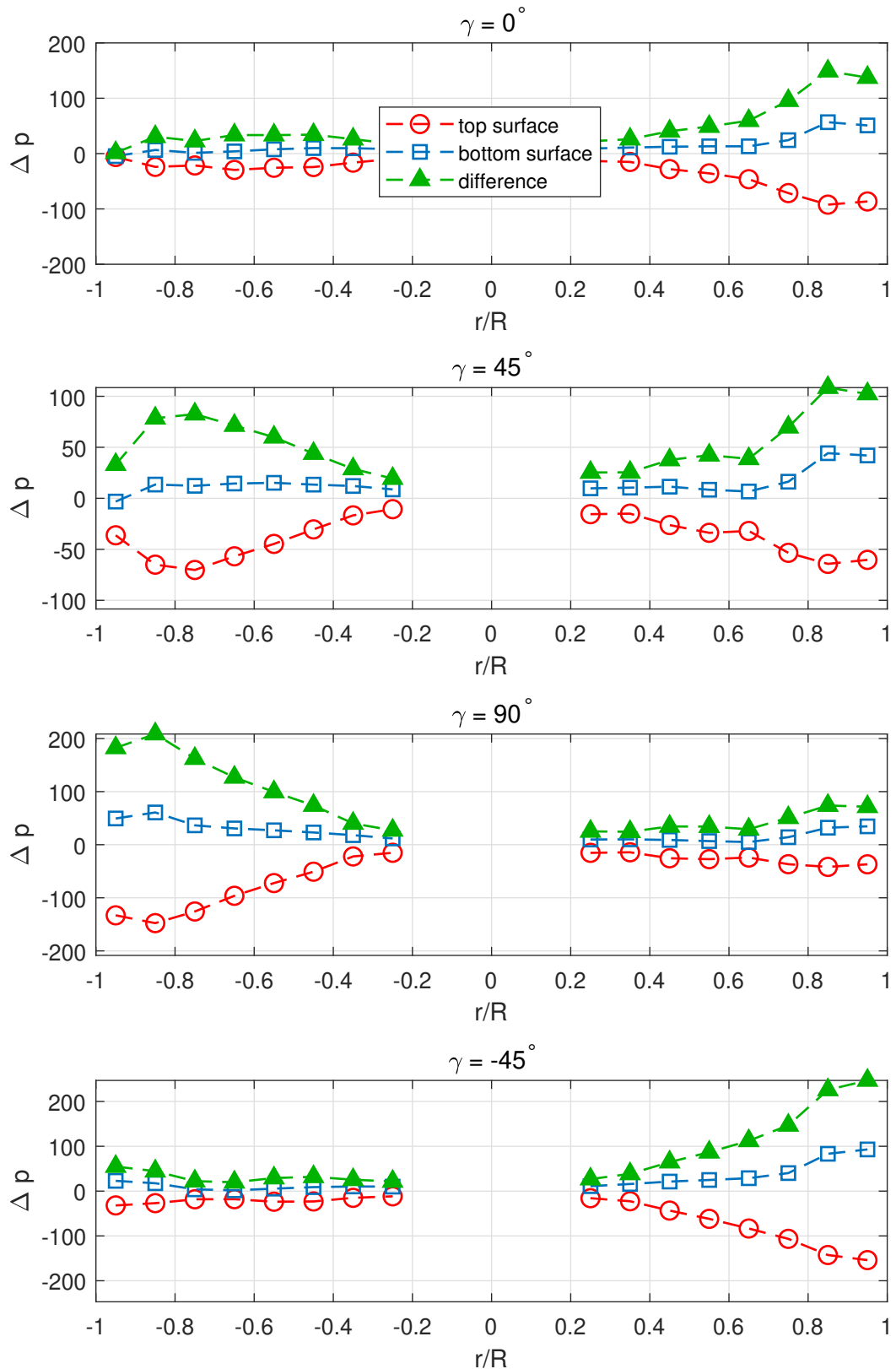


Figure 5.22: As per Figure 5.7 but for the difference between H_0V_2 and O_T . A positive value in the green triangle suggests higher C_T in H_0V_2 .

5.2.3.3 Impact on Thrust

In terms of the flow field upstream of the rotor, inside the tunnel, the quadcopter experiences a similar effect to a single rotor ICE. **As the rotor-ceiling gap decreased, the reduction in the vertical component of the upstream velocity causes the averaged induced velocity across the propeller to reduce, which drives the reduction in the averaged induced angle of attack, as shown in Figure 5.17 and 5.18. As discussed in Section 5.2.3.2, this decrease in induced velocity also induces a reduction in the top blade surface pressure. Therefore, there is an increase in lift production compared to O_T .** This relationship is similar to Robinson et al. (2016)'s finding for a single rotor. Compared to O_T , H_0V_2 experiences less induced velocity going through the outer rotor region as seen in Figure 5.9 and 5.23. This is due to the quadcopter being positioned closer to the low velocity region of the return cycle near the wall as depicted in Figure 5.20.

5.2.4 Comparison with Quadcopter Open Space IGE and ICE

Using the physical experiment results, a comparison between the H_0 cases, OS and the quadcopter IGE and ICE in open space is depicted in Figure 5.24. It is clear that the H_0 cases experience greater thrust variation in the measurement during the experiments compared to all other open space cases. Note that at $\bar{z} = 0$, in theory the OS_c and OS_g cases should align within the error margin of OS because all are at the same physical location. However, $\bar{z} = 0$ for OS_c and OS_g is actually a distance of $6R$ away from the far boundary (ground or ceiling plane) in practice. This distance although considered to be sufficiently far such that the boundary has minimal influence on the rotors, still contributes to about 1% offset in C_T between OS_c and OS as evident in Figure 5.24.

Near the ceiling, H_0 and OS_c show a similar trend with H_0 having slightly higher C_T close to the ceiling and lower C_T near the centre compared to OS_c . This is an indication that inside the tunnel at H_0 , the ceiling plane has a more dominant effect on the rotors than the side walls. In the tunnel, the upstream flow of the rotors is strongly impacted by the small rotor-ceiling gap, similar to the open space quadcopter ICE scenario. Yet, since the rotor-ground distance is relatively greater, the ground plane has a less pronounced effect on the rotors.

Figure 5.24 shows that H_0 differs greatly from OS_g . As discussed in Section 5.2.2, due to the reduced distance from the ground, the radial expansion of the wake boundary at H_0 is similar to ground effect behaviour in open space (Lakshminarayan et al., 2013). However, the return cycle near the wall has shown a great influence on the upstream flow of the rotors, and therefore, increases the overall lift of the quadcopter close to the ground plane compared to OS_g . This aligns with the CFD findings when comparing the C_T at O_T , H_0V_{-1} and H_0V_{-2} as seen in Figure 5.12.

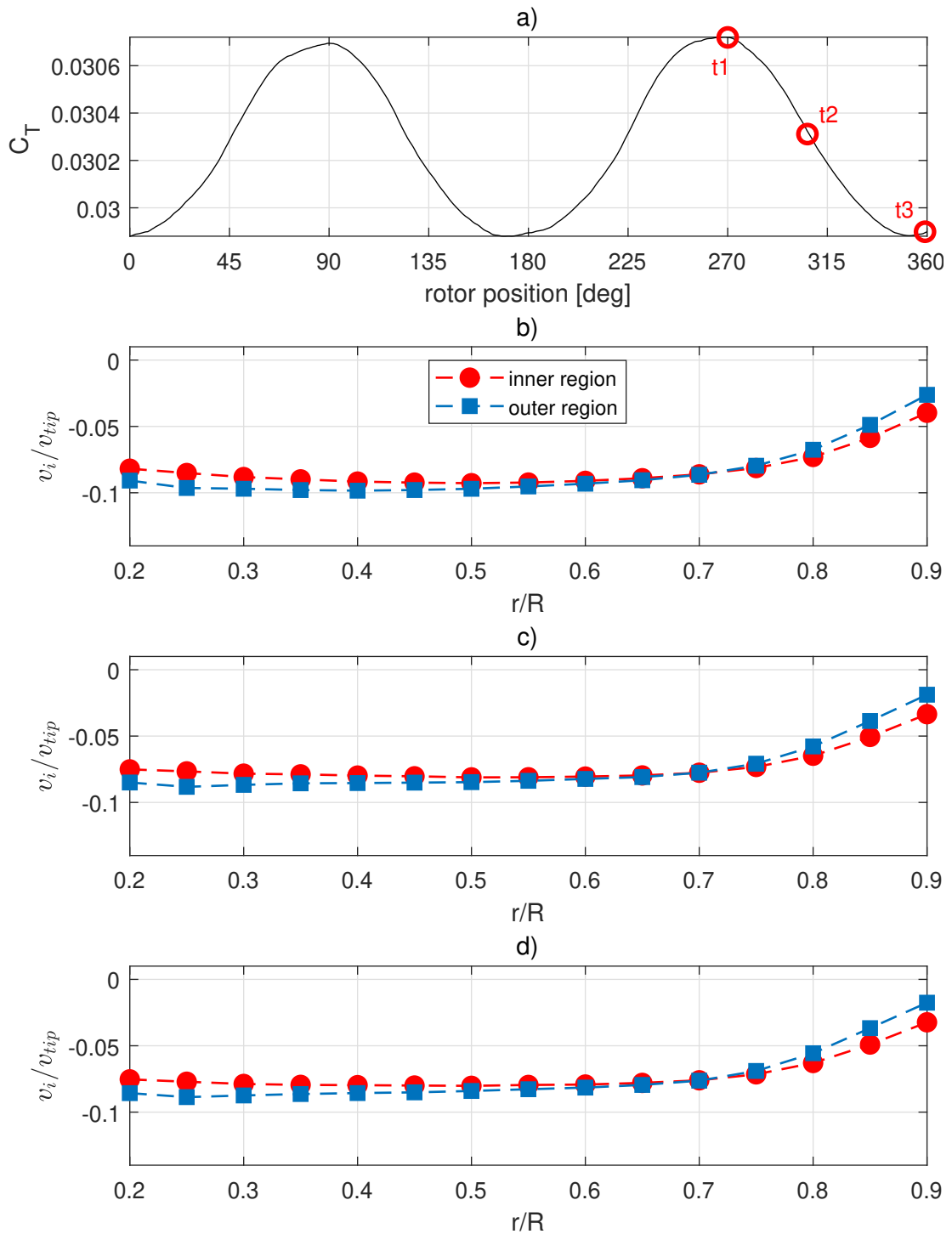


Figure 5.23: As per Figure 5.8 but for the H_0V_2 case.

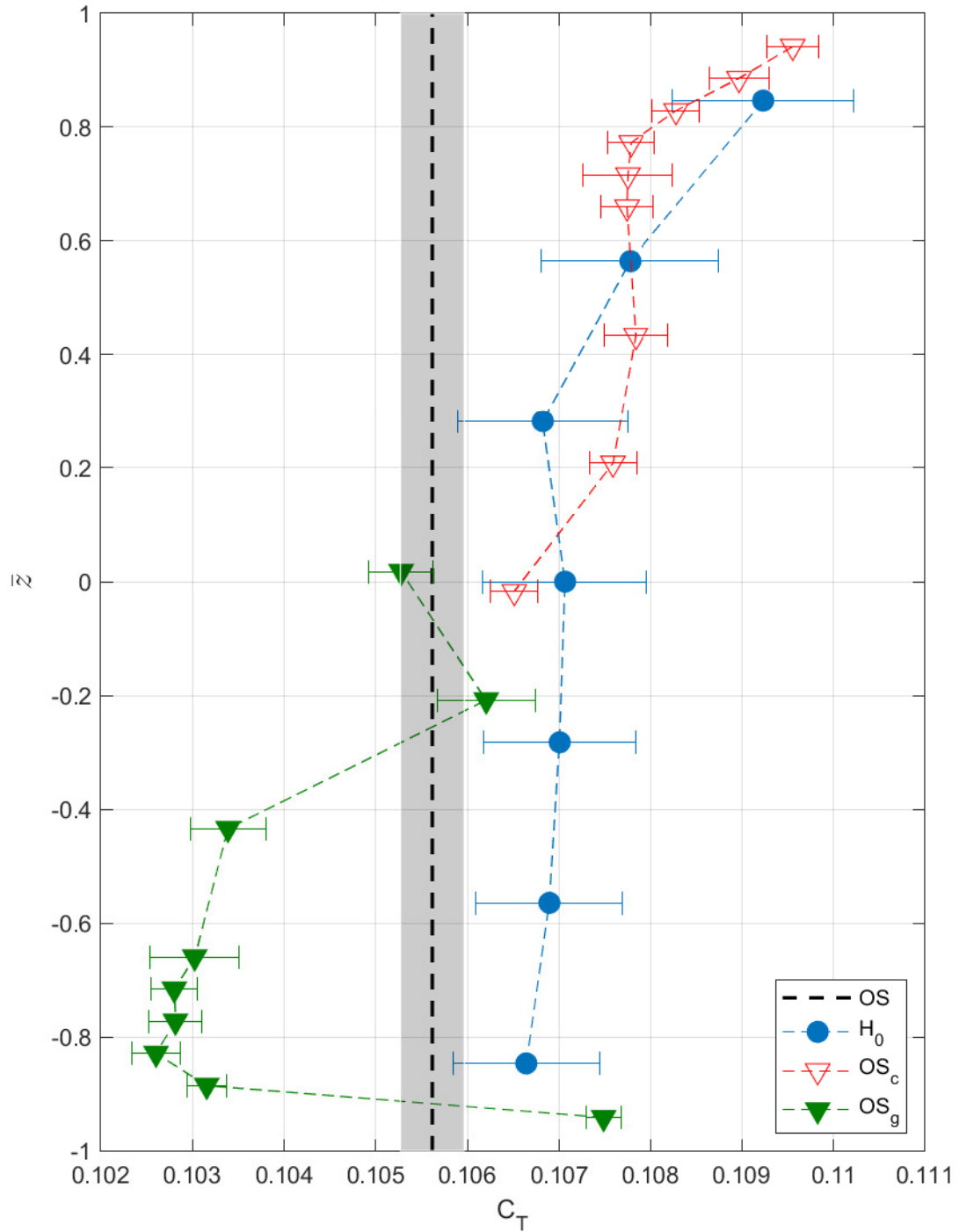


Figure 5.24: Thrust coefficient comparison between physical experiment results of H_0 , OS_c and OS_g . The dark shaded region represents the error region of the OS case.

5.3 Fluid Interactions near Wall

5.3.1 Differences between H_4V_0 and O_T

For the benefit of the reader, in the following discussion, the near wall propeller, P_1 , is labelled as P_w and the near centre propeller, P_3 , is labelled as P_c . When the quadcopter is positioned near the side wall, the flow around P_c and P_w is no longer symmetrical. This difference is highlighted in Figure 5.25, comparing H_4V_0 with O_T .

At H_4V_0 , the wall-to- P_w gap has been reduced and the fluid effect due to the wall becomes the dominant effect on the rotor. The rotor wake boundary is entrained to the flow along the wall and expands further outward radially compared to O_T as shown in Figure 5.25. The wall also confines the tip vortex and inhibiting convection of vorticity out of the outer wake region. Hence, there is an increase in circulation in the outer rotor region of P_w as depicted in Figure 5.27. In addition, the adverse pressure gradient created by the recirculated jet travelling upward causes a boundary layer separation on the wall, which is located close to rotor tip of P_w (in the outer rotor region) as seen in Figure 5.26. When a rotor is close to a vertical wall, the flow around the near-wall side of the rotor tip reduces its radial component of velocity in the vicinity of the wall boundary layer. This in turn increases the vertical component of velocity to conserve momentum (Robinson, 2016). Yet, at H_4V_0 the recirculated flow between the wall and the outer rotor region of P_w counters this effect and induces some radial component of velocity going into the rotor. Therefore, the time-averaged induced velocity of P_w at H_4V_0 is slightly lower than O_T as a result of the recirculated flow. Furthermore, Figure 5.33 and 5.35 show that the blade surface pressure in the inner rotor region has little difference compared to O_T . The majority of the pressure difference (compared to O_T) occurs in the outer rotor region (for $\gamma = 0^\circ, 45^\circ$ and -45°) where the recirculation region is located. Overall the pressure profile in Figure 5.35 also suggests a slight reduction in lift in the outer rotor region of P_w compared to O_T .

Since P_c is further away from the left wall at H_4V_0 , the effect of the left wall has less influence on the wake of the rotor and the viscous actions with the wakes of the adjacent rotors dominates the rotor wake. Similar to OS, the wake of P_c is entrained by the wakes of the adjacent rotors and is angled toward the centre of the quadcopter. This reduction in the horizontal momentum of the P_w rotor wake drives an increase in the horizontal momentum of the P_c wake. Thus, increasing the horizontal component of velocity at the upstream of P_c in the outer rotor region.

The recirculated flow along the wall passes a low velocity region before transitioning into the upstream flow of P_c . As shown in Figure 5.25, there is a greater horizontal component of velocity going into the upstream flow region of P_c (in the outer rotor region) compare O_T . The reduction in induced velocity is also evident in Figure 5.28, especially in the outer rotor region. As a result, there is a reduction in the time-averaged induced velocity going through P_c (Figure 5.30) which also drives an increase in circulation of the tip vortex (Figure 5.27) compared to O_T . The majority of the blade pressure variation (compared to O_T) occurs on the top blade surface rather than the bottom blade surface due to P_c 's relative position to the return cycle having been changed. The surface pressure differential in Figure 5.34 suggests that on average P_c has an improvement in thrust

generation compared O_T .

Note that in Figure 5.29, the waveform of the C_T curve for P_w appears to have another frequency component with high magnitude of energy. Whereas, at H_0 or P_c at H_4V_0 , the C_T curves for the rotors all appear to be a “single” sinusoidal wave. This increased magnitude of another frequency component in C_T for P_w is induced by the proximity to the wall and the second local maximum in C_T (located close to t_2 in Figure 5.29) occurs when the rotor tip is facing the wall at approximately $\pm 45^\circ$. Since frequency analysis of C_T is not in the scope of this thesis, this C_T characteristic for P_w is noted in the following sections in this chapter, but there is no further discussion regarding this characteristic.

In summary, for P_w at H_4V_0 , the recirculated flow between the wall and the rotor induces a greater radial component of velocity near the propeller tip in the outer rotor region. This increases the local effective angle of attack (Figure 5.31) and lift production on the rotor. The increase in thrust is much higher for P_c compared to P_w . This is driven by the increasing horizontal component of velocity in the upstream flow region due to the return cycle on the left wall and the reduction in opposing horizontal momentum from the wake of P_w .

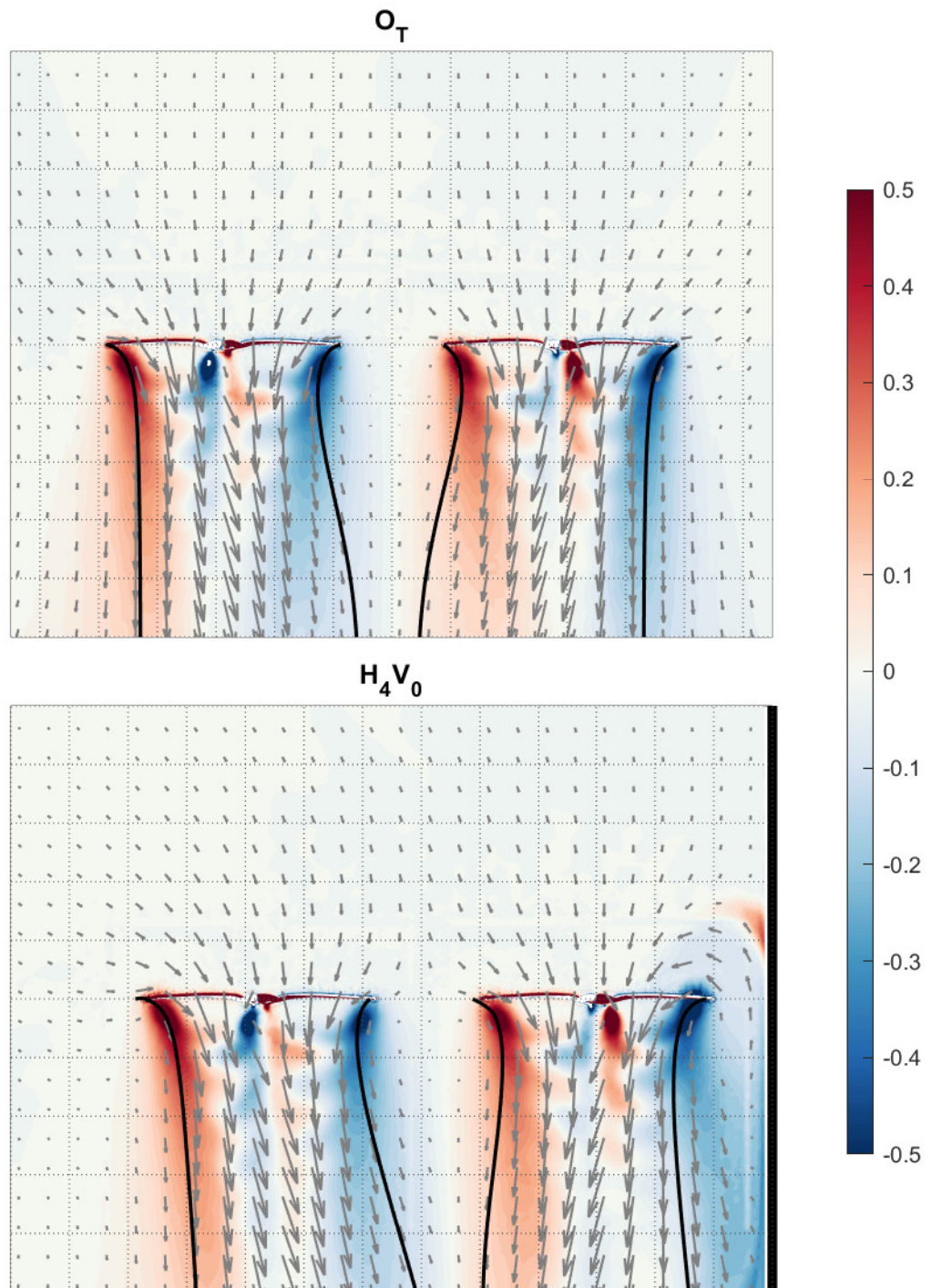


Figure 5.25: Flow field comparison between O_T and H_4V_0 in Cross Section AA. The green dash line is the symmetry line between the left and right propellers. The contour plots show the x - z component of vorticity normalised by the rotation speed, ω_y/Ω . The solid black lines represent the streamlines starting from the propeller's tip.

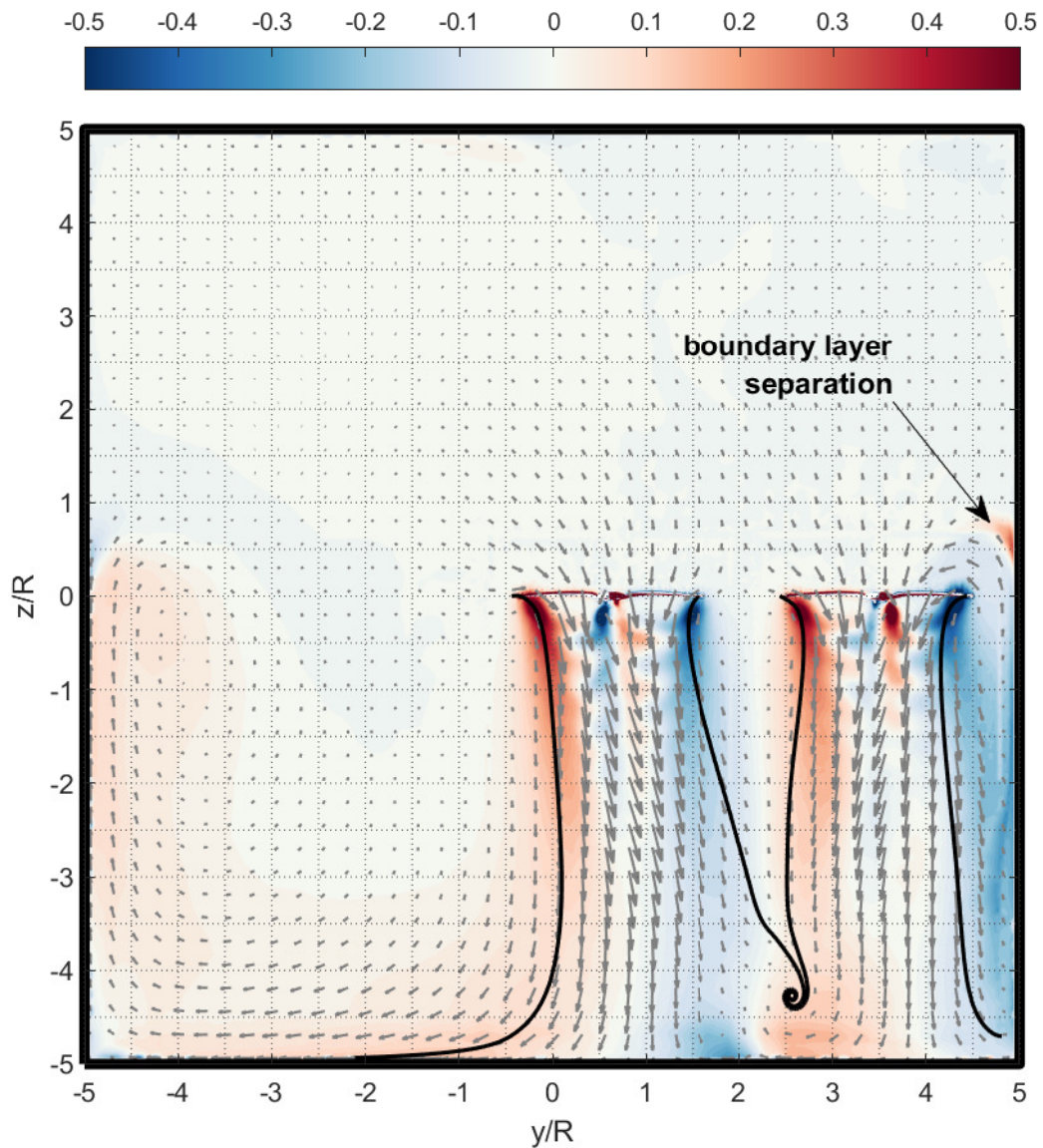


Figure 5.26: Flow field in Cross Section AA, showing P_c and P_w at H_4V_0 . The green dash line is the symmetry line between the left and right propellers. The contour plots show the $x-z$ component of vorticity normalised by the rotation speed, ω_y/Ω . The solid black lines represent the streamlines starting from the propeller's tip.

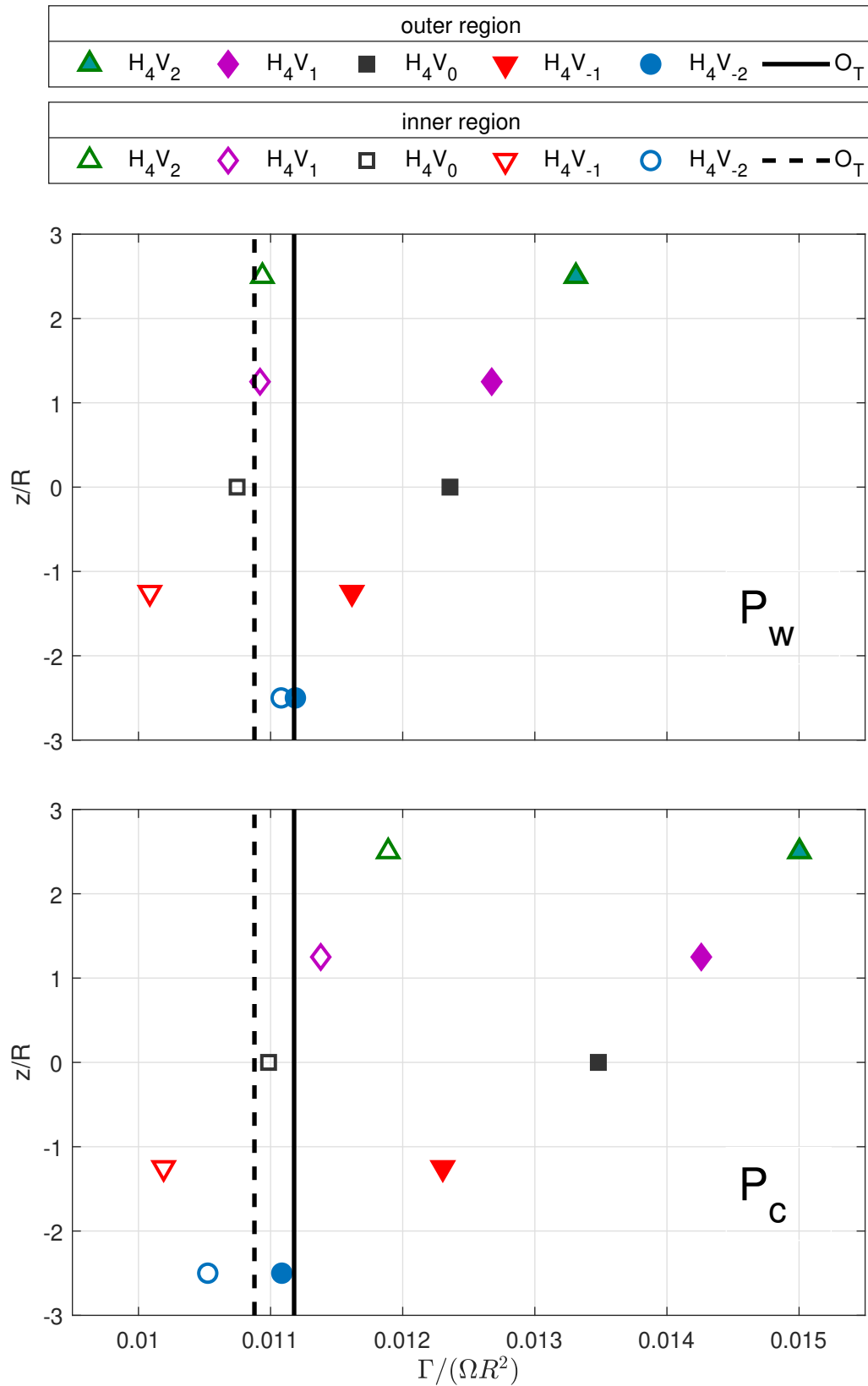


Figure 5.27: Normalised time-averaged tip vortex circulation comparison between P_c and P_w at H_4 .

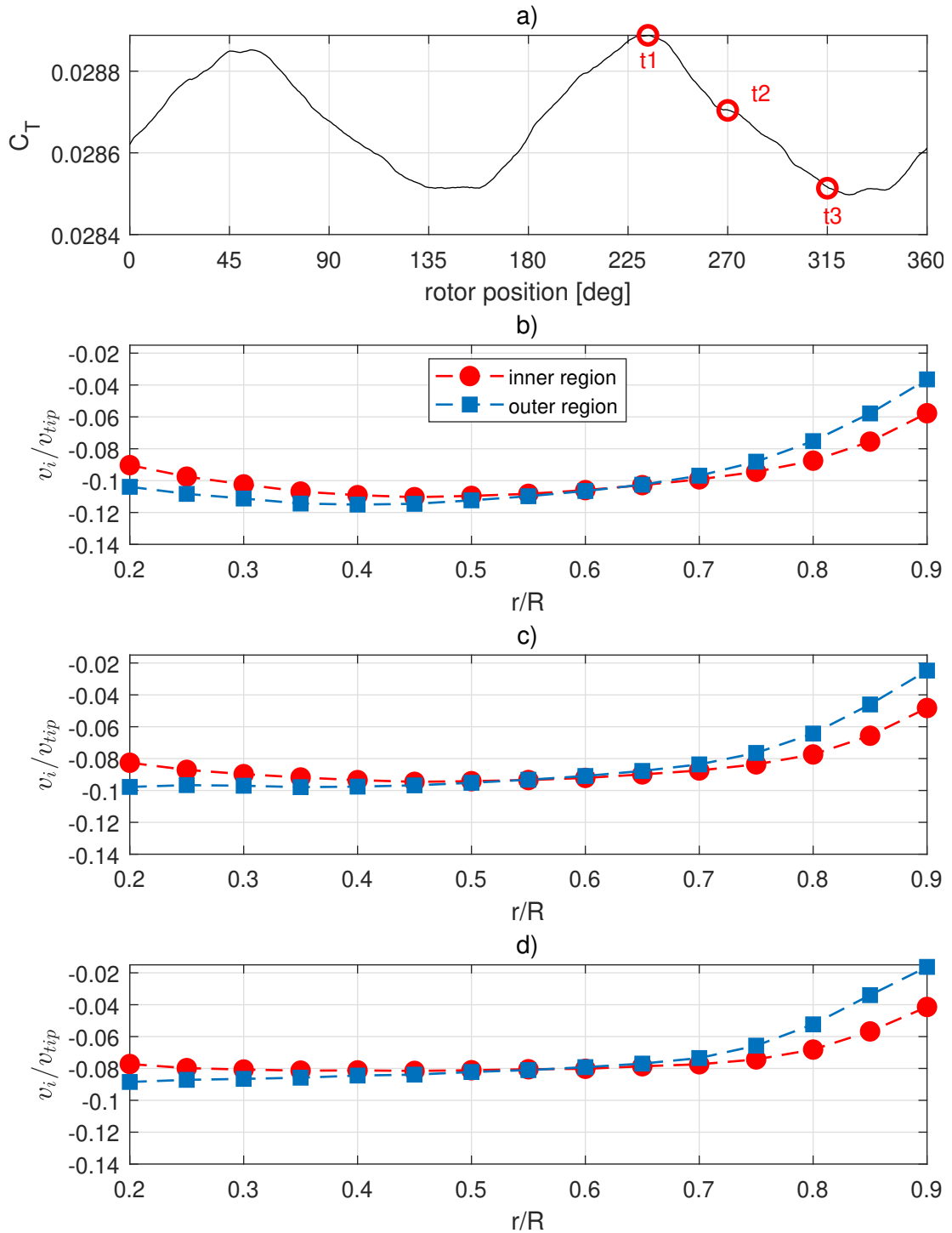
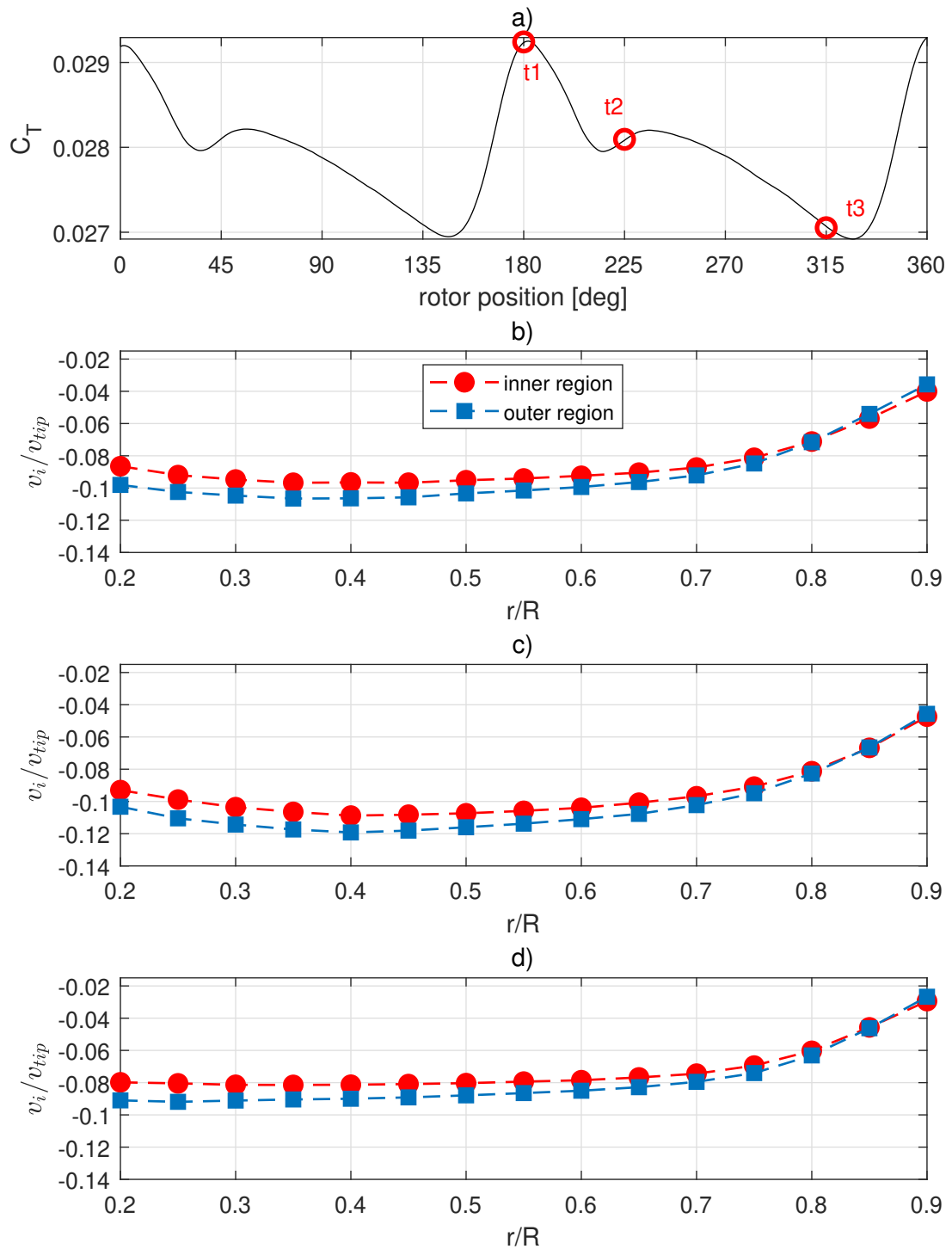


Figure 5.28: Induced velocity comparison between the inner and outer rotor region at different angular rotor positions for P_c at H_4V_0 . a) Computed C_T from CFD vs a rotor revolution. The red circles indicates the chosen angular rotor positions for the induced velocity comparison. b), c) and d) correspond to position t_1 , t_2 and t_3 respectively. The induced velocity is normalised by the speed at the rotor tip and the x -axis is the radial position along the rotor blade. Note that b), c) and d) share the same legend.


 Figure 5.29: As per Figure 5.28 but for P_w at H_4V_0 .

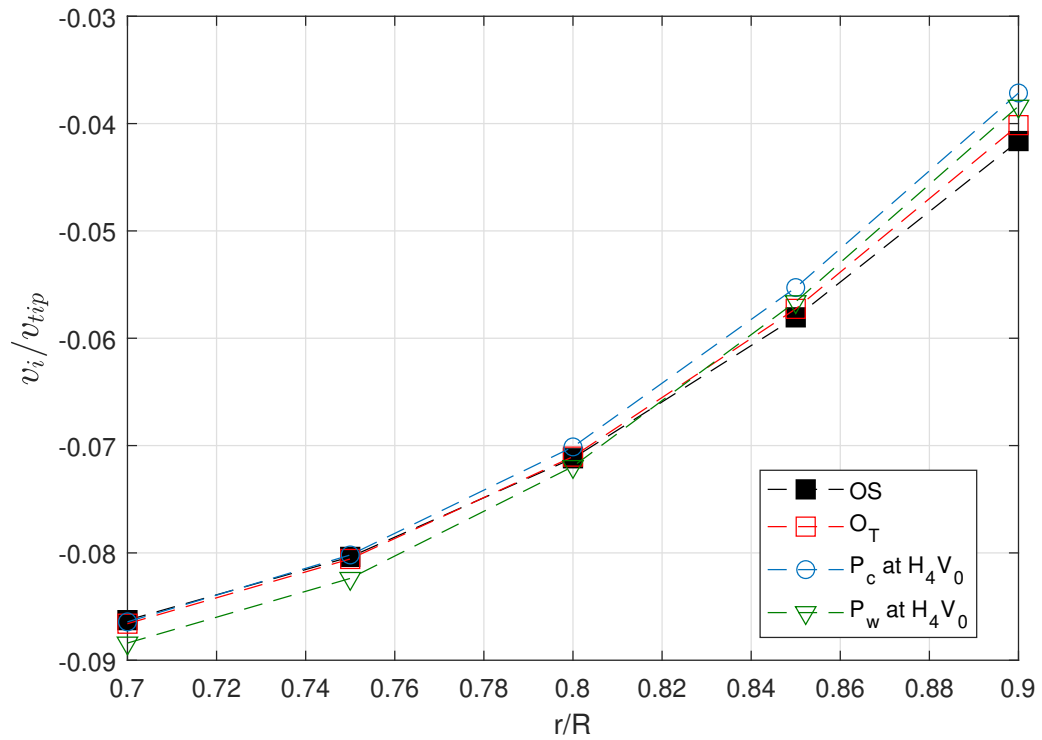


Figure 5.30: Time-averaged induced velocity comparison of P_c and P_w H_4V_0 and the baseline cases along the radial position of the rotor blade. The induced velocities are normalised by the rotor tip velocity.

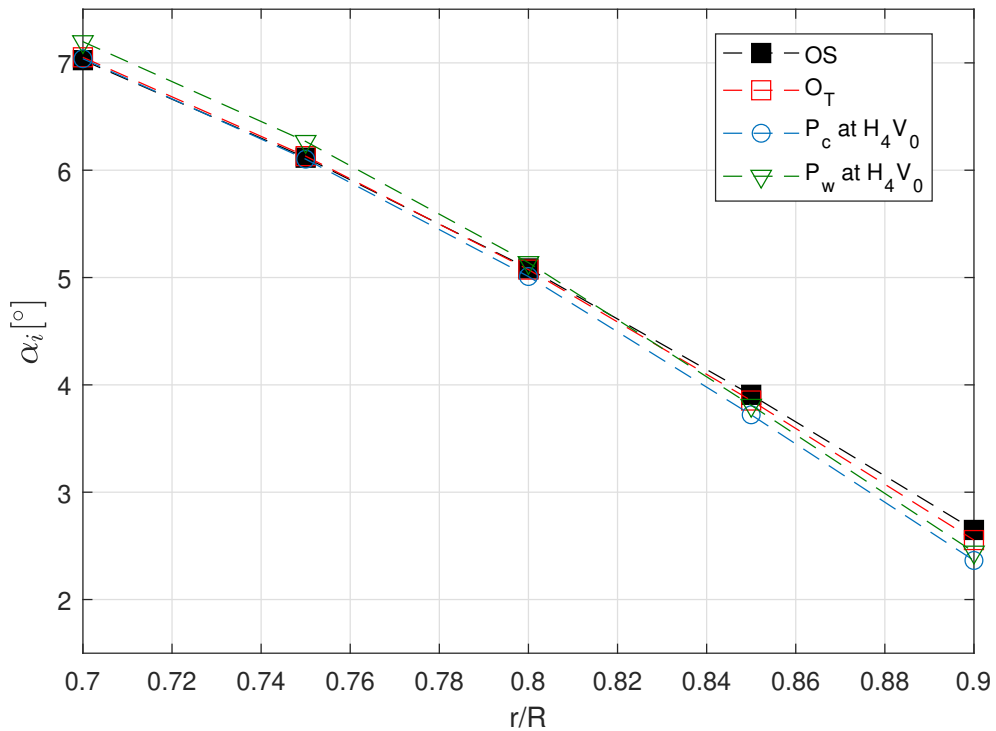


Figure 5.31: Time-averaged induced angle of attack comparison of P_c and P_w H_4V_0 and the baseline cases along the radial position of the rotor blade. Note that an increase in the induced angle of attack is equivalent to a reduction in the effective angle of attack.

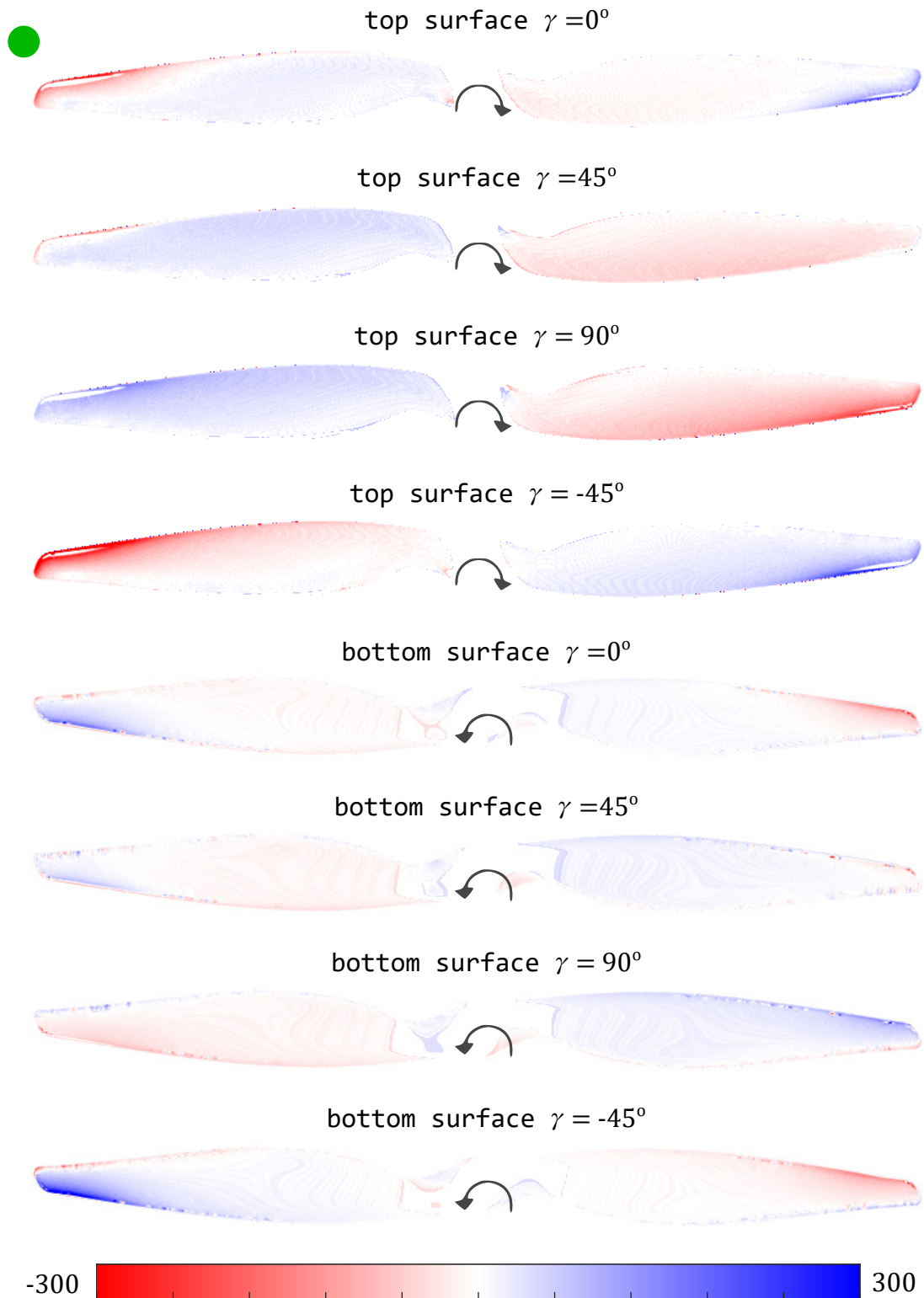


Figure 5.32: Blade surface pressure difference between $P_c H_4V_0$ and O_T at different angular positions of the propeller. The location of the green dot corresponds to the blade position shown in Figure 5.5. The blue contour means O_T has a higher pressure value. Pressure unit in pascal. The pressure range on the individual rotor is approximately $[-3000, 1500]$.

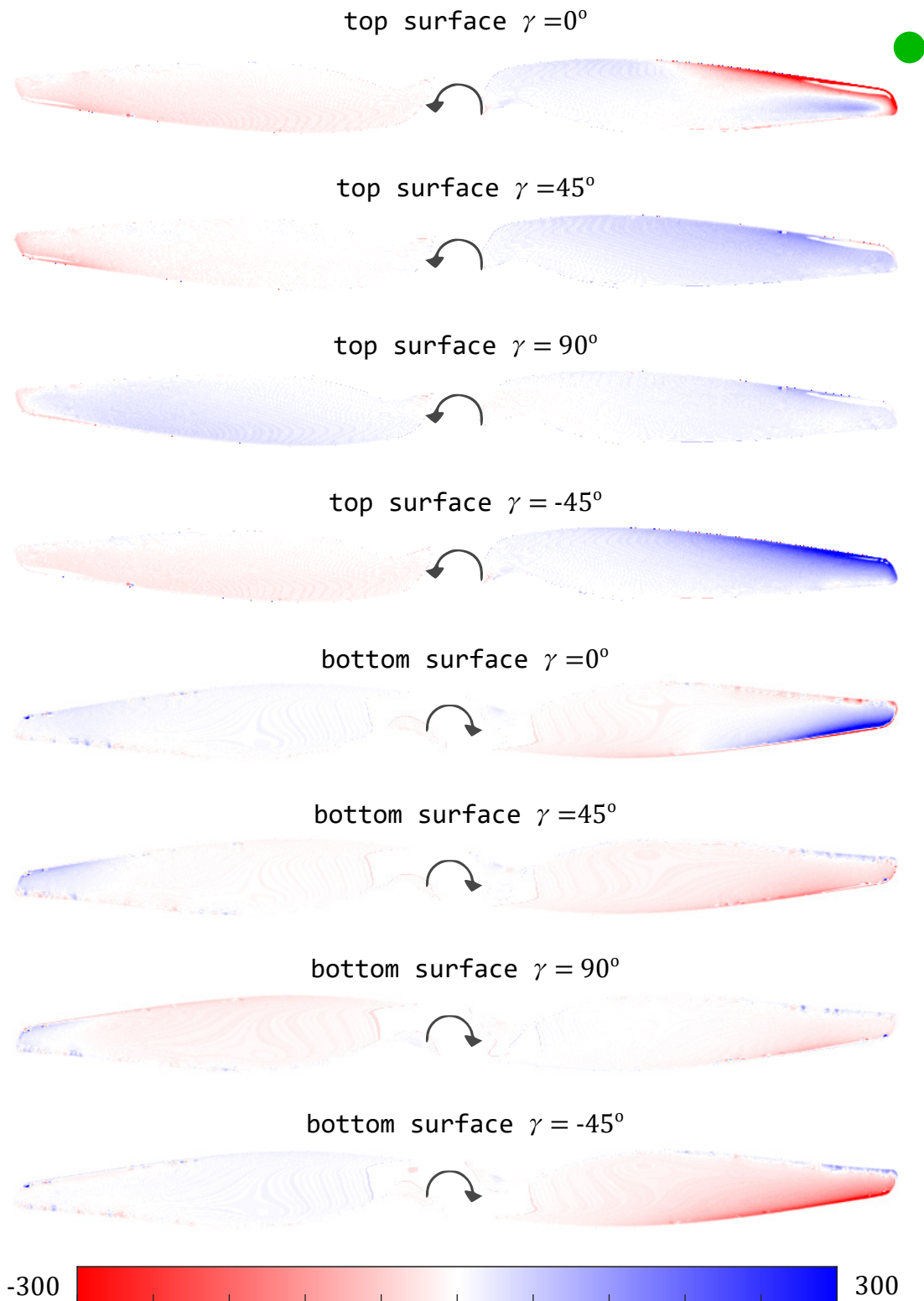


Figure 5.33: As per Figure 5.32 but for the pressure difference between P_w at H_4V_0 and O_T . Blue contour indicates H_4V_0 has higher pressure.

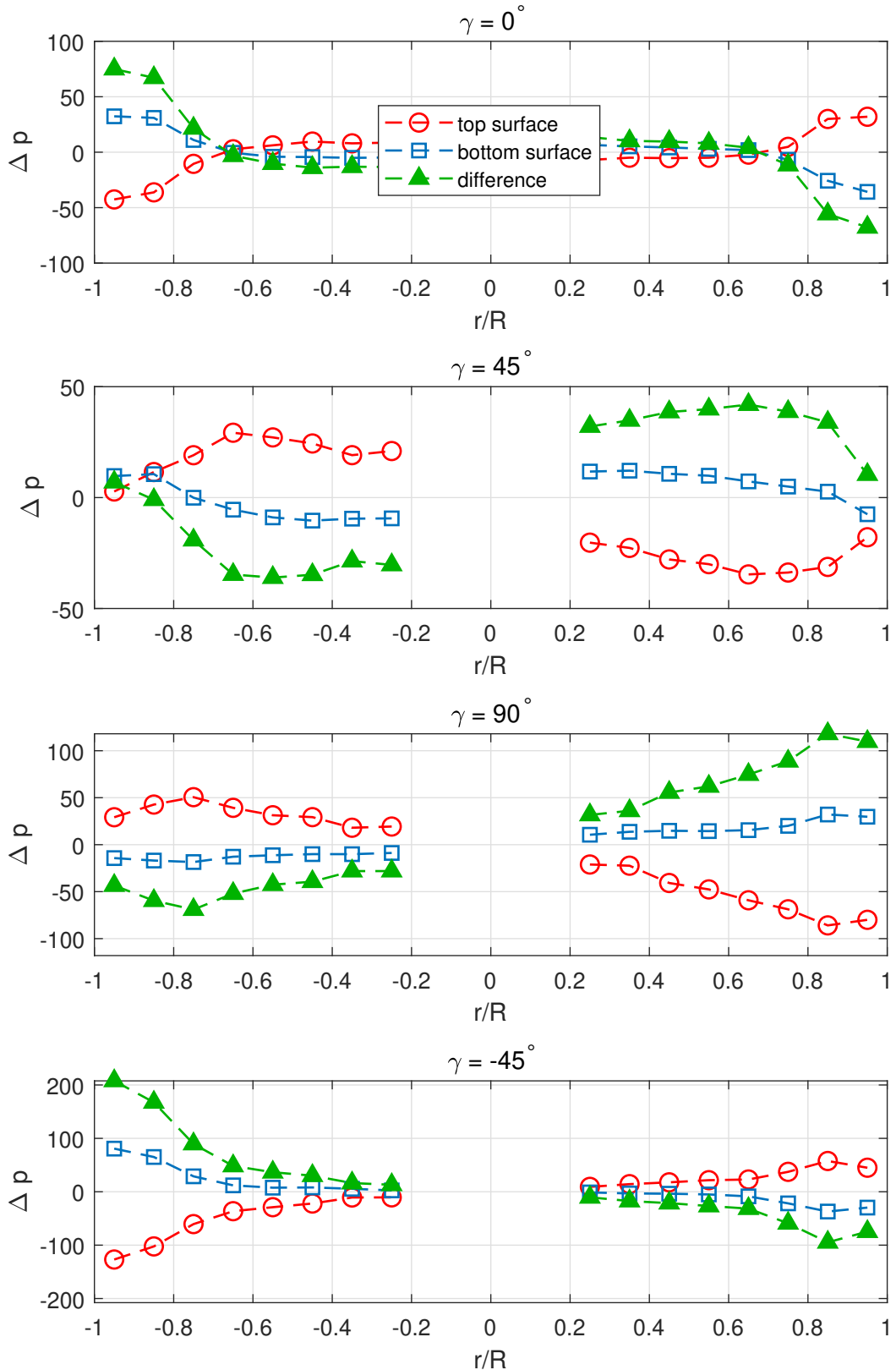


Figure 5.34: Cross sectional blade surface pressure difference between P_c at H_4V_0 and O_T at different angular positions of the propeller (Figure 5.5). The x -axis of the plots is the radial position along the blade. The pressure difference profile has the same rotor orientation as Figure 5.32. The green triangle curve is the difference between the bottom and top surface. A positive value in the green triangle suggests higher C_T in O_T . Pressure unit in pascal.

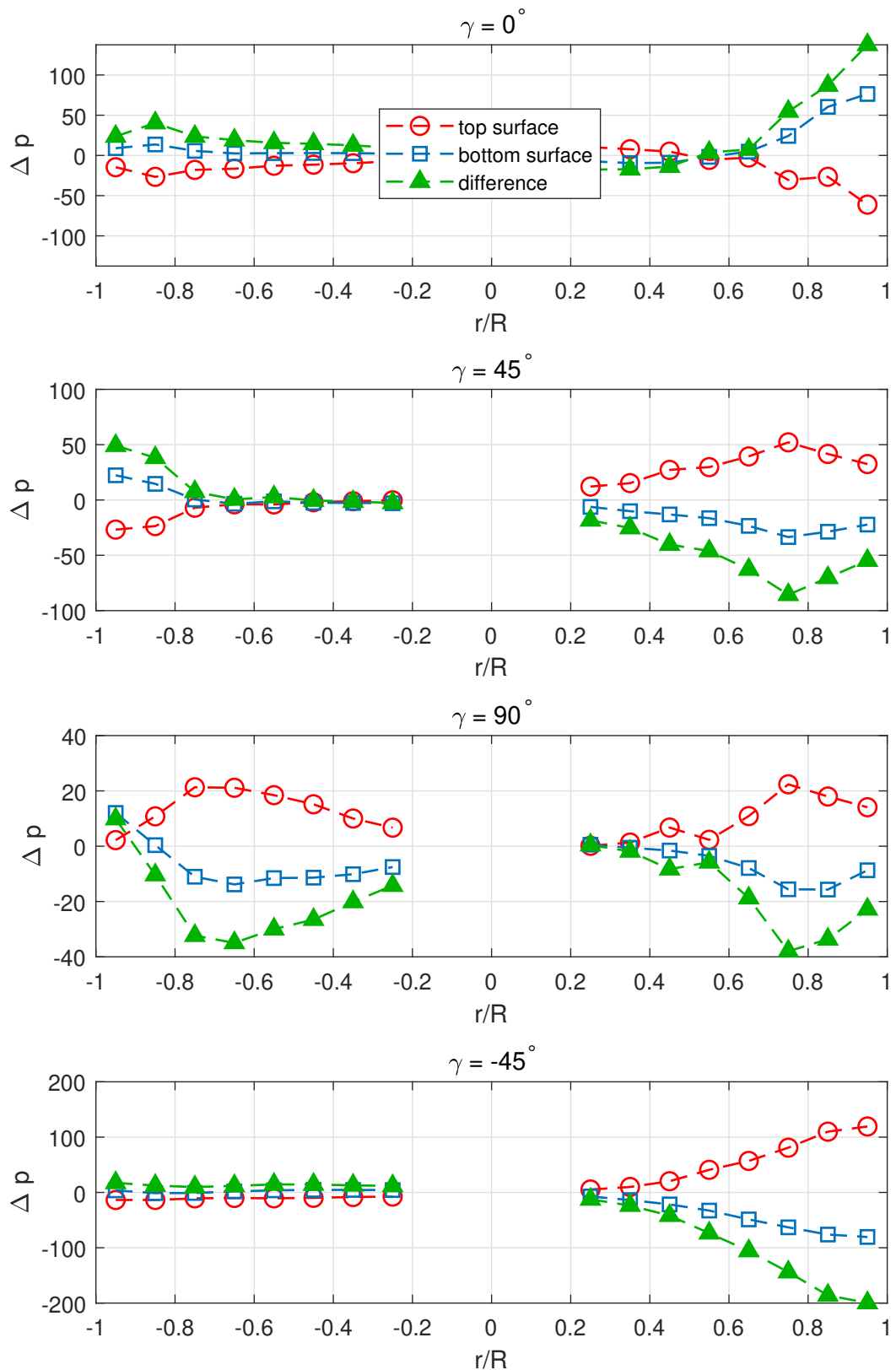


Figure 5.35: As per Figure 5.34 but for the difference between P_w at H_4V_0 and O_T . The pressure difference profile has the same rotor orientation as Figure 5.33. A positive value in the green triangle suggests higher C_T in H_0V_2 .

5.3.2 Difference in Thrust along H_4

At H_4 , the thrust coefficients show a decreasing trend overall as the quadcopter is repositioned from ceiling to ground as seen in Figure 5.36. The C_T gradient difference between the CFD and physical experiment result is also comparable with the result at H_0 (Figure 5.12). The CFD simulations overestimated the thrust coefficients, by 4.24% on average. Unlike H_0 , there is also significant thrust variations between the left and right propeller pairs. Figure 5.37 is obtained by considering the individual contribution of P_c and P_w . The distinct difference between the near wall and near centre propeller pair illustrated in the figure contributes to the rolling moment acting on the quadcopter body, which is further discussed in Section 5.3.3.

5.3.3 Difference in Rolling Moment along H_4

Due to the impact of the non symmetrical flow field on the left and right propeller pairs, there is a rolling moment acting the quadcopter body once its position deviates from H_0 . For the scope of this research, only the relative difference of the rolling moment at different tunnel locations is relevant. Therefore, instead of using the absolute value of the moment or a moment coefficient, the uneven thrust, U , between the left and right propeller pairs is used,

$$U = \frac{\Delta T}{\sum_{i=1}^4 T_i} \times 100\%, \quad (5.1)$$

where $\Delta T = T_1 + T_4 - T_2 - T_3$. Note that U is expressed as a percentage of the total thrust of the corresponding tunnel location. This normalises the value of ΔT for comparison with different

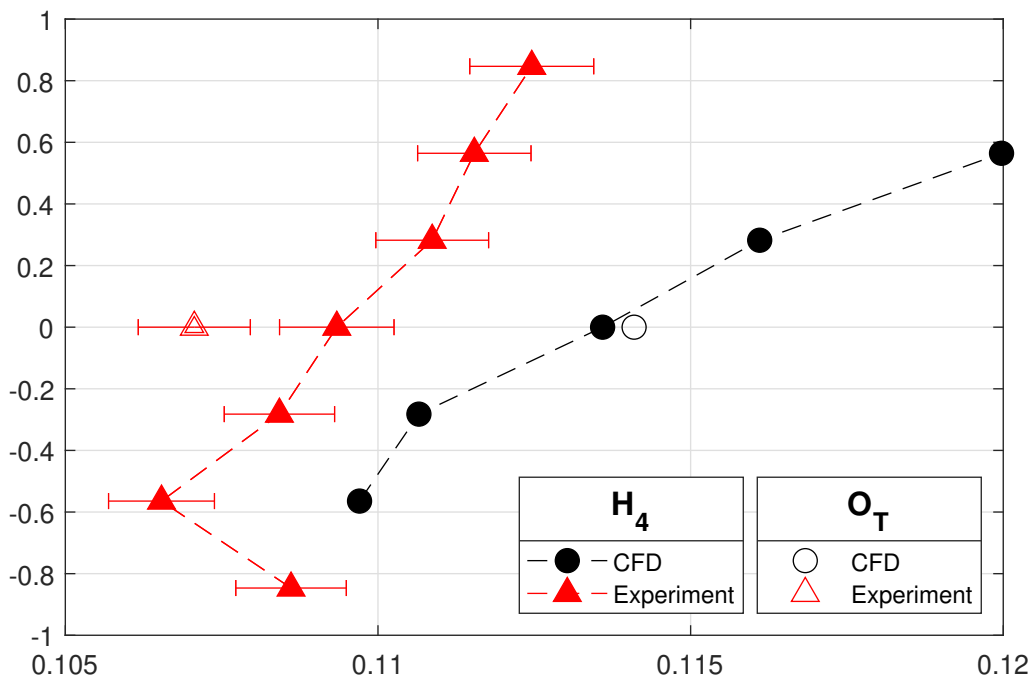


Figure 5.36: Thrust coefficient comparison between CFD and the physical experiments at H_4 .

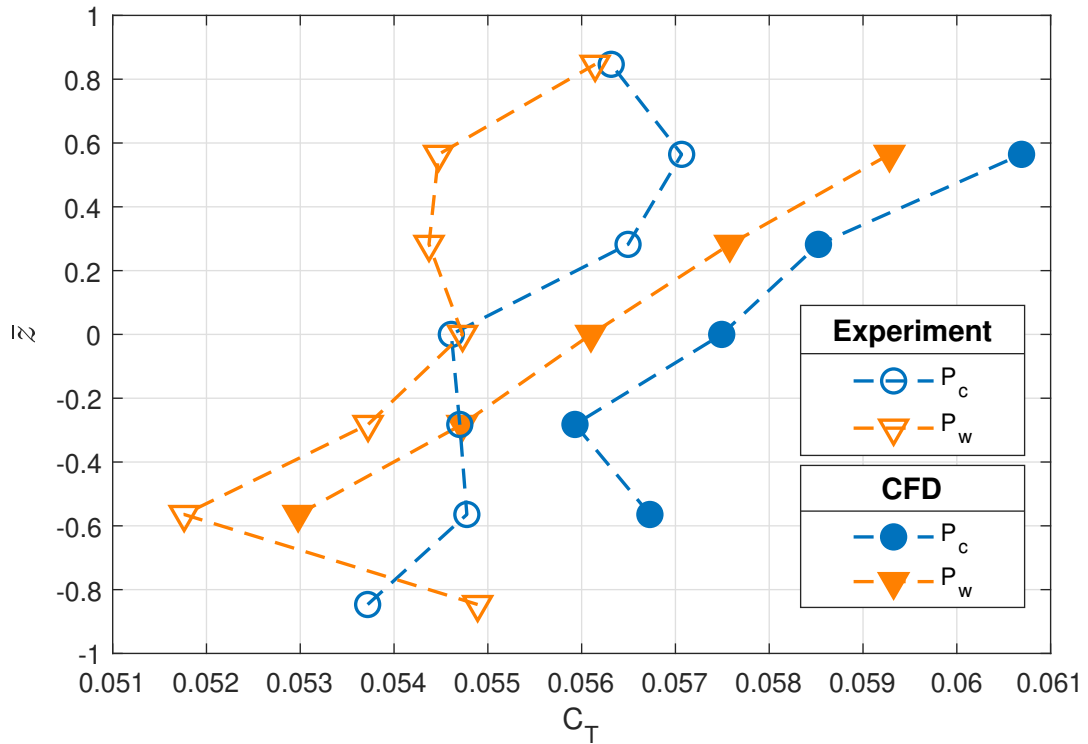


Figure 5.37: Thrust coefficient comparison between P_c and P_w in the CFD simulations and the physical experiments at H_4 .

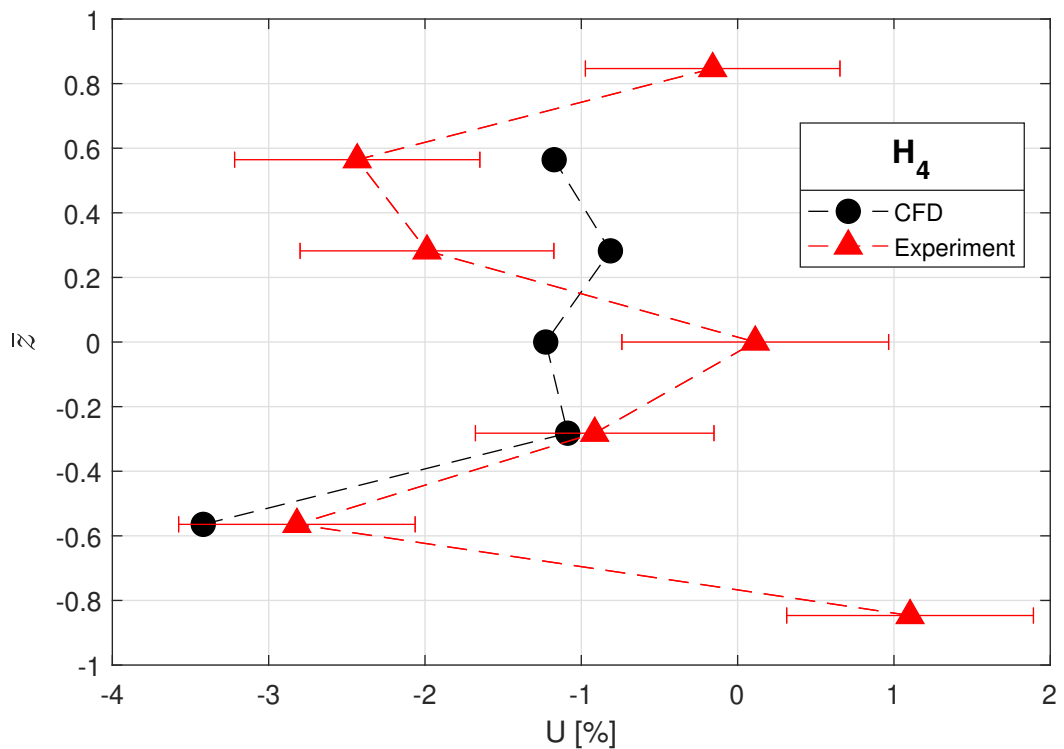


Figure 5.38: Uneven thrust comparison between the CFD simulations and physical experiments at H_4 . Note that negative value of U causes a rolling moment toward the wall.

locations. A comparison between the uneven thrust obtained from the CFD simulations and the experiments at H_4 is shown in Figure 5.38. The CFD simulations and physical experiments show reasonable agreement in U especially near the ground.

5.3.4 Near Ceiling and Wall Corner Fluid Interaction

5.3.4.1 Vorticity and Flow Field in CFD Simulations

At H_4V_2 , due to the increased distance from the ground plane, the wake of P_c and P_w form into a single stream. This expands radially outward further downstream from the stagnation point at the right bottom corner as it approaches the ground, which is illustrated in Figure 5.39. This induces horizontal momentum in the wake of P_w , causing it to tilt toward the centre of the quadcopter. In Figure 5.39, the recirculation region that is observed in the outer region of P_w at H_4V_0 (Figure 5.26), is not observed here at H_4V_2 . Hence, the radial component of velocity in the upstream flow of the rotor has decreased due to the boundary layer on the wall, compared to P_w at H_4V_0 . The ceiling plane becomes the main mechanism to reduce the vertical component of velocity in P_w 's upstream flow region. This drives an increase in the circulation of the tip vortex as indicated in Figure 5.27.

As illustrated in Figure 5.39, there is more radial contraction in the outer wake boundary of P_c at H_4V_2 compared to H_4V_2 or O_T . This induces more radial momentum in both the rotor wake and the upstream flow of the rotor. In combination with the ceiling effect, this induces a large amount of radial velocity component in the upstream flow region of P_c compared to all other cases. Furthermore, the return cycle on the left wall has to travel around the saddle point from the bottom left corner toward the ceiling and merge into the rotor's upstream flow region. This further reduces the vertical momentum of the flow upstream of the outer rotor region. Therefore, this large reduction in the wake kinetic energy drives an increase in circulation of the tip vortex in the outer rotor region of P_c . This is evident in Figure 5.27 showing the increase in circulation (from H_4V_0 to H_4V_2) in P_c is relatively higher than P_w .

5.3.4.2 Blade Pressure Field

Both Figure 5.40 and 5.41 show that there is more pressure variations on the surfaces of both P_c and P_w at H_4V_2 compared to H_0V_2 . In comparison, P_w at H_4V_2 shows less pressure difference with O_T compared to P_c . For P_c , the pressure difference with O_T is particularly pronounced at $\gamma = 90^\circ$ and -45° . Most of this pressure difference with O_T occurs near the rotor tip in the outer rotor region for both P_c and P_w . Overall, from the pressure differential curves in Figure 5.42 and 5.43, both rotors have improved lift production compared to O_T , with P_c having a more significant increase than P_w .

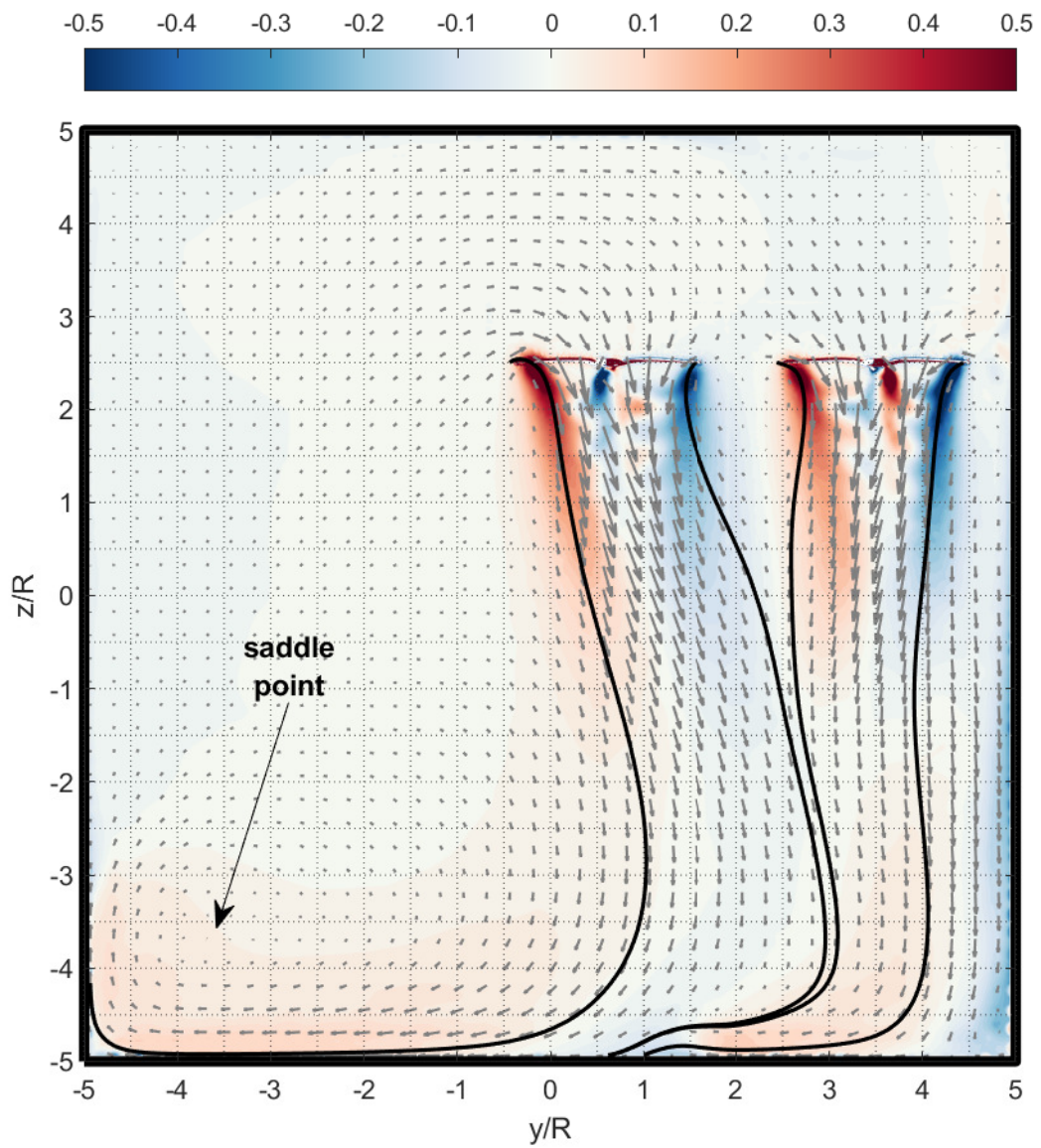


Figure 5.39: As per Figure 5.26 but for quadcopter located at H_4V_2 .

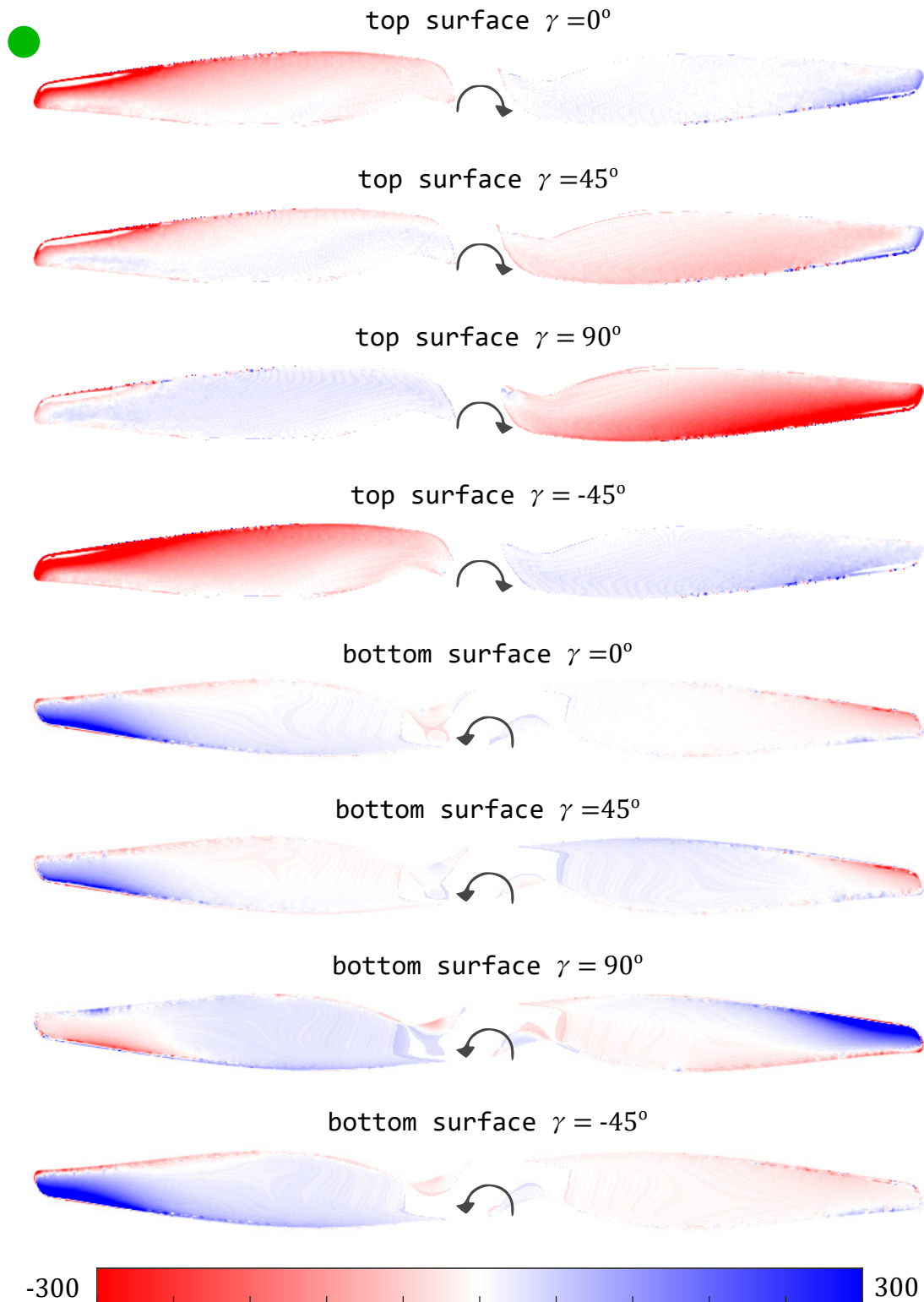


Figure 5.40: As per Figure 5.32 but for the pressure difference between P_c at H_4V_2 and O_T . Blue contour indicates H_4V_2 has higher pressure.

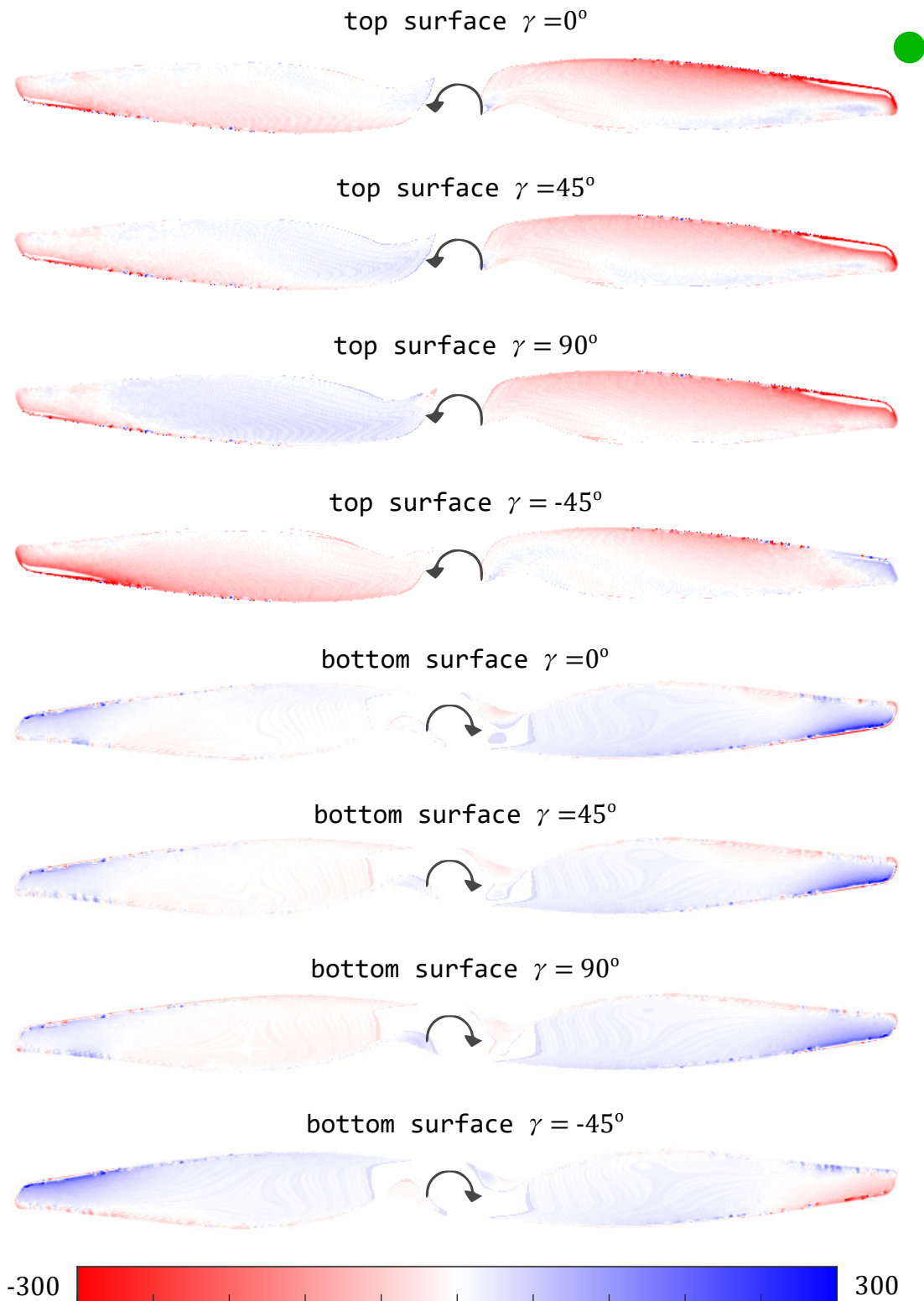


Figure 5.41: As per Figure 5.32 but for the pressure difference between P_w at H_4V_2 and O_T . Blue contour indicates H_4V_2 has higher pressure.

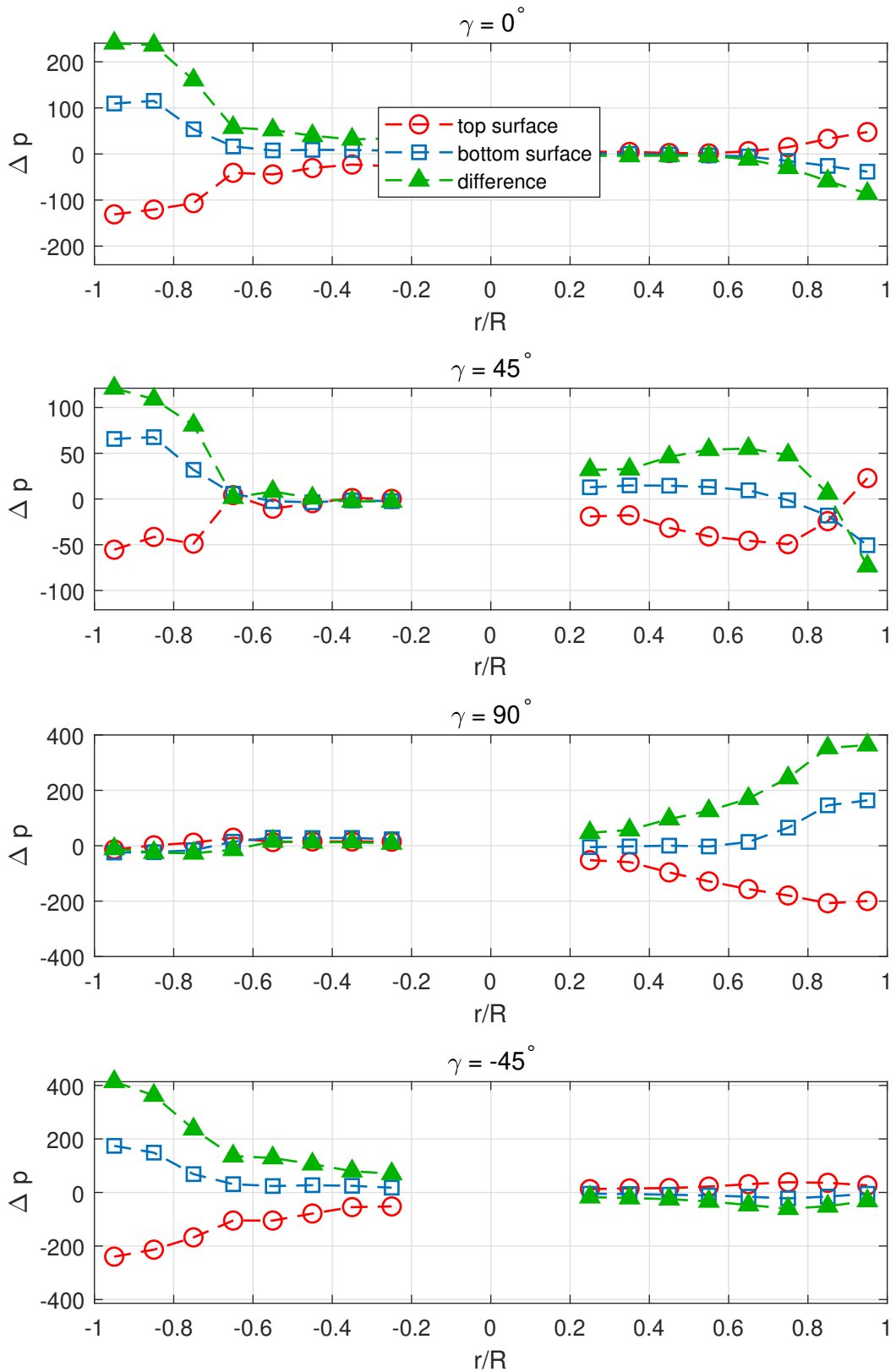


Figure 5.42: As per Figure 5.34 but for the difference between P_c at H_4V_2 and O_T . The pressure difference profile has the same rotor orientation as Figure 5.40. A positive value in the green triangle suggests higher C_T in H_4V_2 .

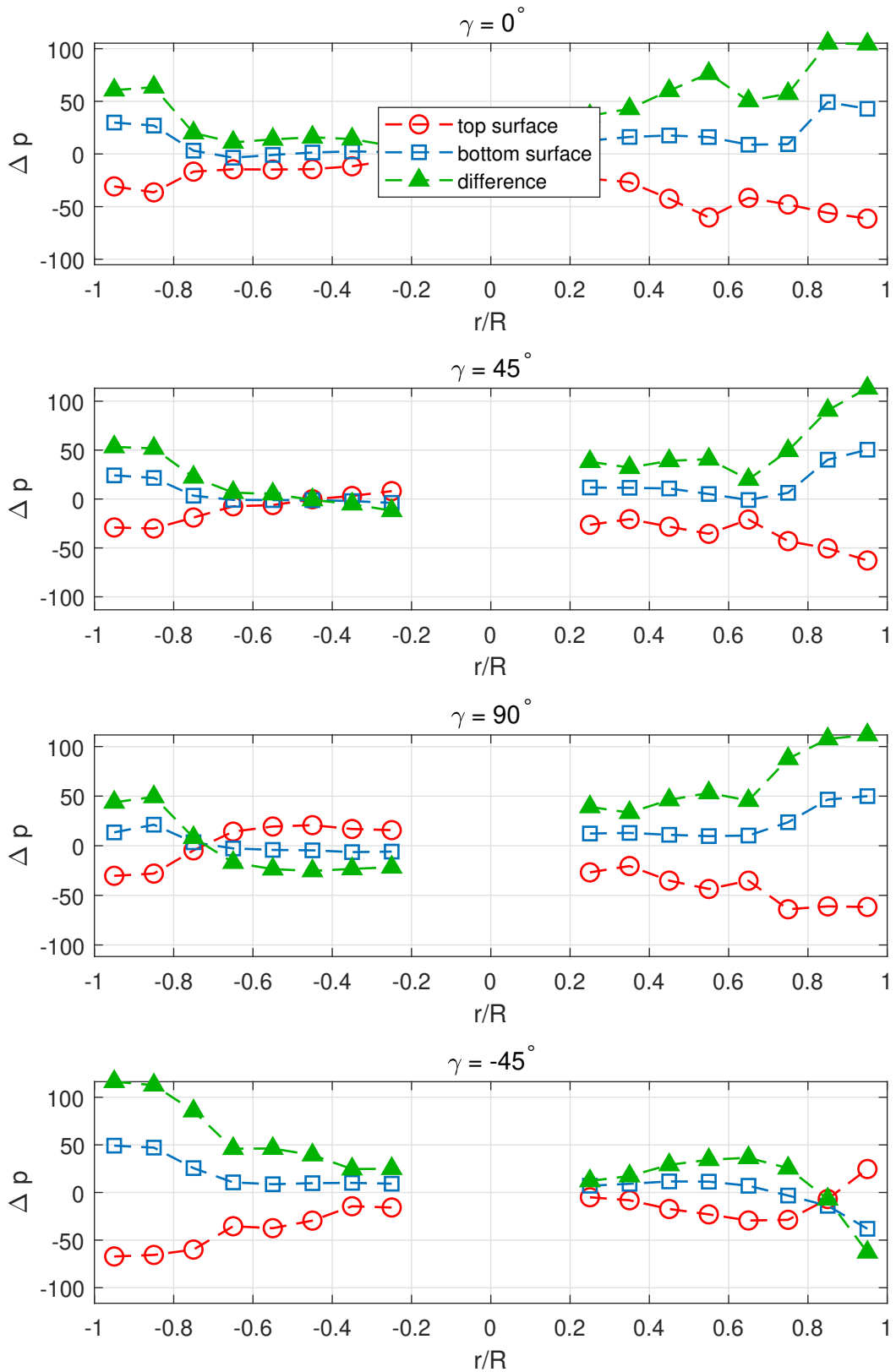
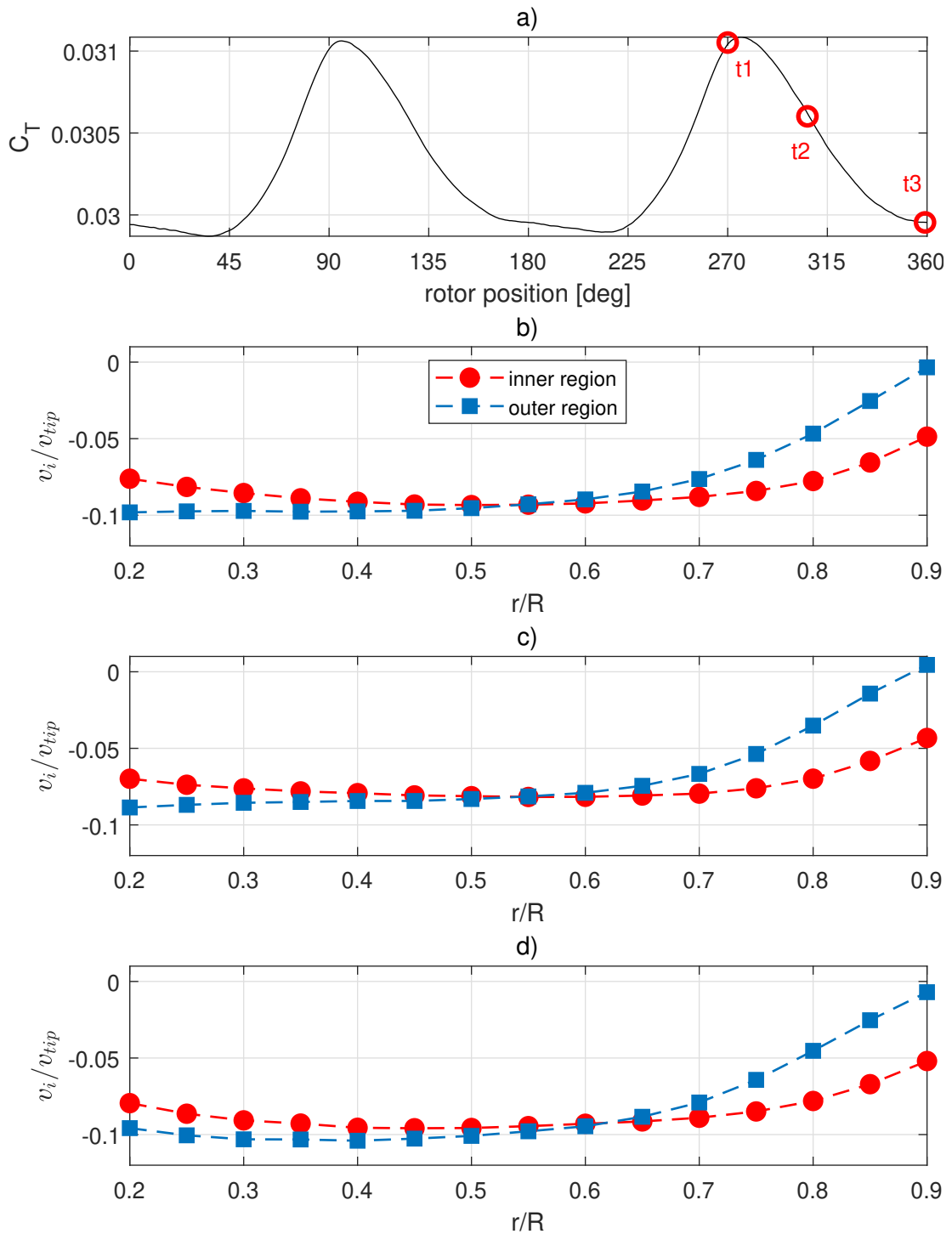


Figure 5.43: As per Figure 5.34 but for the difference between P_w at H_4V_2 and O_T . The pressure difference profile has the same rotor orientation as Figure 5.41. A positive value in the green triangle suggests higher C_T in H_4V_2 .

5.3.4.3 Impact on Thrust

Similar to H_4V_0 , in Figure 5.45 P_w at H_4V_2 has another frequency component with high magnitude of energy in the C_T curve. The second local maximum in C_T also occurs when the rotor tip is facing the wall at approximately $\pm 45^\circ$. The characteristics of the C_T curve and the inner/outer region induced velocity profiles also resemble that of H_4V_0 . **Compared to H_4V_0 , the increase in thrust in P_w is driven by a reduction in the vertical component of velocity due to the ceiling plane, instead of the radial component of velocity induced by the recirculation region between the wall and the rotor. The combination of the return cycle, ceiling plane and the increase in the radial momentum of the wake drastically reduce the induced velocity in the outer rotor region of P_c as depicted Figure 5.44. Thus, there is a greater increase in lift for P_c when located at H_4V_2 , compared to all other H_4 cases as seen in Figure 5.55 and 5.56.**


 Figure 5.44: As per Figure 5.28 but for P_c at H_4V_2 .

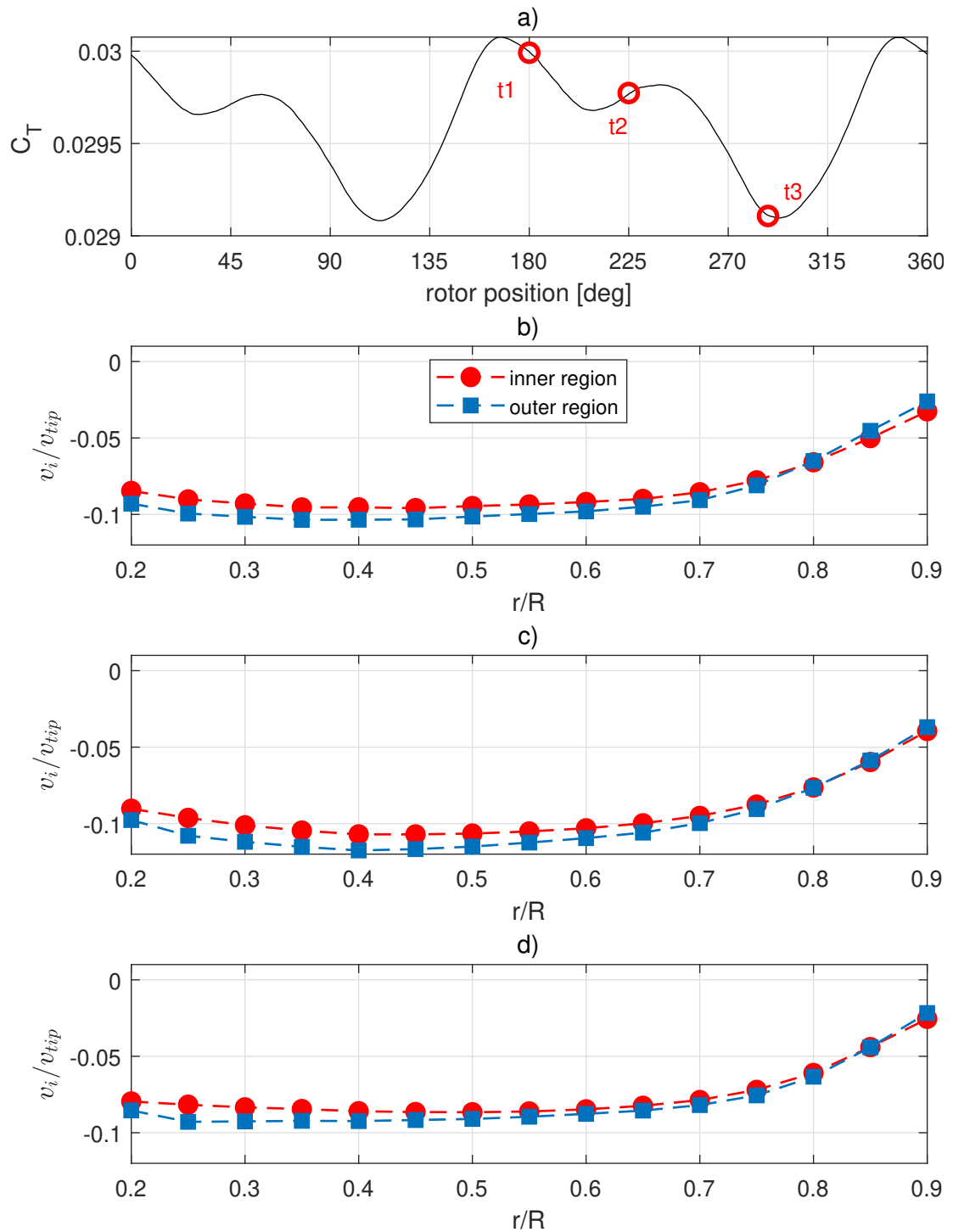


Figure 5.45: As per Figure 5.28 but for P_w at H_4V_2 .

5.3.5 Near Ground and Wall Corner Fluid Interaction

5.3.5.1 Vorticity and Flow Field in CFD Simulations

Similar to H_4V_0 , P_w at H_4V_{-2} also has recirculation in the outer rotor region. Except in this instance, the recirculation region has grown larger and alters the upstream flow of the outer rotor region further towards the centre of the rotor. Whereas, the recirculation region at H_4V_0 mainly influences the flow around the rotor tip in the outer rotor region. This recirculation region also causes the tip vortex to convect at a higher rate, which decreases the circulation of the tip vortex in the outer rotor region compared to H_4V_0 , as shown in Figure 5.27. The recirculation region in the inner region of P_w becomes more confined due to the opposing horizontal momentum from the wake of P_c . Due to this confinement, the tip vortex dissipate at a slower rate and therefore, the circulation of the tip vortex in the inner rotor region of P_w is slightly higher than that of P_c .

Since there is less opposing horizontal momentum from the wake of P_c , the outer rotor region of P_w 's wake contracts more and there is less radial expansion of the wake boundary as it approaches the ground, compared to H_0V_{-2} (Figure 5.14). As P_c at H_4V_{-2} is further away from the left wall compared to H_0V_{-2} , the return cycle has less a reduced effect of inducing more vertical momentum to the rotor's upstream. Hence, allowing a larger radial component of velocity going through the outer rotor region in the upstream. This also drives an increase in circulation in the outer rotor region of P_c at H_4V_{-2} compared to H_0V_{-2} , as depicted in Figure 5.4 and 5.27.

5.3.5.2 Blade Pressure Field

As seen in Figure 5.47 and 5.48, P_w at H_4V_{-2} has a higher blade pressure difference from O_T , compared to P_c . This is due to P_w 's proximity to the wall. For P_w at H_4V_{-2} , the flow within recirculation regions in both the inner and outer rotor region decrease the bottom rotor surface pressure near the centre hub and the upward recirculated flow then increases the bottom rotor surface pressure near the rotor tips. This can be seen in Figure 5.48. Furthermore, these two recirculation regions both increase the top rotor surface pressure along the leading edge. As a result, P_w at H_4V_{-2} produces less thrust compared to O_T , as demonstrated by the pressure differential curves in Figure 5.50.

The surface pressure contours of P_c at H_4V_{-2} closely resemble that of H_0V_{-2} , as they share similar positions in the tunnel. This is evident in Figure 5.15 and 5.47. From Figure 5.49, the majority of the pressure difference from O_T occurs in the inner rotor region, which drives an increase in lift overall when compared to O_T . This behaviour is similarly discussed in Section 5.2.2.2.

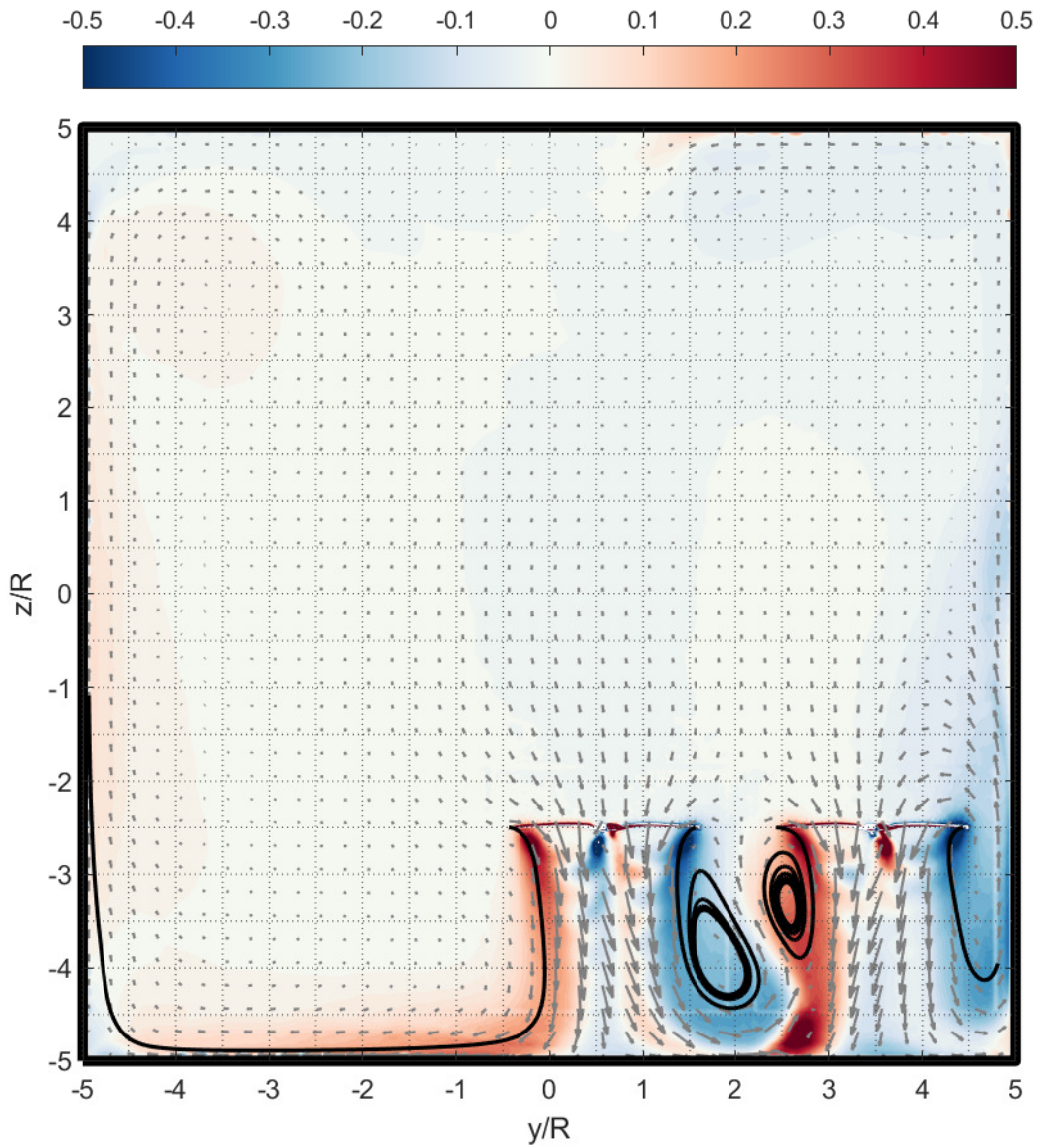


Figure 5.46: As per Figure 5.26 but for quadcopter located at H_0V_{-2} .

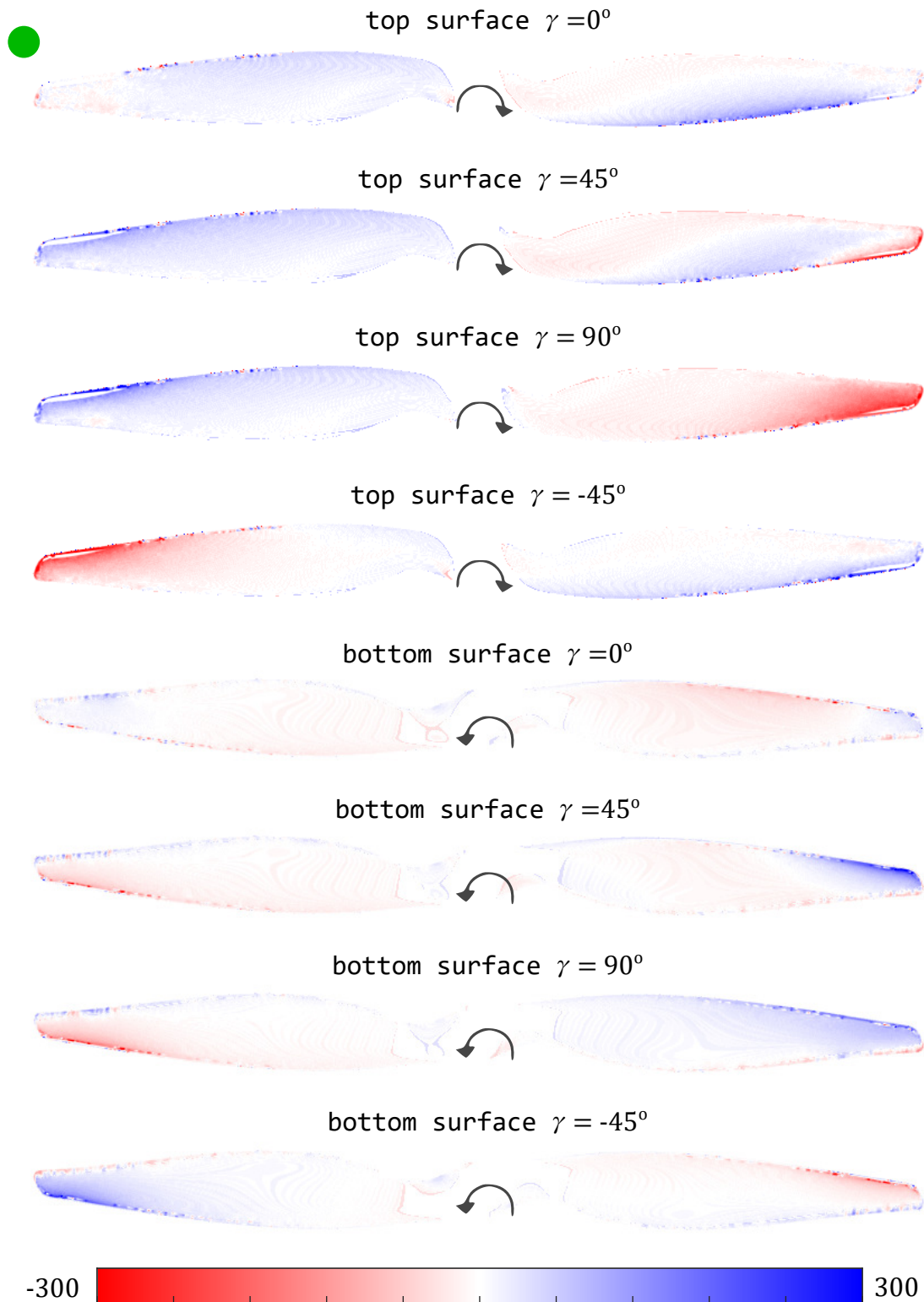


Figure 5.47: As per Figure 5.32 but for the pressure difference between P_c at H_4V_{-2} and O_T . Blue contour indicates H_4V_{-2} has higher pressure.

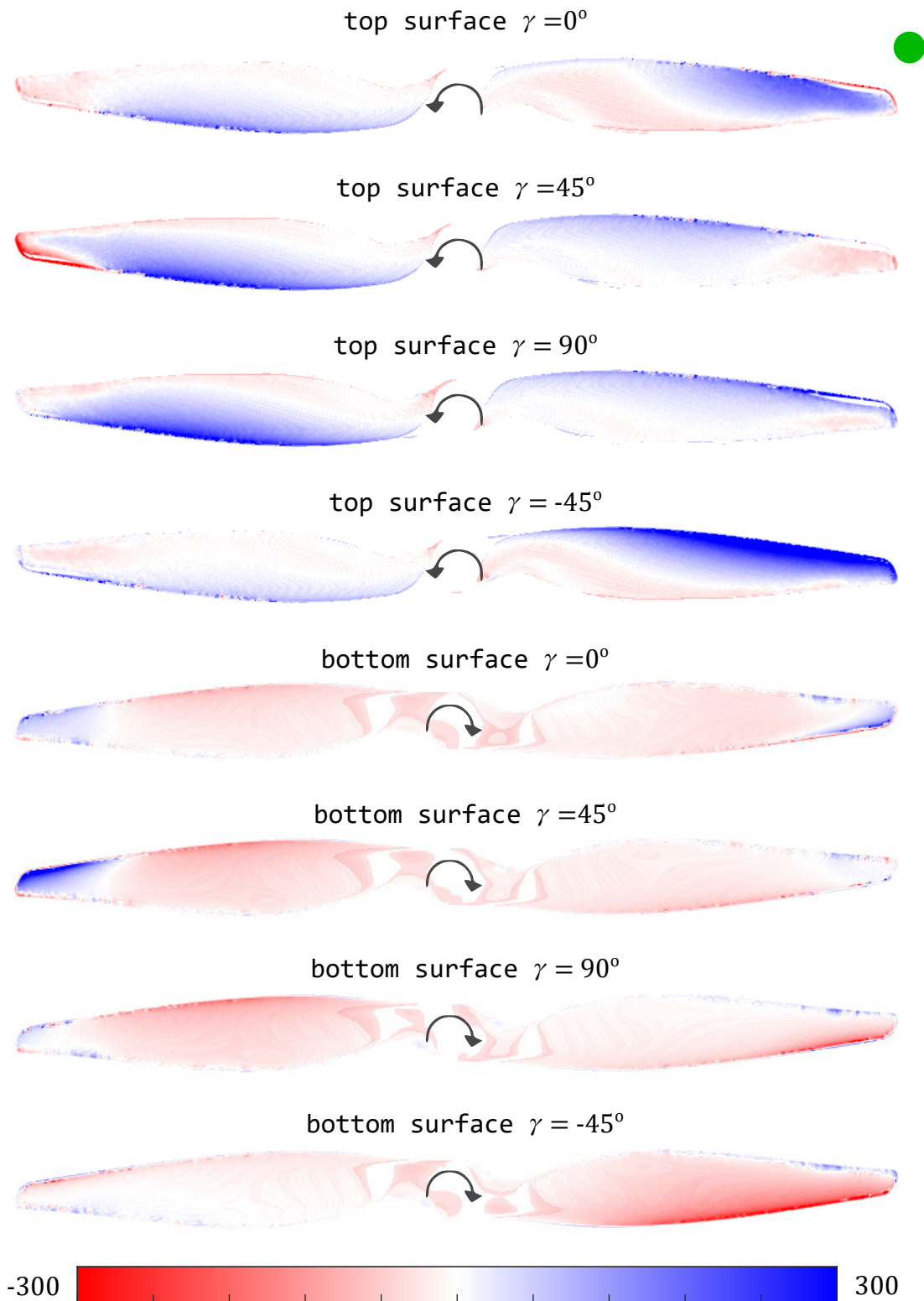


Figure 5.48: As per Figure 5.32 but for the pressure difference between P_w at H_4V_{-2} and O_T . Blue contour indicates H_4V_{-2} has higher pressure.

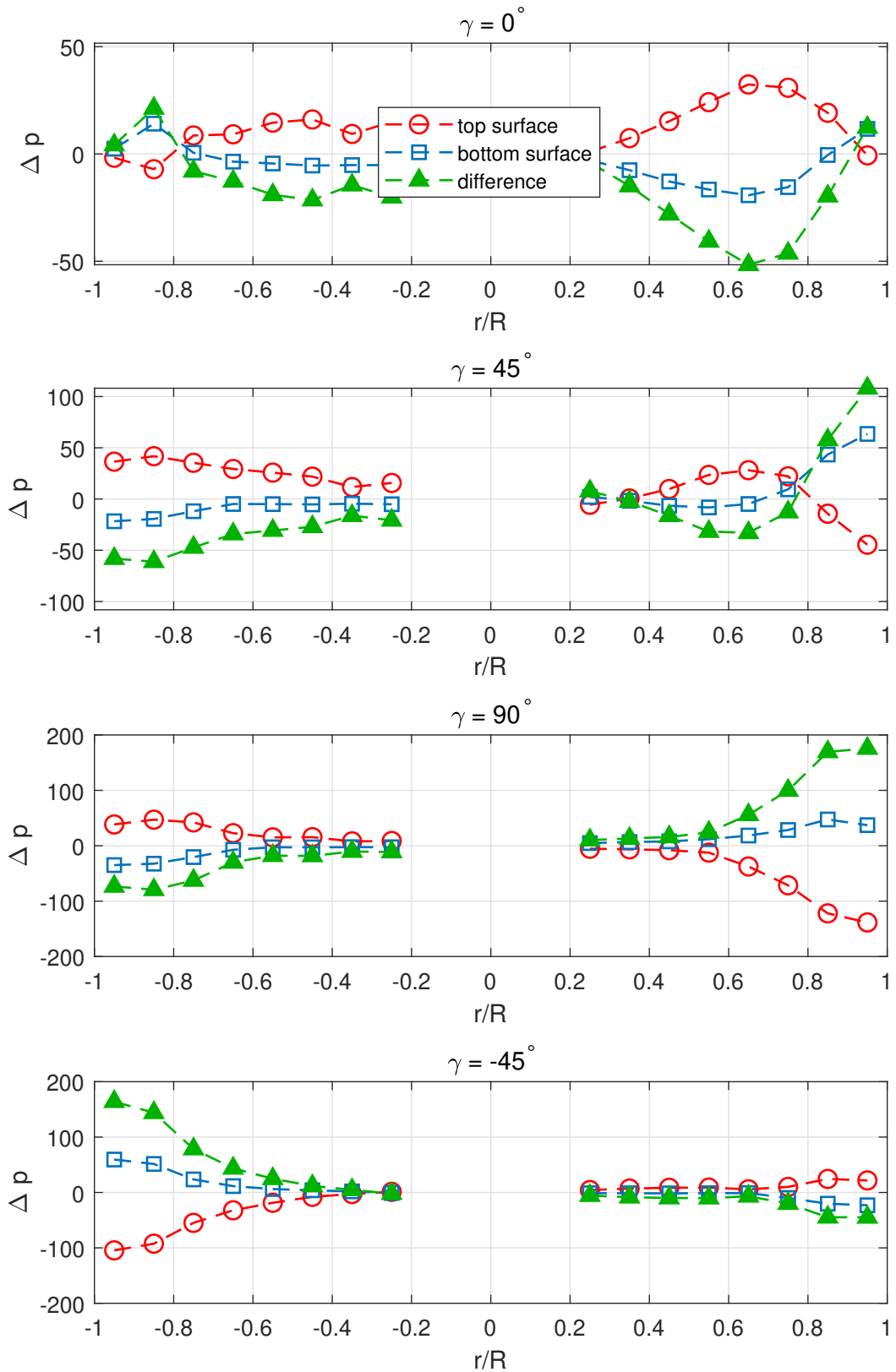


Figure 5.49: As per Figure 5.34 but for the difference between P_c at H_4V_{-2} and O_T . The pressure difference profile has the same rotor orientation as Figure 5.47. A positive value in the green triangle suggests higher C_T in H_4V_{-2} .

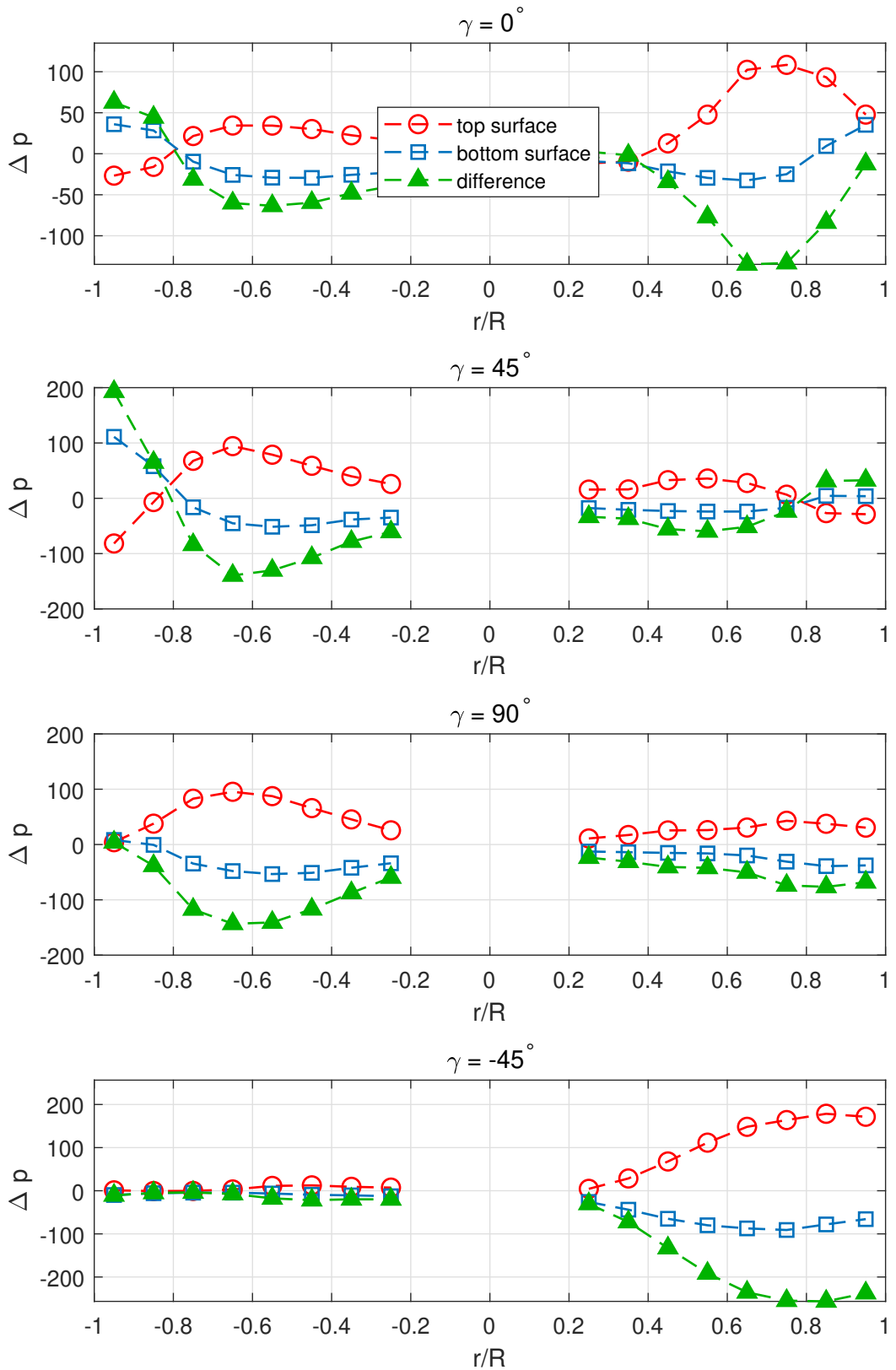


Figure 5.50: As per Figure 5.34 but for the difference between P_w at H_4V_{-2} and O_T . The pressure difference profile has the same rotor orientation as Figure 5.48. A positive value in the green triangle suggests higher C_T in H_4V_{-2} .

5.3.5.3 Impact on Thrust

From Figure 5.53, P_c at H_4V_{-2} has a slight reduction in v_i compared to O_T . This is primarily driven by two phenomena: 1) similar to H_0V_2 , the increased circulation of the tip vortex in the inner rotor region drives a reduction in the induced velocity in the inner rotor region compared to the outer region. This is evident in Figure 5.51; 2) The increased rotor-wall gap (left wall) reduces the vertical component of velocity in the upstream, which also slightly decreases the induced velocity in the outer rotor region compared to H_0V_2 . These result in the increase in local effective angle of attack and the blade pressure differential (as discussed in Section 5.3.5.2). Thus, P_c at H_4V_{-2} produces more thrust compared to O_T .

As for P_w at H_4V_{-2} , in Figure 5.54 there is an increase in the time-averaged induced velocity compared to O_T , hence, an increase in lift. Yet, this contradicts the discussion in Section 5.3.5.2, which the blade pressure differential suggests an overall reduction in lift compared to O_T . As described in Section 4.1.8.2, for P_w at H_4V_{-2} , the rotor passes through two recirculation regions with high vorticity in both the inner and rotor region (Figure 5.46), where flow with high magnitude of local vorticity diminishes the effect of the induced velocity on the pressure. This is why the reduction in C_T for P_w at H_4V_{-2} (Figure 5.37) only correlates to the change in pressure but not the induced velocity. Also note that unlike P_w at H_4V_0 and H_4V_{-2} , a second local maximum does not appear in the C_T curve of P_w at H_4V_{-2} , as depicted in Figure 5.52.

In summary, as P_w at H_4V_{-2} passes through the recirculation regions with high magnitude of local vorticity, the pressure differential on the rotor surfaces decrease, causing a reduction in lift. This effect counters the lift increase in P_c . Therefore, the quadcopter generates less thrust at H_4V_{-2} compared to O_T overall.

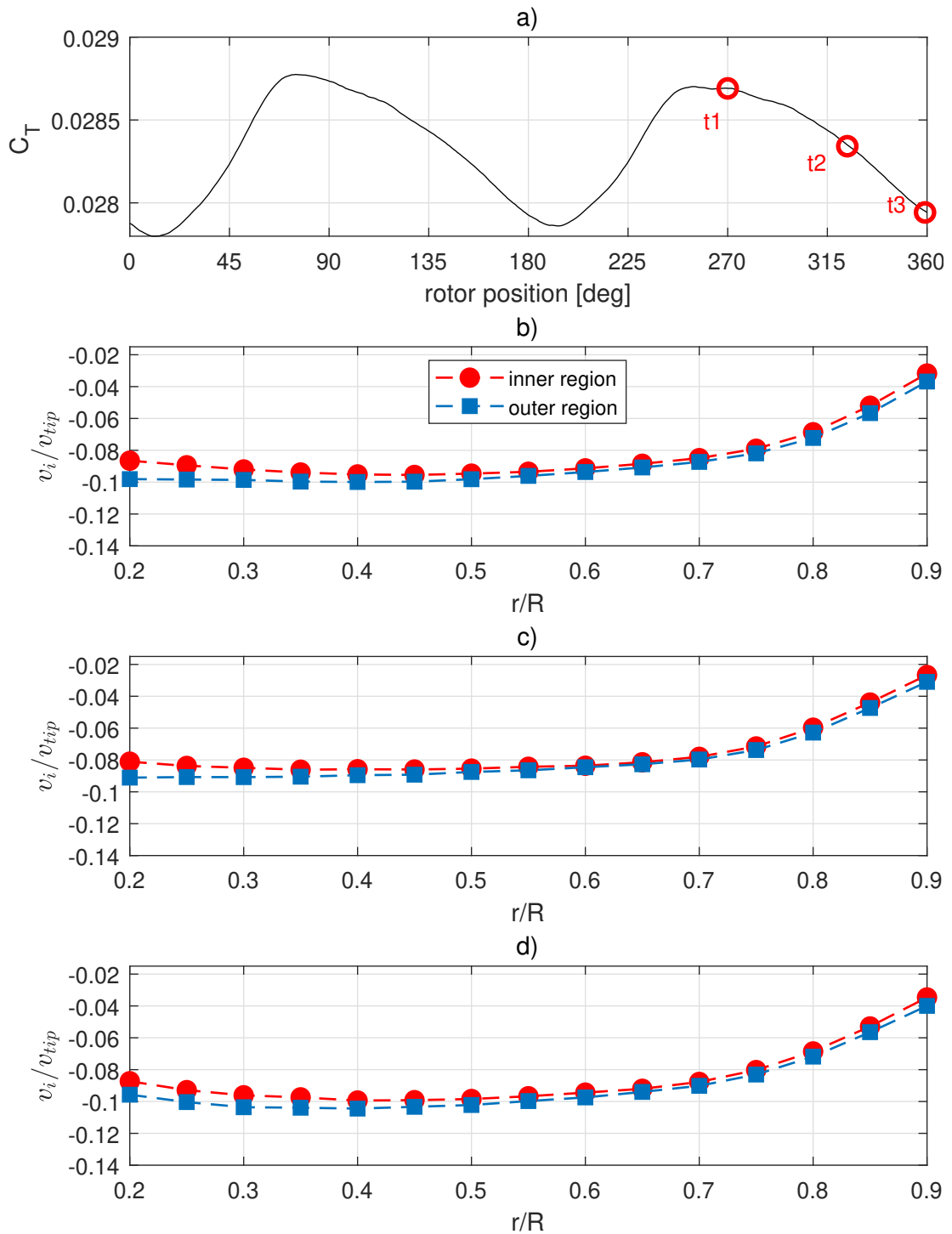
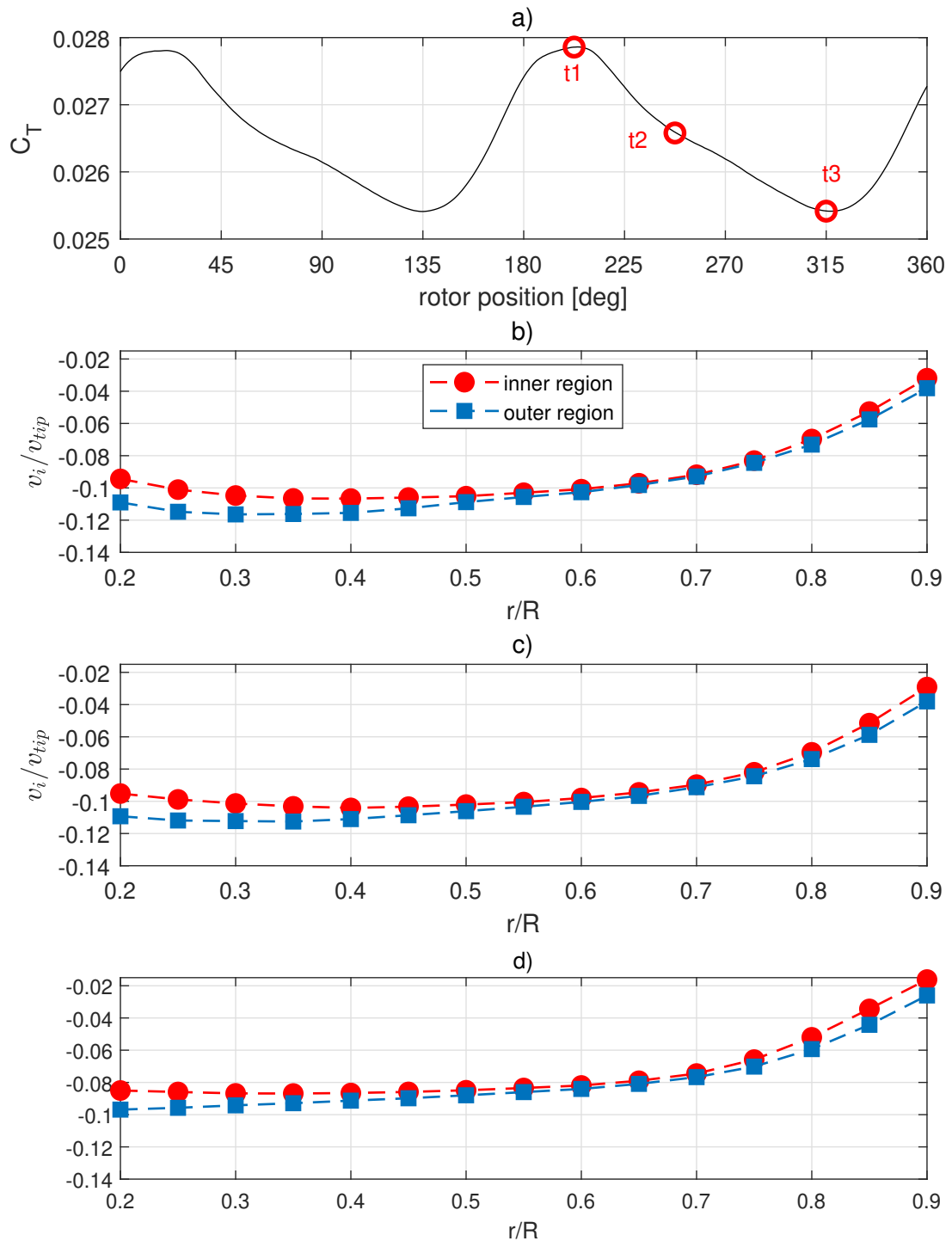


Figure 5.51: As per Figure 5.28 but for P_c at H_4V_{-2} .


 Figure 5.52: As per Figure 5.28 but for P_w at H_4V_{-2} .

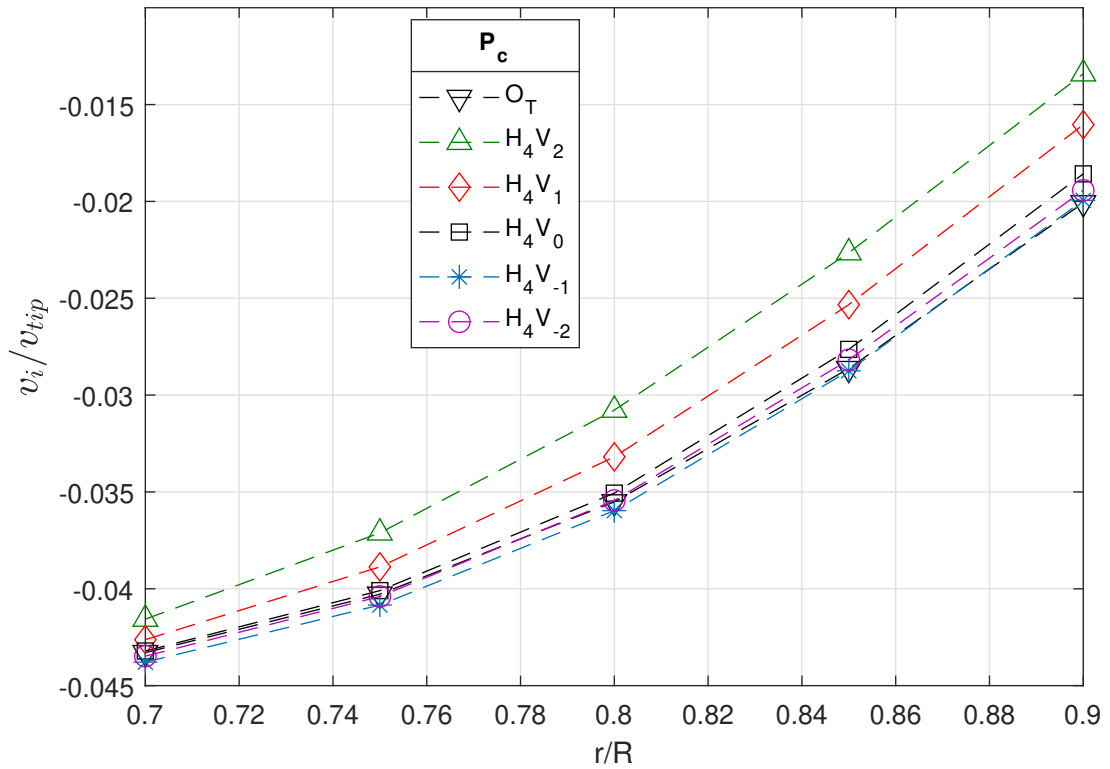


Figure 5.53: Time-averaged induced velocity comparison of P_c at H_4 along the radial position of the rotor blade. The induced velocities are normalised by the rotor tip velocity.

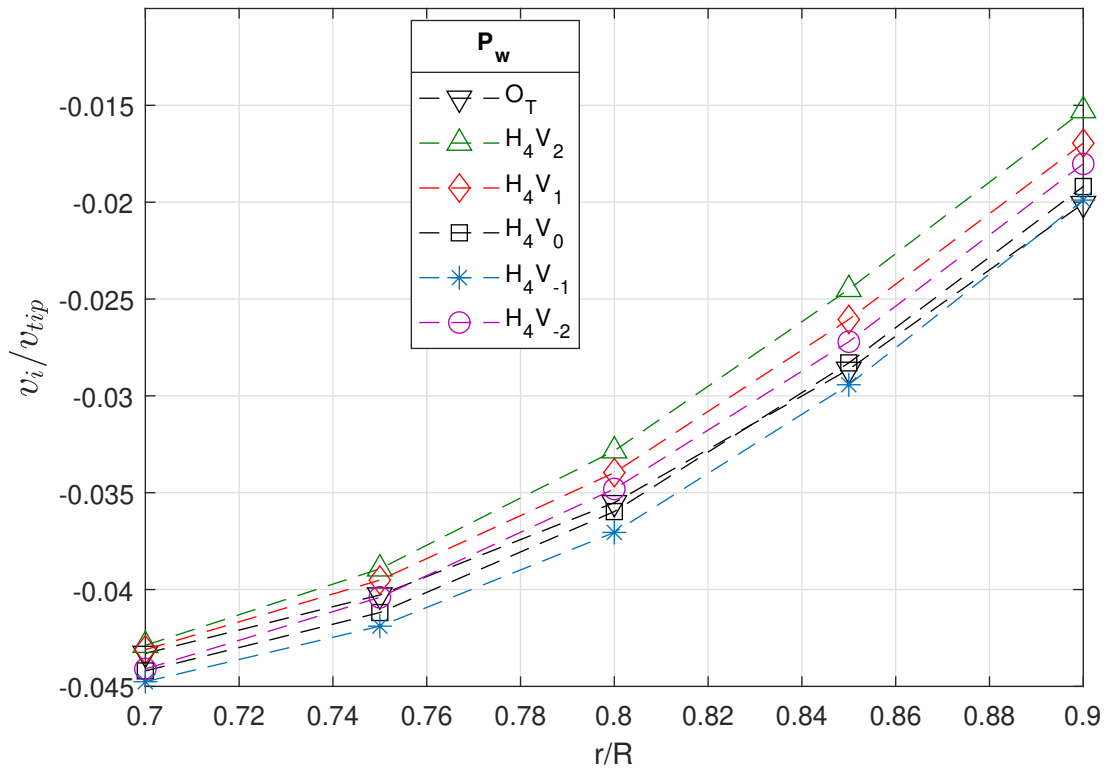


Figure 5.54: Time-averaged induced velocity comparison of P_w at H_4 along the radial position of the rotor blade. The induced velocities are normalised by the rotor tip velocity.

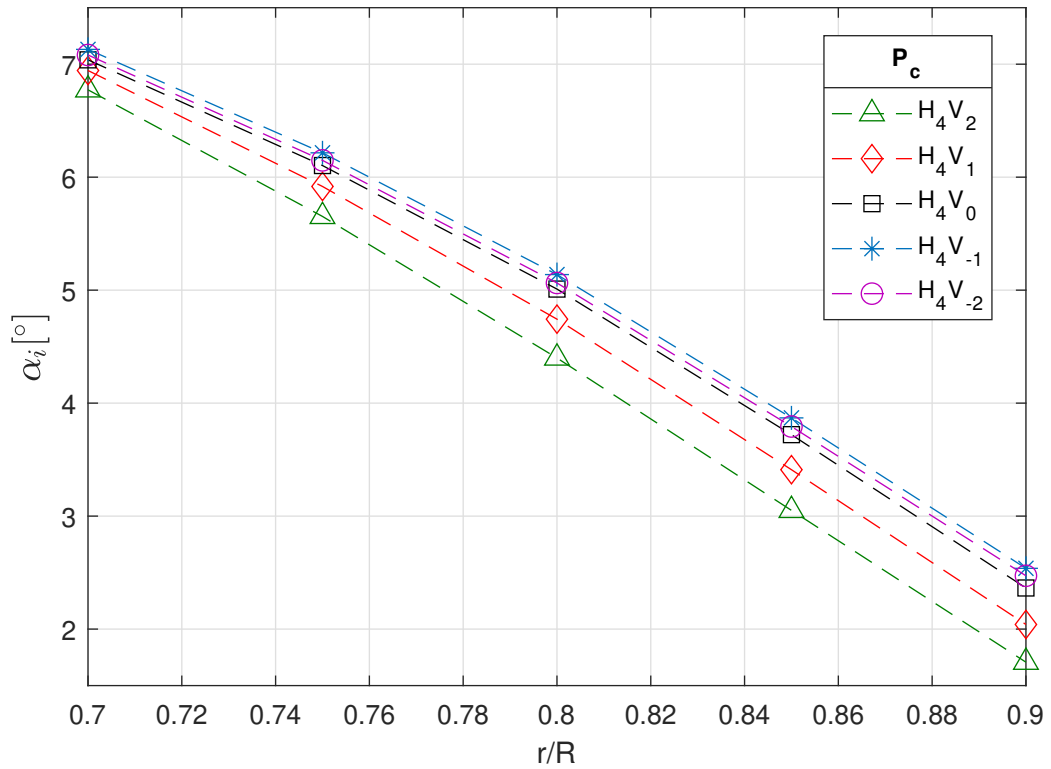


Figure 5.55: Time-averaged induced angle of attack comparison of P_c at H_4 cases along the radial position of the rotor blade. Note that an increase in the induced angle of attack is equivalent to a reduction in the effective angle of attack.

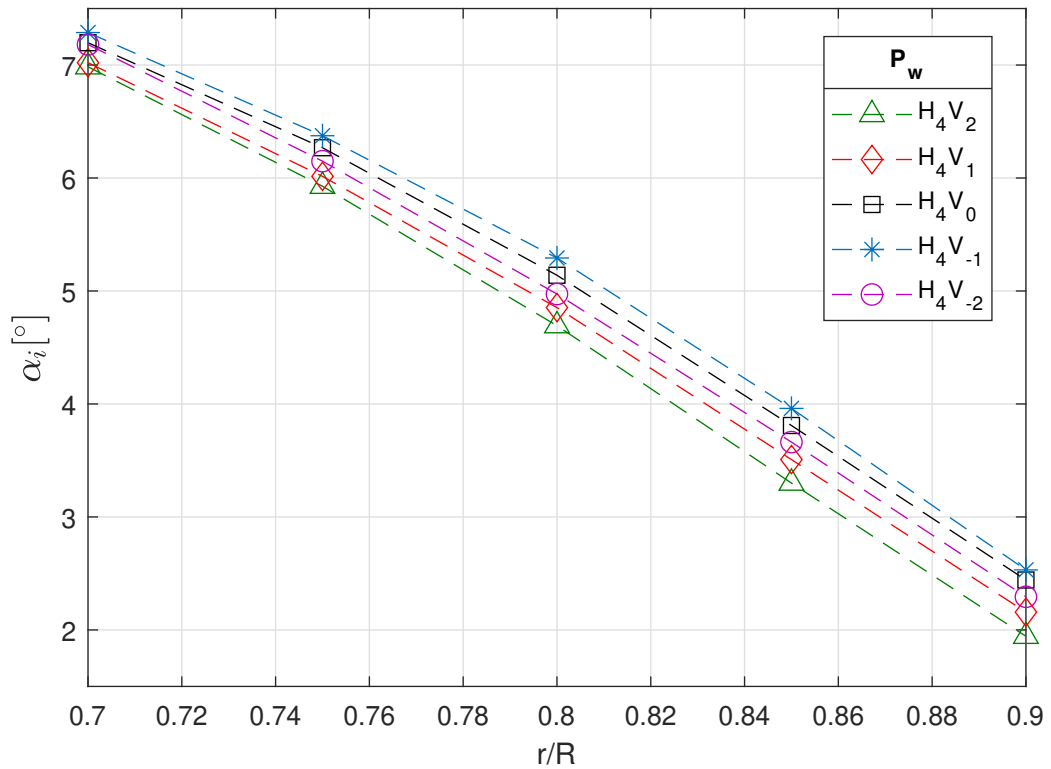


Figure 5.56: Time-averaged induced angle of attack comparison of P_w at H_4 cases along the radial position of the rotor blade.

5.3.6 Impact on Attitude

As depicted in Figure 5.38, there is a rolling moment acting on the quadcopter across H_4 , causing it to accelerate toward to right wall. This is due to the break in symmetry between flow field around P_w and P_c , inducing a difference in lift production. From the figure, both the CFD and physical experiment results indicate U has the highest magnitude at H_4V_{-2} . This is predominantly due to the presence of the ground and right wall having significantly different effects on P_w and P_c (as discussed in Section 5.3.5.3), which alters their lift production. However, the physical experiment shows that at H_4V_{-3} (Figure 5.38), U becomes close to zero. It is speculated that this is due to the reduced rotor-ground gap further confining the rotor wakes and tip vortices. As a result, the thrust increase due to the increase in circulation of the tip vortices in the inner rotor region (as discussed in Section 5.2.2.1) becomes dominant and diminishes the effect of the recirculation regions due to the walls.

5.3.7 Comparison with Quadcopter Open Space IGE and ICE

In this section, H_4 is compared with quadcopter IGE and ICE in open space using the results from the physical experiments. Similar to H_0 , H_4 exhibits open space ICE behaviour because the ceiling plane has a strong influence on the rotors' upstream flow field regardless of the presence of the walls. H_4 still resembles the open space ICE trend as shown in Figure 5.57. Furthermore, as discussed in Section 5.3.4, the recirculation region next to the left wall further reduces the induced velocity of P_c for the near ceiling cases. This explains the overall increase in C_T for H_4 compared the OS_c and OS_g .

5.4 Quadcopters in Tunnel Effects

Addressing the objectives in this thesis (Section 1.3), this section summaries the characteristics of *Tunnel Effects* as discussed in chapter. Using the scenarios included in the scope of this thesis, these effects can be broadly split into two categories: symmetrical and asymmetrical flow fields.

Tunnel effects with a symmetrical flow field:

Positioning the quadcopter at any location along H_0 , the flow field around the quadcopter is symmetrical about the centre plane of the quadcopter. Compared to OS , at O_T there is a return cycle of the wake due to the combined effect of the ground plane and wall. Since the position of the rotor is relatively close to the saddle point of the return cycle, the flow velocity advecting into the rotor's upstream flow from the return cycle is relatively low. This reduces the induced velocity going through the rotor. Near the ceiling (H_0V_2), there is a reduction in the vertical flow momentum in the rotor's upstream flow region due to the proximity to the planar surface. This drives a decrease in the induced velocity and improves lift production. When the quadcopter is positioned close to the ground (H_0V_{-2}), the saddle point of the return cycle is positioned relatively higher to the rotor (compared to O_T). The recirculated flow travelling vertically upward along the wall reduces the radial component of velocity in the upstream flow of the rotor, which reduces lift in the outer rotor

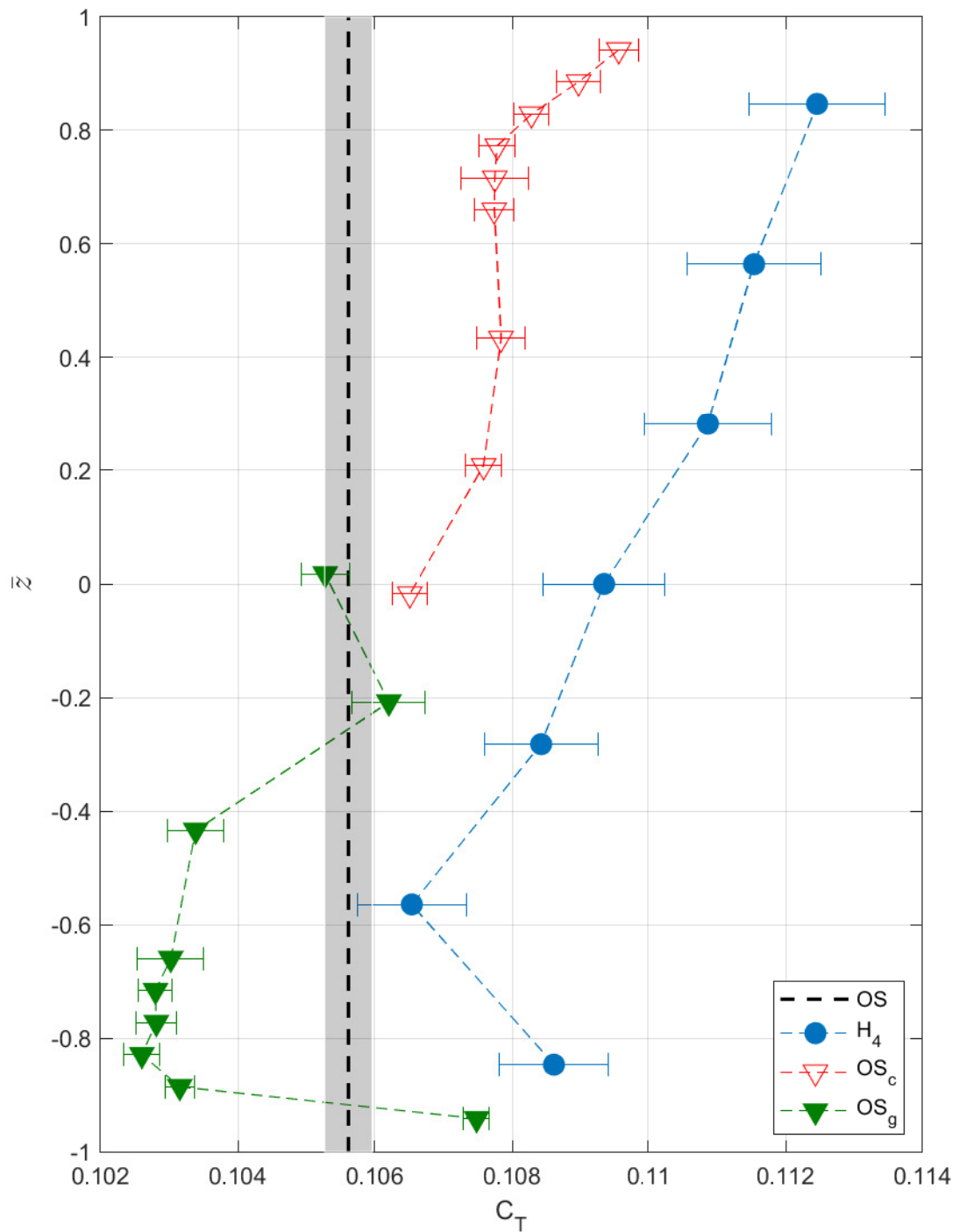


Figure 5.57: Thrust coefficient comparison between the physical experiment results of H_4 , OS_c and OS_g . The dark shaded region represents the error region of the OS case.

region. In the inner rotor region, the confinement of the ground and symmetry plane inhibits the dissipation of vorticity. As described in Section 4.1.8.2, the location of the vortex affects the local flow field. Since this recirculation region is below the rotor, it rotates the fluid impinging on the blade such that the magnitude of induced velocity is reduced. Combined, these effects result in an overall reduction in thrust compared to O_T , as the lift reduction in the outer rotor region is more significant than the increase in the inner region.

Tunnel effects with an asymmetrical flow field:

Once the quadcopter's position deviates from H_0 , the flow field around the quadcopter is no longer symmetrical. As a result, there is an imbalance in the lift production between the P_c and P_w , which generates a rolling moment acting on the quadcopter body. The presence of the wall obstructs the component of fluid momentum in the direction normal to the wall. Focusing on the near wall propeller, as the rotor is closer to the wall, fluid travels predominantly parallel to the wall. This decreases the radial component of momentum near the rotor. Therefore, increasing the induced velocity in the rotor's upstream flow (Robinson, 2016). Close to the ceiling corner (H_4V_2), this effect is countered by the ceiling effect for P_w , resulting in only a slight increase in thrust compared to O_T . As for P_c , the combination of the ceiling effect and the pumping effect of the return cycle induces a greater amount of radial component of velocity in the rotor's upstream flow. Thus, the lift improvement for P_c is greater compared to P_w . The flow characteristics at the ground corner (H_4V_{-2}) is an important finding in this research. The characteristics of P_c 's flow field at H_4V_{-2} resembles that of H_0V_{-2} . Nevertheless, since the rotor-wall distance has increased, the vertical flow momentum of the return cycle has a reduced effect of decreasing the radial component of velocity in P_c 's upstream flow. Thus, there is a slight increase in thrust for P_c at H_0V_{-2} compared to O_T . However, P_w at H_4V_{-2} experiences a dissimilar flow effect from rotors in other cases. Similar to the inner rotor region (as described in Section 5.3.5.1), the wall and the ground plane confines the tip vortex in the outer rotor region of P_w , inhibiting vorticity to dissipate out of that region. When P_w passes through two recirculation regions, the flow with high magnitude of vorticity diminishes the effect of the induced velocity on the pressure. As a result, the reduction in lift for P_w at H_4V_{-2} only correlates to the decrease in the blade surface pressure differentials but not the induced velocity. This lift reduction for P_w counters the lift increase in P_c , resulting in a decrease in thrust at H_4V_{-2} compared to O_T . At H_4 , or other non H_0 cases, P_w always generates less thrust than P_c due to the proximity to the wall. Therefore, the rolling moment acting on the quadcopter body will always cause the quadcopter to roll and accelerate toward the closest wall.

Overall trend in thrust and rolling moment across the tunnel:

In order to provide a better visualisation of the raw thrust coefficients shown in Figure 4.17, a new set of values is defined using

$$\Delta C_T = \frac{C_T}{C_{T_0}} \times 100\%, \quad (5.2)$$

where C_{T_0} is the C_T value at O_T and ΔC_T is the percentage change in C_T relative C_{T_0} at each tunnel location. This set of ΔC_T values is interpolated into a contour plot shown in Figure 5.58. Note that since the contour in the figure is numerically interpolated, although the ΔC_T value at O_T should be zero, it has slightly increased to a non zero value due to the interpolation. The rolling moment on the quadcopter body is represented as % uneven thrust (as described in Section 5.3.3) and the values at different locations are also interpolated into a contour plot shown in Figure 5.59 for better visualisation.

Comparing Figure 5.58 and 5.59, tunnel effects appear to have a stronger impact on thrust than the rolling moment, since there is larger variation in C_T cross different location. The largest C_T variation occurs near the wall, which means both ascending or descending maneuver near the wall would experience extra acceleration in the direction of travel. As depicted in Figure 4.17, improvement of lift efficiency due to the ground plane becomes more prominent as the quadcopter is positioned closer to the wall. Whereas, ceiling effect is most prominent near H_3 but the effect gradually reduces when the quadcopter is closest the to wall due to the increasing reduction in radial component of velocity in P_w 's upstream flow because of the wall.

The largest U variation occurs near V_{-1} . The quadcopter would experience increasing acceleration toward to the wall when maneuvering from H_0V_{-1} to H_5V_{-1} . In the other regions, the rolling moment is of lower magnitude which is less challenging for flight. The magnitude of the moment disturbance appears to be the lowest along V_0 as illustrated in Figure 5.59.

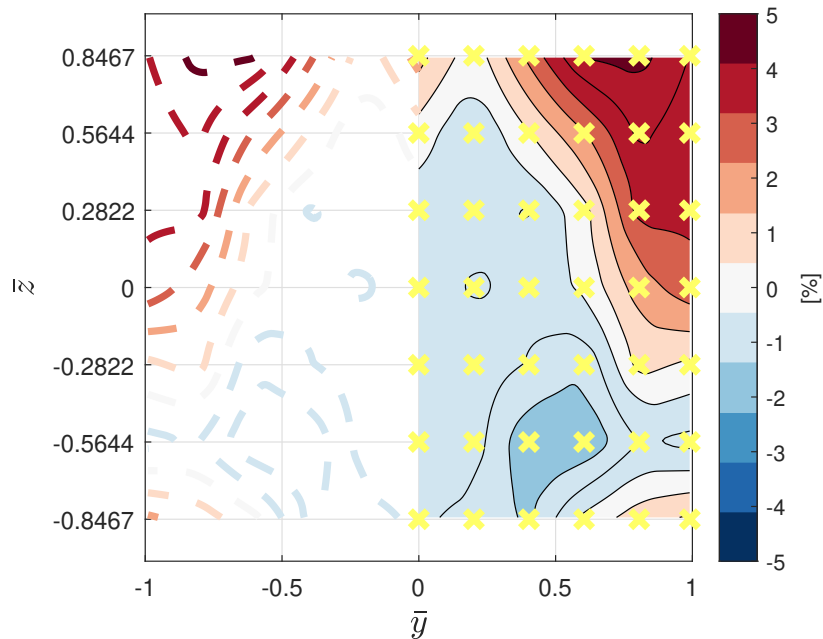


Figure 5.58: Cross section contour of the change in thrust coefficient at different experiment location relative to C_T at O_T . The yellow crosses represent the locations at which the experiments were conducted. Note that the dashed lines on the left side are the mirrored contour lines from the experiment result, as those locations were not included in the experiment.

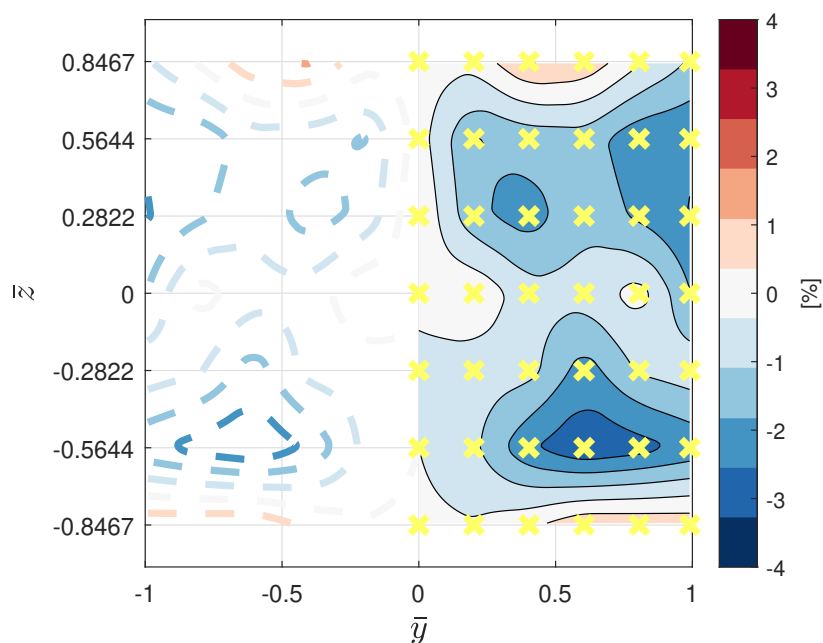


Figure 5.59: Cross section contour of the % uneven thrust, U at different experiment locations. The yellow crosses represent the locations at which the experiments were conducted. Note that the dashed lines on the left side are the mirrored contour lines from the experiment result. Note that negative value of U causes a rolling moment toward the wall.

5.5 The Effect of Tunnel Size

This section is a preliminary study on how the size of the tunnel influences the tunnel effect at the origin of the tunnel using the CFD results. The last rotor revolution of the simulations is used to produce the C_T comparison plot shown in Figure 5.60. Figure 5.62 to Figure 5.65 are the cross sectional flow field and vorticity contour plots for tunnel size, $w_t = \{15R, 10R, 7.5R, 6R\}$ respectively. Note that $w_t = 10R$ is the O_T case.

As shown in Figure 5.60, decreasing the tunnel size from $w_t = 15R$ to $w_t = 10R$ decreases the mean C_T . Yet, both two cases still show slight increased in the average C_T compared to OS. As discussed in Section 5.1, this increase is primarily due to the rotor's relative position to the return cycle and its saddle point. As illustrated in Figure 5.62, the saddle point of the return cycle is positioned lower than the rotor compared to O_T (Figure 5.63). The return cycle travels upward around the saddle point and gradually loses its vertical momentum due to the adverse pressure gradient before advecting into the rotor's upstream flow. This effectively reduces the induced velocity in the outer region for the $w_t = 15R$ case, thus, increasing the overall thrust compared to O_T and OS. However, there is a point of diminishing return as the tunnel size increases, the location of the return cycle will be too far away from the rotor to have a significant effect of the flow around the rotor.

Decreasing the tunnel size from $w_t = 10R$ to $w_t = 6R$ further decreases C_T to be lower than O_T and OS. For $w_t = 7.5R$, in the outer rotor region, the proximity to the wall reduces the radial component of velocity in the upstream flow field. Whereas, in the inner rotor region, the rotor-ground and rotor-ceiling gaps are yet to be close enough to have a sufficient influence on countering the lift reduction in the outer rotor region. Thus, the overall thrust decreases compared O_T . For $w_t = 6R$, it is difficult for the vorticity to dissipate due to the confinement of all the planar boundaries. Similar to the discussion in Section 5.3.5.3, the high vorticity flow which the rotor travels pass predominantly reduces the effect of the inviscid flow on the surface pressure on the rotor, hence, altering the local effective angle of attack. Furthermore, there is vorticity accumulated at the saddle point near the ceiling next the symmetry plane. This accelerates the flow travelling downward toward the inner rotor region of the rotor's upstream. Thus, increasing the induced velocity and countering the effect of the ground plane in the inner rotor region¹⁸. In this case ($w_t = 6R$), the combination of all four planar surfaces in the tunnel induce the reduction in thrust.

There is a clear relationship between the change in lift and the rotor-boundary distance. As an example, δ_y is the gap between the tunnel wall and the tip of the rotor, and it is defined as

$$\delta_y = 0.5w_t - y_q - R_{qy} - R, \quad (5.3)$$

where y_q is the y position of the quadcopter and R_{qy} is the distance from the centre to the rotor in the y direction. Figure 5.61 shows a nonlinear trend of decrease in C_T as the tunnel size decreases. This highlights that there are other parameters, such as rotor-ceiling/ground distance which need to be considered to determine the characteristic of C_T . Recommendations for how to consider this

¹⁸Section 5.2.2.1: proximity ground plane increases circulation of the tip vortex in the inner rotor region

parameter in future studies is discussed in Chapter 7.

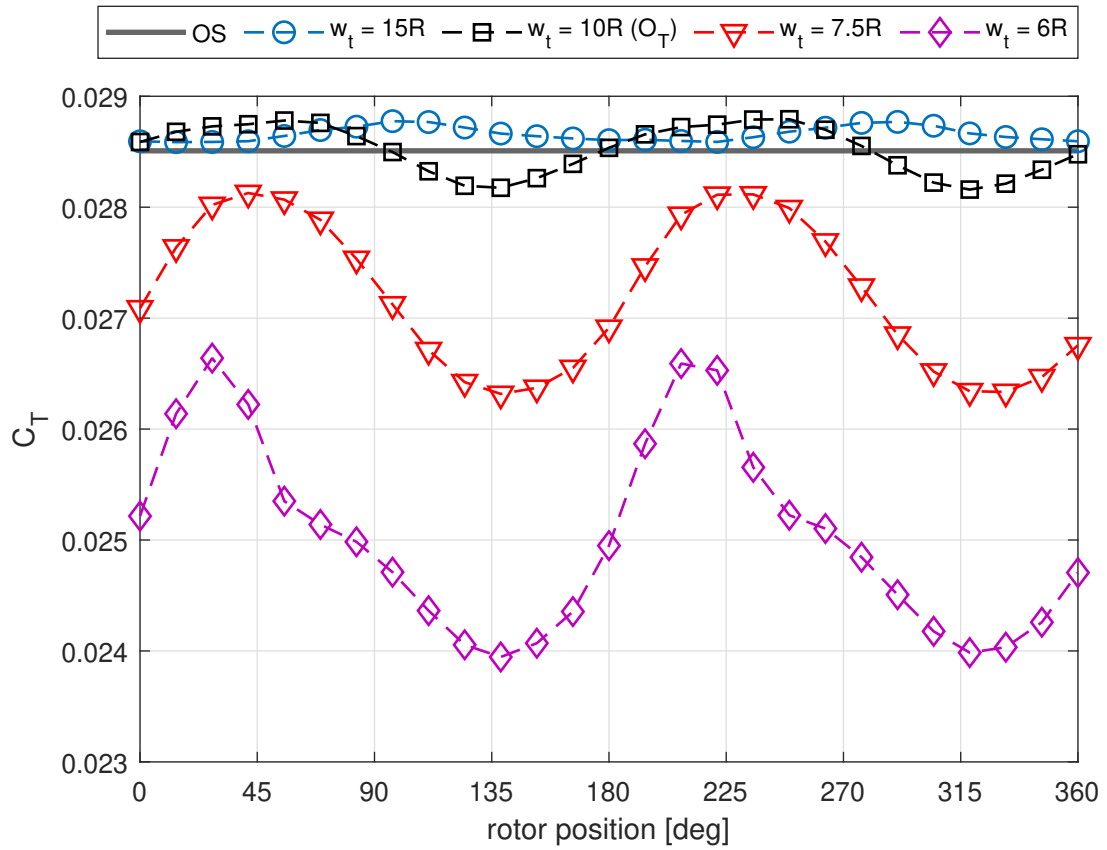


Figure 5.60: Thrust coefficient comparison for the quadcopter in OS and various sizes of tunnels (hovering at O_T location). The x -axis shows the last revolution of the rotor rotation in the CFD simulations.

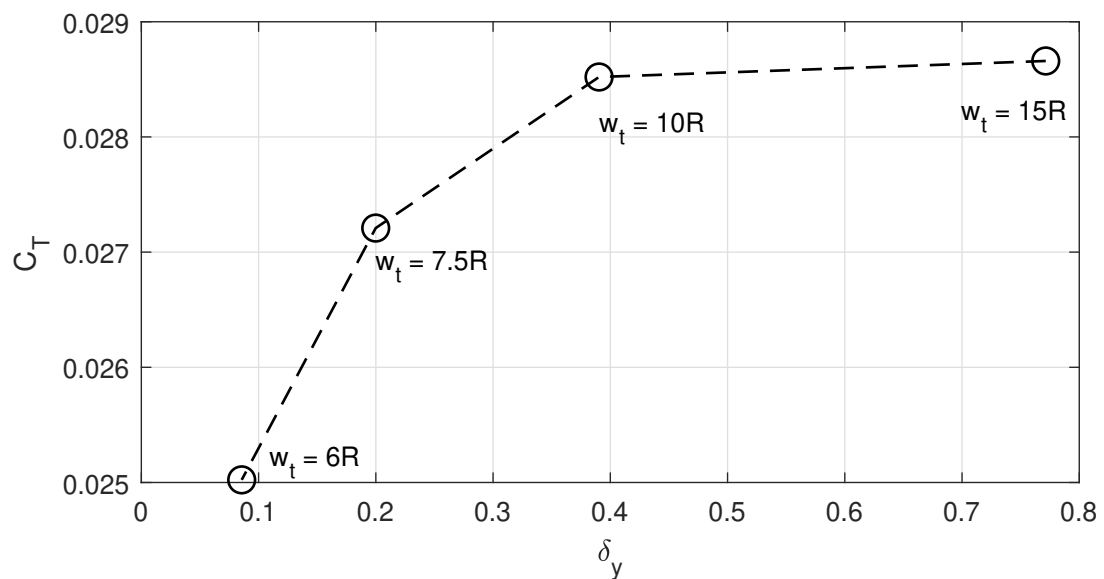


Figure 5.61: Correlation between thrust coefficient and the rotor-wall gap, δ_y .

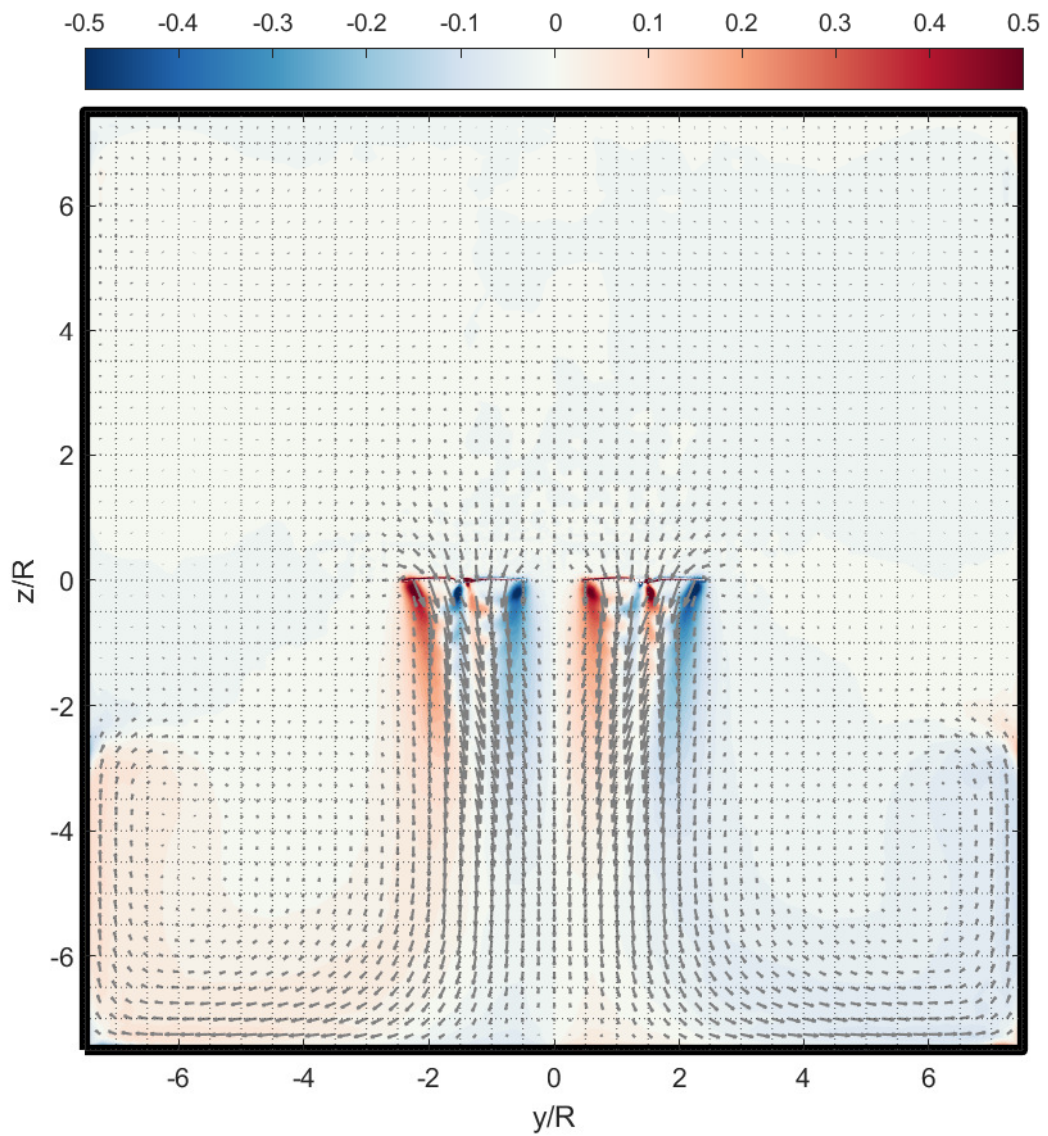


Figure 5.62: Flow field in Cross Section AA, showing the front two propellers in the $w_t = 15R$ tunnel size case. The contour plots show the x - z component of vorticity normalised by the rotation speed, ω_y/Ω .

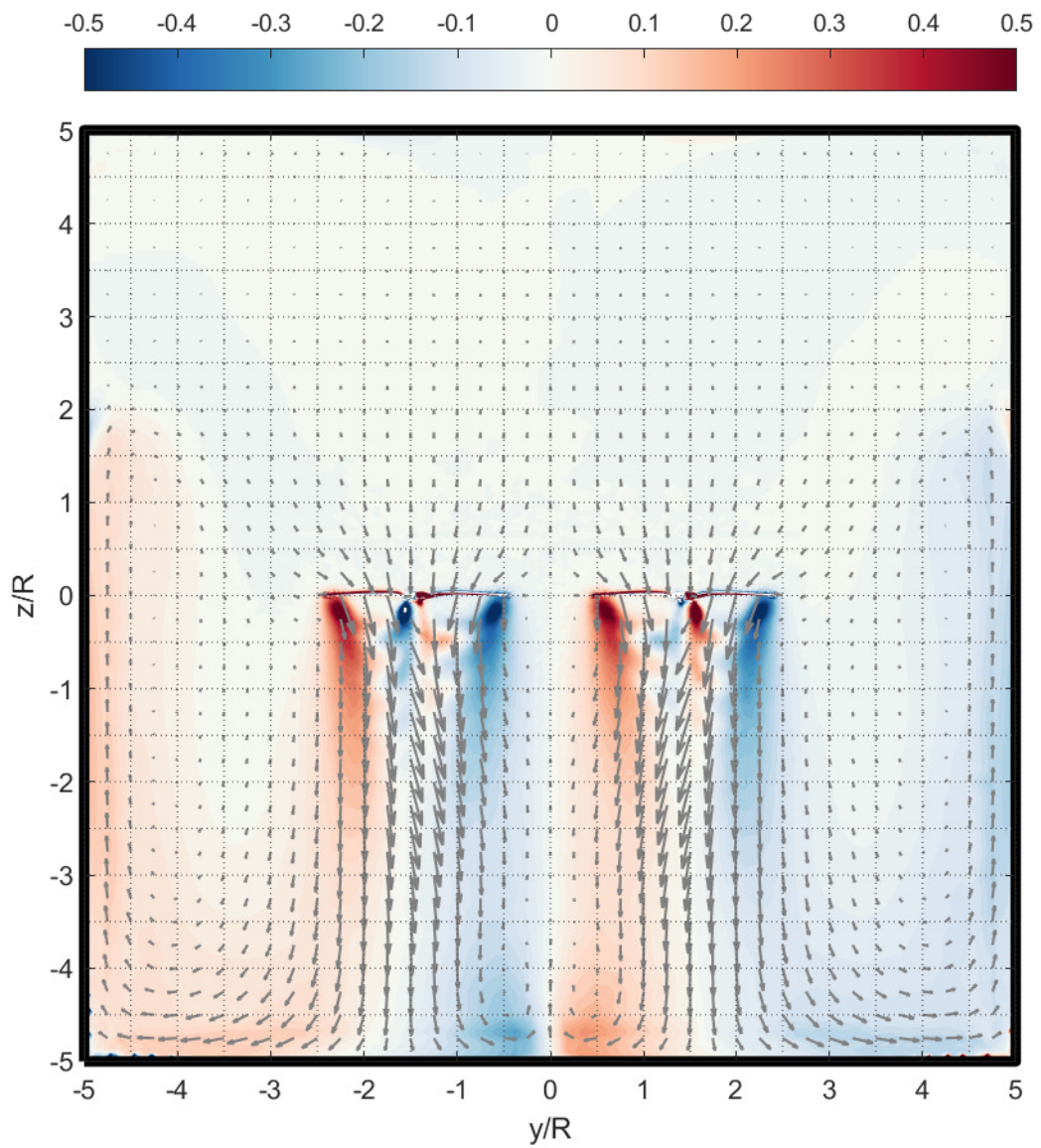


Figure 5.63: As per Figure 5.62 but for the $w_t = 10R$ tunnel size case (same as the O_T case).

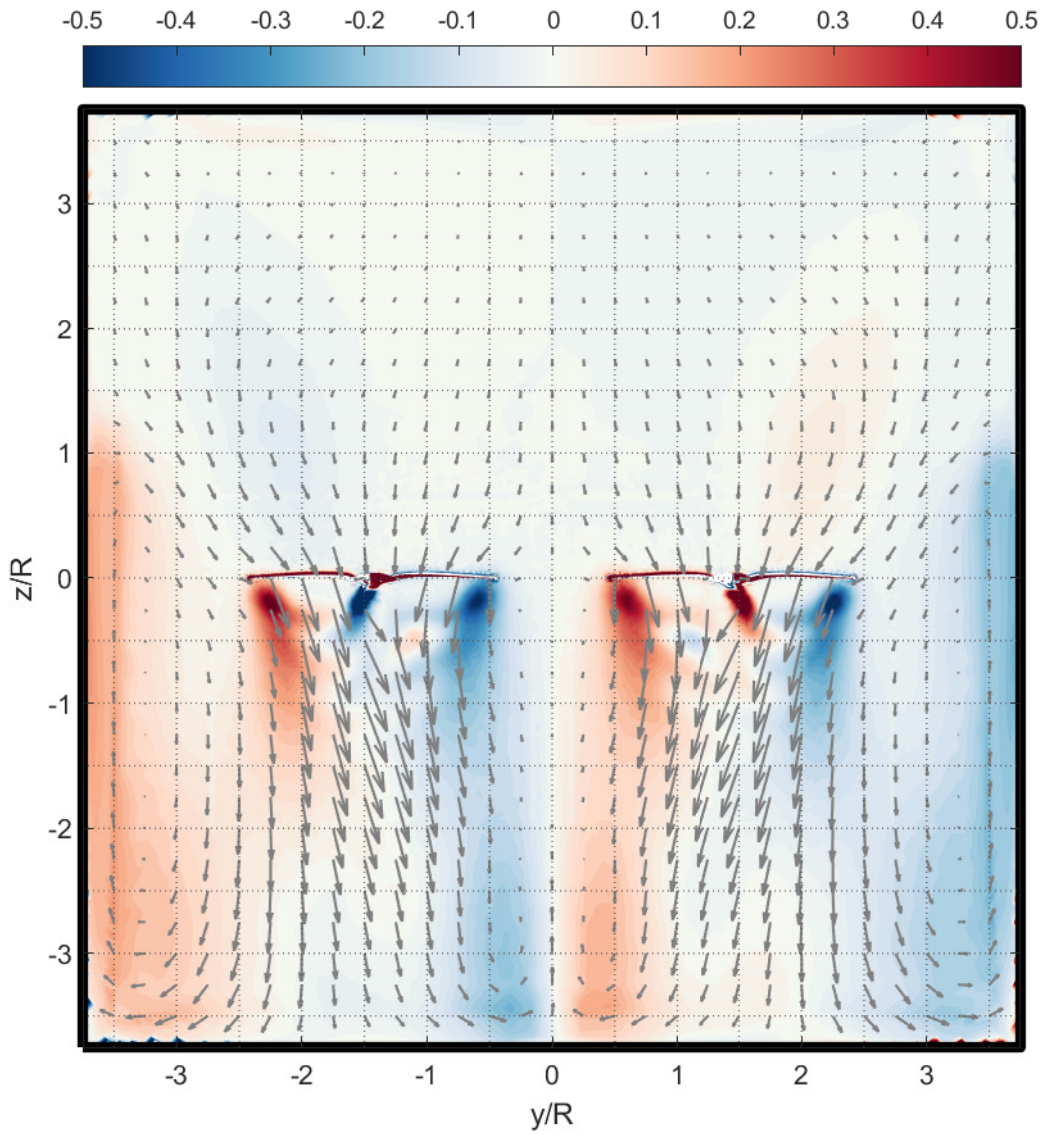


Figure 5.64: As per Figure 5.62 but for the $w_t = 7.5R$ tunnel size case.

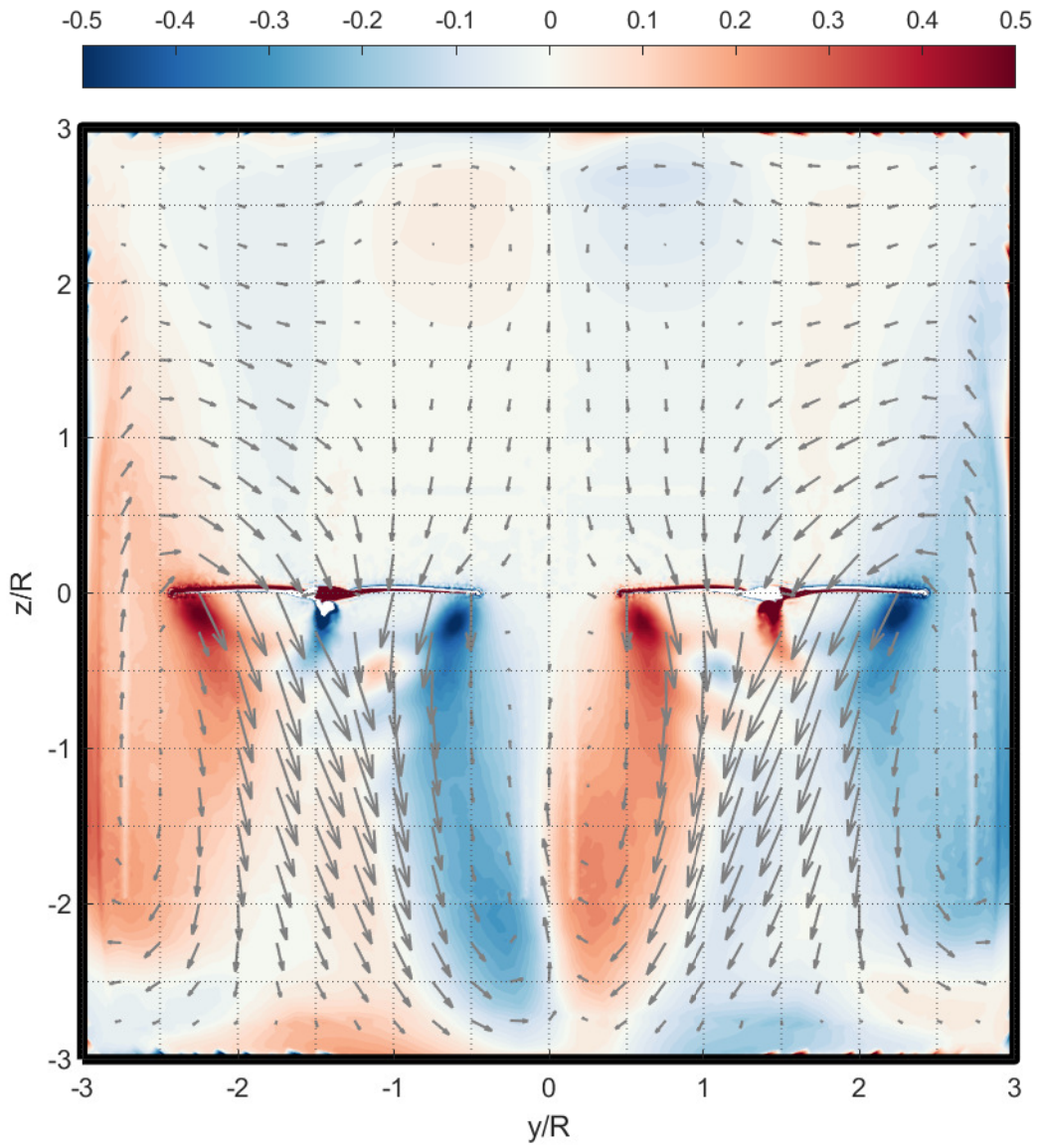


Figure 5.65: As per Figure 5.62 but for the $w_t = 6R$ tunnel size case.

Chapter 6

Control of Quadcopters under Tunnel Effects

In order to navigate the quadcopter inside small tunnels, it is crucial to have a reliable sensing and localisation system. This chapter describes the localisation strategy used in this thesis, as well as providing validation and evaluation on the accuracy of this localisation method. Using this position information, a controller is designed in order to mitigate the tunnel effects described in Chapter 5. The performance of the quadcopter system was evaluated with flight experiments and the system has performed a flight test in a real-world tunnel.

6.1 Localisation Strategy

Visual Odometry (VO) and Visual Simultaneous Localisation and Mapping (VSLAM) are popular choices for indoor navigation in GPS-denied environments. However, VO is inherently prone to drift (Kerl et al., 2013) and Tunnel-like environments reduce the reliability of VSLAM due to the inability to perform loop closure while observable features are plain and repetitious in nature, making VSLAM techniques even more unreliable.

In this work, we only consider tunnel-like environments, which implies that the vehicle can move relatively freely in longitudinal direction while its motion in the cross-sectional plane is harshly constrained. For this reason, self-stabilisation in the y - z plane is safety-critical in our application and we need rather a simple but robust localisation scheme than a complicated and fragile VSLAM or other SLAM techniques. Scan matching is an intuitive alternative to utilise LIDAR scan data to estimate cross-sectional position.

6.1.1 Hough Transform

The Hough transform (HT) is a popular mathematical tool for line segment detection. A graphical illustration of the Hough transform is shown in Figure 6.1. Suppose that there is a set of points from a LIDAR scan, $\mathbf{p} = \{(y, z) | (y_i, z_i) \in \mathbb{R}^2, i = 1, \dots, N\}$. A point $(y_i, z_i) \in \mathbf{p}$ can be transformed into a sinusoidal curve in the parameter space $\mathcal{H}(\beta, \rho)$ (Hough domain), using the following polar

representation of lines:

$$\rho = y_i \cos \beta + z_i \sin \beta. \quad (6.1)$$

For the implementation of HT-based scan matching, $\mathcal{H}(\beta, \rho)$ is discretised into the Discrete Hough Transform (DHT) in order to reduce computational cost by reducing (β, ρ) to a finite set (Duda and Hart, 1971). Let us define

$$\beta_k \triangleq k\Delta\beta, \quad k \in \{0, 1, 2, 3, \dots, N_\beta\} \quad (6.2)$$

$$\rho_m \triangleq -\rho_{\max} + m\Delta\rho, \quad m \in \{0, 1, 2, 3, \dots, N_\rho\}, \quad (6.3)$$

where N_β and N_ρ are the number of intervals in β_k and ρ_k respectively. $\Delta\rho = 2\rho_{\max}/N_\rho$, $\Delta\beta = 180^\circ/N_\beta$ and we assume N_β is an even number such that $\beta_{N_\beta/2} = 90^\circ$.

Let us define H_i as the matrix representation of DHT of the i -th scan point in \mathbf{p} , where $H_i \in \mathbb{R}^{(N_\beta+1) \times (N_\rho+1)}$. The elements of H_i are defined as

$$H_i(k, m) = \begin{cases} 1 & \rho_m \leq y_i \cos \beta_k + z_i \sin \beta_k < \rho_{m+1} \\ 0 & \text{otherwise} \end{cases}. \quad (6.4)$$

Typically, ρ_{\max} is set to the maximum LIDAR scanning range. Thus, if (y_i, z_i) has ρ value bigger than ρ_{\max} , it is considered as noise and all the elements of H_i is set to zero. With these discrete variables, each point in the scan, (y_i, z_i) is transformed and discretised into the corresponding set of parameter pairs, (β_k, ρ_m) forming a sinusoidal curve using Equation (6.1) as illustrated in Figure 6.1. The accumulator matrix H is the discrete representation of the superposition of all the sinusoidal curves in H_i , $i = 1, \dots, N$, and can be defined by

$$H = \sum_{i=1}^N H_i. \quad (6.5)$$

The effects of applying translation and rotation to an example LIDAR scan in Hough domain is illustrated in Figure 6.2. An advantage of performing scan matching in Hough domain is that

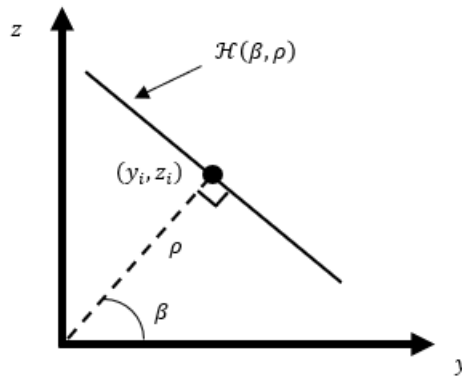


Figure 6.1: Illustration of the Hough transform of point (y_i, z_i) .

translation and rotation are decoupled in Hough domain, which is shown in Figure 6.2. Applying translation, $\mathbf{d} = \begin{bmatrix} \Delta y & \Delta z \end{bmatrix}^\top$ to a scan moves the curves along the ρ -axis in Hough domain by $\delta\rho$, while rotation, $\delta\beta$ moves the curves along the β -axis. This is given by

$$\mathcal{H}'(\beta, \rho) = \mathcal{H}(\beta + \delta\beta, \rho + \delta\rho), \quad (6.6)$$

where \mathcal{H}' is the transformed scan of \mathcal{H} in Hough domain and $\delta\rho = \begin{bmatrix} \cos \beta & \sin \beta \end{bmatrix} \mathbf{d}$ using Equation (6.1). Furthermore, since the dominant line features appear as local maxima in Hough domain, small variations in minor features such as refuge bays, overhead cable trays or noise have less impact on the overall matching result.

6.1.2 Hough Scan Matching

This localisation algorithm assumes the environment to be tunnel-like, and similar in cross-sectional shape and dimensions throughout its length. The target environments for this work are small railway culverts and tunnels, where ceilings and walls have flat surfaces instead of being completely circular, which contributes to very distinctive local maxima (i.e. red circles in Figure 6.2) in H , thus, increasing the accuracy of the scan matching method. Small variations in cross-section such as overhead lighting and cable trays are allowed as long as the planar surfaces are still the dominant features. Although circular or oval cross sections in the environments are also acceptable for the algorithm, the magnitude of the local maxima in H would decrease and be distributed in other area, which may decrease the accuracy of the scan matching method and make the localisation more prone to noise.

The HSM method used in this work is similar to Censi et al. (2005), except we use the angular orientation obtained from the IMU instead of computing it from the Hough Spectrum to minimise computation time. The HSM method computes the transformation between two LIDAR scans in the Hough domain. A reference scan is taken at the entrance of the tunnel, and then translate the origin of the reference scan to the location of the world frame, \mathcal{F}_W as shown in Figure 3.4. HSM is then performed by matching this reference scan with the acquired scan as the quadcopter is traversing along the tunnel.

The DHT of the reference scan, denoted as \bar{H} , is computed first and stored in the memory. For each cross-sectional LIDAR scan, it is rotated using the attitude obtained from the IMU to align the coordinate frame of the scan with \mathcal{F}_W . Then, the DHT of the scan H is computed. Similar to (6.1), $\mathbf{d} = \begin{bmatrix} \Delta y & \Delta z \end{bmatrix}^\top$, the DHT for a given translation between two scans is given by

$$\delta\rho_k = \Delta y \cos \beta_k + \Delta z \sin \beta_k. \quad (6.7)$$

Two β_k values are required to solve for the unknown \mathbf{d} . Although any k of β_k can be chosen, $\beta_0 = 0^\circ$ and $\beta_{N_\beta/2} = 90^\circ$ are the most reasonable choices for minimal computation, given that the environments are structured with vertical and horizontal planar surfaces as dominant features, and the scan's orientation is approximately aligned with the reference frame. By initially rotating the current raw scan to \mathcal{F}_W , we can ensure that the distinctive local maxima (similarly shown by

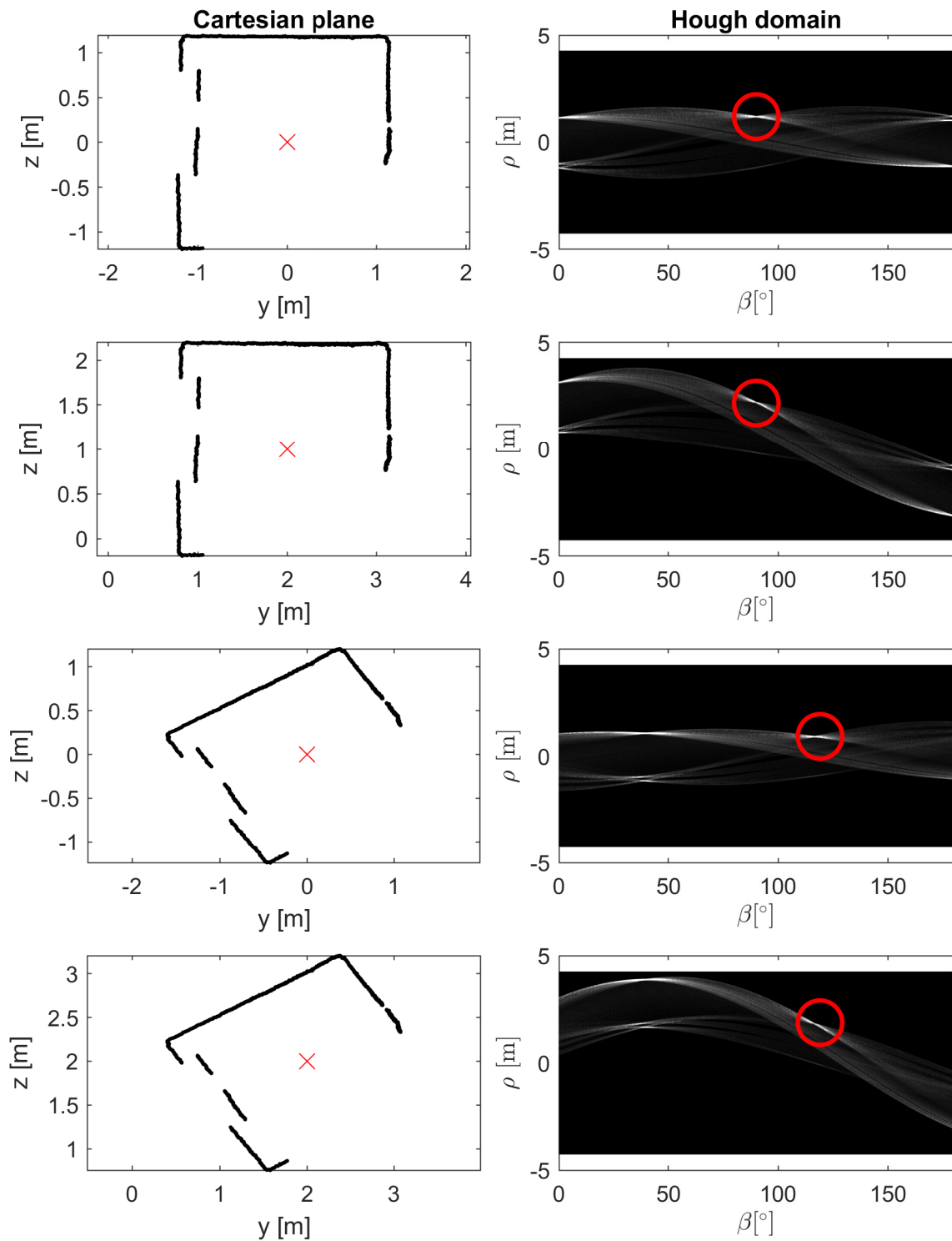


Figure 6.2: Effects of translation and rotation on an example LIDAR scan in Cartesian plane and Hough domain. The red crosses represent centroid of the LIDAR scan and the red circles represent the locations of the same peak in Hough domain. Row 1 to 4 of the figure are the scan at origin, with pure translation, with pure rotation, and translation with rotation respectively.

the red circled regions in Figure 6.2) are located near $\beta_k = 0^\circ, 90^\circ$ and 180° . Using β_0 and $\beta_{N_{\beta/2}}$, Equation (6.7) can be simplified to

$$\delta\rho_0 = \Delta y \quad \text{and} \quad \delta\rho_{N_{\beta/2}} = \Delta z. \quad (6.8)$$

For simplicity, let $H_k \triangleq H(k, \cdot)$, the k -th column vector of H . In order to solve for \mathbf{d} , $\delta\rho_0$ and $\delta\rho_{N_{\beta/2}}$ first need to be estimated from the cross correlation vector between \bar{H}_k and H_k , $(\bar{H}_k \star H_k) \in \mathbb{R}^{(N_\rho+1)}$, whose m -th component is computed by

$$(\bar{H}_k \star H_k)(m) = \sum_{j=0}^{N_\rho} \bar{H}_k(j) H_k(m+j), \quad m = 1, \dots, N_\rho + 1. \quad (6.9)$$

Note that when the index for matrix H_k , $(m+j) > N_\rho$ in (6.9), it wraps around such that the index becomes $(m+j - N_\rho)$ for H_k in (6.9). From (6.6), $\delta\rho_k$ is also defined as the displacement between the k -th column of the reference and source scan, \bar{H}_k and H_k , and it is determined using

$$\delta\rho_0 = \rho(j_0^*) \quad \text{and} \quad \delta\rho_{N_{\beta/2}} = \rho(j_{N_{\beta/2}}^*), \quad (6.10)$$

where

$$j_k^* = \arg \max_j \{(\bar{H}_k \star H_k)\}.$$

j_k^* is the row index achieving maximum of $(\bar{H}_k \star H_k)$, indicating the displacement between \bar{H}_k and H_k in the ρ direction, at which the \bar{H}_k and H_k are cross-correlated the most. Finally, \mathbf{d} is determined using (6.8) and (6.10). The onboard computer, Odroid XU4 is able to compute HSM at 30Hz with ± 10 mm resolution. The accuracy of this algorithm is discussed later in Section 6.1.4.

The current localisation algorithm using the HSM does not consider the heading of the system. Hence, the heading is assumed to be fixed by the heading stabilisation system using a magnetometer and with the aid of the pilot. For stabilisation in the tunnel cross section, yaw angle drift up to $\pm 10^\circ$ contributes to less than ± 50 mm error in the y -axis, which is acceptable especially when the desired lateral position is around the centre of the tunnel. Detailed explanation of this is discussed in the experimental validation presented in Section 6.1.4, showing that the proposed localisation scheme is robust against the violation of this assumption.

6.1.3 Kalman Filtering

Position updates from HSM at 30Hz is relatively slow in the presence of disturbances. To overcome this issue, a basic kinematic Kalman filter was implemented to fuse the onboard inertial measurement unit (IMU) data with the HSM output to provide more frequent updates on the position estimation.

Let the states of the system $\mathbf{x} = \begin{bmatrix} \mathbf{x}_1^\top & \mathbf{x}_2^\top \end{bmatrix}^\top$, and the accelerations measured from the IMU are used as inputs, $\mathbf{a} = \begin{bmatrix} a_y & a_z \end{bmatrix}^\top$ in the world frame. Then, the kinematics of the quadrotor position

in the y - z plane can be expressed in the following form

$$\begin{aligned}\mathbf{x}_k &= \mathbf{F}\mathbf{x}_{k-1} + \mathbf{G}\mathbf{a}_{k-1} + \mathbf{w} \\ \mathbf{y}_k &= \mathbf{H}\mathbf{x}_k + \mathbf{v},\end{aligned}\tag{6.11}$$

where

$$\mathbf{F} = \begin{bmatrix} 1 & \Delta t & 0 & 0 \\ 0 & 0 & 1 & \Delta t \\ 0 & 1 & 0 & 0 \\ 0 & 0 & 0 & 1 \end{bmatrix}, \quad \mathbf{G} = \begin{bmatrix} \frac{\Delta t^2}{2} & 0 \\ 0 & \frac{\Delta t^2}{2} \\ \Delta t & 0 \\ 0 & \Delta t \end{bmatrix}$$

and $\mathbf{H} = \begin{bmatrix} 1 & 0 & 0 & 0 \\ 0 & 1 & 0 & 0 \end{bmatrix}$. The process and measurement noise vectors, \mathbf{w} and \mathbf{v} respectively are estimated from the sensors' datasheets.

The state prediction is calculated using

$$\hat{\mathbf{x}}_{k|k-1} = \mathbf{F}\hat{\mathbf{x}}_{k-1} + \mathbf{G}\mathbf{a}_{k-1},\tag{6.12}$$

where the predicted state error covariance is updated as

$$\mathbf{P}_{k|k-1} = \mathbf{F}\mathbf{P}_{k-1}\mathbf{F}^\top + \mathbf{Q}.$$

The Kalman gain is computed by

$$\mathbf{K}_k = \mathbf{P}_{k|k-1}\mathbf{H}^\top(\mathbf{H}\mathbf{P}_{k|k-1}\mathbf{H}^\top + \mathbf{R})^{-1},\tag{6.13}$$

which is used in the state correction

$$\hat{\mathbf{x}}_k = \hat{\mathbf{x}}_{k|k-1} + \mathbf{K}_k(\mathbf{y}_k - \mathbf{H}\hat{\mathbf{x}}_{k|k-1})\tag{6.14}$$

using the position measurement \mathbf{y}_k produced by HSM. Finally, the state error covariance is updated by

$$\mathbf{P}_k = (\mathbf{I} - \mathbf{K}_k\mathbf{H})\mathbf{P}_{k|k-1}.\tag{6.15}$$

\mathbf{Q} and \mathbf{R} are the process noise covariance matrix and measurement noise covariance matrix respectively. The values for \mathbf{Q} and \mathbf{R} were first estimated from datasheets and educated guesses, then tuned through simulation and experiments. The \mathbf{Q} and \mathbf{R} values used in this work are 0.0225 and 0.0025 respectively. The state prediction is updated at 400Hz when the IMU data is available and the state correction is computed at approximately 30Hz when the position is computed from HSM. This allows the control system to receive position and velocity information at 400Hz, which significantly boosts the performance of the controller.

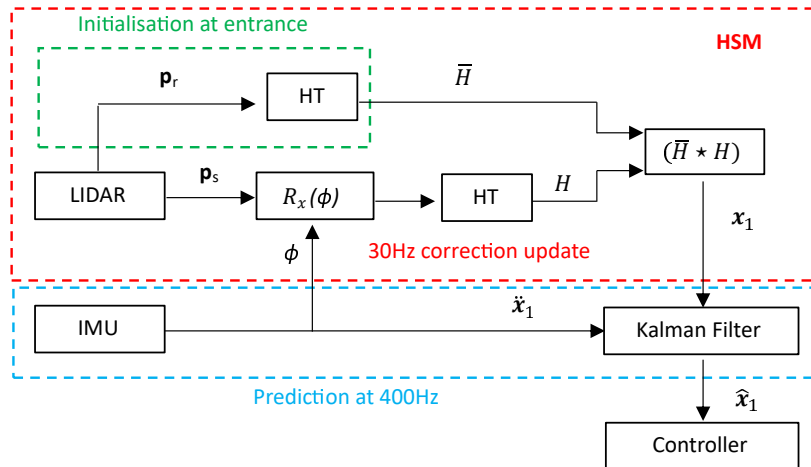


Figure 6.3: Localisation algorithm structure.

6.1.4 Localisation Validation

A motion capture system¹⁹ was used to validate the accuracy of the localisation scheme. The experiment was setup inside 1.5m tunnel (see Section 3.4). Two different experiments were conducted by manually moving the system, and using the motion capture system as the tracking reference. In Experiment 1, the orientation of the system was rotated in the x , y and z -axis sequentially. The angular motions were designed to highlight the impact of the angular perturbations or drifts on the accuracy of the system's localisation. Experiment 2 involved moving the system in a circular-like path. It shows the overall performance of the localisation scheme under the normal operating condition in a controlled environment.

The accuracy of the localisation scheme due to the individual rotational axis is highlighted in Experiment 1. From time $t = 12$ seconds (s) to $t = 20$ s in Figure 6.4, the perturbation in the yaw angle, ψ indicates a clear relationship with the localisation error in the y -axis. A perturbation of $\psi \approx -40^\circ$ corresponded to 55mm of localisation error in the y -axis. On the other hand, changes in the roll and pitch angle only had small impacts on the tracking error in the y -axis. Oscillation of $\pm 30^\circ$ of the roll and pitch angle resulted in ± 25 mm error in the y -axis, which was likely to be caused by the quantisation error of the Hough transform or the measurement noise of the LIDAR.

As for the z -axis, from $t = 5$ s to $t = 10$ s in Figure 6.4, the pitch angle, perturbation in θ has shown minor impact on the z -axis tracking error. A perturbation with $\theta = -25^\circ$ at $t = 6$ s corresponded to less than 20mm localisation error in the z -axis. Also note that the position of the system changes the magnitude of localisation error caused by the angular perturbation. This was observed at $t = 6$ s and $t = 9$ s, similar magnitude of θ perturbation did not result in the same amount of localisation error in the z -axis. However, perturbations in the roll and yaw angles have not indicated any clear relation to the z -axis localisation error.

From Experiment 2, the localisation performance of the system moving in circular motion is shown in Figure 6.5 and 6.6. Overall, the localisation scheme showed reasonable performance with

¹⁹The setup consists of eight OptiTrack Flex 13 cameras placed at both end of the 1.5m tunnel. Link to the Flex 13 camera: <https://optitrack.com/products/flex-13/>

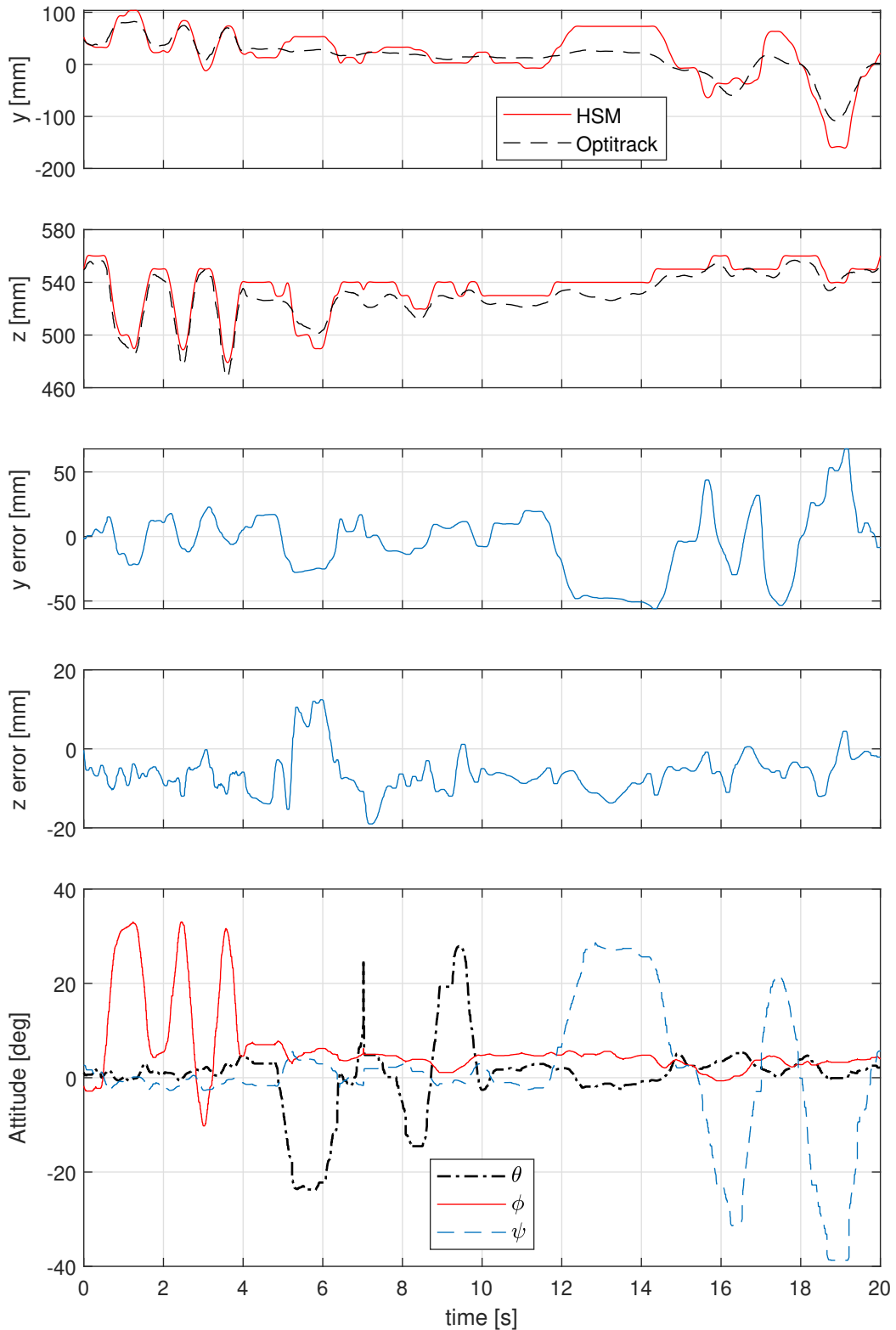


Figure 6.4: Localisation validation results from Experiment 1. A time series comparison between position and tracking error, along with the attitude perturbation. Note that all the subplots share the same time scale.

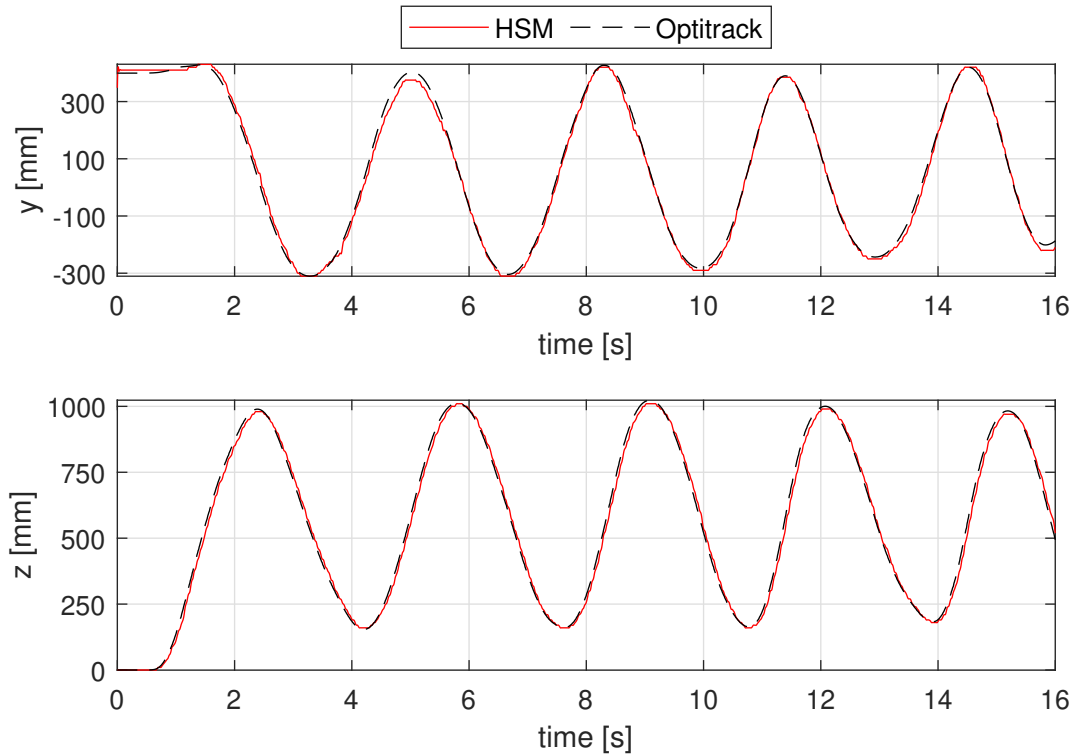


Figure 6.5: Localisation validation results from Experiment 2 - Position over time

maximum of $\pm 50\text{mm}$ error in both the y -axis and z -axis.

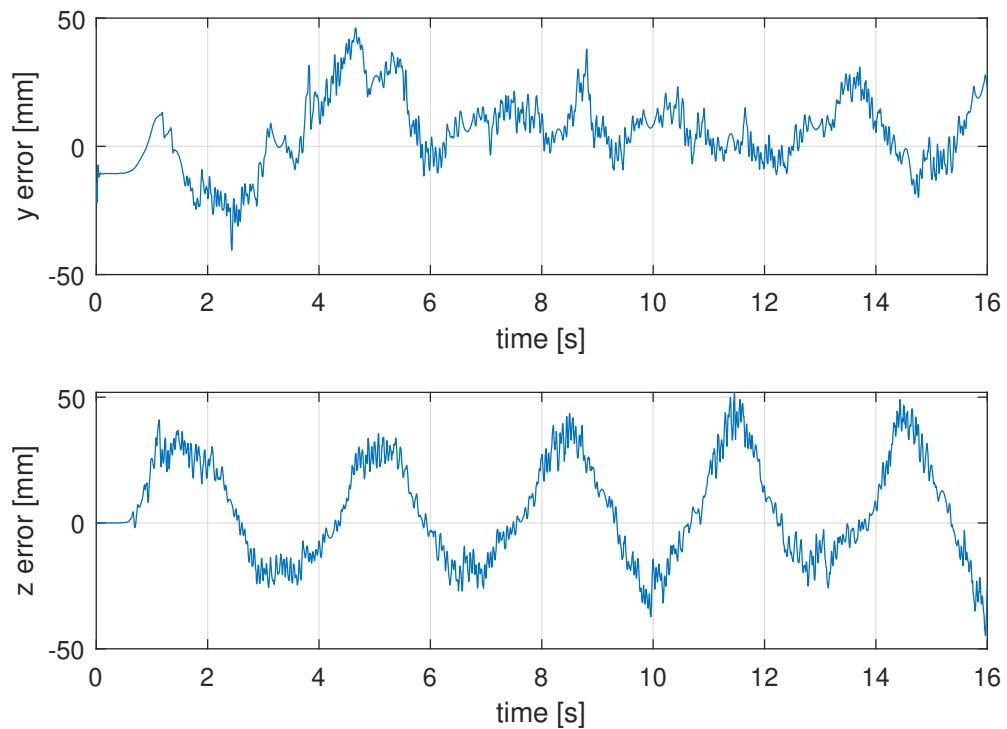


Figure 6.6: Localisation validation results from Experiment 2 - Position error over time.

6.2 Controller Design

6.2.1 Benchmark Controller

For this research, a PID controller is chosen to be the baseline controller to evaluate the performance of the IBS controller. The lateral position is controlled by a generic PID controller,

$$u_\phi = K_p e_y + K_i \int e_y dt + K_d \frac{de_y}{dt}, \quad (6.16)$$

where u_ϕ is the desired roll angle for the attitude controller, $e_y = y_d - y$, and K_p, K_i and K_d are positive constants. For altitude control, the existing altitude hold controller²⁰ from Arducopter (AC) is used. It is a 3-layer cascaded PID controller that produces target thrust to the AC attitude-heading controller.

6.2.2 Integral Backstepping Controller Design

In this section, we derive the IBS controller following the procedures similar in (Jasim and Gu, 2015). It should be noted that we assume a low-level attitude and heading controller as shown in Figure 6.7.

First, let us define the position tracking error

$$\mathbf{e}_p = \begin{bmatrix} e_{p_y} \\ e_{p_z} \end{bmatrix} = \mathbf{x}_{1d} - \mathbf{x}_1, \quad (6.17)$$

where $\mathbf{x}_{1d} = [y_d \quad z_d]^\top$ is the desired position. Then we define a Lyapunov function candidate,

$$V_1 = \frac{1}{2} \mathbf{e}_p^\top \mathbf{e}_p + \frac{1}{2} \boldsymbol{\beta}^\top \mathbf{K}_1 \boldsymbol{\beta}, \quad (6.18)$$

where $\mathbf{K}_1 = \begin{bmatrix} k_{1_y} & 0 \\ 0 & k_{1_z} \end{bmatrix}$ is a positive definite matrix and $\boldsymbol{\beta} = \int \mathbf{e}_p dt$. The time derivative of (6.18) becomes

$$\dot{V}_1 = \mathbf{e}_p^\top (\dot{\mathbf{x}}_{1d} - \mathbf{x}_2) + \boldsymbol{\beta}^\top \mathbf{K}_1 \boldsymbol{\beta}. \quad (6.19)$$

Let $\boldsymbol{\alpha} = \mathbf{x}_2$ be a virtual control input and choose

$$\boldsymbol{\alpha} = \dot{\mathbf{x}}_{1d} + \mathbf{K}_2 \mathbf{e}_p + \mathbf{K}_1 \boldsymbol{\beta}, \quad (6.20)$$

where $\mathbf{K}_2 = \begin{bmatrix} k_{2_y} & 0 \\ 0 & k_{2_z} \end{bmatrix}$ is a positive definite matrix. After substituting (6.20) into (6.19), \dot{V}_1 becomes negative definite as

$$\dot{V}_1 = -\mathbf{e}_p^\top \mathbf{K}_2 \mathbf{e}_p < 0 \quad (6.21)$$

if $\|\mathbf{e}_p\| \neq 0$.

²⁰Arducopter Altitude Hold Mode - <https://ardupilot.org/copter/docs/alholdmode.html>

Now, the velocity tracking error can be defined as

$$\mathbf{e}_v = \begin{bmatrix} e_{v_y} \\ e_{v_z} \end{bmatrix} = \mathbf{x}_2 - \boldsymbol{\alpha}. \quad (6.22)$$

Defining a new Lyapunov function

$$V_2 = V_1 + \frac{1}{2} \mathbf{e}_v^\top \mathbf{e}_v, \quad (6.23)$$

gives the time derivative of V_2 as

$$\dot{V}_2 = \dot{V}_1 + \mathbf{e}_v^\top \dot{\mathbf{e}}_v. \quad (6.24)$$

From (3.6), (6.20) and (6.22) we can get

$$\dot{\mathbf{e}}_v = \begin{bmatrix} u_1 \cos \phi \cos \theta - g - \ddot{z}_d - k_{1_z} e_{p_z} - k_{2_z} \dot{e}_{p_z} \\ -u_1 \sin \phi - \ddot{y}_d - k_{1_y} e_{p_y} - k_{2_y} \dot{e}_{p_y} \end{bmatrix} \quad (6.25)$$

with positive control gains k_{1_z} , k_{2_z} , k_{1_y} , and k_{2_y} . Now the control law for input u_1 can be chosen as

$$u_1 = \frac{1}{\cos \phi \cos \theta} (g + \ddot{z}_d + k_{1_z} e_{p_z} + k_{2_z} \dot{e}_{p_z} - k_{3_z} e_{v_z}). \quad (6.26)$$

Similarly, let $\sin \phi$ be a virtual input, and

$$\sin \phi = \frac{-1}{u_1} (\ddot{y}_d + k_{1_y} e_{p_y} + k_{2_y} \dot{e}_{p_y} - k_{3_y} e_{v_y}), \quad (6.27)$$

where $k_{3_z} > 0$, $k_{3_y} > 0$ are additional control gains.

By substituting (6.19), (6.25), (6.26) and (6.27) into (6.24), it can be shown that the time derivative of the Lyapunov function candidate becomes negative definite as

$$\dot{V}_{2_y} = -\mathbf{e}_p^\top \mathbf{K}_2 \mathbf{e}_p - \mathbf{e}_v^\top \mathbf{K}_3 \mathbf{e}_v \leq 0, \quad (6.28)$$

where $\mathbf{K}_3 = \begin{bmatrix} k_{3_y} & 0 \\ 0 & k_{3_z} \end{bmatrix}$.

Using (6.20) and (6.22), the control laws, (6.26) and (6.27) can be simplified to

$$u_1 = \frac{1}{\cos \phi \cos \theta} (g + \ddot{z}_d + a_1 e_{p_z} + a_2 \dot{e}_{p_z} + a_3 \beta_z), \quad (6.29)$$

where $a_1 = k_{1_z} + k_{2_z} k_{3_z}$, $a_2 = k_{2_z} + k_{3_z}$ and $a_3 = k_{1_z} k_{3_z}$, and similarly,

$$\sin \phi = \frac{-1}{u_1} (\ddot{y}_d + c_1 e_{p_y} + c_2 \dot{e}_{p_y} + c_3 \beta_y), \quad (6.30)$$

where $c_1 = k_{1_y} + k_{2_y} k_{3_y}$, $c_2 = k_{2_y} + k_{3_y}$ and $c_3 = k_{1_y} k_{3_y}$. From (6.30), ϕ can be regarded as the input target roll angle, ϕ_d , which is the input to the attitude controller.

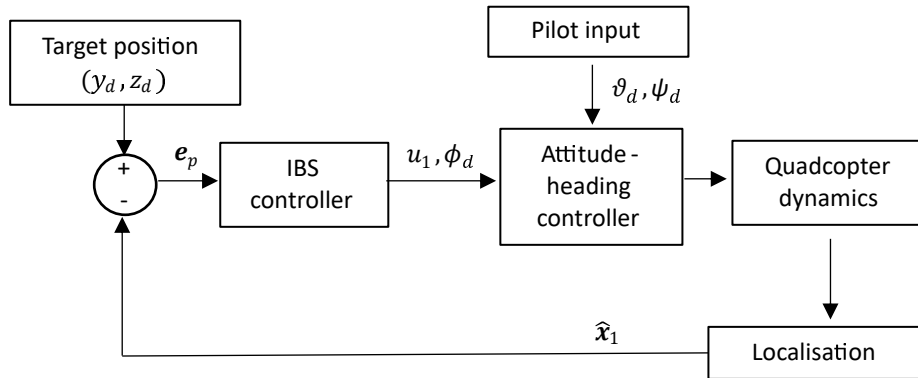


Figure 6.7: Control system of the quadcopter using the IBS controller.

The attitude of the system is controlled by the cascaded PID attitude-heading controller²¹ in the Arducopter firmware. In the outer loop, the controller consists of a square root control to act as a “proportional” angle controller, which outputs the desired angular rate to the PID rate controller in the inner loop. A feedforward term is also added to the angular rate controller to decrease response time of the system. The control diagram of the system is shown in Figure 6.7. The work described in this section has been published in Vong et al. (2019).

6.3 Flight Performance

The flight performance of the system has been evaluated via multiple flight scenarios. A simple straight line trajectory was initially used to evaluate the performance of the implementation of the IBS controller. As described in Section 5.4, the tunnel effects are expected to be more significant near the corners of a square tunnel. Therefore, the straight line trajectory was generated to travel from the upper corner to the bottom diagonal corner. This trajectory has a constant acceleration of $\pm 0.1m/s^2$ using the acceleration and velocity profile shown in Figure 6.8. The line trajectory for the IBS controller in the 2.4m tunnel and its tracking error plot are shown in Figure 6.9 and 6.10 respectively. As in the Figure 6.10, the IBS controller had a maximum tracking error of $\pm 50mm$ in the z -axis. Although the initial tracking error in the y direction went up to approximately 75mm, the controller was able to quickly stabilise the system within $\pm 50mm$ in the lateral axis. The work described in this section has been submitted for review at the time of writing (Vong et al., 2021b).

6.3.1 IBS versus PID Hover Performance

Before comparing IBS and PID in trajectory tracking flights, both controllers were tuned inside the 2.4m tunnel to achieve comparable hover performance in order to have fair performance comparisons between the two controllers. The controllers were set to track a setpoint at the centre of the tunnel, where the magnitude of the disturbances is expected to be relatively low, to establish a baseline performance for both controllers. Figure 6.11 and Figure 6.12 show the setpoint tracking errors of

²¹ArduCopter attitude controller - <http://ardupilot.org/dev/docs/apmcopter-programming-attitude-control-2.html>

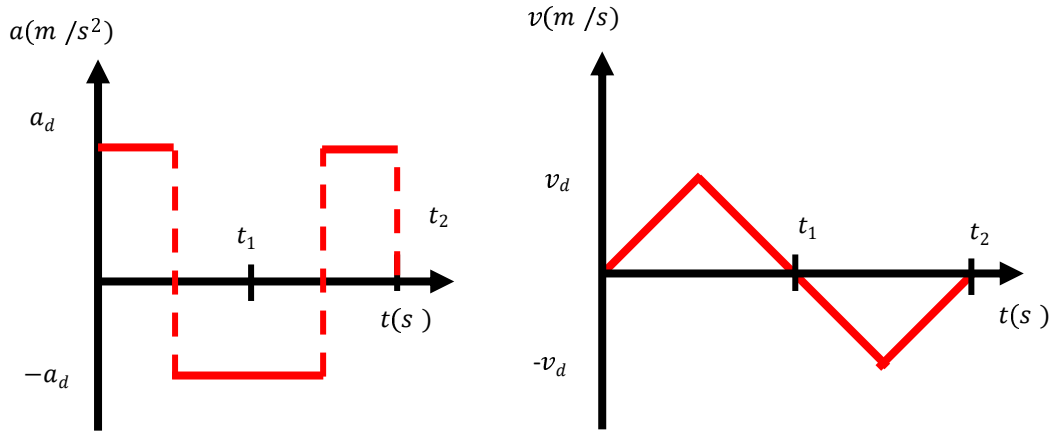


Figure 6.8: Acceleration and velocity profile for the diagonal trajectory.

both tuned controllers in the y - and z -axis respectively. The two controllers show comparable flight performance under static hover condition, and their tracking errors remain within $\pm 60\text{mm}$ in both axes. During all the flights in the simulated tunnels, one end of the tunnel was closed to minimise the effect of the longitudinal wind during the experiments.

6.3.2 IBS versus PID Trajectory Tracking Performance

6.3.2.1 Flight Setup

Ladder Trajectory

The ladder trajectory simulates when an inspection is taken place near the a wall. The system hovers at a fixed position in the y -axis, in this case at $y = 290\text{mm}$. Then the height changes after a period of time, using 0.2m/s^2 acceleration during the height transition. The target path of this experiment is shown in Figure 6.13.

Circular Trajectory

Circular trajectory was also chosen to evaluate the flight performance of the controllers as it consists of coupled motion in both y - and z -axis, and it can simulates inspection flights near the walls and ceiling. Two circular trajectories were generated inside the tunnels to evaluate the tracking performance of the controllers. For the 2.4m tunnel, the following equations were used:

$$\begin{cases} y = 700 \sin 200\pi t \\ z = 700 \cos 200\pi t + 900 \end{cases} \quad (6.31)$$

As for the 1.5 tunnel, the following were used,

$$\begin{cases} y = 300 \sin 460\pi t \\ z = 300 \cos 460\pi t + 650 \end{cases} \quad (6.32)$$

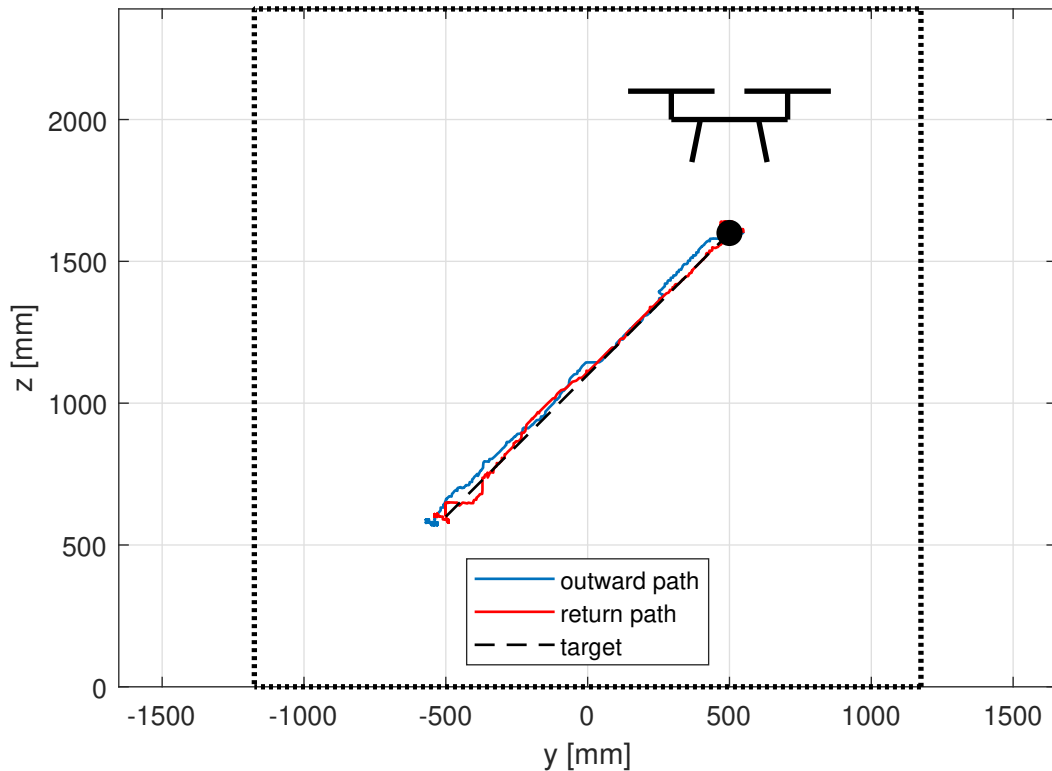


Figure 6.9: Diagonal trajectory for the IBS controller in the 2.4m tunnel. The dotted lines represent the tunnel boundaries, the solid black dot is the starting/ending position of the path and the quadcopter is placed on the diagram to illustrate its scale relative to the tunnel.

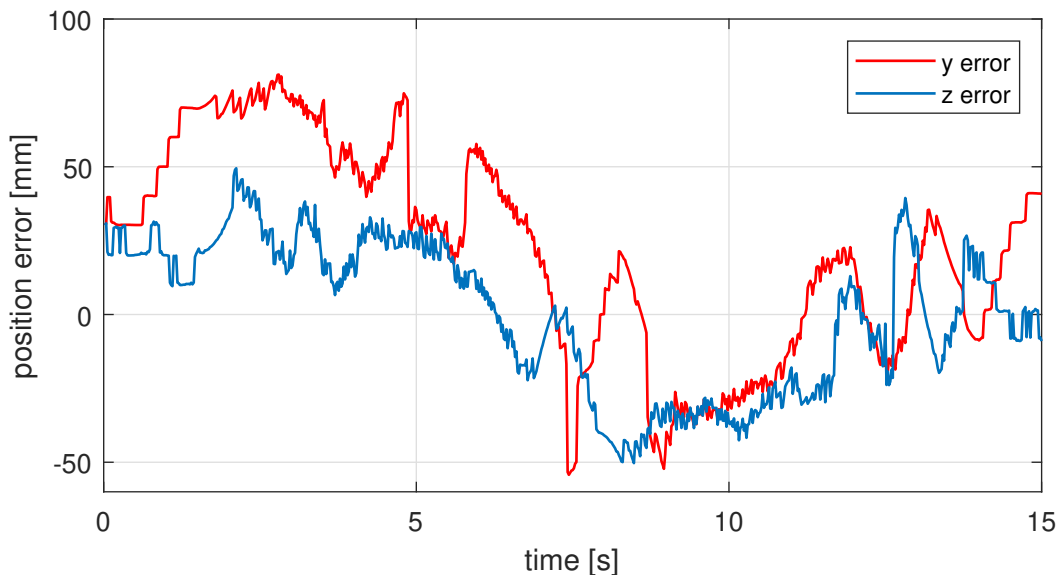
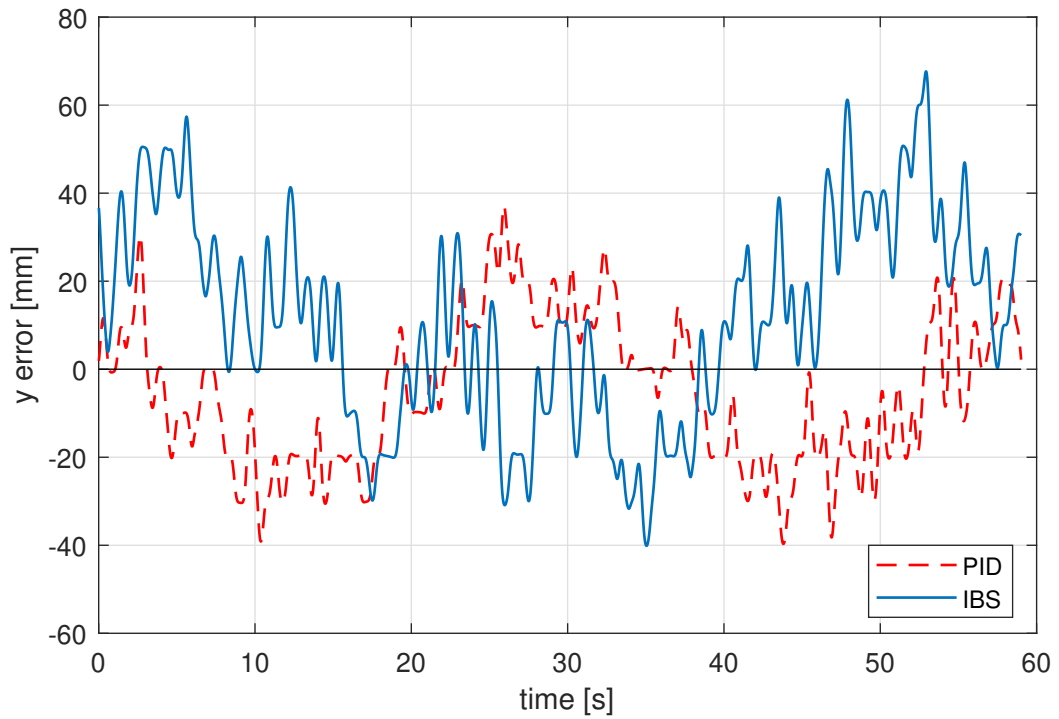
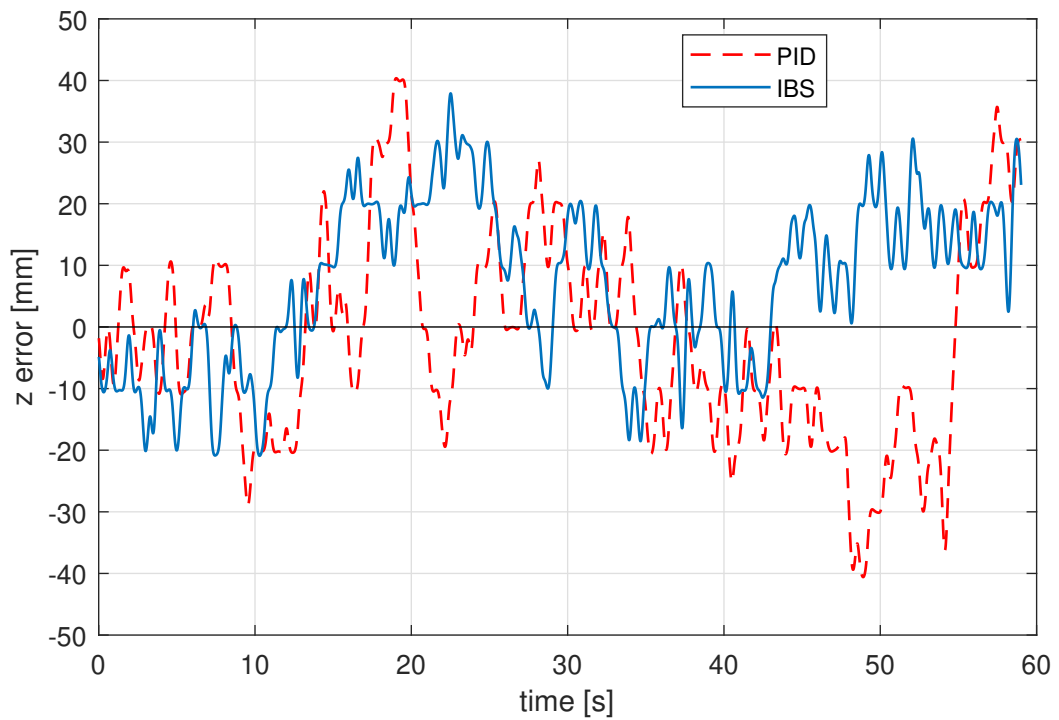


Figure 6.10: Tracking error plot for the diagonal trajectory in the 2.4m tunnel.

Note that the units are in mm. The periods of two trajectories are made different in order to match their tangential velocities, which helps to see the impact of the tunnel effects on the tracking performance clearer. Both trajectories were repeated for the IBS and the PID controller for comparison.

Figure 6.11: y -axis tracking error during hover at the centre of the 2.4m tunnelFigure 6.12: z -axis tracking error during hover at the centre of the 2.4m tunnel

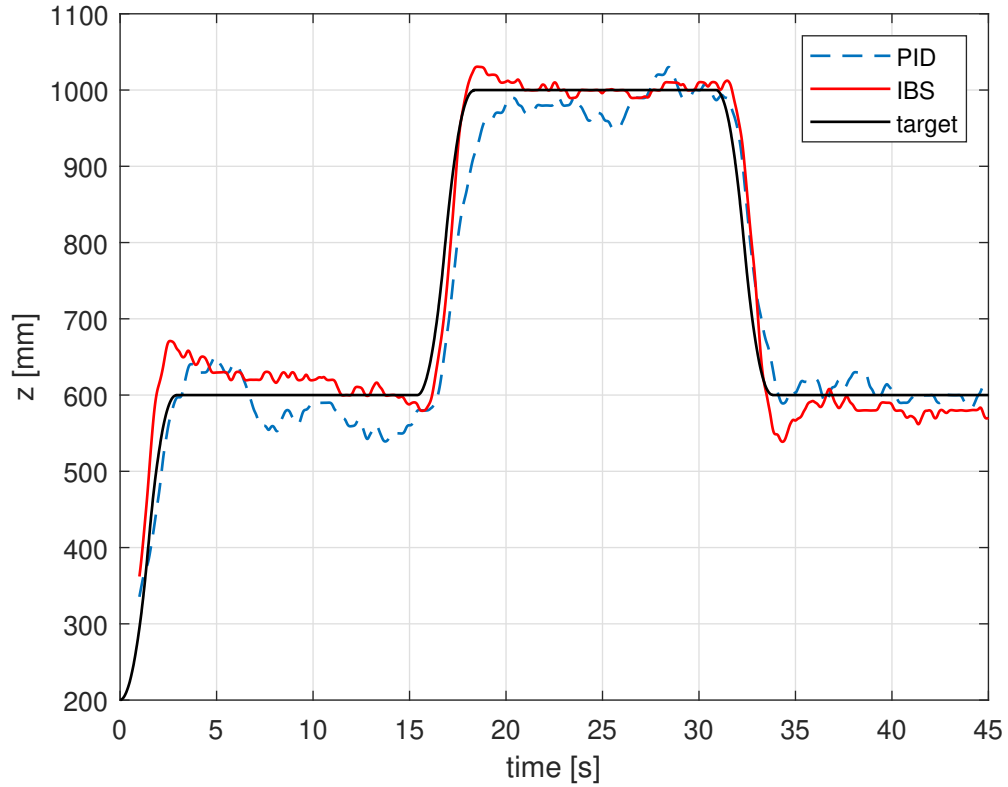


Figure 6.13: z position of the ladder flight experiment.

6.3.2.2 Performance Analysis

Ladder Trajectory Tracking performance in 2.4m tunnel

Overall, the IBS and PID controller has shown similar performance in ladder trajectory flight experiment. Figure 6.14 shows that the IBS and PID has comparable performance in the y -axis, with maximum of $\pm 60\text{mm}$ tracking error. In terms of altitude tracking, the IBS controller has shown slightly better tracking performance especially during the height transition at approximately $t = 15\text{s}$ and $t = 30\text{s}$ as depicted in Figure 6.15.

Circular Trajectory Tracking performance in 2.4m tunnel

Inside the 2.4m tunnel, the tunnel's width is approximately three times the width of the quadcopter, which is a reasonably small ratio. As depicted in Figure 6.16, the IBS controller was able to closely track the target trajectory. The tracking error plots in Figure 6.17 show that the IBS controller has comparable performance between the y - and z -axis, with approximately $\pm 50\text{mm}$ tracking error.

On the other hand, the PID controller did not track the trajectory very well near the top right and bottom left corners of the 2.4m tunnel. The path taken by the PID controller appeared to be an oval shape as illustrated in Figure 6.16. The tracking error plot (Figure 6.17) indicates that the PID controller had poor tracking performance in the z -axis in particular, with approximately $\pm 200\text{mm}$ error margin. One reason for this is that, unlike the IBS control laws in (6.29) and (6.30), the cascaded altitude PID controller does not take the target acceleration and attitude (which

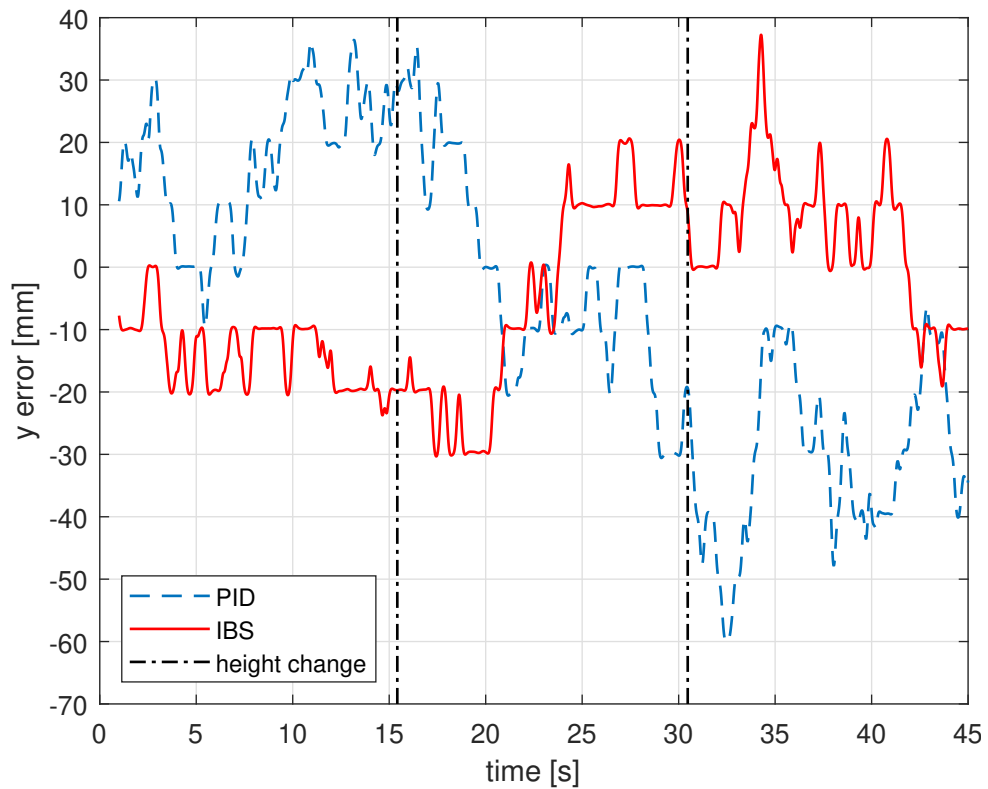


Figure 6.14: Tracking error in the y -axis for the ladder flight experiment. The dot-dash lines indicate when the height transitions start to occur.

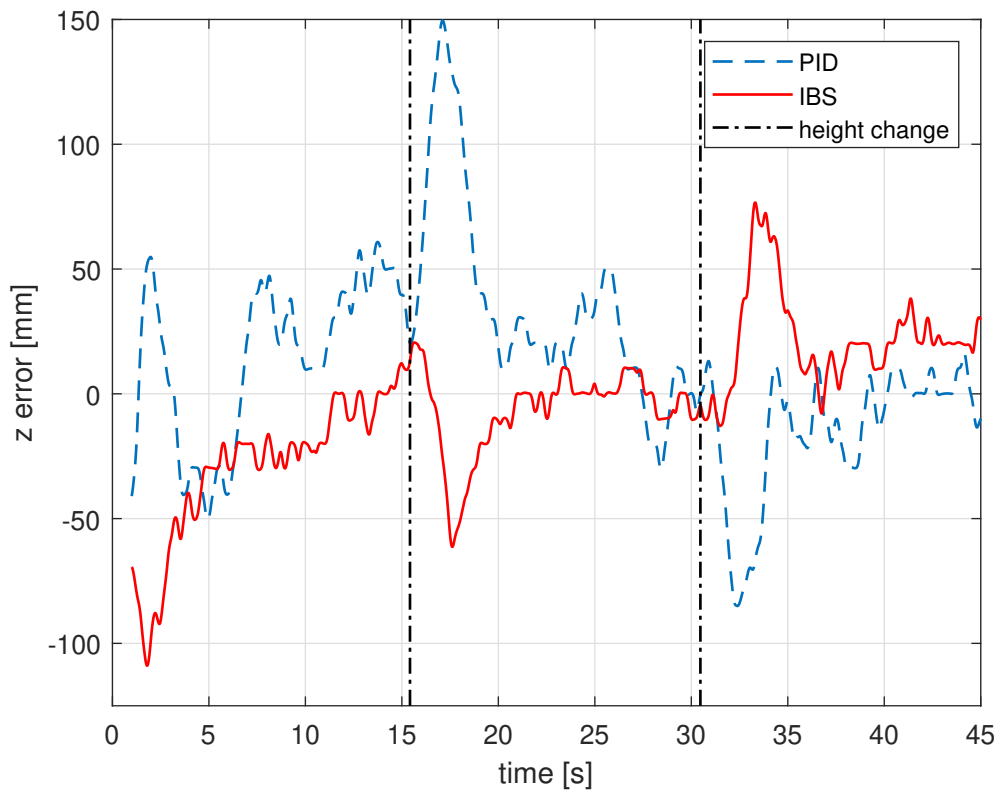


Figure 6.15: As per Figure 6.14 but for the z -axis.

influences the vertical thrust) into account. Therefore, the cascaded altitude PID controller has a large delay in the transient response with the given trajectory as seen in Figure 6.17. Additionally, as described in Section 5.4, Figures 5.58 and 5.59 suggest that the disturbances become most severe at the corners of the tunnel. At the top corner, the PID overshoot in both y - and z -axis due to the increase in thrust and the additional rolling moment. Whereas, at the bottom corner, the downward momentum along with the loss in thrust efficiency and the roll moment has driven the quadcopter toward the bottom corner. The large nonlinear variation in thrust efficiency at different height inside the tunnel as depicted in Figure 5.58 is also a contributing factor to deteriorate the flight performance of the quadcopter. However, the IBS controller was able to demonstrate its robustness in these situations as discussed earlier.

Circular Trajectory Tracking performance in 1.5m tunnel

The width of the 1.5m tunnel is approximately two times the width of the quadcopter, which greatly restricted the motion of the quadcopter and only allowed small margin of tracking error during the flights. The PID controller was unable to properly track the target trajectory inside the 1.5m tunnel and safety guards of the quadcopter made several contacts with the tunnel's wall during the experiment. This is shown in Figure 6.18 around $t = 1$ and $t = 5.1$. The system has increasing tracking error in the negative y direction and then suddenly bounces back due to the impacts. The impact locations can also be seen from Figure 6.16 as indicated by the arrow markers. Once again the flight path with the PID controller resembled an oval shape instead of being the reference circular shape. Similar to the discussion above, the tunnel effects also caused the quadcopter to have a tendency to accelerate toward the corners of the 1.5m tunnel.

As for the IBS controller, it showed similar performance in the y -axis compared to when it was in the 2.4m tunnel, with ± 50 mm tracking error in the y -axis as shown in Figure 6.18. However, Figure 6.18 shows that the IBS controller had slightly degraded tracking performance in the z -axis, with position offset in the positive z direction. It is also worth noting that the amount of error in the positive z direction was slowly decreasing over time as suggested in Figure 6.18.

As suggested by the tracking error plots (Figures 6.17 and 6.18) and the observations discussed above, the tunnel effects seem to have a more significant impact on the quadcopter's thrust than its attitude inside this smaller tunnel. Although the IBS controller has shown better tracking performance than the PID controller, the impact of the tunnel effects can still be observed on the IBS controller at the smaller-size tunnel, which implies that the tunnel effects intensify as the size of a tunnel gets smaller.

The experiments highlight the impact of the tunnel effects on the tracking performance and the importance of developing a better, more robust control system to mitigate the effects.

6.3.3 Flight Performance in Real-World Tunnel

During this research project, a permission was granted to test the proposed system at the Yarra Valley Railway (YVR) tunnel in Victoria, Australia. Although the tunnel is relatively large (height $\approx 16.7h_q$ and width $\approx 6.3w_q$) compared to the quadcopter platform, and the impacts of the tunnel

effects were likely small on the system's performance, it was still a valuable experience to test the proposed system in a real-world setup, where dusts and longitudinal wind gusts were unavoidable.

To simulate a real tunnel inspection, we have designed the test flight as the following scenario. The UAV is first set to travel along the tunnel at location $(0, 0.6)$ starting from the entrance of the tunnel. Then, the inspector finds a crack on the wall from the video stream and sets a new waypoint at location $(1, 1.1)$ for a closer view of the crack line. Moments later, another waypoint is set at location $(1, 1.5)$ to follow the extension of this crack line. After the inspector gathers the information he needs, the system is sent back to location $(0, 0.6)$ and returned back to the inspector outside the tunnel. This flight scenario was performed on the same day using both the IBS and PID controller in two different flights for comparison.

The quadcopter's flight path inside the tunnel is shown in Figure 6.20. Both the IBS and PID controller were tested under similar conditions, with mild longitudinal wind inside the tunnel.

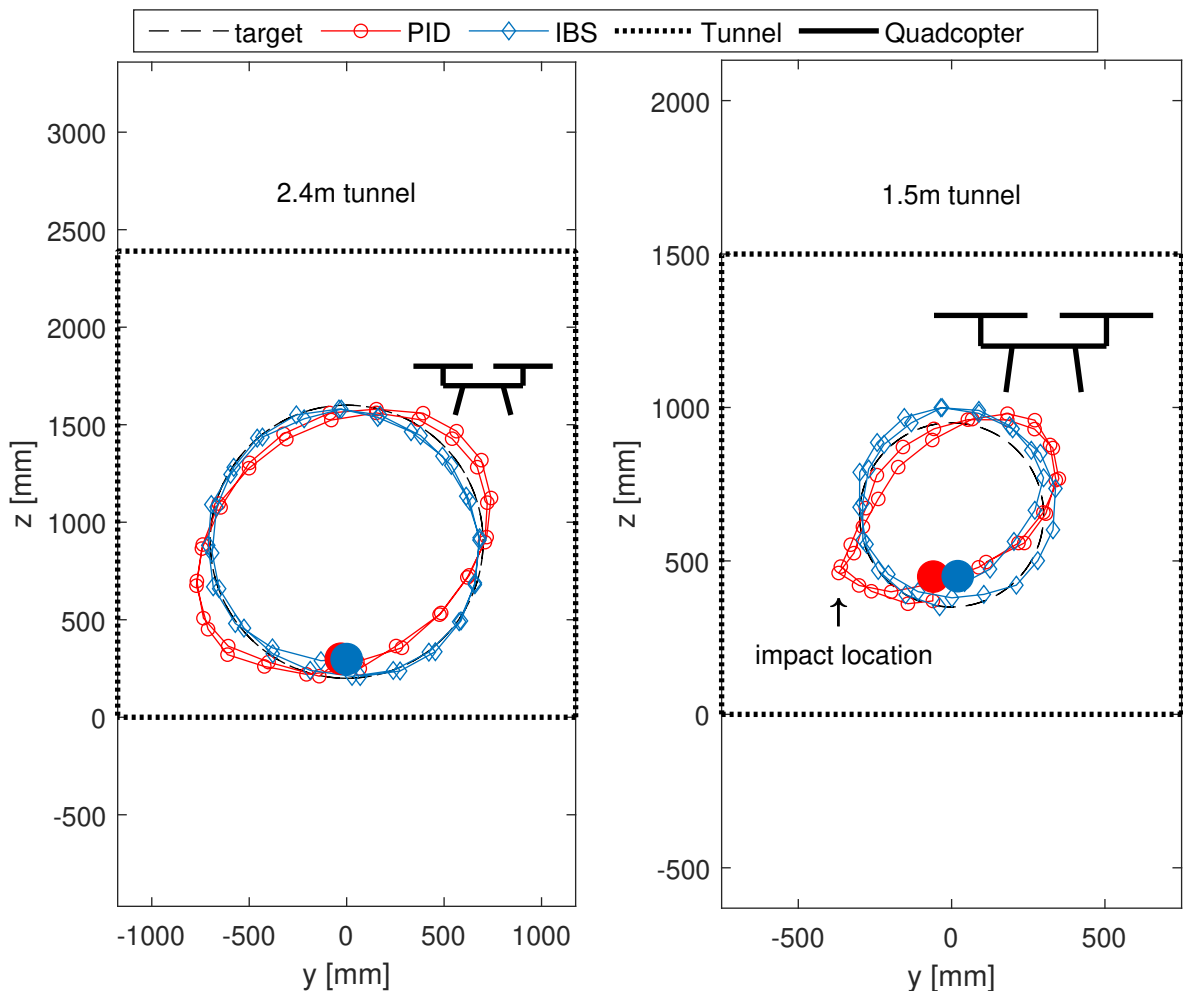


Figure 6.16: Flight trajectories inside the 2.4m and 1.5m tunnel. The solid red and blue circles are the starting points of the trajectories. The tunnel (dotted line) and the quadcopter symbol (black solid line) are shown in the plots to illustrate the actual scale between the two. Note that in the 1.5m tunnel, around location $(370, 460)$, the safety guard of the quadcopter has bumped into the side wall of the tunnel multiple times.

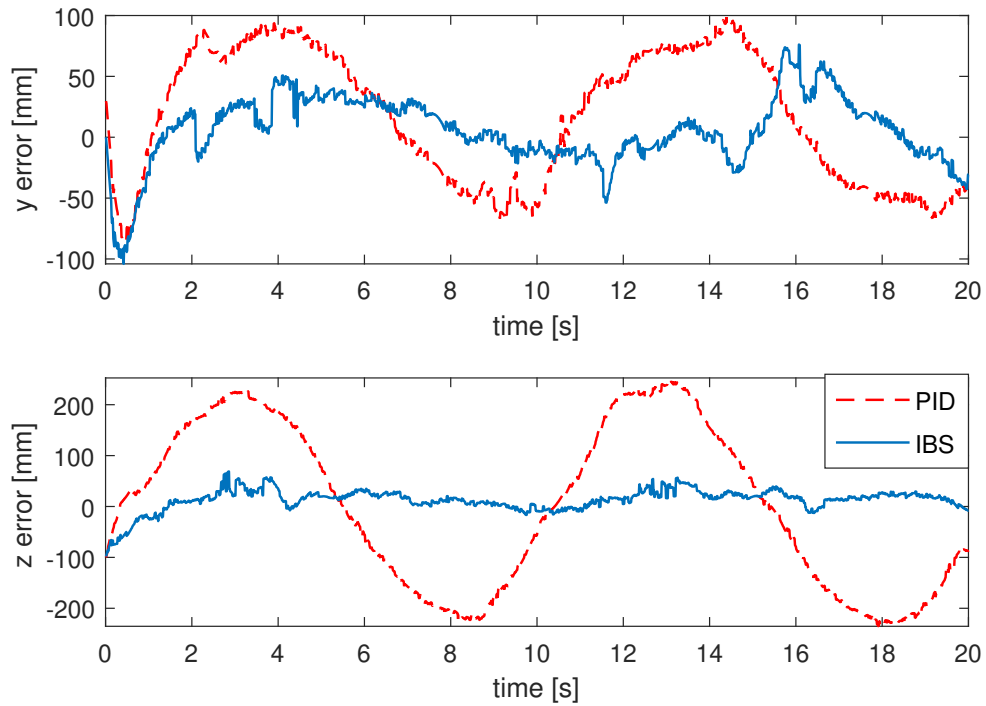


Figure 6.17: Position tracking error comparison between the IBS and PID controller inside the 2.4m tunnel. The initial error spikes are due the starting position was not on the target trajectory.

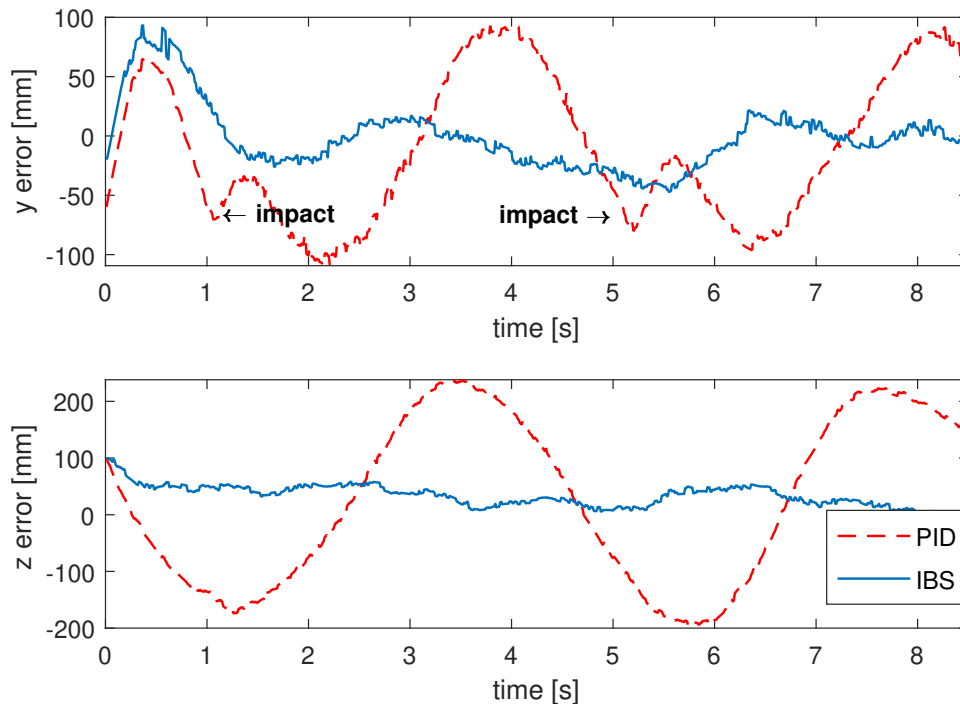


Figure 6.18: Position tracking error comparison between the IBS and PID controller inside the 1.5m tunnel. The initial error spikes are due the starting position was not on the target trajectory. The arrow markers indicate when the quadcopter made an impact with the tunnel's side wall and bounced back using the PID controller.



Figure 6.19: The proposed system flying inside the YVR tunnel.

According to the tracking errors shown in Figure 6.21, the IBS controller had good tracking performance in the railway tunnel in both the y - and z -axis. On the other hand, despite being inside a large tunnel the PID controller did not perform as well in the both axes during 30s to 35s time period. The degraded performance of the PID controller compared to when it was in the custom built testing tunnel is possibly due to the additional longitudinal wind gust in the railway tunnel.

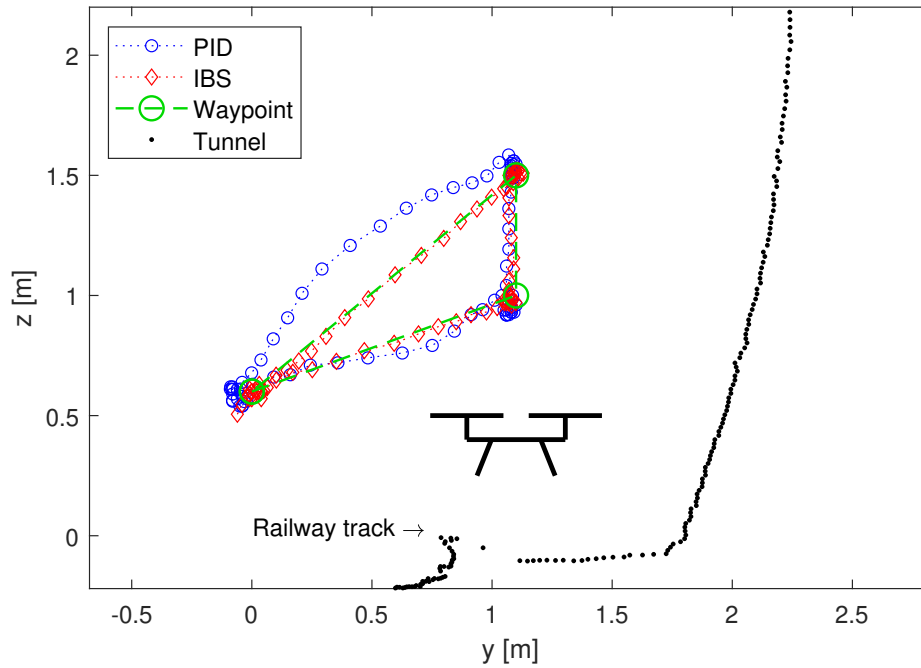


Figure 6.20: The flight path inside the YVR tunnel. The quadcopter symbol (black solid line) is placed in the plot to portray its relative size and distance from the wall of the tunnel (dotted data points from a LIDAR scan).

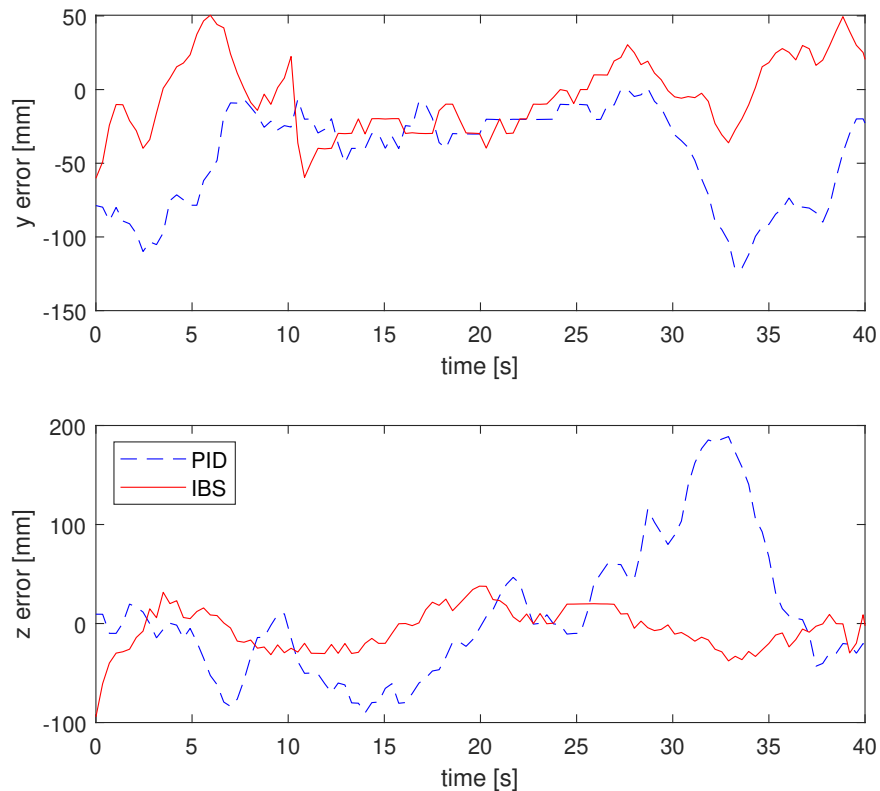


Figure 6.21: Position tracking error comparison between the IBS and PID controller inside the YVR tunnel.

Chapter 7

Conclusions and Future Work

This thesis reported the aerodynamic disturbances associated with quadcopter flights at different locations inside a square cross section tunnel. These scenarios have been modelled in CFD simulations and cross validated using physical experiments. A low-level cross-sectional localisation scheme along with an IBS position controller have been designed with the intent of controlling a semi-autonomous quadcopter system navigating within tunnel environments under such disturbances. The concluding remarks are presented in Section 7.1 and recommendations for future work are discussed in Section 7.2 in this Chapter.

7.1 Conclusions

When a quadcopter is hovering inside a square tunnel, the quadcopter experiences in-tunnel effects, a combined effect from the ceiling, ground and wall which alters the flow field around the rotor significant compared to open space. At H_0 (the horizontal centre of the tunnel), the flow field around the quadcopter shows undisturbed symmetry. Near the ceiling (H_0V_2), the dominant effect which alters the rotor's upstream flow is the reduction of vertical component of velocity due to the ceiling plane. This drives an increase in the local effective angle of attack and increase the lift production. Close to the ground (H_0V_{-2}), the walls induce a vertical momentum in the recirculated flow, which reduces the radial component of velocity going into the upstream flow of the outer rotor region. In the inner rotor region, the confinement of the tip vortex due to the ground and symmetry plane delays the dissipation of vorticity, driving an increase in the circulation of the inner tip vortex and a decrease in the induced velocity in the region. Combined, this increases thrust in the inner rotor region which is countered by the decrease in thrust in the outer rotor region, resulting in an overall slight reduction in thrust compared to O_T .

Once the quadcopter deviates from H_0 , there is a break in symmetry in the flow field around the quadcopter. This causes an imbalance in the thrust between the rotors, inducing a rolling moment acting on the quadcopter body, resulting in an acceleration toward the wall closest to the quadcopter. Considering H_4 as an example, the primary reason of this imbalance is because the wall reduces the radial component of velocity in the P_w 's upstream flow (outer rotor region) as the rotor-wall gap decreases. As a result, the overall lift of P_w is less than P_c . There is an important finding at

H_4V_{-2} . While the flow field characteristics of P_c at H_4V_{-2} resembles that of H_0V_{-2} , P_w at H_4V_{-2} experiences an effect which is dissimilar from rotors in all other cases. P_w at H_4V_{-2} passes through the high vorticity recirculation regions in both the inner and outer regions. The viscous effect of the flow has a significant impact on the blade surface pressure. Ultimately, this drives a reduction in lift for P_w at H_4V_{-2} regardless of a decrease in the induced velocity. This increase significance of the viscous terms also occurs when the tunnel-to-quadcopter size ratio decreases. In confined regions, particularly recirculation regions, vorticity, generated from the quadcopter rotor, does not dissipate. Instead, it is entrained to the inlet flow field. By contrast, when the tunnel-to-quadcopter size ratio increases, vorticity is not entrained into the inlet flow field. The combined effect of the ceiling, ground and walls are dominated by inviscid flow forces, which generally enhance lift production as demonstrated in Chapter 5.

In order to navigate the quadcopter system inside tunnel environments, a cross-sectional localisation scheme using the Hough Scan Matching method was developed in Chapter 6. This aims to provide robust location information in the tunnel's cross section for stabilisation purposes. A Kalman filter is added to this localisation scheme to improve the localisation update rate from 30Hz to 400Hz. Using this location information, a robust nonlinear controller, the IBS controller was designed in Chapter 6 to stabilise the system against the tunnel effects described in Chapter 5. Together, these become a semi-autonomous system which allows non-skilled personnel to operate the UAV in tunnel environments. Finally, baseline flight tests have shown that the IBS and PID controller had comparable performance when hovering at the centre of the square tunnel. Yet, the IBS controller has maintained superior performance and robustness against disturbances in various trajectory flight experiments when compared to the PID controller in the simulated tunnel. The quadcopter system has also performed a simulated inspection task in a real-world railway tunnel, with promising results as a semi-autonomous craft, enabling a platform to aid inspectors with minimal piloting skill.

7.2 Recommendations for Future Work

7.2.1 Tunnel Effect Analysis

Flying a quadcopter inside a tunnel creates a complex fluid dynamic problem and there are certainly many other parameters which have not be explored in the scope of this thesis. Section 5.5 is merely a preliminary study on the effect of tunnel size. Further investigation on the effect of varying the height and width of the tunnel independently could be more practical in real-world settings than square tunnels. It would help to determine the relationship between the rotor distance to planar surfaces or the return cycle and C_T , similar to Figure 5.61. Similarly, parameterising the moment arm also changes the rotor-wall distance, which influences the rolling moment and lift production at the same time.

Furthermore, the Reynolds number is another important parameter (by varying rotor radius or rotation speed) to investigate, since Reynolds number has a strong influence on the rotor's lift characteristics (Winslow et al., 2018). As the Reynolds number increase, the effect of viscosity

decreases. This means even in a smaller tunnel, although the rotor passes through high vorticity region of flow, the effect of the viscous term will not be as significant. Therefore, the reduction in thrust is likely to be less than what has been described in Section 5.5. This provides a new dimension in the parameter space of this study.

In real-world tunnels, wind gusts are a natural phenomenon which frequently occurs. The behaviours of wind inside tunnels (where wind gust is likely to resemble one dimensional flow inside a pipe) is certainly different from open space. Including wind in the model will greatly alter the flow field around the rotors and the return cycle, and possibly help with dissipation of vorticity. The frequency and duration of gust will also add another level of complexity to this problem.

7.2.2 Quadcopter System

Due to time constraints of this research, the findings of the tunnel flow effects were only superficially incorporated into the control system design. An extension of the work could incorporate the findings of the flow disturbances deeply into the control system design for improved performance and robustness. This extension may also include the design of a more enhanced low-level attitude controller in the control system, since the current attitude controller uses a commercially available PID controller which does not consider the system's dynamics and is not as robust against disturbances. As mentioned in Section 7.2.1, for practical real-world application of this system, the longitudinal wind gust is an important factor that should be considered. Although there is an existing wind model for control system design in the prior work of (Bannwarth et al., 2016; Waslander and Wang, 2009; Xiang et al., 2016), the behaviour of longitudinal wind is likely to be different inside tunnel environment. Therefore, enhancements to the current control system should be made to compensate for this.

For localisation in tunnel environments, the current HSM method is mainly optimised for rectangular tunnel cross sections and it is less robust against circular tunnels. Techniques such as Circle Hough Transform (Yuen et al., 1990) can be added to the current localisation scheme to enhance the cross-sectional localisation robustness against a wider variation of tunnel cross-sectional shapes. In addition, since the current localisation scheme acts as a robust low level cross-sectional location estimator for stability purposes, high level localisation algorithms can be added to the system architecture to achieve the full 3D localisation and complete autonomy.

Bibliography

- Achtelik, M., Bachrach, A., He, R., Prentice, S., and Roy, N. (2009). Stereo vision and laser odometry for autonomous helicopters in gps-denied indoor environments. In *Unmanned Systems Technology XI*, volume 7332, page 733219. International Society for Optics and Photonics.
- Alfonsi, G. (2009). Reynolds-averaged navier–stokes equations for turbulence modeling. *Applied Mechanics Reviews*, 62(4).
- Allison, S., Bai, H., and Jayaraman, B. (2019). Estimating wind velocity with a neural network using quadcopter trajectories. In *AIAA Scitech 2019 Forum*, page 1596.
- Allison, S., Bai, H., and Jayaraman, B. (2020). Wind estimation using quadcopter motion: A machine learning approach. *Aerospace Science and Technology*, 98:105699.
- Anderson Jr, J. D. (2010). *Fundamentals of aerodynamics*. Tata McGraw-Hill Education.
- ANSYS Inc. (2010). ANSYS CFX-Solver Theory Guide. *Release 11.0*.
- ANSYS Inc. (2016). ANSYS Fluent Theory Guide. *Release 17.2*.
- Bannwarth, J., Chen, Z., Stol, K., and MacDonald, B. (2016). Disturbance accomodation control for wind rejection of a quadcopter. In *2016 International Conference on Unmanned Aircraft Systems (ICUAS)*, pages 695–701. IEEE.
- Censi, A., Iocchi, L., and Grisetti, G. (2005). Scan matching in the hough domain. In *Proceedings of the 2005 IEEE International Conference on Robotics and Automation*, pages 2739–2744. IEEE.
- Céspedes, J. F. and Lopez, O. D. (2019). Simulation and validation of the aerodynamic performance of a quadcopter in hover condition using overset mesh. In *AIAA Aviation 2019 Forum*, page 2824.
- Cheeseman, I. and Bennett, W. (1955). The effect of ground on a helicopter rotor in forward flight.
- Christiansen, M. P., Laursen, M. S., Jørgensen, R. N., Skovsen, S., and Gislum, R. (2017). Designing and testing a uav mapping system for agricultural field surveying. *Sensors*, 17(12):2703.
- Conyers, S. A. (2019). *Empirical Evaluation of Ground, Ceiling, and Wall Effect for Small-scale Rotorcraft*. PhD thesis, University of Denver.

- Conyers, S. A., Rutherford, M. J., and Valavanis, K. P. (2018a). An empirical evaluation of ceiling effect for small-scale rotorcraft. In *2018 International Conference on Unmanned Aircraft Systems (ICUAS)*, pages 243–249. IEEE.
- Conyers, S. A., Rutherford, M. J., and Valavanis, K. P. (2018b). An empirical evaluation of ground effect for small-scale rotorcraft. In *2018 IEEE International Conference on Robotics and Automation (ICRA)*, pages 1244–1250. IEEE.
- Curtiss, H., Sun, M., Putman, W., and Hanker, E. (1984). Rotor aerodynamics in ground effect at low advance ratios. *Journal of the American Helicopter Society*, 29(1):48–55.
- De Moura, C. A. and Kubrusly, C. S. (2013). The courant–friedrichs–lewy (cfl) condition. *AMC*, 10:12.
- Delmerico, J., Cieslewski, T., Rebecq, H., Faessler, M., and Scaramuzza, D. (2019). Are we ready for autonomous drone racing? the uzh-fpv drone racing dataset. In *2019 International Conference on Robotics and Automation (ICRA)*, pages 6713–6719. IEEE.
- Duda, R. O. and Hart, P. E. (1971). Use of the hough transformation to detect lines and curves in pictures. Technical report, Sri International Menlo Park Ca Artificial Intelligence Center.
- Falanga, D., Kleber, K., Mintchev, S., Floreano, D., and Scaramuzza, D. (2018). The foldable drone: A morphing quadrotor that can squeeze and fly. *IEEE Robotics and Automation Letters*, 4(2):209–216.
- Forster, C., Zhang, Z., Gassner, M., Werlberger, M., and Scaramuzza, D. (2016). Svo: Semirect visual odometry for monocular and multicamera systems. *IEEE Transactions on Robotics*, 33(2):249–265.
- Galdi, G. (2011). *An introduction to the mathematical theory of the Navier-Stokes equations: Steady-state problems*. Springer Science & Business Media.
- Gao, S., Di Franco, C., Carter, D., Quinn, D., and Bezzo, N. (2019). Exploiting ground and ceiling effects on autonomous uav motion planning. In *2019 International Conference on Unmanned Aircraft Systems (ICUAS)*, pages 768–777. IEEE.
- Guntur, S. and Sørensen, N. N. (2014). An evaluation of several methods of determining the local angle of attack on wind turbine blades. In *Journal of Physics: Conference Series*, volume 555, page 012045. IOP Publishing.
- Guruswamy, G. P. (2013). Time-accurate aeroelastic computations of a full helicopter model using the navier-stokes equations. *International Journal of Aerospace Innovations*, 5.
- Hamelin, P., Mirallès, F., Lambert, G., Lavoie, S., Pouliot, N., Montfrond, M., and Montambault, S. (2019). Discrete-time control of linedrone: An assisted tracking and landing uav for live power line inspection and maintenance. In *2019 International Conference on Unmanned Aircraft Systems (ICUAS)*, pages 292–298. IEEE.

- Hashim, A. S. and Tamizi, M. S. M. (2018). Development of drone for search and rescue operation in malaysia flood disaster. *International Journal of Engineering & Technology*, 7(3.7):9–12.
- He, X. and Leang, K. K. (2020). Quasi-steady in-ground-effect model for single and multirotor aerial vehicles. *AIAA Journal*, 58(12):5318–5331.
- He, X., Yang, X., Luo, Z., and Guan, T. (2020). Application of unmanned aerial vehicle (uav) thermal infrared remote sensing to identify coal fires in the huojitu coal mine in shenmu city, china. *Scientific Reports*, 10(1):1–13.
- Hsiao, Y. H. and Chirarattananon, P. (2018). Ceiling effects for surface locomotion of small rotorcraft. In *2018 IEEE/RSJ International Conference on Intelligent Robots and Systems (IROS)*, pages 6214–6219. IEEE.
- Ikedo, T., Yasui, S., Fujihara, M., Ohara, K., Ashizawa, S., Ichikawa, A., Okino, A., Oomichi, T., and Fukuda, T. (2017). Wall contact by octo-rotor uav with one dof manipulator for bridge inspection. In *2017 IEEE/RSJ International Conference on Intelligent Robots and Systems (IROS)*, pages 5122–5127. IEEE.
- Jasim, W. and Gu, D. (2015). Integral backstepping controller for quadrotor path tracking. In *Advanced Robotics (ICAR), 2015 International Conference on*, pages 593–598. IEEE.
- Jones, E., Sofonia, J., Canales, C., Hrabar, S., and Kendoul, F. (2020). Applications for the hovermap autonomous drone system in underground mining operations. *Journal of the Southern African Institute of Mining and Metallurgy*, 120(1):49–56.
- Kang, H. J. and Kwon, O. J. (2002). Unstructured mesh navier-stokes calculations of the flow field of a helicopter rotor in hover. *Journal of the American Helicopter Society*, 47(2):90–99.
- Kaufmann, E., Gehrig, M., Foehn, P., Ranftl, R., Dosovitskiy, A., Koltun, V., and Scaramuzza, D. (2019). Beauty and the beast: Optimal methods meet learning for drone racing. In *2019 International Conference on Robotics and Automation (ICRA)*, pages 690–696. IEEE.
- Kaya, D., Kutay, A. T., and Tekinalp, O. (2017). Experimental investigation of optimal gap distance between rotors of a quadrotor uav. In *AIAA Atmospheric Flight Mechanics Conference*, page 3894.
- Kerl, C., Sturm, J., and Cremers, D. (2013). Dense visual slam for rgb-d cameras. In *2013 IEEE/RSJ International Conference on Intelligent Robots and Systems*, pages 2100–2106. IEEE.
- Kutz, B., Kowarsch, U., Kessler, M., and Kraemer, E. (2012). Numerical investigation of helicopter rotors in ground effect. In *30th AIAA Applied Aerodynamics Conference*, page 2913.
- Lakshminarayan, V. K., Kalra, T. S., and Baeder, J. D. (2013). Detailed computational investigation of a hovering microscale rotor in ground effect. *AIAA journal*, 51(4):893–909.
- Lee, T. E., Leishman, J. G., and Ramasamy, M. (2010). Fluid dynamics of interacting blade tip vortices with a ground plane. *Journal of the American Helicopter Society*, 55(2):22005–22005.

- Li, F., Yang, W., Liu, X., Sun, G., and Liu, J. (2018). Using high-resolution uav-borne thermal infrared imagery to detect coal fires in majiliang mine, datong coalfield, northern china. *Remote Sensing Letters*, 9(1):71–80.
- Light, J. S. (1993). Tip vortex geometry of a hovering helicopter rotor in ground effect. *Journal of the American helicopter society*, 38(2):34–42.
- Liu, J. and Luo, S. (2017). Navier-stokes equations based flow simulations of low reynolds number propeller for unmanned aerial vehicle. In *55th AIAA Aerospace Sciences Meeting*, page 0728.
- Lu, Y. and Song, D. (2015). Robustness to lighting variations: An rgb-d indoor visual odometry using line segments. In *2015 IEEE/RSJ International Conference on Intelligent Robots and Systems (IROS)*, pages 688–694. IEEE.
- Luukkonen, T. (2011). Modelling and control of quadcopter. *Independent research project in applied mathematics, Espoo*, 22.
- Mac, T. T., Copot, C., De Keyser, R., and Ionescu, C. M. (2018). The development of an autonomous navigation system with optimal control of an uav in partly unknown indoor environment. *Mechanics*, 49:187–196.
- Mansouri, S. S., Castaño, M., Kanellakis, C., and Nikolakopoulos, G. (2019). Autonomous mav navigation in underground mines using darkness contours detection. In *International Conference on Computer Vision Systems*, pages 164–174. Springer.
- Mason, P. J. (1994). Large-eddy simulation: A critical review of the technique. *Quarterly Journal of the Royal Meteorological Society*, 120(515):1–26.
- Menter, F. R. (1994). Two-equation eddy-viscosity turbulence models for engineering applications. *AIAA journal*, 32(8):1598–1605.
- Misiorowski, M., Gandhi, F., and Oberai, A. A. (2018). A computational study on rotor interactional effects for a quadcopter in edgewise flight. In *74th Annual Forum of the American Helicopter Society*, number 74-2018, page 1266.
- Misiorowski, M., Gandhi, F., and Oberai, A. A. (2019). Computational study on rotor interactional effects for a quadcopter in edgewise flight. *AIAA Journal*, pages 1–11.
- Moin, P. and Mahesh, K. (1998). Direct numerical simulation: a tool in turbulence research. *Annual review of fluid mechanics*, 30(1):539–578.
- Özaslan, T., Loianno, G., Keller, J., Taylor, C. J., Kumar, V., Wozencraft, J. M., and Hood, T. (2017). Autonomous navigation and mapping for inspection of penstocks and tunnels with mavs. *IEEE Robotics and Automation Letters*, 2(3):1740–1747.
- Özaslan, T., Shen, S., Mulgaonkar, Y., Michael, N., and Kumar, V. (2015). Inspection of penstocks and featureless tunnel-like environments using micro uavs. In *Field and Service Robotics*, pages 123–136. Springer.

- Papachristos, C., Khattak, S., Mascarich, F., and Alexis, K. (2019). Autonomous navigation and mapping in underground mines using aerial robots. In *2019 IEEE Aerospace Conference*, pages 1–8. IEEE.
- Patel, P. N., Patel, M. A., Faldu, R. M., and Dave, Y. R. (2013). Quadcopter for agricultural surveillance. *Advance in Electronic and Electric Engineering*, 3(4):427–432.
- Paz, C., Suárez, E., Gil, C., and Baker, C. (2020). Cfd analysis of the aerodynamic effects on the stability of the flight of a quadcopter uav in the proximity of walls and ground. *Journal of Wind Engineering and Industrial Aerodynamics*, 206:104378.
- Powers, C., Mellinger, D., Kushleyev, A., Kothmann, B., and Kumar, V. (2013). Influence of aerodynamics and proximity effects in quadrotor flight. In *Experimental robotics*, pages 289–302. Springer.
- Roache, P. J. (1998). Fundamentals of computational fluid dynamics. *Albuquerque, NM: Hermosa Publishers, 1998*.
- Roache, P. J. and Knupp, P. M. (1993). Completed richardson extrapolation. *Communications in Numerical Methods in Engineering*, 9(5):365–374.
- Robinson, D. (2016). *Modelling and estimation of aerodynamic disturbances acting on a hovering micro helicopter in close proximity to planar surfaces*. PhD thesis, Monash University.
- Robinson, D. C., Chung, H., and Ryan, K. (2014). Computational investigation of micro helicopter near-wall effect. In *Australasian Fluid Mechanics Conference, Melbourne, Australia, Dec*, pages 8–11.
- Robinson, D. C., Chung, H., and Ryan, K. (2016). Numerical investigation of a hovering micro rotor in close proximity to a ceiling plane. *Journal of Fluids and Structures*, 66:229–253.
- Sanchez-Cuevas, P., Heredia, G., and Ollero, A. (2017). Characterization of the aerodynamic ground effect and its influence in multirotor control. *International Journal of Aerospace Engineering*, 2017.
- Schmid, K., Tomic, T., Ruess, F., Hirschmüller, H., and Suppa, M. (2013). Stereo vision based indoor/outdoor navigation for flying robots. In *2013 IEEE/RSJ International Conference on Intelligent Robots and Systems*, pages 3955–3962. IEEE.
- Segun, A., Sunday, O. I., Ogunti, E. O., and Akingbade, F. K. (2018). Solution to bird pest on cultivated grain farm: A vision controlled quadcopter system approach. *International Journal of Engineering Research and Technology (IJERT)*, 7(10):213–219.
- Shen, S., Michael, N., and Kumar, V. (2013). Obtaining liftoff indoors: Autonomous navigation in confined indoor environments. *IEEE Robotics & Automation Magazine*, 20(4):40–48.
- Spalart, P. and Allmaras, S. (1992). A one-equation turbulence model for aerodynamic flows. In *30th aerospace sciences meeting and exhibit*, page 439.

- Steijl, R. and Barakos, G. (2008). Sliding mesh algorithm for cfd analysis of helicopter rotor–fuselage aerodynamics. *International journal for numerical methods in fluids*, 58(5):527–549.
- Tanner, P. E., Overmeyer, A. D., Jenkins, L. N., Yao, C.-S., and Bartram, S. M. (2015). Experimental investigation of rotorcraft outwash in ground effect. In *Proceedings of the 71th Annual Forum of the American Helicopter Society*, pages 1–26.
- Ventura Diaz, P. and Yoon, S. (2018). High-fidelity computational aerodynamics of multi-rotor unmanned aerial vehicles. In *2018 AIAA Aerospace Sciences Meeting*, page 1266.
- Vong, C. H., Ryan, K., and Chung, H. (2019). Integral backstepping position control for quadrotors in tunnel-like confined environments. In *2019 International Conference on Robotics and Automation (ICRA)*, pages 6425–6431. IEEE.
- Vong, C. H., Ryan, K., and Chung, H. (2021a). Quadcopters in tunnel effects: Aerodynamics analysis of a quadcopter in a tunnel environment. In *Journal of Fluid and Structures [under preparation]*.
- Vong, C. H., Ryan, K., and Chung, H. (2021b). Trajectory tracking control of quadcopters under tunnel effects. In *Mechatronics [under review]*.
- Waite, C. E., van der Heijden, G. M., Field, R., and Boyd, D. S. (2019). A view from above: Unmanned aerial vehicles (uav s) provide a new tool for assessing liana infestation in tropical forest canopies. *Journal of Applied Ecology*, 56(4):902–912.
- Waslander, S. and Wang, C. (2009). Wind disturbance estimation and rejection for quadrotor position control. In *AIAA Infotech@ Aerospace conference and AIAA unmanned... Unlimited conference*, page 1983.
- Winslow, J., Otsuka, H., Govindarajan, B., and Chopra, I. (2018). Basic understanding of airfoil characteristics at low reynolds numbers (10 4–10 5). *Journal of Aircraft*, 55(3):1050–1061.
- Xiang, X., Wang, Z., Mo, Z., Chen, G., Pham, K., and Blasch, E. (2016). Wind field estimation through autonomous quadcopter avionics. In *2016 IEEE/AIAA 35th Digital Avionics Systems Conference (DASC)*, pages 1–6. IEEE.
- Yang, S., Scherer, S. A., Yi, X., and Zell, A. (2017). Multi-camera visual slam for autonomous navigation of micro aerial vehicles. *Robotics and Autonomous Systems*, 93:116–134.
- Yang, Y., Liu, Y., Li, Y., Arcondoulis, E., Wang, Y., Li, W., and Huang, B. (2018). Aerodynamic and aeroacoustic characteristics of a multicopter propeller during forward flight. In *2018 Joint Propulsion Conference*, page 4892.
- Yoon, S., Diaz, P. V., Boyd Jr, D. D., Chan, W. M., and Theodore, C. R. (2017). Computational aerodynamic modeling of small quadcopter vehicles. In *American Helicopter Society (AHS) 73rd Annual Forum Fort Worth, Texas*.

- Yoon, S., Lee, H. C., and Pulliam, T. H. (2016). Computational analysis of multi-rotor flows. In *54th AIAA Aerospace Sciences Meeting*, page 0812.
- Yuen, H., Princen, J., Illingworth, J., and Kittler, J. (1990). Comparative study of hough transform methods for circle finding. *Image and vision computing*, 8(1):71–77.
- Zlot, R. and Bosse, M. (2014). Efficient large-scale 3d mobile mapping and surface reconstruction of an underground mine. In *Field and service robotics*, pages 479–493. Springer.